# A Transportable Ytterbium Optical Lattice Clock with Eighteen Digits of Accuracy

by

**Wesley Brand**

B.A., University of Minnesota Morris, 2015

A thesis submitted to the
Faculty of the Graduate School of the
University of Colorado in partial fulfillment
of the requirements for the degree of
Doctor of Philosophy
Department of Physics
2024

Committee Members:
Andrew Ludlow, Chair
Elizabeth Donley
Laura Sinclair
Scott Papp
Henry Kapteyn

Brand, Wesley (Ph.D., Physics)

A Transportable Ytterbium Optical Lattice Clock with Eighteen Digits of Accuracy

Thesis directed by Dr. Andrew Ludlow

This thesis presents the development and uncertainty evaluation of a transportable ytterbium optical lattice clock, achieving a total systematic uncertainty level of $3.7 \times 10^{-18}$. Built into a compact rack-mounted design, this clock combines portability with high accuracy, suitable for a range of scientific applications. A detailed examination of the clock's construction and operational mechanisms is provided, highlighting the integration of technologies that facilitate its transportability without compromising accuracy and providing guidance to future users. The uncertainty budget is emphasized, describing the details of each measurement needed to characterize the systematic shifts on the clock frequency. In addition, this thesis encompasses a field test conducted at the US Naval Observatory, demonstrating the system's robustness and reliability in transportation and operation under varied conditions. This work not only sets a new standard in portable optical lattice clock technology, but also demonstrates the clock's utility in advancing global timekeeping and geodetic measurements with near-centimeter resolution, significantly contributing to the fields of relativistic geodesy and the potential redefinition of the SI second.

# Dedication

To my loving family and friends, your encouragement and belief in me have made all the difference. I am forever grateful for your support.

# Acknowledgements

This work would not have been possible without the contributions of many friends and colleagues.

First, I thank Andrew Ludlow, “a true Clock Hero,” [1] for his mentoring and wisdom throughout my PhD.

I especially thank everyone who has a part of the portable clock project: Richard Fox, Yun-Jhih Chen, Jonathan Friduss, Chris Oates, and, in particular: Toby Bothwell, who built a darn tough cavity and pushed me to be a better scientist, and Robbie Fasano, who brought enthusiasm and incredible technical ability to the project along with friendship. I also thank the colleagues who will carry on the portable torch: Tristan Rojo and Eric Swiler, who are always impressing me with their ability to learn and contribute to the experiment; Adam Halaoui, who is bringing in new vigor and a willingness to master the experiment; and Roger Brown, who has brought an immense amount of timekeeping knowledge and guiding voice to the project.

I thank the many people who have worked on the lab Yb clocks during my time at NIST for their stimulating conversations and wealth of expertise: Kyle Beloy, Jacob Siegal, Ben Hunt, Chun-Chia Chen, Youssef Hassan, Tanner Grogan, Takume Kobayashi, Daniele Nicolodi, Will McGrew, and Xiaogang Zhang.

Many of our coolest custom tools on the portable experiment were made by the electronics wizards of the NIST Phase Noise Metrology group: Marco Pomponio, Craig Nelson, and Archita Hati.

A huge thanks to the folks at the US Naval Observatory for graciously hosting us and putting in extra time while we were visiting: Steven Peil, Thomas Akin, and Joseph Whalen.

Thank you to the many friends who have helped me make it though graduate school, especially Drew Morrill, Jose Valencia, Max Urmey, Patrick Duvall, Sean Michael Kelly, and Max Chen. Thank you to those who have generously given their time to the Boulder improv community, particularly Jay Murdoch and Rebecca Bradford.

Finally, I express my profound gratitude to my family. To my mom, dad, and sister who have supported me all the way.

# Contents

**Chapter**

**Appendix**

# Tables

Table

# Figures

Figure

# Chapter 1

# Clocks with 18-Digit Accuracy Enable Interesting and Useful Applications

This thesis is aimed at technical users wishing to build and operate a portable lattice clock with eighteen digits of accuracy. Therefore, this introduction will be brief, and fluency in the basic ideas of time-keeping such as stability and precision measurement will be assumed. For more background, the optical clocks review article by Ludlow et al. [2] discusses the field of optical timekeeping and the previous thesis on the portable clock by R. J. Fasano [3] discusses clock stability and accuracy design goals of the NIST portable Yb optical lattice clock.

Transportable optical lattice clocks, with their high accuracy and stability, are nearing technological readiness to advance several scientific fields [4, 5]. In relativistic geodesy, these clocks will facilitate chronometric leveling with unprecedented precision. A portable clock with $1 \times 10^{-18}$ accuracy is capable of resolving 1 cm height differences due to gravitational redshift, thus improving geodetic measurements and aiding earthquake prediction research [6, 7, 8, 9, 10, 11].

Notably, transportable strontium optical lattice clocks (OLCs) and single ion clocks have reported uncertainties in the mid $10^{-18}$ decade [12, 13, 14, 15, 16, 17]. These technological strides in transportable optical clocks are pivotal for a range of applications, including the redefinition of the SI second [18], searches for new physics and gravitational phenomena [19, 20, 21, 22, 23, 24, 25, 26, 27], enhancements to terrestrial and ultimately spaceborne Very Long Baseline Interferometry [28], and geodetic measurements [6, 7, 8, 9, 11]. These clocks have been deployed in proof of concept measurement campaigns, demonstrating their prospects for utility in both chronometric leveling [29, 30, 10] and tests of general relativity [31].

State-of-the-art laboratory optical clocks have reached systematic uncertainties and reproducibilities at or below the $1 \times 10^{-18}$level [32, 33, 34, 35, 36, 37, 38, 39]. While transportable lattice clocks have not matched their laboratory-based peers in systematic uncertainty, continued efforts to reach low 18-digit accuracies will enable practical applications and fundamental measurements; in particular, this accuracy is required for advancements in geodesy beyond classical techniques.

The potential redefinition of the SI second hinges critically on the advancements in optical clock technology. The Consultative Committee for Time and Frequency stipulates that for a successful redefinition, multiple comparisons of optical clocks—both of the same atomic species and frequency ratios of different species—at various metrological institutions are essential, with verified uncertainty budgets below $5 \times 10^{-18}$ [18, 40, 41]. These comparisons not only validate the performance of individual clocks, but also ensure the consistency and reliability of the frequency standards across different platforms and locations, a prerequisite for the global acceptance of a new definition for the second.

Currently, time and frequency transfer techniques, such as fiber networks and free-space transfer methods, have shown the capability to transfer average frequencies well below $1 \times 10^{-18}$. Fiber links, for instance, have demonstrated high precision in frequency transfer over considerable distances [42, 43, 44, 45, 46, 47, 48]. Similarly, free-space links have been employed for optical frequency transfer with promising results demonstrating robust frequency transfer capabilities well below the $10^{-18}$ level [49, 50, 51, 52, 53, 54, 55, 56]. However, these methods are not yet suited for the intercontinental transfer necessary for the redefinition of the SI second, although important work towards that goal continues. In contrast, Two-Way Satellite Time and Frequency Transfer (TWSTFT) and Very Long Baseline Interferometry (VLBI) techniques, operating over global baselines, have not yet demonstrated the ability to average down to the low eighteen digit level, which is essential for redefinition goals and global-scale applications [57, 58, 59, 60, 61]. Uniquely, transportable clocks offer a platform capable of making intercontinental frequency comparisons at the required level for redefining the SI second.

In VLBI, the improved stability of these clocks is useful for enhancing resolution, particularly in the development of future space-borne VLBI systems [28, 62, 63]. Furthermore, the deployment of these clocks in diverse geographical locations, and later in space, offers significant potential for probing dark matter, testing variations in fundamental constants, or searching for gravitational waves, thereby contributing to our understanding of new physics and gravitational phenomena [19, 20, 21, 22, 23, 24, 25, 26, 27, 64, 65, 66].

Building on advancements in optical lattice clocks, we demonstrate for the first time a portable ytterbium optical lattice clock system. This system represents a step in technological readiness towards the aforementioned scientific goals and has demonstrated remote deployment at a location 2700 km away from its home lab [67]. Our clock system is characterized by its rack-mounted, modular design, high uptime, and 18-digit accuracy, making it a viable tool for both laboratory experiments and field deployments. **In this thesis, we report a $\mathbf{3.7 \times 10^{-18}}$ uncertainty evaluation.**

# Chapter 2

# The Experimental Apparatus

## 2.1 Overview

The atomic system described here is modular like other transportable clock designs [68, 69, 13, 70, 71] and is built into two 24U 19” rack units. The apparatus is shown in Figure 2.1. Details of the layout of the racks are shown in Figure 2.2. These racks contain all of the lasers for atom cooling, trapping, and state preparation excluding the clock laser. They also contain the computer and central control system. In addition to the atomic system, we employ an optical frequency comb from Menlo Systems that may be phase locked to the clock laser. Three of the four trapping and state preparation lasers may then be phase-locked to this comb. Prior to locking with the comb, we used a multi-color cavity to lock these lasers with the Pound-Drever-Hall (PDH) technique. For our previous deployment [67], we developed an ultrastable clock laser system; however, for the measurements described in our uncertainty budget, we used a laboratory clock laser system. Many particular products will be mentioned in this chapter; they are named for specificity and do not constitute an endorsement by NIST.

Discussion in this chapter will be in two primary sections describing separately the physics package 2.2 and the laser systems 2.3. Both sections will be arranged to describe components in approximate operational order for a clock operation sequence: in-vacuum atomic beam generation, 399 nm laser MOT cooling, 556 nm laser MOT cooling, 759 nm laser lattice trapping, quenched sideband cooling with the 1388 nm repump laser and 578 nm clock

Figure 2.1: A pair of 19” server racks houses the atomic trapping and control infrastructure. Specific components are detail in Figure 2.2. More recent additions include laser curtains around the physics package and lattice laser module that are both for laser safety and shielding the atoms from room temperature changes or resonant light sources. The Keithley digital multimeter for temperature readout is also not included in this picture. This view is from the “front.”

Figure 2.2: Layout of the racks. Yellow boxes indicate general infrastructure for the system such as electrical power and control interfaces. Blue boxes indicate hardware for controlling the physics package. Lavender boxes indicate hardware for the 399 nm laser system. Green boxes indicate space occupied by the 556 nm laser system. Red boxes indicate space occupied 759 nm laser hardware. Orange boxes indicate space occupied by the 1388 nm repump laser system. About 20% of the racks are empty space, reduction of which presents one of the most straightforward ways to reduce system size and weight. Additional low-hanging targets for SWAP reduction are bloated control electronics packages for the 759 nm and 399 nm laser systems and omission of ion gauges.

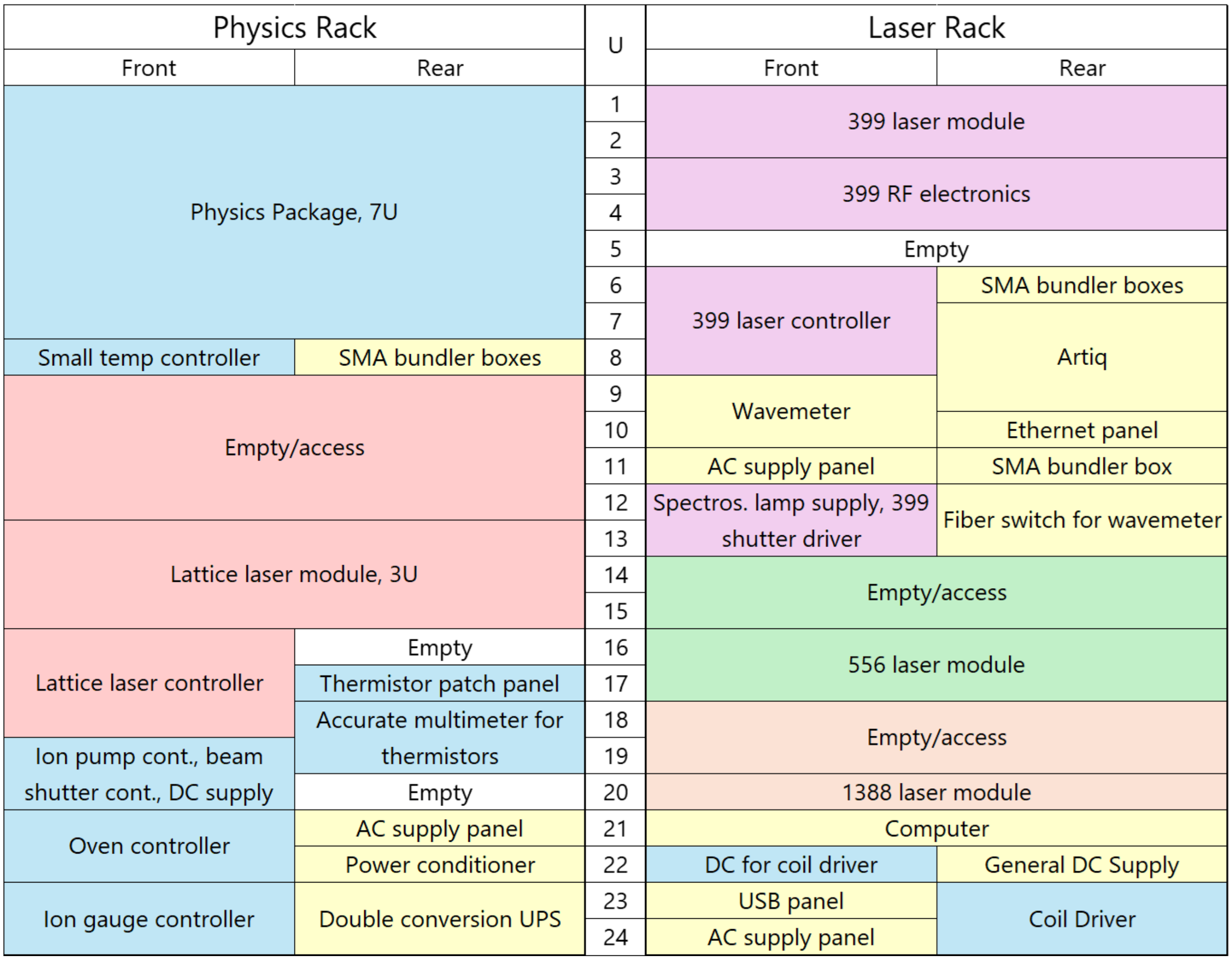

| Physics Rack | | U | Laser Rack | |
|---|---|---|---|---|
| Front | Rear | | Front | Rear |
| Physics Package, 7U | | 1 | 399 laser module | |
| | | 2 | | |
| | | 3 | 399 RF electronics | |
| | | 4 | | |
| | | 5 | Empty | |
| | | 6 | 399 laser controller | SMA bundler boxes |
| | | 7 | | Artiq |
| Small temp controller | SMA bundler boxes | 8 | | |
| Empty/access | | 9 | Wavemeter | |
| | | 10 | | Ethernet panel |
| | | 11 | AC supply panel | SMA bundler box |
| | | 12 | Spectros. lamp supply, 399 shutter driver | Fiber switch for wavemeter |
| Lattice laser module, 3U | | 13 | | |
| | | 14 | Empty/access | |
| | | 15 | | |
| Lattice laser controller | Empty | 16 | 556 laser module | |
| | Thermistor patch panel | 17 | | |
| | Accurate multimeter for thermistors | 18 | Empty/access | |
| Ion pump cont., beam shutter cont., DC supply | | 19 | | |
| | Empty | 20 | 1388 laser module | |
| Oven controller | AC supply panel | 21 | Computer | |
| | Power conditioner | 22 | DC for coil driver | General DC Supply |
| Ion gauge controller | Double conversion UPS | 23 | USB panel | Coil Driver |
| | | 24 | AC supply panel | |

laser, spin polarization, clock spectroscopy, and state readout. The physics package section will give the majority of details related to clock operation and only supporting descriptions of the lasers will be provided in those sections. Some aspects of the physics package and laser systems have already been described in the previous thesis on this project [3]. To avoid redundancy, relevant sections of that thesis will be pointed to for its hardware descriptions; this thesis will then focus on hardware changes and key operational details that have been learned since then. For example, the system was largely spread across optical tables rather than in racks at that time. Also new are most details of both the transportable clock laser system and the control scheme for the lab clock laser system that are unique to the portable system. Minor operational details such as alignment and detailed schematics of the laser systems will be covered in the appendices for operation A and construction of the system B. The next subsection will discuss some details of the rack infrastructure that might be skipped by the reader more interested in physics.

### 2.1.1 Rack Infrastructure

The two racks (C2F194236BK1, Hammond Manufacturing) are 1.25 m tall × 0.58 m wide × 0.91 m long occupying a combined volume of 1.37 $\mathrm{m}^3$. They are estimated to each have a mass between 100 and 120 kg. The racks have both caster wheels for movement and leveling feet for reduced vibration operation (in practice, we usually only lower the feet on the physics rack). The square holes support mounting our control PC and a choice of square nut mounting components. It is our strong recommendation in portable systems for 1) the use of heavy gauge screws to reduce the risk of failure or seizing from transportation stresses and, 2) the use of a thread locking adhesive to prevent screws from backing out in transportation. In particular, M6 screws are the heaviest gauge common rack screws and medium strength thread locker in glue-stick packaging works well with these screws. No manufacturer currently makes what we consider to be the ideal rack mounting hardware which would be; a G-style cage nut for 14 gauge sheet and M6 screws with: a dog-point, a large pan head, a deformable lock washer to mate with the square hole, and a modern anti-cam out drive. We presently use screw-cage nut hardware from Startech (CABSCREWM6) where the cage nuts are placed with a specialty tool (106-7566, RackSolutions).

The atomic system is powered with a single 20 Amp AC input. The power first goes through a power conditioner (P-8 PRO C, Furman) for protection from both sustained and transient over-voltage conditions. The power from the conditioner is fed directly into a double conversion uninterruptible power supply (UPS) (9PX2000RT-L, Eaton). The double-conversion UPS topology where power is always supplied from battery DC-AC conversion provides greater protection from changes to line voltage conditions and also suppresses ground loop noise by setting the AC neutral to the clean battery low voltage. Prior experience with moving the system has shown that "away" labs may have lower quality AC power than the home lab and that plugging the system components into several wall outlets can create significant ground-loop issues. From the UPS, AC power is radiated in a star pattern to different components in the physics package and a single cable takes power from the physics package UPS to the AC distribution in the laser rack. Key vacuum components in the physics rack are connected to the high priority bank of the UPS. With all other components off, the UPS can provide these components with power for over two hours. Both racks have copper ground bus bars connected to earth ground and all units with chassis ground connections are bonded to the bus bar with heavy gauge wires to ensure electrical safety. Most DC power originates from a home-built[1] 1U switching power supply that feeds regulators in the laser modules with several DC voltages: typically ±5 V, ±12 V, and 15 V. The physics rack has relatively high demand for ±12 V and 24 V so it has compact additional power modules for these voltages. The total power demand for the system in operation is typically 700 W as read from the UPS panel.

The operational sequence of the system is orchestrated from the M-Labs Artiq field programmable gate array (FPGA) hardware. A rack-mounted PC programs Artiq with a

---

[1] by the NIST Phase Noise Metrology Group's Marco Pomponio and Craig Nelson

control sequence and communicates with the hardware for data-acquisition and executing real-time updates to the control sequence. This communication is managed by home-made control code called "Argent." Most details about Argent can be found in the associated Git repository [2] and in [3], section 2.11. In brief, Artiq is capable of executing a sequence with nanosecond timing precision of transistor-transistor logic (TTL) trigger pulses, radio frequency (RF) frequency and amplitude modulation for acousto-optic modulator (AOM) devices, digital-to-analog (DAC) signals for voltage control of electronics, and analog-to-digital (ADC) sampling for voltage measurements. Subsequent timing diagrams shown are based on the relevant parts of the Argent graphical user interface. More recently, we have added an oven-controlled crystal oscillator (OCXO) unit[3] to the Artiq box that may be phased locked to an external 10 MHz reference (a timescale maser when at NIST). The OCXO has outputs at 10 MHz, 100 MHz, and 1 GHz, of which, we use the 100 MHz to reference the Artiq direct digital synthesizers (DDS) for accurate frequency generation to the clock laser AOM(s).

## 2.2 Physics Package

The physics package, shown in Figure 2.3, is built on top of a custom aluminum breadboard to reference the optics to the chamber geometry. This section will first describe the vacuum chamber and then describe the physics of the operational sequence in order to describe the components of the physics package.

### 2.2.1 Vacuum Chamber

The vacuum chamber is divided into an oven section and a spectroscopy chamber separated by a differential pumping aperture, a layout similar to other transportable clock vacuum systems [72, 73, 74]. The entire vacuum chamber is 59 cm long and fabricated

---

[2] https://github.com/robertfasano/argent

[3] made by the NIST Phase Noise Metrology Group's Craig Nelson and Marco Pomponio

Figure 2.3: The optical and vacuum layout around the spectroscopy chamber was designed for both low volume and ease of alignment. The labelling color scheme follows that of Figure 2.2, with the change that yellow now refers to the 578 nm (yellow) clock laser.

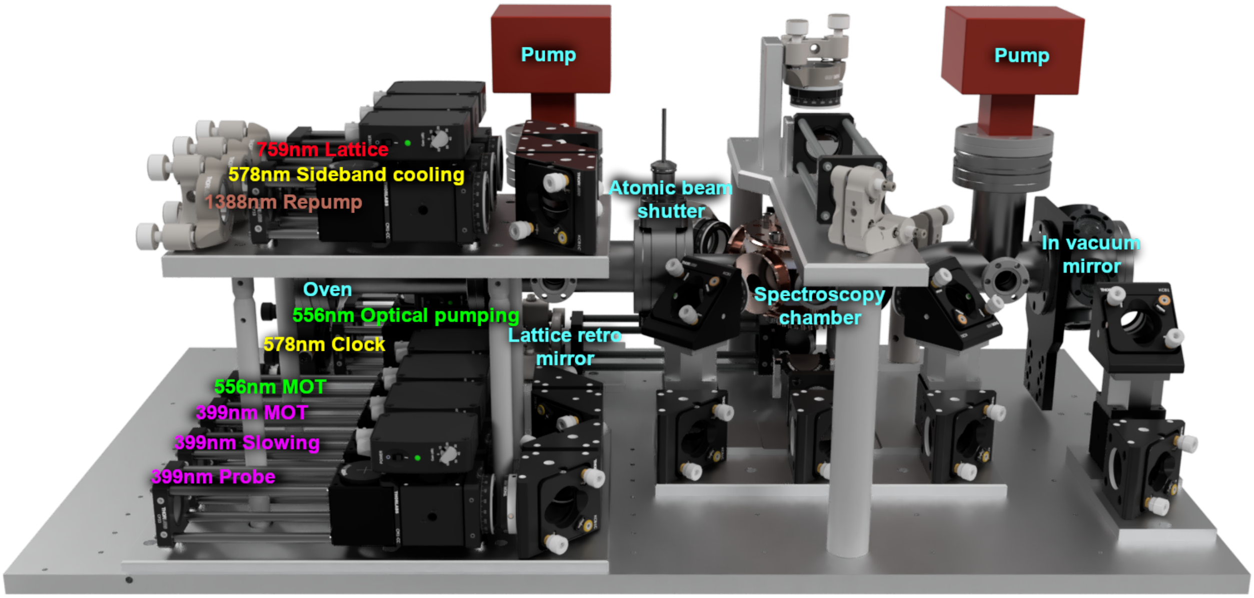

from several custom parts mated together using CF flanges. Each section is pumped by a combination ion-non evaporable getter (NEG) pump (Z-100, NexTorr). The ion gauge (BA600DYE, Instrutech) on the spectroscopy chamber measures an X-ray-limited pressure $5 \times 10^{-10}$ Torr which was reached at the end of the chamber bakeout while the spectroscopy chamber was at 130 C, down from a maximum of 150 C. The ion gauge is not normally on during clock operation due to thermal outgassing. The oven side of the chamber originally had an ion gauge, but it was found to have a small atmospheric leak during the first bakeout and was replaced with a blank CF flange. The ion pump on the oven side of the chamber typically reads $2 \times 10^{-9}$ Torr during clock operation, but will fall to its reading limit if the oven temperature is turned down. The spectroscopy chamber-side ion pump typically reads $1.2 \times 10^{-11}$ Torr during clock operation, a value that is lower than it should be trusted at due to leakage currents. At these low pressures, the ion pumps sometimes will not start their sputtering currents. Two useful techniques to get them started are 1) to increase the pressure by degassing the ion gauge or (briefly) starting the NEG activation sequence, 2) setting the ion pump controller to a thirty second “Hi-Pot” start at 7 kV which uses higher voltage to start the current flow. Banging on the ion pumps is not a good method for anything but denting the metal in our experience.

The vacuum chamber is initially pumped down with a turbomolecular pump backed by a dry scroll pump. At the end of the bakeout, the pressure is below $1 \times 10^{-10}$ Torr as measured by the larger pumping station ion gauge. Residual gas analysis indicates that hydrogen gas dominates the background gas spectrum by a factor of 100, an important detail for the background gas systematic shift which assumes a hydrogen-dominated vacuum atmosphere. The chamber is sealed off from the pumping station with a pair of 3/4” OD copper pinch-off tubes with a compressive cold-welding device. Further details of vacuum techniques used to reach these low pressures and to successfully use large diameter pinch-off tubes are contained in the appendix B.

An oven loaded with 20 g of sublimed dendritic ytterbium metal supplies an atomic vapor to the spectroscopy chamber. The oven is divided into two zones, the main crucible is usually operated at 465 C and the tip of the oven is kept at 515 C to prevent clogging. In other experiments where the oven temperature is varied, the tip is always kept 50 C hotter than main crucible. A solenoid-driven wobblestick shutters the atoms during clock spectroscopy. Both the physical stops of the wobblestick and electronic control stops are calibrated to ensure the wobblestick consistently moves to a completely open and completely closed position. When taking accurate data, these stops should be recalibrated every few weeks to ensure blocking of both the ytterbium beam and oven blackbody radiation (BBR) which cause systematic shifts. The solenoid (191995-030, Ledex) wears out every 6 months (it gets "sticky") and it is prudent to keep a stock of replacements on hand. A differential pumping aperture is built into the atom chamber to suppress the excess pressure from the oven. The narrow differential pumping aperture also limits the solid angle of BBR emitting surfaces far from the spectroscopy chamber where temperatures are carefully measured.

The spectroscopy chamber, shown in Figure 2.4, was manufactured from titanium with a BBR aperture-limiting geometry inspired by the design of our laboratory lattice clock [75]. The spectroscopy chamber was designed to be compact (25 mm x 55 mm x 55 mm), which helps to reduce the power consumption of the MOT coils and, in turn, reduce coil-generated BBR inhomogeneities. The interior of the spectroscopy chamber was coated with a high emissivity electrically conductive material (MLS-SB-85-C, AZ Technology) to homogenize the blackbody radiation (BBR) shift. The 14 mm diameter N-BK7 viewports are anti-reflection coated for our laser wavelengths on both sides. The inner faces of the viewports are coated with indium tin oxide (ITO) and attached to the chamber with a low-temperature brazing technique that forms a Faraday shield around the atoms. The ability to attach the viewports with a low temperature process is an important consideration because the thin ITO coating is not rated for temperatures above 200 C. Our original chamber, which was the one used in the deployment to the US Naval Observatory, had viewports bonded with a vacuum-compatible epoxy (H77T, Epoxy Technology). The epoxy seals also could be made with low temperatures. The epoxy seals also had the desirable feature of letting the ITO coatings be used as electrodes accessible with electrical feedthroughs in the epoxy. Howeverm the epoxy was susceptible to gaseous diffusion. The epoxy-sealed chamber originally pumped down to a $5 \times 10^{-10}$ Torr pressure, but climbed to a pressure of $2.2 \times 10^{-8}$ Torr over several months.

Figure 2.4: The compact spectroscopy chamber was fabricated from titanium which one of vendors claimed was most suitable for a low-temperature brazing technique to attach the windows. Thermistors for BBR evaluation are secured in the drilled holes or the window braze ring grooves. The high-emissivity “black” coating for homogenizing the BBR can be seen inside the chamber. The differential pumping tube towards the oven can be seen on the far side of the chamber. The top viewport might be noted to have a slight tilt (2°) which was designed on all of the viewports to prevent optical etalons around the atoms.

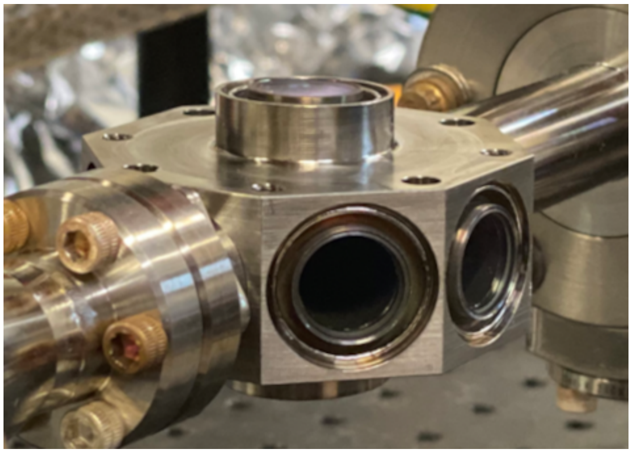

The spectroscopy chamber has eight viewports providing optical access for the MOT, lattice, clock, and state preparation lasers. Additional optical access is available on the atomic beam axis by reflection off of an in-vacuum mirror opposite the atomic beam oven. The mirror is aluminum coated and was designed to have the capability of being heated to 400 C to purge ytterbium buildup in-situ. A later test, however found that the some trace metal in the 6061 aluminum mirror mount outgassed at these temperatures, and sputtered onto the window. This effect reduced the slowing window transmission to nearly zero.

Early work on the portable system included testing a grating MOT (GMOT) [76, 3, 77] for use in the spectroscopy chamber. We were not able to capture an adequate number of atoms in the first stage of cooling of the side-loaded GMOT for advancing towards clock spectroscopy. While, future transportable lattice clocks might benefit from the simplicity and robustness of a single beam GMOT, this work will not further consider this design.

The quadrupole coils are designed to minimize their potential to create an inhomogeneous thermal environment around the spectroscopy chamber. An important physical principle in low power coil design is that: *for a coil occupying a fixed volume and wound from a wire of constant cross-sectional area, $A$, (with perfect packing efficiency) the power dissipated by the coil to generate a fixed magnetic field some distance away is independent of $A$.* That is, your choice of wire geometry cannot improve power dissipation through purely electrical considerations. This principle restricts our choices of methods to manage heat in a passively-cooled design. However, we can design the coils to 1) reduce the distance between the coils and the atoms since magnetic field strength is proportional to $1/r^3$, 2) increase the packing efficiency of the wire, and 3) use wire geometry to improve thermal conduction away from the area we want to avoid heating.

The chamber and quadrupole coils were designed together such that the quadrupole coils have a 28 mm spacing between their surfaces. The coils are made from 1 mm x 7 mm rectangular wire (040X289 HPM, S & W Wire) to maximize wire packing efficiency and improve thermal conduction to the coil heat sink by having the long axis of the rectangular profile lead between chamber and heat sink. The design is similar to much higher power coils used to access Feshbach resonances [78]. In operation, the coils draw 20 A to produce a 4.5 mT/cm trapping field and at a typical 8% duty cycle use a cycle-averaged power of 0.35 W. This power is within 5% of the design power as calculated from integrating the Biot-Savart law over the coil volume. While this calculation is computationally straightforward, a useful trick is that since only calculation of a field gradient is required for trapping, one may apply the fundamental theorem of calculus and cancel the most difficult integral. A rigid polypropylene shield (a low thermal conductivity printable plastic) separates the coils from the chamber and mates with both the chamber and coils for precision alignment. When the experiment is set up for accurate performance, the temperature gradient throughout the chamber does not exceed 35 mK.

Figure 2.5: The low power trapping coils are made with rectangular wire bonded to a convective heat sink with a thermally conductive epoxy. The techniques of fabricating these coils are described in appendix B.

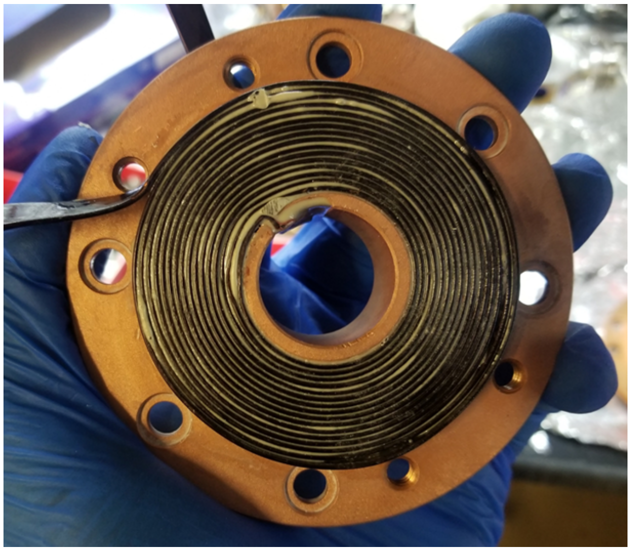

Three pairs of bias coils are used to control the magnetic field during spectroscopy and state preparation. All four of the coil pairs are supplied by a home-made[4] coil control system capable of switching even the quadrupole coil fields in less than 1 ms. The coil control system additionally has temperature controlled current sense resistors for stable long-term reproducibility of the bias fields. The maximum fields of the X and Y bias coils are 12 G and the maximum field of the Z bias coil is 2 G. In normal operation, the sum of the X and Y fields points towards the photomultiplier tube and the Z field points upwards.

---

[4] by the NIST Phase Noise Metrology Group's Marco Pomponio and Craig Nelson

### 2.2.2 Cooling and trapping

To capture atoms in a lattice at $< 10$ $\mu$K starting with a 465 C atomic beam, several stages of laser cooling on two different atomic transitions are used. The full cooling sequence is shown in Figure 2.6. For all sequence diagrams described in this and the following sections, the following notations are used. TTL "high" (5 V) is marked by green boxes and TTL "low" (0 V) is marked by red boxes. Optical powers are usually notated by dB of attenuation relative to the highest power. For some optical power control, an intensity servo is not used and only Artiq control of RF power, these are marked with asterisks to note that the dB attenuation is applied to the RF power and may not reflect the exact optical power due to nonlinear AOM effects. Optical frequencies are usually notated as detunings from the unperturbed atomic transition in natural linewidth units(for the 399 nm transition, the natural linewidth $\Gamma = 2\pi \times 29$ MHz, and for the 556 nm transition $\Gamma = 2\pi \times 180$ kHz). When arrows connect two quantities in the same cell, Artiq implements a linear digital ramp between those quantities. Usually the ramp has ten steps unless smoother ramping is desired as is the case for adiabatic lattice ramps. When an arrow is alone in a cell, the control implemented in the previous cell is maintained until either another change is performed or the sequence begins again.

Atoms are initially captured in the chamber by a six beam 399 nm magneto-optical trap (MOT). Both of the 399 nm beams and 556 nm MOT beams are launched from a distribution module where the two MOT beams are overlapped. A slowing beam six atomic linewidths red-detuned assists the first-stage MOT and is directed from the in-vacuum mirror [79]. The slowing and probe beams are launched from the same distribution module where they are overlapped and sent down the atomic beam axis of the chamber. The fiber launch modules include polarization cleanup optics and photodiode pick-offs for intensity control or monitoring.

The strong dipole allowed ${}^1S_0 \rightarrow {}^1P_1$ transition at 399 nm supplies the force necessary

Figure 2.6: The timing sequence for cooling and trapping atoms in the lattice.

| Stage | 399 MOT | Hand off 1 | Hand off 2 | 556 Transfer | 556 Cool | 556 Compression 1 | 556 Compression 2 | Lattice Transfer |
|---|---|---|---|---|---|---|---|---|
| | 80 ms | 1 ms | 1 ms | 11 ms | 8 ms | 13 ms | 16 ms | 8 ms |
| TTLs | | | | | | | | |
| Slowing shutter open | 🟩 | 🟥 | 🟥 | 🟥 | 🟥 | 🟥 | 🟥 | 🟥 |
| 399 MOT shutter open | 🟩 | 🟩 | 🟩 | 🟥 | 🟥 | 🟥 | 🟥 | 🟥 |
| 556 Max power | 🟩 | 🟩 | 🟩 | 🟩 | 🟥 | 🟥 | 🟥 | 🟥 |
| 578 SB optical switch | 🟥 | 🟥 | 🟥 | 🟥 | 🟥 | 🟥 | 🟩 | 🟩 |
| 578 SB RF switch | 🟥 | 🟥 | 🟥 | 🟥 | 🟥 | 🟥 | 🟥 | 🟩 |
| Optical powers | | | | | | | | |
| 399 Slowing | ~15 mW = 0 dB | Light off, AOM "on" | | | | | | |
| 399 MOT* | ~15mW = 0 dB | -15 dB | -22 dB | Off | → | | | |
| 556 MOT | ~3mW = 0 dB | → | | | -3.2 dB → -7.8 dB | -7.8 dB → -23.8 dB | -23.8dB | -23.8 dB |
| 759 Lattice | 150 Er | → | | | | | | |
| 578 Sideband* | Off | → | | | | | | -21 dB |
| Optical detunings | | | | | | | | |
| 399 Slowing | - 6 Γ | - 7.2 Γ, Frequency is out of AOM passband and extinguishes light while avoiding thermalization issues | | | | | | → |
| 399 MOT | - 0.5 Γ | → | | | | | | |
| 556 MOT | - 25.7 Γ | - 25.7 Γ | - 25.7 Γ → - 15.4 Γ | - 15.4 Γ | - 15.4 Γ → - 5.96 Γ | - 5.96 Γ → -3.18 Γ | - 3.18 Γ → -2.07 Γ | -2.07 Γ |
| 759 Lattice | Magic wavelength | → | | | | | | |
| 578 Sideband | Off | → | | | | | | 0 kHz |
| Samplers | | | | | | | | |
| 399 MOT power, PD | Mean, 10 samples | Off | → | | | | | |
| 399 slowing power, PD | Mean, 10 samples | Off | → | | | | | |
| Other DAC | | | | | | | | |
| Quadrupole field | 45 G/cm | 26 G/cm | 6.5 G/cm | → | | 6.5 → 11.5 G/cm | 11.5 → 21.5 G/cm | 21.5 G/cm |
| Atomic beam shutter | 0.5 V | → | | 0.5 V→ 0.42 V | 0.42 V → 0.34 V | 0.34 V→ 0.27 V | 0.27 V | → |

to cool and trap atoms from the oven's thermal beam. Details about the physics of the first stage MOT in the portable clock may be found in [3] Section 2.2. For reference, we include the level diagram for $^{171}$Yb, in Figure 2.7, which determines much of the important physics in the clock. The 399 nm MOT is loaded for 80 ms in the high accuracy operational mode. More atoms may be captured with longer loading times, up to 300 ms, but comes with the drawback that the quadrupole coils generate more heat and subsequently decrease the homogeneity of the BBR environment. Atom number in the 399 nm MOT is difficult to quantify with high accuracy due to the 399 nm probe beam diameter's optimization for interrogating the lattice at a high saturation intensity, which results in undersampling the MOT volume. However, based on the radiant intensity of the MOT, we expect that the 80 ms MOT traps $\approx$ 100,000 atoms. The Doppler limit is given by the formula $k_B T = \hbar\Gamma/2$ and for the 399 nm MOT is $T = 700$ $\mu$K [80]. Since this temperature is too hot to load atoms at accessible lattice depths in the portable system, we must further cool the atoms on a transition with a narrow linewidth.

The spectrally narrower ($\Gamma = 2\pi \times 180$ kHz) $^1S_0 \rightarrow\ ^3P_1$ transition at 556 nm provides the next stage of cooling. In the last two years, details of the 556 nm MOT have been more heavily optimized both for increasing final lattice trapped atom number and so that we have the benefit of a reliable sequence when setting up the clock in a remote location. Most of the optimization was performed with Artiq using two-dimensional sweeps on pairs of correlated variables to optimize final lattice trapped atom number. Prior to having a reliable sequence, setting up in a new location required multi-step optimization of this MOT to have adequate lattice-trapped atom numbers and potentially required time-of-flight imaging to ensure an adequately cold atomic cloud before attempting to trap atoms in the lattice. When we went to USNO, we instead only needed to optimize the 'global green' frequency offset and alignment of the MOT. Now, with the upgrade of a comb-referenced lock for the 556 nm laser, we should only require alignment optimization. Methods for aligning this MOT may be found in appendix A.

Figure 2.7: The level diagram for $^{171}$Yb. The first stage of cooling occurs on the dipole allowed $^1S_0 \rightarrow^1 P_1$ transition that is strong enough to cool atoms from a thermal beam. The second stage cooling occurs on the $^1S_0 \rightarrow\ ^3P_1$ inter combination transition that permits cooling to the single $\mu$K level. The $^1S_0 \rightarrow\ ^3P_0$ clock transition is "doubly forbidden" since it violates both the spin selection rule ($S = 0 \rightarrow S' = 1$, while total spin cannot change for electric dipole transitions) and the angular momentum selection rule ($J = 0 \rightarrow J' = 0$, which cannot occur since photons carry angular momentum). Therefore the clock transition can only be weakly excited and results in its exceptionally narrow linewidth. The 759 nm wavelength is not a transition, but the magic wavelength which perturbs both clock states equally. The $^3P_0 \rightarrow\ ^3D_1$ transition is used for pumping out of the metastable $^3P_0$ state.

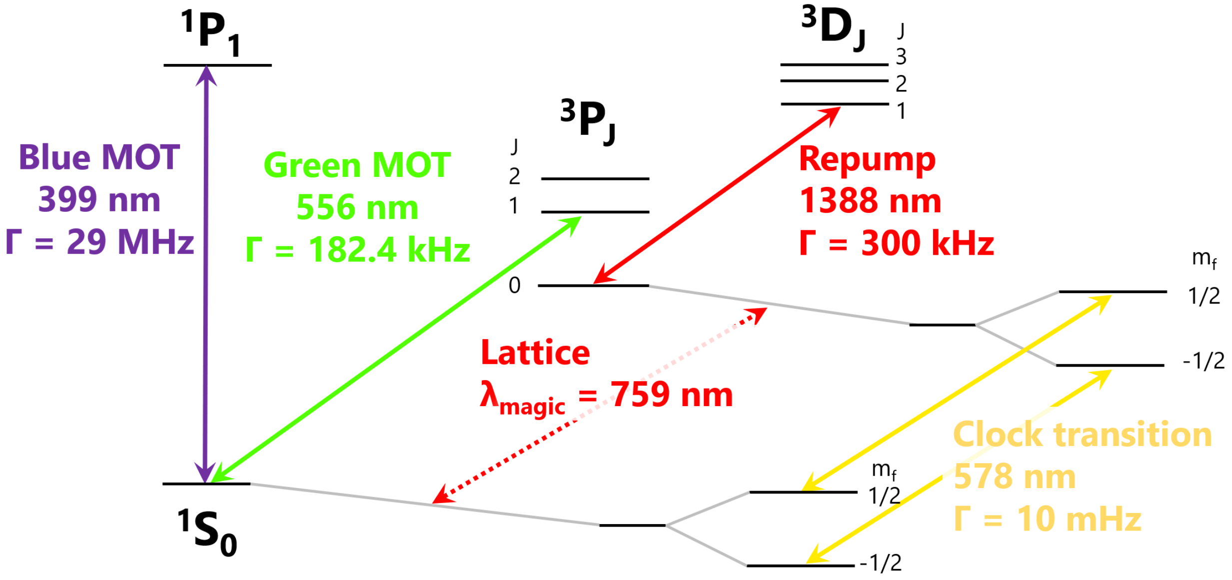

The 556 nm MOT beams are already on at maximum power and red-detuned by -26 $\Gamma$ during the 399 nm MOT. This assistance to the 399 nm MOT was found to increase the final atom number by $\approx 5\%$. The transfer can be performed with $> 90\%$ efficiency by instantaneous AOM shuttering of the 399 nm beams, but we've found that a more controlled hand off technique permits transfer efficiencies indistinguishable from 100% (assessed by fluorescence from flickering the 399 nm MOT beams). In this technique, two 1 ms steps are used. In the first, the slowing beam is shuttered immediately, the RF power to the 399 MOT AOM is dropped by 15 dB, and the magnetic field gradient is approximately halved. In the second, the RF power to the 399 MOT AOM is dropped by another 7 dB, the magnetic field gradient is taken to a level one seventh that of the 399 nm MOT, and the 556 nm detuning is decreased to -15 $\Gamma$. The centers of the 399 nm and 556 nm MOTs are spatially dislocated and we expect that the benefit of this technique comes from more gradual transport of the atoms between these locations.

Now that the atoms are in a purely 556 nm MOT, they begin a process of cooling and compressing their phase-space density. The first "transfer" stage of the 556 nm MOT thermalizes the atoms in a high intensity 556 nm MOT and begins the process of gently closing the atomic beam shutter which is completed before the lattice transfer. In the second "cooling" step, the laser intensity servo is activated and detuning of the laser is ramped to -6 $\Gamma$. The following two "compression" steps have the laser intensity and detuning dropped even further while the magnetic field gradient is stepped up to half the value used in the 399 nm MOT. The goal of this process is to match the size and temperature of the MOT to the spatial and temperature modes of the lattice [81]. Some of the parameters in this sequence have relatively narrow tolerable ranges to work optimally, such as detuning and gradient. Other parameters such as intensity work over relatively large ranges; step length is especially insensitive to changes so we erred on the side of short step lengths to suppress Dick effect.

In the final step of the lattice loading process, 556 nm laser parameters are maintained from the compression sequence and resonant clock light is turned on from the sideband port at a relatively low power. This technique has been found to boost the final atom number by 10-15%. We expect that in the cold dense final MOT, atoms scatter photons that may interact with other atoms. Scattered photons will no longer have the correct polarization and detuning properties to cool and will instead heat the sample [80]. The clock light then selectively shelves the coldest atoms that are already lattice trapped. Only lattice trapped atoms will interact with the clock light since untrapped atoms will witness clock laser light that has been Doppler-broadened by many kHz, suppressing the transition. The shelving then prevents the coldest atoms from being heated out of the lattice by scattered photons. Using either time of flight measurements [3] or spectroscopic measurements described in the next section, we find that atoms are at $10(2)\mu$K after completion of the 556 nm MOT sequence. This temperature is above the Doppler limit of the 556 nm transition, but is consistent with temperatures observed in the lab clocks.

### 2.2.3 State preparation

In preparation for clock spectroscopy, the lattice trapped atoms are 1) cooled to the motional ground state in the axial direction of the lattice, 2) polarized into a single $m_F = \pm 1/2$ magnetic sublevel, and 3) adiabatically ramped to a lower trap depth where the shifts from lattice light and collisions are smaller. This state preparation sequence is shown in Figure 2.8. This section will also contain some description of the physics of lattice trapping in preparation for further discussion related to uncertainty characterization in chapter 4.

The 759 nm lattice laser, the 578 nm sideband cooling/spectroscopy laser, and the 1388 nm repump laser are launched near-coaxially from the upper mezzanine breadboard with dichroic mirrors to overlap the beams. The beams are focused with a 225 mm lens, and descend through the atom chamber at a 15°angle relative to gravity. The beams are then re-collimated with a second 225 mm lens and then retroreflected from a mirror that acts as the clock laser phase reference. The other beams are intentionally slightly askew so that

Figure 2.8: The timing sequence for preparing the states of lattice trapped atoms.

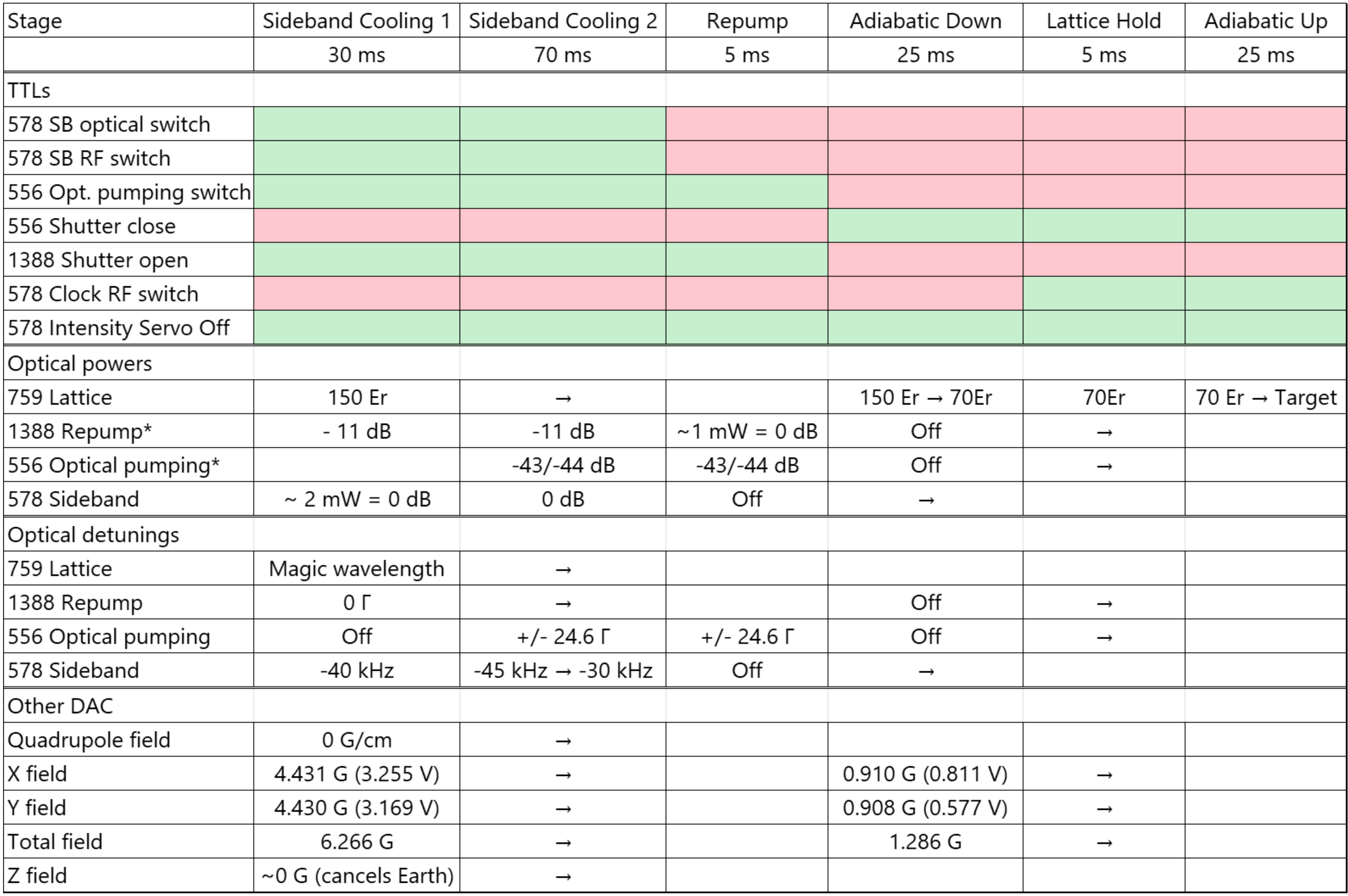

| Stage | Sideband Cooling 1 | Sideband Cooling 2 | Repump | Adiabatic Down | Lattice Hold | Adiabatic Up |
|---|---|---|---|---|---|---|
| | 30 ms | 70 ms | 5 ms | 25 ms | 5 ms | 25 ms |
| TTLs | | | | | | |
| 578 SB optical switch | 🟩 | 🟩 | 🟥 | 🟥 | 🟥 | 🟥 |
| 578 SB RF switch | 🟩 | 🟩 | 🟥 | 🟥 | 🟥 | 🟥 |
| 556 Opt. pumping switch | 🟩 | 🟩 | 🟩 | 🟥 | 🟥 | 🟥 |
| 556 Shutter close | 🟥 | 🟥 | 🟥 | 🟩 | 🟩 | 🟩 |
| 1388 Shutter open | 🟩 | 🟩 | 🟩 | 🟥 | 🟥 | 🟥 |
| 578 Clock RF switch | 🟥 | 🟥 | 🟥 | 🟥 | 🟩 | 🟩 |
| 578 Intensity Servo Off | 🟩 | 🟩 | 🟩 | 🟩 | 🟩 | 🟩 |
| Optical powers | | | | | | |
| 759 Lattice | 150 Er | → | | 150 Er → 70Er | 70Er | 70 Er → Target |
| 1388 Repump* | - 11 dB | -11 dB | ~1 mW = 0 dB | Off | → | |
| 556 Optical pumping* | | -43/-44 dB | -43/-44 dB | Off | → | |
| 578 Sideband | ~ 2 mW = 0 dB | 0 dB | Off | → | | |
| Optical detunings | | | | | | |
| 759 Lattice | Magic wavelength | → | | | | |
| 1388 Repump | 0 Γ | → | | Off | → | |
| 556 Optical pumping | Off | +/- 24.6 Γ | +/- 24.6 Γ | Off | → | |
| 578 Sideband | -40 kHz | -45 kHz → -30 kHz | Off | → | | |
| Other DAC | | | | | | |
| Quadrupole field | 0 G/cm | → | | | | |
| X field | 4.431 G (3.255 V) | → | | 0.910 G (0.811 V) | → | |
| Y field | 4.430 G (3.169 V) | → | | 0.908 G (0.577 V) | → | |
| Total field | 6.266 G | → | | 1.286 G | → | |
| Z field | ~0 G (cancels Earth) | → | | | | |

they do not retroreflect and form standing waves in the spectroscopy chamber. Because the clock laser input for narrow-line spectroscopy has a 99.8% reflective mirror for fiber phase noise cancellation, the sideband spectroscopy input permits a much higher clock laser optical intensity than the narrow-line clock laser input. This high power is useful for performing resolved sideband spectroscopy, which is the experimental basis for the following discussion of the lattice trap depth.

Lattice trapping is fundamentally important to the lattice clock architecture: it permits Doppler-free spectroscopy of the atoms. In the lattice, atoms are confined to quantized motional states and no longer have the Doppler spectrum of a free gas, which even at the low temperatures in the MOT would result in a prohibitively large linewidth (several kHz) for high-resolution spectroscopy. Moreover, the recoil from atomic absorption of clock laser photons would create a large shift on the transition. In the Lamb-Dicke regime [82], the strong confinement of the lattice absorbs these recoils, preventing impact on the interactions between atoms and clock photons.

The lattice laser creates a spatial potential confining the atoms in the axial direction ($z$) and the radial directions ($\rho^2 = x^2 + y^2$)

$$V_0(z, \rho) = -\frac{E_0^2}{4}\alpha_{E1}(\nu_L)\exp\left(\frac{-2\rho^2}{w_0^2}\right)\cos^2\left(\frac{2\pi\nu_L z}{c}\right) \tag{2.1}$$

where $E_0$ is the electric field of the lattice, $w_0$ is the waist of lattice at the beam focus ($1/e^2$ radius of intensity), and $\alpha_{E1}(\nu_L)$ is the electric dipole ($E1$) polarizibility at the lattice frequency, $nu_L$ [83]. As discussed in more detail later 4.2, the lattice wavelength is chosen so that polarizabilities of the ground and excited states are the same, a condition that defines the “magic wavelength.” Both the Gaussian terms and the $\cos^2$ terms may be approximated as quadratics for the potential at sufficiently high trap depth, hence we may consider the atomic motional states to be like those of quantum simple harmonic oscillator. Our lattice achieves a maximum operational depth of 160 $E_r$ where recoil units are defined by the relation

$$E_r = \frac{h^2}{2m\lambda^2} \tag{2.2}$$

where $h$ is Planck's constant, $\lambda$ is the lattice laser wavelength and $m$ is the mass of a $^{171}$Yb atom. We will maintain the notation $U$ to refer to the trap depth of a lattice in recoil units, and $V_0$ to refer to the spatial potential of the lattice throughout discussion of the lattice. This trap depth may be measured with resolved sideband spectroscopy which probes the transitions between motional states with the clock laser. The clock laser excites the transition $^1S_0, n_z = n \rightarrow\ ^3P_0, n_z = n \pm 1$ which occurs at a detuning from the clock transition frequency less than the axial trap frequency

$$\nu_z = 2\sqrt{\frac{UE_r}{h^2}} \tag{2.3}$$

[84]. For lattice depths usable in the portable clock, these frequencies range from 30 kHz to 52 kHz. Figure 2.9 shows examples of sideband spectroscopy on atoms trapped at a similar trap depth both with and without additional stages of cooling. The corner frequencies, $\nu_z$, at 50 kHZ indicate these measurements were made near 150 $E_r$.

Likewise, the radial trap frequency is given by

$$\nu_r = \sqrt{\frac{U}{m\pi^2 w_0^2}} \quad \rightarrow \quad w_0 = \frac{\lambda}{2\pi\sqrt{2}}\frac{\nu_z}{\nu_r} \tag{2.4}$$

which gives a spectroscopic means to measure the trap waist. We used the main clock laser to measure the radial sideband frequencies as shown in 2.10. These corner frequencies were found to be 165 Hz at 130 $E_r$ corresponding to a $1/e^2$ intensity radius of 50 $\mu$m. This value closely agrees with a calculation of 47.5 $\mu$m using lens equations, however due to uncertainty about the lattice delivery fiber's wavelength-dependent numerical aperture, we use the spectroscopically derived quantity. The trap waist then characterizes the length scale for radial trapping in equation 2.1.

With atoms trapped in this lattice potential, we cool them even further with quenched sideband cooling. This process benefits clock operation by permitting lower operational trap depths which reduces the shifts from both the lattice light and cold-collisions. In the first step of sideband cooling, the clock light is tuned to the peak of the red-detuned axial sideband

Figure 2.9: Both figures show resolved axial sideband spectroscopy of the lattice trapped atoms. (a) is an older spectrum showing a sample that has not been subject to further sideband cooling. The excitation on the red-detuned side is from the transition ${}^1S_0, n_z = n \rightarrow {}^3P_0, n_z = n-1$ and therefore was in an excited motional band prior to the transition. The excitation on the blue-detuned side is from the transition ${}^1S_0, n_z = n \rightarrow {}^3P_0, n_z = n+1$. The center line is the carrier transition ${}^1S_0, n_z = n \rightarrow {}^3P_0, n_z = n$. The sharp edges of the sideband spectrum at ±50 kHz define the corner frequencies of the spectrum and are determined by the trap depth [84]. (b) shows a sample that has been sideband cooled and filtered at a lower trap depth. As a result, no atoms are available in excited motional bands for the red-detuned transition. Additionally, the filtering reduced the radial temperature of the sample resulting in a narrower range of available radial excitations and a decreased width of the blue-detuned sideband. We use the fitted line [84] to extract a trap depth, axial temperature, and radial temperature. A useful alignment technique is to use the atom population in the blue side of the blue sideband to align the lattice retroreflector mirror. The number of excited atoms is a sensitive signal with which to optimize the trap depth.

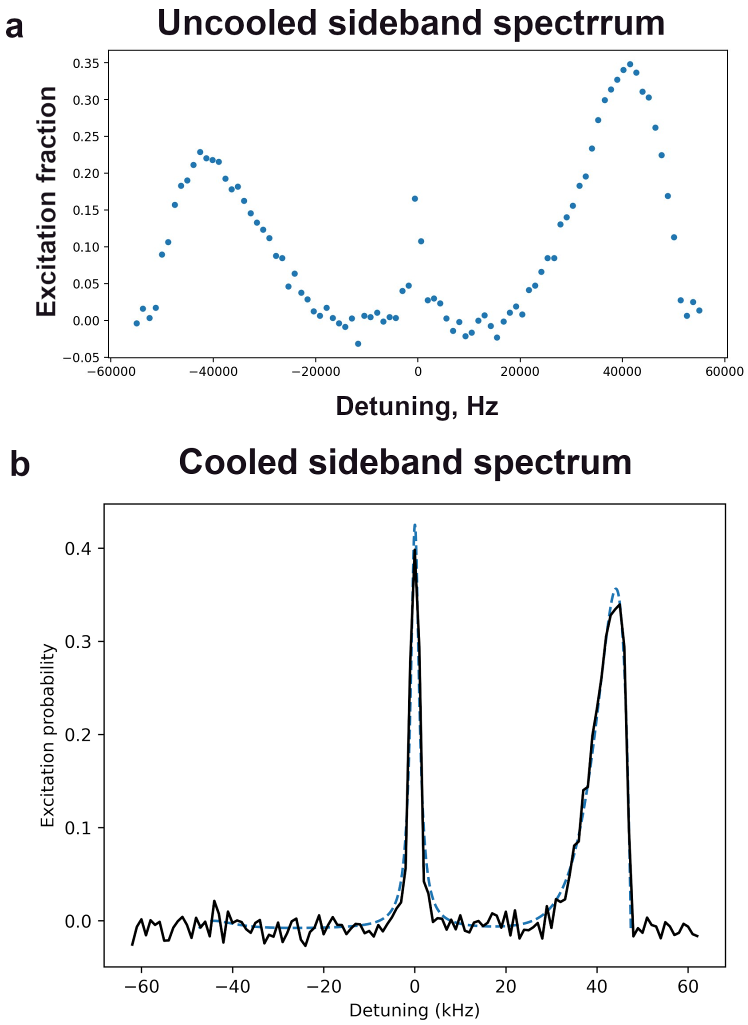

Figure 2.10: Measurement of the radial sideband corner frequencies. The primary clock laser is used for these measurements because of the high resolution required. Since the clock laser is coaxial to the lattice, it only weakly couples to these modes. We misaligned the clock laser by translating its positions relative to the lattice on the retroreflector so that it would hit the atoms slightly off-axis and be able to excite these motional modes. Even so, the coupling was weak enough (Rabi frequency low enough) that a 5 s spectroscopy time under high intensity conditions was required to excite a sufficient population in the sidebands to make a measurement. We measured the corner frequency to be 165 Hz.

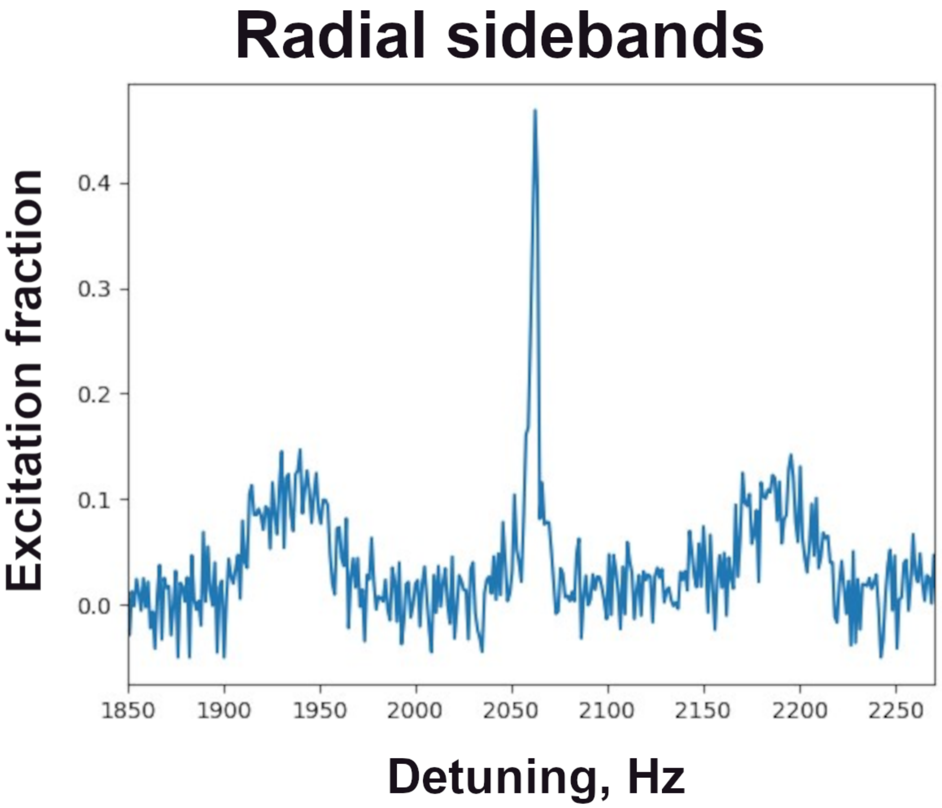

at 45 kHz and a low intensity repump beam is turned on. The quenching repump laser is tuned to the $6s6p^3P_0 \rightarrow 5d6s^3D_1, F = 3/2$ transition. While repumping to the $F = 1/2$ (3.05 GHz higher frequency [85]) state works nearly as well, we observe that it requires a slightly higher optical power and has less stable final atom numbers. We suspect this is due to greater magnetic broadening of the $F = 3/2$ transition and that the repump laser has the broadest linewidth ($\approx$ 1 MHz) of any of our lasers. From the $^3D_1$ state, the atom decays back to the ground state where it may undergo another cycle of cooling. The level diagram for sideband cooling is shown in 2.11(a). In the second step, the quench is maintained and the sideband laser frequency is tuned across the entire sideband line shape in order to cool atoms in other radial modes. Additionally, the optical pumping light is turned on. The historical reason for a two-step sideband cooling scheme is not due to more efficient cooling, but due to reproducibility in the $> 25$ ms switching time for the micro-electromechanical system (MEMS) switch that transitions the 556 nm laser between the MOT and optical pumping outputs. The effect of sideband cooling is to increase the population of atoms after reducing the trap depth to 70 $E_r$ by 50%. This effect is shown in 2.11(b) for a lattice servo setpoint at 0.55 V.

Optical pumping is the process of purifying the atoms into a single ground state magnetic sublevel. High spin purity is desirable both because it doubles the signal-to-noise ratio from clock spectroscopy and because it suppresses collisional shifts from distinguishable particles. The 556 nm optical pumping beam is delivered to the chamber along the magnetic field quantization axis. A 6 Gauss bias field separates the magnetic sublevels of the $^3P_1$ state by $\approx$ 10 MHz, which the optical pumping beam may separately address. The directions of the strong pumping bias field and weaker spectroscopy are the same and chosen to define the quantization axis for clock spectroscopy. The quantization axis is orthogonal to both the atomic beam axis and gravity is matched to the direction of the lattice laser electric field polarization. The pumping beam is tuned to one of the two $^1S_0, m_F = \pm 1/2 \rightarrow {}^3P_1, \mp 1/2$ transitions and empties the population in the targeted ground state magnetic sublevel. Fig-

Figure 2.11: (a) Shows the energy level diagram relevant to quenched sideband cooling. Atoms in the state ${}^1S_0, n_z = n$ are sent ${}^3P_0, n_z = n-1$ with the clock laser on continuous high power $\approx 2$ mW. The atoms in the excited clock state are then sent to the ${}^3D_1$ state with the 1388 nm repump laser continuously on low power $\approx 80$ $\mu$W. From the short-lived ${}^3D_1$ state the atoms spontaneously decay back to the ground state. Although the atoms may acquire a quantum of motion in their decay from the excited state, the continuous application of the sideband cooling scheme ensures that the atoms undergo many cycles of cooling and ultimately ends up in the motional ground state. (b) shows the main value of sideband cooling, more atoms are available at lower trap depths. The x-axis is the lattice laser intensity servo setpoint; 1.2 V corresponds to about 150 $E_r$ and 0.55 V corresponds to 70 $E_r$. At lower trap depths, the lattice light shift and cold collision shift are both reduced, along with their uncertainties.

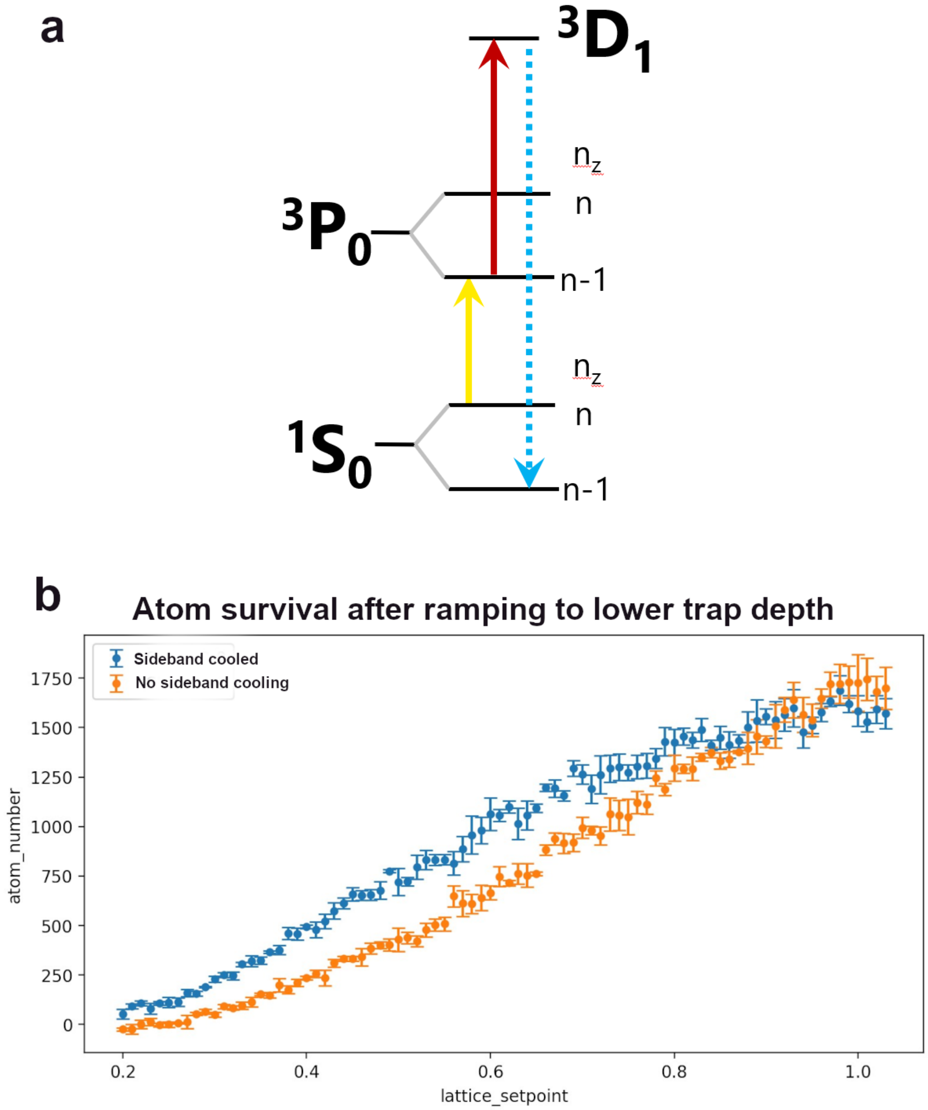

ure 2.12(a) shows the atomic levels addressed in this process. As measured in section 4.3.2, we achieve a very high level of spin purity ($> 99.9\%$) during our state preparation in order to suppress otherwise large collisional shifts. For operational efficiency, we perform optical pumping at the same time as sideband cooling as in [86], which results in atoms migrating to the doubly dark state at the ground motional state and target ground magnetic state. We do not, however, use the technique of [86] where the repumping laser is set to address $^3D_1$ magnetic levels that also have favorable branching ratios to the target ground magnetic state.

Previous estimates of attainable spin purity suggested the lowest impurity that could be reached with this simple technique is only 1% [87]. However, this estimate used a very conservative value for laser polarization purity at 1% which sets the achievable spin purity. Our polarizing beam splitter is rated for a transmission purity at 2200:1 which permits a greater final purity by forbidding the $\pi$ transitions. Additionally, a key aspect of our spin-polarizing scheme is that the two opposite $\sigma$ transitions are highly resolved in energy. We optically pump for a comparatively long time (75 ms), at very low powers (an ND=4.0 is in the beam path, in addition to AOM RF attenuation), and with a larger bias field (6 Gauss). All of this combined suppresses off-resonant pumping of the opposite $\sigma$ transition by increasing the detuning between the peaks and suppressing power broadening.

After the main sideband cooling and optical pumping steps, a brief “repumping” step ensures that no atoms are remaining in the $^3P_0$ state, which would contaminate clock spectroscopy measurements.

After preparing the atoms in the targeted spin state and ground axial motional mode, we adiabatically ramp the lattice down to a 70 $E_r$ trap depth. Adiabatic ramping maintains atoms in the same quantum harmonic modes as in the higher depth while the lattice intensity is decreased. We tried using a discontinuous decrease in lattice intensity and found that this increased the atomic temperature and lost more atoms. The adiabatic ramp is made smoothly linear with additional steps in the Artiq control sequence over 25 ms and a

Figure 2.12: (a) shows the Zeeman-separated level diagram of the optical pumping scheme. Linearly polarized light is used to drive the $\sigma$ transitions: $^1S_0, m_F = \pm 1/2 \rightarrow \ ^3P_1, \mp 1/2$. The branching ratio of the decaying excited state favors decay into the same $m_F$ state. Atoms that decay back to the same $m_F$ state they started in are pumped again. This process is repeated until high single $m_F$ state purity is obtained. The $^1S_0, m_F \pm 1/2$ states are nearly degenerate under the fields we apply; since they are in a $J = 0$ state, they only experience an energy difference proportional to the nuclear magneton rather than the Bohr magneton. Therefore, high polarization purity is required to prevent de-pumping the targeted $m_F$ state from $\pi$ transitions. (b) shows the transitions spectroscopically where the y-axis is the atom fraction excited by $^1S_0, m_F = -1/2 \rightarrow \ ^3P_0, m_F = -1/2$ clock transition. Note that the transitions to $m_F = \pm 3/2$ primarily change sample spin purity by heating atoms out of the trap rather than flipping their spins. A process of decreasing the pumping optical power with ND filters and narrower resolution spectroscopy on the pumping transition is used to optimize these frequencies for clock operation. The magnetic field applied for this figure is less than in current operation.

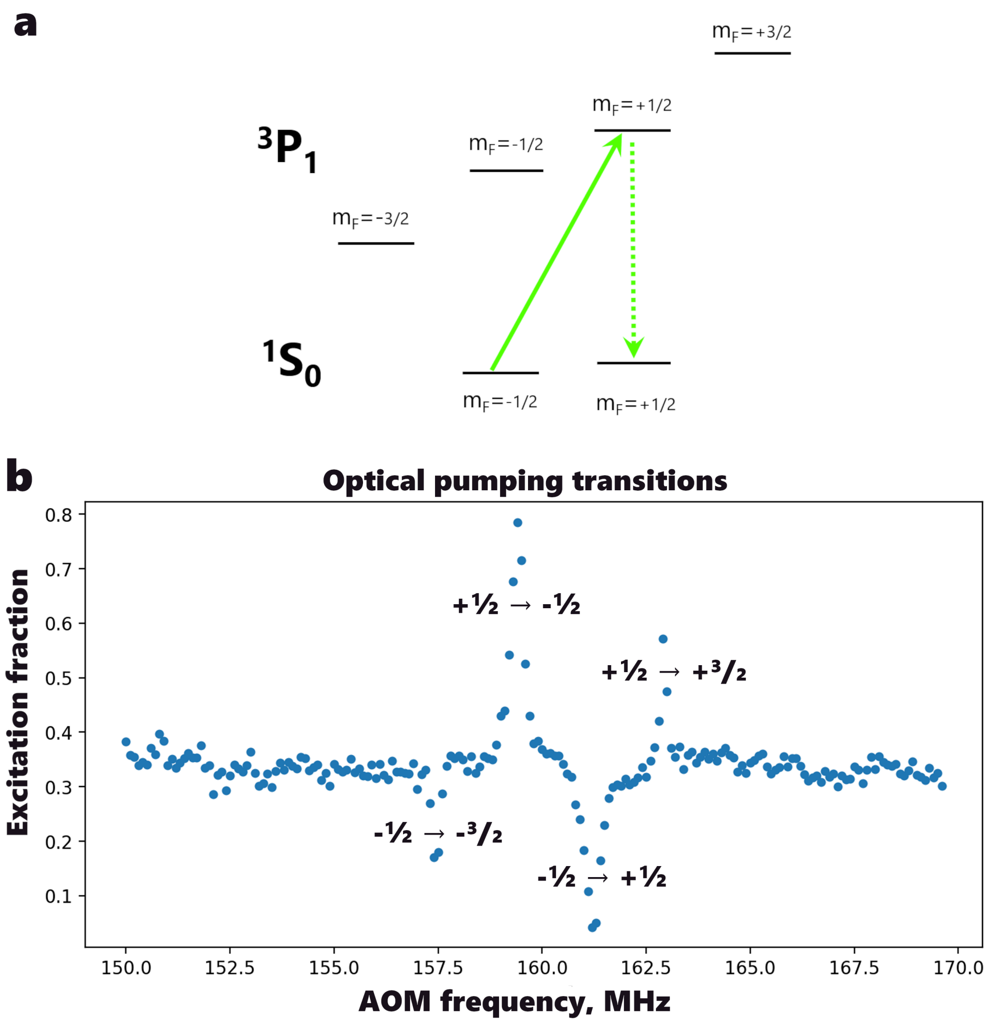

capacitive filter on the voltage control input of the lattice intensity servo. For making lattice Stark comparisons at different trap depths, the atoms are held at the low depth for 5 ms and then ramped up to a higher target depth. In normal operational mode, they are simply held for 30 ms. The bias magnetic fields are switched to a 1.2 Gauss field at the beginning of the ramp step. The 55 ms of time during the ramping and hold steps ensures that transient magnetic fields decay before clock spectroscopy begins.

As shown previously, we can use sideband spectroscopy to characterize the temperatures of lattice trapped atoms. These temperatures also play an important role in the systematic shifts on the clock transition frequency. We characterize the atomic temperatures before any significant clock transition measurement. Measurements of the axial and radial temperatures from datasets for lattice Stark shift evaluation are shown in Figure 2.13. The data shows that the process of sideband cooling and filtering the atoms results in a sample that is much colder than maximum temperature that a lattice at that depth can trap. Our typical operational lattice depth is 70 $E_r$, and with sideband cooling and adiabatic lattice ramping, the atomic sample at this depth has an axial temperature of $0.4(2)$ $\mu$K and a radial temperature of $3.0(5)$ $\mu$K.

The thermal ensemble of atoms in the lattice can then be characterized by the mean quantum motional state that it occupies. The mean motional mode in the $i$-direction can be calculated from the Maxwell-Boltzmann distribution in the classical limit

$$\langle n_i \rangle = \frac{1}{\exp\left(\frac{\hbar\omega_i}{k_B T_i}\right) - 1} \tag{2.5}$$

where $\omega_i$ and $T_i$ are the trap angular frequency and atomic temperature in the $i$-direction [88]. A plot for this calculation from the lattice Stark dataset is shown in Figure 2.14. This data will later be used in the calculation of scaling for the lattice light and cold-collision shifts.

Figure 2.13: The axial (blue squares) and radial temperatures (orange diamonds) of the atoms as a function of trap depth. The error bars are statistical only. Also displayed in gray is the maximum temperature atoms that a lattice at the same depth can trap. The axial temperatures are much colder as a result of quenched sideband cooling. Both linear and radical fits accurately capture the temperature changes as a function of trap depth with reduced $\chi^2 < 0.3$ although the radical fit is better justified on physical principles since the final trap depth is reached from an adiabatic ramp from 70 $E_r$.

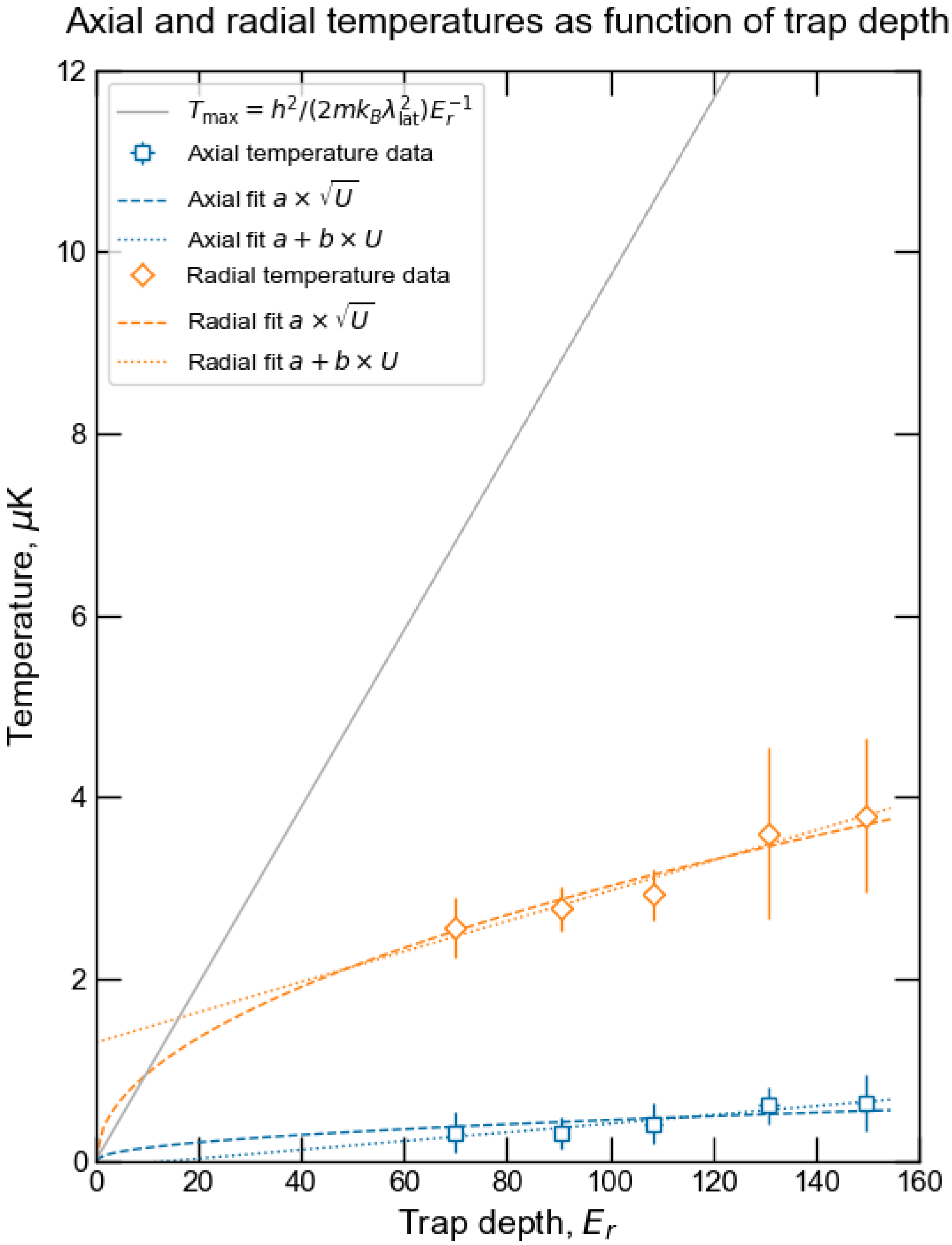

Figure 2.14: The mean occupied lattice motional mode as a function of trap depth according to 2.5 given measured temperatures. (a) shows the axial motional mode occupation and demonstrates that our resolved sideband cooling process effectively cools atoms down to the motional ground state of the lattice. (b) shows the radial motional mode occupation which is not further cooled after the 556 nm MOT, however, the hottest atoms are filtered away at a 70 $E_r$ trap depth. Both have constant uncertainty-weighted fits as a function of trap depth since adiabatic ramping is expected to maintain consistent mode occupation numbers. The mean $\langle n_z \rangle$ value is 0.005(3) that fits with a reduced $\chi^2$ value of 0.18 and the mean $\langle n_r \rangle$ value is 395(7) that fits with a reduced $\chi^2$ value of 0.11.

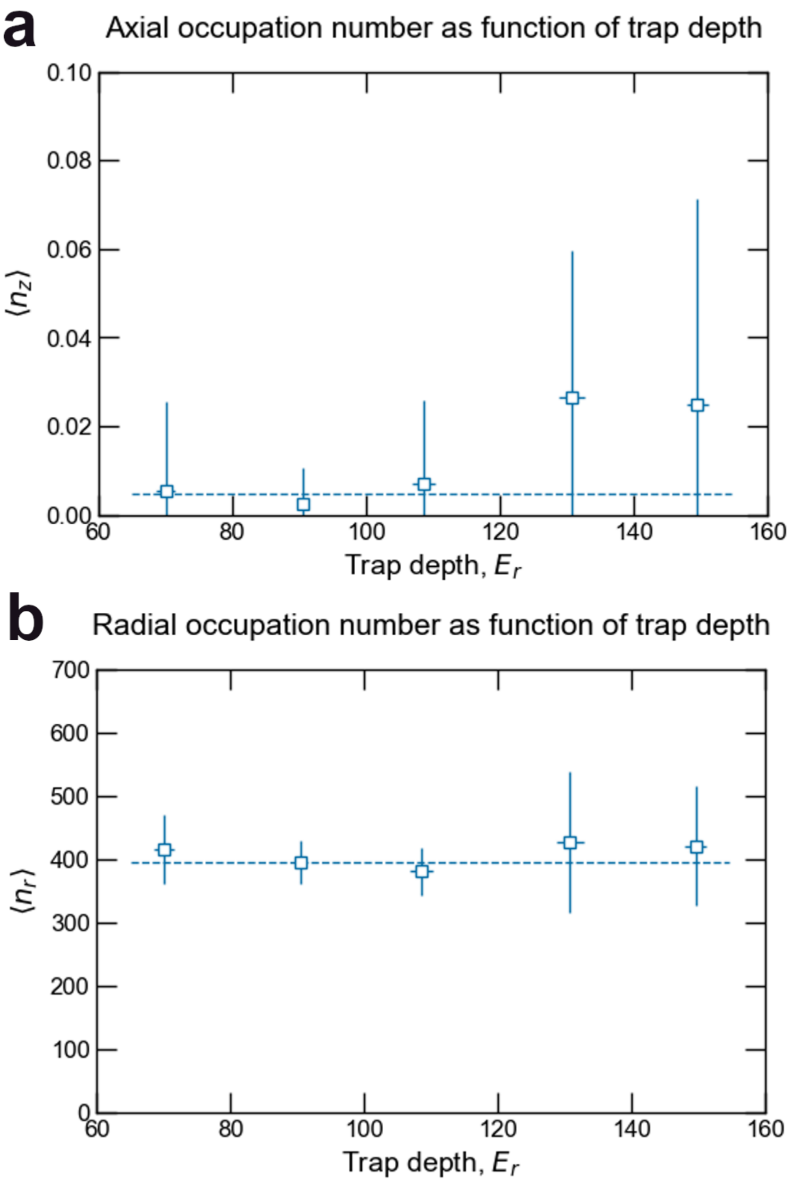

### 2.2.4 Spectroscopy and state readout

The final part of the control sequence is Rabi spectroscopy and the normalized excited state detection that gives high-signal-to noise clock performance. This state preparation sequence is shown in Figure 2.15.

The 578 nm clock laser uses the lattice retro-reflector as the phase reference mirror [89], which fixes the clock laser phase to the atomic reference frame. This mirror is 99.8% reflective at 578 nm which means most light is used for fiber phase noise cancellation (PNC) and only a sub-$\mu$W power reaches the atoms ensuring a low Rabi frequency. The clock light passes through a Faraday rotator immediately after collimation to enforce polarization discrimination that helps achieve high signal to background for fiber phase noise cancellation. A 5-axis kinematic mount (Polaris K1XY, Thorlabs) for the clock laser collimator has all of the necessary degrees of freedom for optimal alignment. First, angular alignment is used to achieve a large retroreflection signal from the phase reference mirror, since for both optimal lattice retroreflection and clock PNC retroreflection, the beams must be exactly orthogonal to the reference surface. Second, translational alignment is used to center the clock beam inside the lattice beam for alignment to the atoms. The collimation diameter of the clock laser beam is much tighter than the lattice beam ($<$ 1/5 diameter) since the clock beam will then be less tightly focused at the atoms which suppresses effects from inhomogeneous atomic sampling of the clock laser.

The atomic fluorescence probe beam enters the chamber near-coaxially with the slowing beam to measure successively the ground state population, a background light level, and the excited state population. Atomic fluorescence is detected with a photomultiplier tube (PMT) (H10723-210, Hamamatsu [90]) that receives light from a 2f-2f imaging lens 50.8 mm from the atomic sample. A 10 nm bandpass filter (FBH400-10, Thorlabs) transmits 93.0(5)% of the 399 nm light collected from the chamber. The filter has been characterized on a rotation mount and found to have a nearly flat transmission between ±15.25° while the maximum angle of photons from the imaging setup should be within ±13.8°. The PMT signal is electronically integrated with a home-built circuit[5] and then read by the Artiq sampler. More useful details about the atom number calibration and background subtraction technique may be found in [3] sections 2.2.1 and 2.5.1. Some of the exact values of coefficients in the PMT calibration have changed since then however.

As part of high accuracy measurement, we calibrate our PMT setup on a daily basis. This involves first, measuring the time-dependent PMT and signal integrator electronic offsets for the three pulses, which are at the single mV level. Second, the gain of the integrator is calibrated by comparing the average integrated measurement to an average oscilloscope trace of the atomic fluorescence. Third, the saturation parameter of the probe beam is measured. An example of such a calibration is shown in Figure 2.16 where the probe beam power is modulated and the integrated PMT signal collected. The calibration has stayed at the 315(10) atoms/volt level for the last year. This value is added as an Artiq variable and atom numbers are recorded directly with clock data.

## 2.3 Laser Modules

The atomic state preparation laser modules have been discussed previously in [3] so these lasers will be discussed in overview and updates since then. Operational details intended for users of these modules will be provided in the appendix A. Our clock lasers and comb laser, on the other hand, will be discussed in more detail here.

### 2.3.1 Cooling and state preparation lasers

The 399 nm laser module occupies a 2U free-space breadboard as described in [3] section 2.2.2. A 120 mW external cavity diode laser (ECDL) at 399 nm is offset locked to the $^{171}$Yb $^1S_0 \rightarrow\ ^1P_1$ transition with modulation transfer spectroscopy through a hollow cathode lamp [91] with an FPGA control loop developed at NIST [92]. There are three

---

[5] by the NIST Phase Noise Metrology Group's Marco Pomponio and Craig Nelson

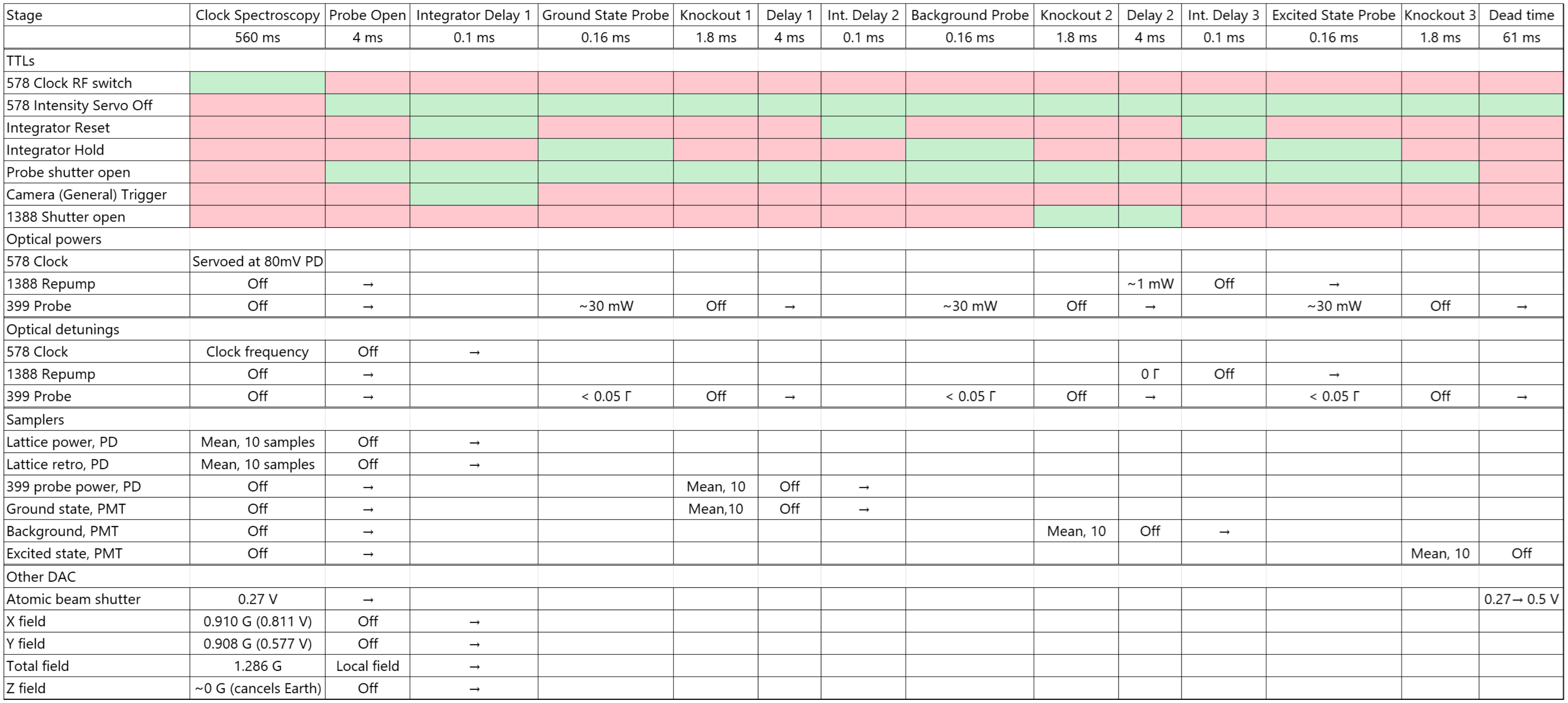

Figure 2.15: The timing sequence for clock spectroscopy and state readout.

| Stage | Clock Spectroscopy | Probe Open | Integrator Delay 1 | Ground State Probe | Knockout 1 | Delay 1 | Int. Delay 2 | Background Probe | Knockout 2 | Delay 2 | Int. Delay 3 | Excited State Probe | Knockout 3 | Dead time |
|---|---|---|---|---|---|---|---|---|---|---|---|---|---|---|
| | 560 ms | 4 ms | 0.1 ms | 0.16 ms | 1.8 ms | 4 ms | 0.1 ms | 0.16 ms | 1.8 ms | 4 ms | 0.1 ms | 0.16 ms | 1.8 ms | 61 ms |
| TTLs | | | | | | | | | | | | | | |
| 578 Clock RF switch | 🟩 | 🟥 | 🟥 | 🟥 | 🟥 | 🟥 | 🟥 | 🟥 | 🟥 | 🟥 | 🟥 | 🟥 | 🟥 | 🟥 |
| 578 Intensity Servo Off | 🟥 | 🟩 | 🟩 | 🟩 | 🟩 | 🟩 | 🟩 | 🟩 | 🟩 | 🟩 | 🟩 | 🟩 | 🟩 | 🟩 |
| Integrator Reset | 🟥 | 🟥 | 🟩 | 🟥 | 🟥 | 🟥 | 🟩 | 🟥 | 🟥 | 🟥 | 🟩 | 🟥 | 🟥 | 🟥 |
| Integrator Hold | 🟥 | 🟥 | 🟥 | 🟩 | 🟥 | 🟥 | 🟥 | 🟩 | 🟥 | 🟥 | 🟥 | 🟩 | 🟥 | 🟥 |
| Probe shutter open | 🟥 | 🟩 | 🟩 | 🟩 | 🟩 | 🟩 | 🟩 | 🟩 | 🟩 | 🟩 | 🟩 | 🟩 | 🟩 | 🟥 |
| Camera (General) Trigger | 🟥 | 🟥 | 🟩 | 🟥 | 🟥 | 🟥 | 🟥 | 🟥 | 🟥 | 🟥 | 🟥 | 🟥 | 🟥 | 🟥 |
| 1388 Shutter open | 🟥 | 🟥 | 🟥 | 🟥 | 🟥 | 🟥 | 🟥 | 🟥 | 🟩 | 🟩 | 🟥 | 🟥 | 🟥 | 🟥 |
| Optical powers | | | | | | | | | | | | | | |
| 578 Clock | Servoed at 80mV PD | | | | | | | | | | | | | |
| 1388 Repump | Off | → | | | | | | | | ~1 mW | Off | → | | |
| 399 Probe | Off | → | | ~30 mW | Off | → | | ~30 mW | Off | → | | ~30 mW | Off | → |
| Optical detunings | | | | | | | | | | | | | | |
| 578 Clock | Clock frequency | Off | → | | | | | | | | | | | |
| 1388 Repump | Off | → | | | | | | | | 0 Γ | Off | → | | |
| 399 Probe | Off | → | | < 0.05 Γ | Off | → | | < 0.05 Γ | Off | → | | < 0.05 Γ | Off | → |
| Samplers | | | | | | | | | | | | | | |
| Lattice power, PD | Mean, 10 samples | Off | → | | | | | | | | | | | |
| Lattice retro, PD | Mean, 10 samples | Off | → | | | | | | | | | | | |
| 399 probe power, PD | Off | → | | | Mean, 10 | Off | → | | | | | | | |
| Ground state, PMT | Off | → | | | Mean,10 | Off | → | | | | | | | |
| Background, PMT | Off | → | | | | | | | Mean, 10 | Off | → | | | |
| Excited state, PMT | Off | → | | | | | | | | | | | Mean, 10 | Off |
| Other DAC | | | | | | | | | | | | | | |
| Atomic beam shutter | 0.27 V | → | | | | | | | | | | | | 0.27→ 0.5 V |
| X field | 0.910 G (0.811 V) | Off | → | | | | | | | | | | | |
| Y field | 0.908 G (0.577 V) | Off | → | | | | | | | | | | | |
| Total field | 1.286 G | Local field | → | | | | | | | | | | | |
| Z field | ~0 G (cancels Earth) | Off | → | | | | | | | | | | | |

Figure 2.16: Calibrating the the probe saturation parameter. The probe power is normally at 1 V as measured by the probe photodiode pick off. This value translates to a saturation parameter of 13(1), relatively deep into saturation which helps make the fluorescence insensitive to exact values of probe beam power. The fluorescence rate calculation in [3], sections 2.2.1, is fit to the data to measure the saturation parameter at the operational intensity.

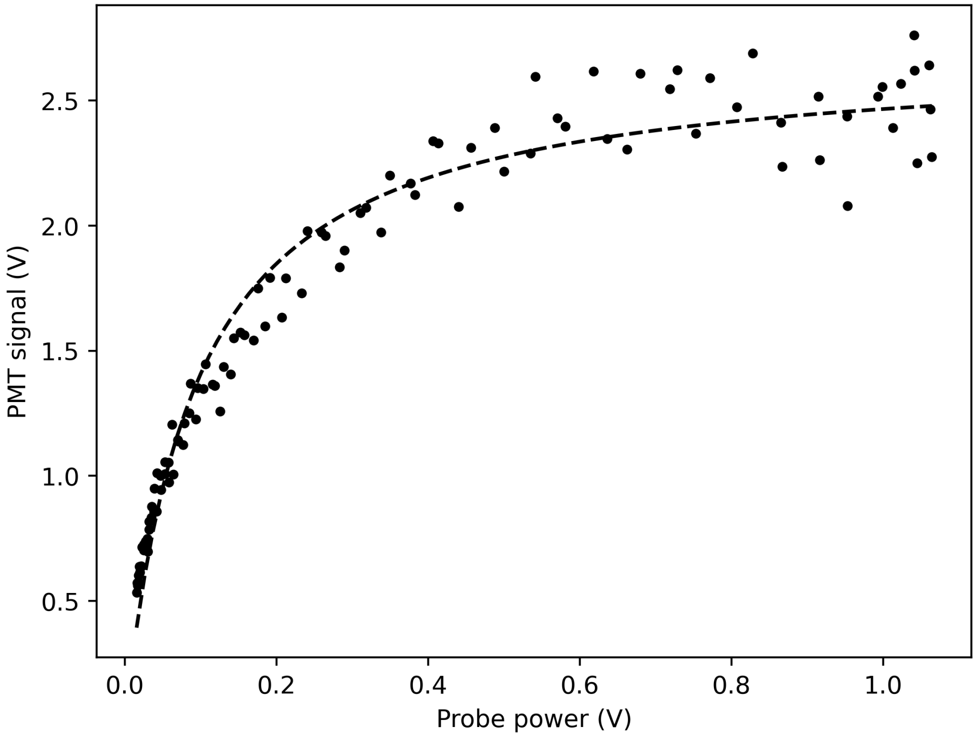

independent beam paths for slowing, MOT cooling, and probe detection; each path has separate acousto-optic modulators (AOMs) and shutters for timing, detuning, and intensity control. Since 2022, we have made the update of swapping the MEMS mirrors for dielectric mirrors since the 10% loss from the MEMS was deemed unacceptable. Additionally, we replaced the fiber optic cables (PMC-360Si-3-18E, Schafter-Kirchoff) which appeared to lose their polarization-maintaining quality over time, perhaps from either ultraviolet solarization or abuse by transportation. More details on this module are in appendix A.4.

The 556 nm laser module is entirely fiber-based and occupies a 2U sliding drawer as described in [3] section 2.3.2. An 1112 nm Yb:fiber laser (Koheras Basik Y10, NKT) seeds a fiber amplifier (Mantaray OEM, Cybel) and is locked to the optical frequency comb with a $<$ 10 Hz in-loop beat linewidth. This narrow lock is achieved with fast AOM and slow piezo feedback from the comb. The 1112 nm light is doubled in a single-pass periodically-poled lithium niobate waveguide and then sent to an AOM for frequency and intensity control. A series of fiber switches permit shuttering the light, and switching between MOT, optical pumping, and a “blowaway” beam (useful for quickly aligning the lattice after each deployment). The optical and electronic layout of this module are available in appendix A.5.

The magic-wavelength-optical lattice laser at 759 nm uses a free-space ECDL to seed a tapered amplifier as described in [3], section 2.4.1. The seed is locked to the optical frequency comb and the amplified laser is filtered by reflection from a 10 GHz bandpass volume Bragg grating to reduce the unwanted amplified spontaneous emission of the tapered amplifier [93]. The light is intensity controlled and delivered to the atoms via a photonic crystal fiber which eliminates stimulated-Brillouin scattering at high laser powers in-fiber. The optical and electronic layout of this module are available in appendix A.7.

The 1388 nm laser is used to depopulate the $^3P_0$ clock state after spectroscopy, [3], section 2.6. The laser is an 8 mW distributed feedback (DFB) diode laser (QDFBLD-1390-10, QPhotonics). This module is also entirely fiber-based and occupies a 1U sliding drawer. Intensity control with an AOM and MEMS shutter permit $>$ 125 dB of extinction to prevent stray light shifts on the clock transition. The optical and electronic layout of this module are available in appendix A.6.

### 2.3.2 Lab clock laser

Measurements for the uncertainty budget used light stabilized by a laboratory optical cavity with $2 \times 10^{-16}$ stability at 1 s [94]. Since details of this cavity system have been discussed elsewhere [94, 33, 41], we will focus on the portable branch of this system. Stable laser light is generated from a commercial ECDL at 1156 nm and amplified by a tapered amplifier. Light is separated for cavity locking, stable light distribution, and frequency doubling in a single-pass waveguide. About 110 mW of 578 nm light are generated, of which the majority is distributed to the lab clocks. The portable branch receives 7 mW of 578 nm light that passes through an optical isolator to prevent reflections from interfering with lab clock operation.

The portable distribution branch is shown in Figure 2.17. The laser light is split with a polarizing beam-splitter cube (PBS) in a Michelson type interferometer with 2 mW in the short reference arm and the remainder collected into fiber for distribution to the atoms. An AOM shutters the light and controls the optical frequency with a nominal 99 MHz tone applied to achieve resonance with the $^1S_0 \rightarrow\ ^3P_0$ clock transition. A fiber-based MEMS switch directs the light towards either the sideband cooling and sideband spectroscopy port or the clock spectroscopy port. In sideband mode, a relatively large optical power of clock can be delivered to the the atoms for driving the weak sideband transition. In clock spectroscopy mode, a photodiode pick off in the physics module collects light for intensity servo stabilization to maintain a consistent $\pi$ pulse. Additionally, the lattice retroreflector surface directs most of the 578 nm light back into fiber where it picks up a second frequency shift. The returning clock spectroscopy light is overlapped with the reference arm light in the PBS. The interfering waves are then collapsed into the same polarization state with a PBS tilted at 45° and focused onto a high speed photodiode for collecting the approximately

198 MHz interference frequency. Since the light returning into interferometer from the fiber-distribution will have acquired twice the phase of a single transmission, half of this phase may be subtracted with the AOM to provide phase-stable light [89].

Most of the control scheme complication for this system comes from switching between high-power unstabilized operation for sideband cooling and low-power phase-stable operation for clock spectroscopy. Artiq itself switches between a near 99 MHz DDS frequency for directly driving the AOM during sideband interrogation and a near 198 MHz reference frequency for clock spectrosocpy. The reference frequency is mixed with the phase noise photodiode frequency to generate an error signal. The error signal is propagated through a 5 MHz bandwidth PI loop filter (PI200, Koheron) and provides feedback control for a synthesizer (E4400B, HP) at 99 MHz that feeds the AOM. More details are discussed in appendix A.

Before our deployment to the United States Naval Observatory (USNO), we assessed the stability of the portable clock system in comparison to laboratory clock Yb1. A great benefit of using the lab light is the ease of atomic frequency comparison. The lab clocks can provide global laser frequency correction and the portable clock simply needs to record the frequency offset applied to the light it is supplied. As shown in Figure 2.18, we averaged down to $3 \times 10^{-18}$ in 10,000 s. This comparison was done before we had evaluated our uncertainty budget or started to control our time-varying systematics. The frequency offset between the clocks was $2 \times 10^{-16}$ which we found acceptable since no attempts to control the portable clock uncertainty had yet been made. This offset is easily within the possible range for uncorrected BBR and magnetic shifts. Additionally, it was taken before our more recent round of upgrades that resulted in improved vacuum lifetime, colder atoms from sideband cooling, and the use of the optical frequency comb as an absolute frequency reference for the lattice laser. Nonetheless, this comparison showed that the portable clock was ready for its scientific goals at USNO of comparing with a rubidium fountain at the $1 \times 10^{-15}$ instability level.

Figure 2.17: The optical and electrical schematic of the 578 nm clock laser distribution in 1G106. Artiq sends an RF tone at (approximately) either 99 MHz or 198 MHz. A pair of switches determine whether that tone is distributed for directly driving an AOM or is used for fiber noise cancellation. When using the 99 MHz RF tone the switches direct it straight to the AOM where the RF controls sideband cooling and sideband spectroscopy without fiber noise cancellation; the direct AOM drive enables a greater frequency scanning range and optical power availability. When using the 198 MHz RF tone, the first switch directs the tone to a mixer with the fiber noise cancellation photodiode signal to generate a frequency error signal. The frequency error signal is fed to a PI filter that then controls a synthesizer's near 99 MHz tone that is directed to the AOM through the second RF switch for phase stable optical control.

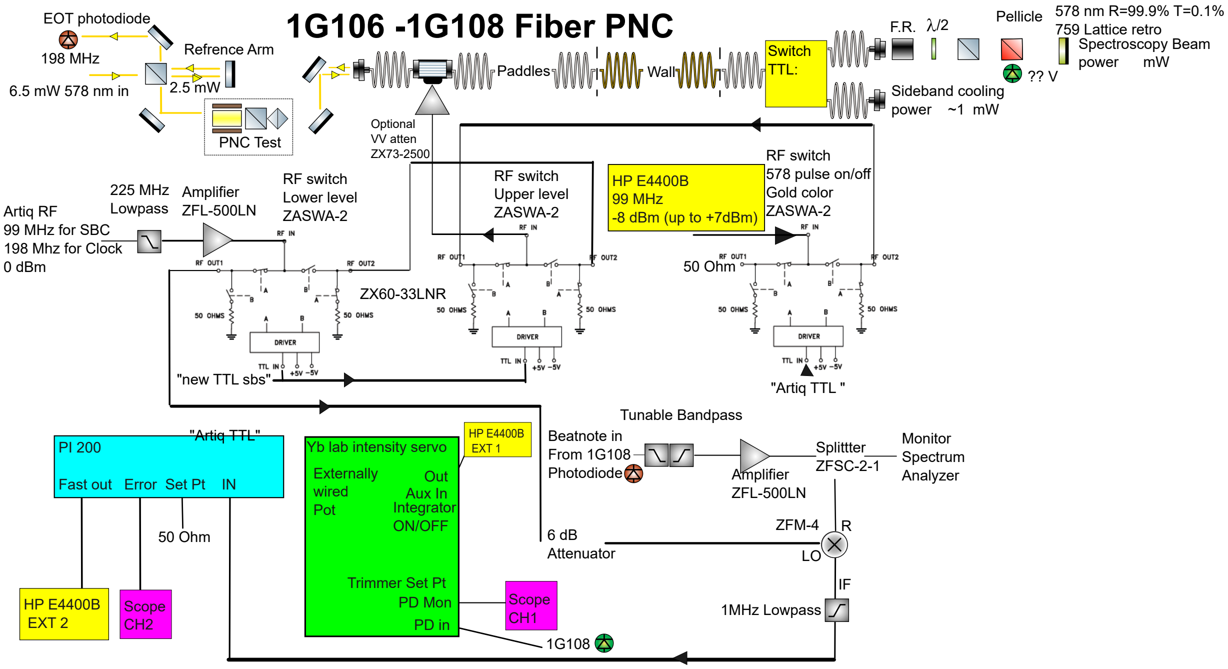

Figure 2.18: Direct frequency comparison to Yb1 laboratory clock using the same clock laser. The instability averages down to $3 \times 10^{-18}$ at 10,000 s.

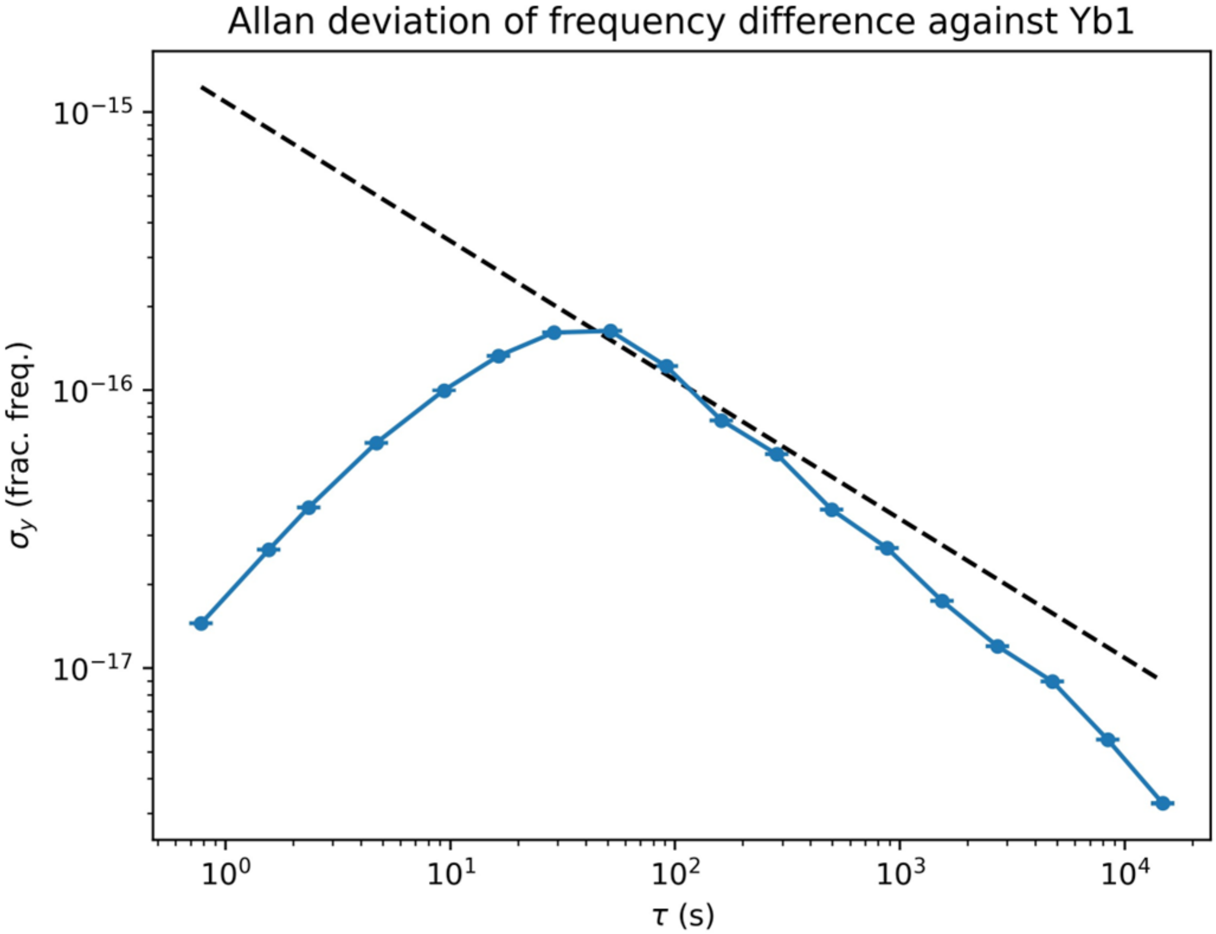

### 2.3.3 Portable clock laser

This section describes the **preliminary** version of the transportable clock laser that was developed to meet our scientific goals at USNO. We will discuss first, the optical cavity, and second, the laser system. Planned upgrades will be discussed in chapter 5.

We developed a prototype optical cavity for the deployed system, shown in Figure 2.19(a). The cavity serves as the phase-coherent local oscillator (LO) of the transportable clock. The cavity, based on a cubic design [95], realizes an extended cuboid design with cut vertices and vent holes designed to minimize acceleration sensitivity [3]. Prior work on the cavity design used FEA simulation [96] to analyze a configuration that has the force insensitivity of the design in [95] while obtaining the stability benefits of a longer cavity without the volume increase of a cubic cavity. The details of this work can be found in [3] Chapter 4. The 10 cm long cavity is built with ultra-low expansion (ULE) glass and uses crystalline mirrors for reduced thermal noise [97, 98, 99]. The cavity is rigidly held within an FeNI36 ("Invar") cage via four vacuum-compatible plastic balls on fine-adjusting screws, enabling robust transport.

Acceleration sensitivities at the mid $10^{-11}$/g (fractional frequency per standard gravity) were found in an earlier version of the cavity, data shown in 2.19(b). The acceleration sensitivity was determined by repeated flip tests of the cavity that was enabled by its relatively compact size and rigid mounting. In a flip test, the cavity vacuum chamber is inverted and the cavity frequency is compared between $+g$ and $-g$ [100]. Repeated measurements of the acceleration sensitivity of the cavity after re-mounting in the FeNi36 cage found degraded acceleration sensitivity. This variation in acceleration sensitivity, suspected to arise from imbalanced forces in mounting, is currently under investigation. We are hopeful that experiments to improve the repeatability of mounting conditions with the aid of precision-made parts will permit reliable low acceleration sensitivity operation. The version deployed to USNO was found to have an acceleration sensitivity at the mid $10^{-10}$/g level.

Figure 2.19: **(a)**Image of the prototype optical cavity in the commercial vacuum chamber. For early testing, tape ensured contamination was unable to enter the cavity vent holes and compromise finesse. **(b)** The measured cavity acceleration from repeated flip tests.

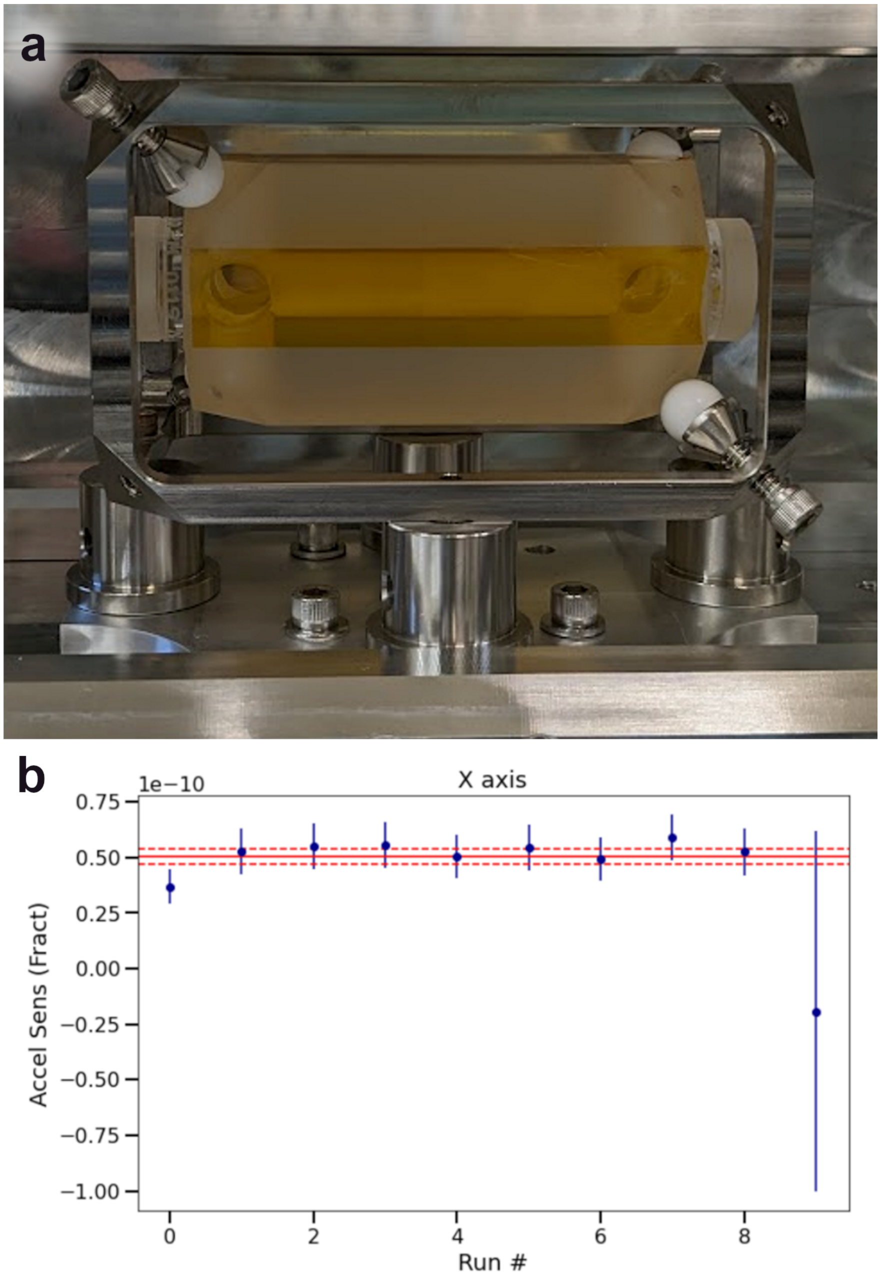

For rapid development of our prototype cavity we used a commercial vacuum chamber (P108245, Ideal Vacuum). The vacuum chamber was sealed with FKM elastomer ("Viton") gaskets and (with effort) achieved a final pressure of $7 \times 10^{-7}$ Torr. This chamber had no in-vacuum thermal shielding which we aim to rectify with the new vacuum chambers that we have since built. The ULE cavity was found to have a zero-crossing of thermal expansion near 22 C, necessitating temperature control using peltier heating and cooling. Despite operation at the zero-crossing, we found the thermal control of the cavity to be the limiting systematic for stability, well explained by the prototype's lack of in-vacuum thermal shielding that low pass filters ambient temperature effects [101].

While the prototype cavity performance is insufficient for long term optical comparison goals, it sufficed for a first deployment and testing of the improved stability of the Rb fountain operation at USNO. As shown in Figure 2.20, the cavity supported 35 ms Rabi $\pi$-pulses and regularly exhibited instabilities in the low to mid $10^{-15}$ level at timescales relevant for clock operation.

Figure 2.20: **a)** Rabi line shape for a 35 ms $\pi$-pulse with no drift cancellation. Data was taken at USNO after shipping. **b)** Modified Allan deviations of the optical cavity stability before and after shipping, as well as full Yb transportable OLC as measured by laboratory based clocks at NIST.

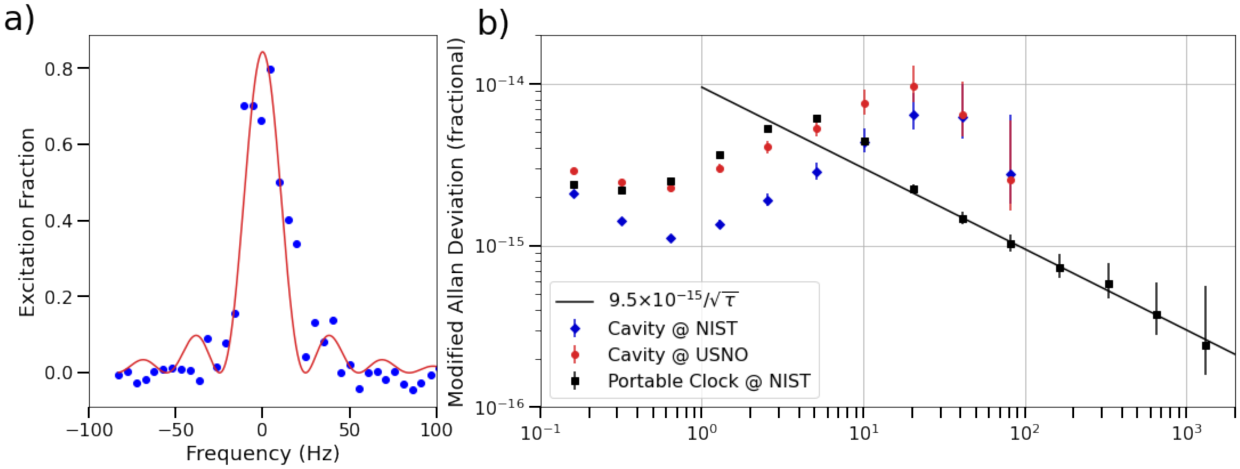

The full cavity assembly and the clock laser were combined into a single module. The schematic for the clock laser system is shown in 2.21 and a picture of the system is shown in 2.22(a). 1 W of optical power at 1156 nm is generated by a tapered amplifier laser system (TA Pro, Toptica) and distributed between the optical reference cavity, a fiber phase noise cancelled [89] output to the optical frequency comb, and a second harmonic generation unit to create the 578 nm light used for clock spectroscopy. A low noise frequency servo with 10 MHz bandwidth (D2-125, Vescent Photonics) locks the laser to the cavity reference. This module has hydraulic feet that permit raising the system up to roll a scissor lift beneath the module for placing into its shipping crate. When at its destination, the feet can be fully retracted so that the assembly is on the ground reducing vibration pick-up of the cavity system.

This version of the clock laser provided basic capabilities for clock spectrosocpy, but did not have the fully capabilities of either the lab-based clock laser system or the new clock laser system that we are building. An AOM in the 578 nm light path applies both phase noise cancellation and frequency offsets for clock spectroscopy in a manner substantially similar to the lab clock laser setup. This module did not support the capability to sideband cool the atoms which was added to the lab clock laser system in our round of upgrades following the deployment to USNO. To perform sideband spectrosocpy, the lattice retroreflector had to be switched to a mirror that was more transmissive at 578 nm. The lab clock system cancels cavity drift with a continuously ramping frequency to an offset AOM. In this deployable system, we instead used the Artiq control to apply drift cancellation from direct atomic measurement of the clock transition. This configuration was functional, but experimentally inconvenient since the experimenter was required to keep track of the current drift offset and rate while performing preliminary measurements.

Before deployment the full Yb transportable OLC system was tested against the lab-based Yb OLCs at NIST [33, 94]. The optical cavity, with performance as indicated in Figure 2.20(b), was steered by the atomic error signal, realizing a fully independent system

Figure 2.21: Schematic diagram for the portable clock laser system. Light is distributed between the cavity reference, the optical frequency comb for comparisons, and a second-harmonic generation unit for atomic interrogation. Phase stabilization and intensity servos were run on-board Moglabs DDS units that tended to have negative effects system up time. This diagram does not exactly reflect the final deployed system due to changes in the two weeks before shipping the system to USNO.

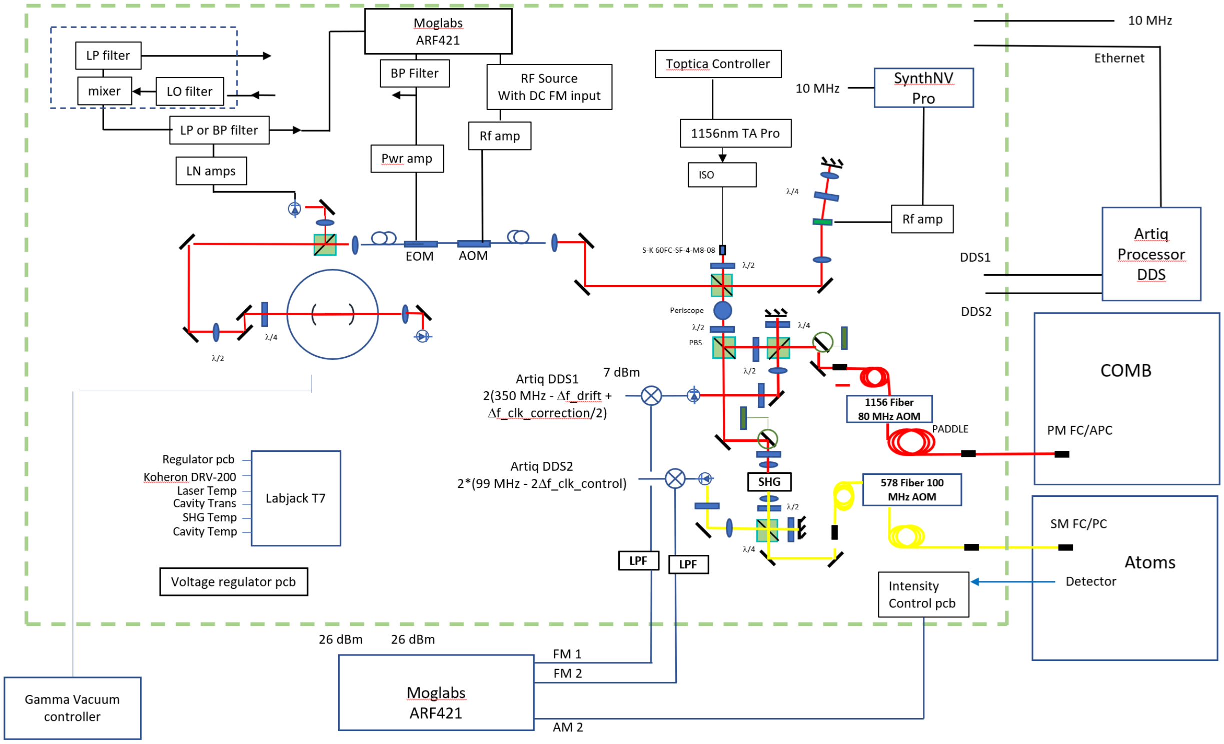

to compare against the laboratory Yb OLC. Comparison with the lab based Yb OLC showed a frequency instability of $9.5 \times 10^{-15}/\sqrt{\tau}$, a factor of 10 lower instability compared with the USNO Rb fountain. We note that we anticipate improved instability from forthcoming upgrades to the optical cavity.

### 2.3.4 Optical frequency comb

We use an optical frequency comb, pictured in 2.22, for comparisons to clocks that do not share the same clock laser. The comb repetition rate may be locked to stable 1156 nm (or 1550 nm light) from our optical clock. Comb light is generated with the commercial "Figure 9" design for sub-Hz comb lines when locked to our stable light source [102]. Several low phase noise branches permit high stability comparisons at 1156 nm, 698 nm (Sr optical lattice clock, ${}^1S_0 \rightarrow {}^3P_0$), and 871 nm (Yb ion clock, ${}^2S_{1/2} \rightarrow {}^2D_{3/2}$) [103]. Additionally, the comb has 10 GHz photonic microwave output to permit comparison with either microwave clocks or with other optical clocks having microwave outputs [104]. The microwave output was used for the comparison at USNO.

Recently, we began using the comb for locking several of the atomic trapping and state preparation lasers. These highly robust frequency locks have contributed to the high up times that have helped measure our uncertainty budget at the low 18-digit level.

Figure 2.22: **(a)**Image of the clock laser module at USNO. **(b)**Image of the optical frequency comb from Menlo Systems.

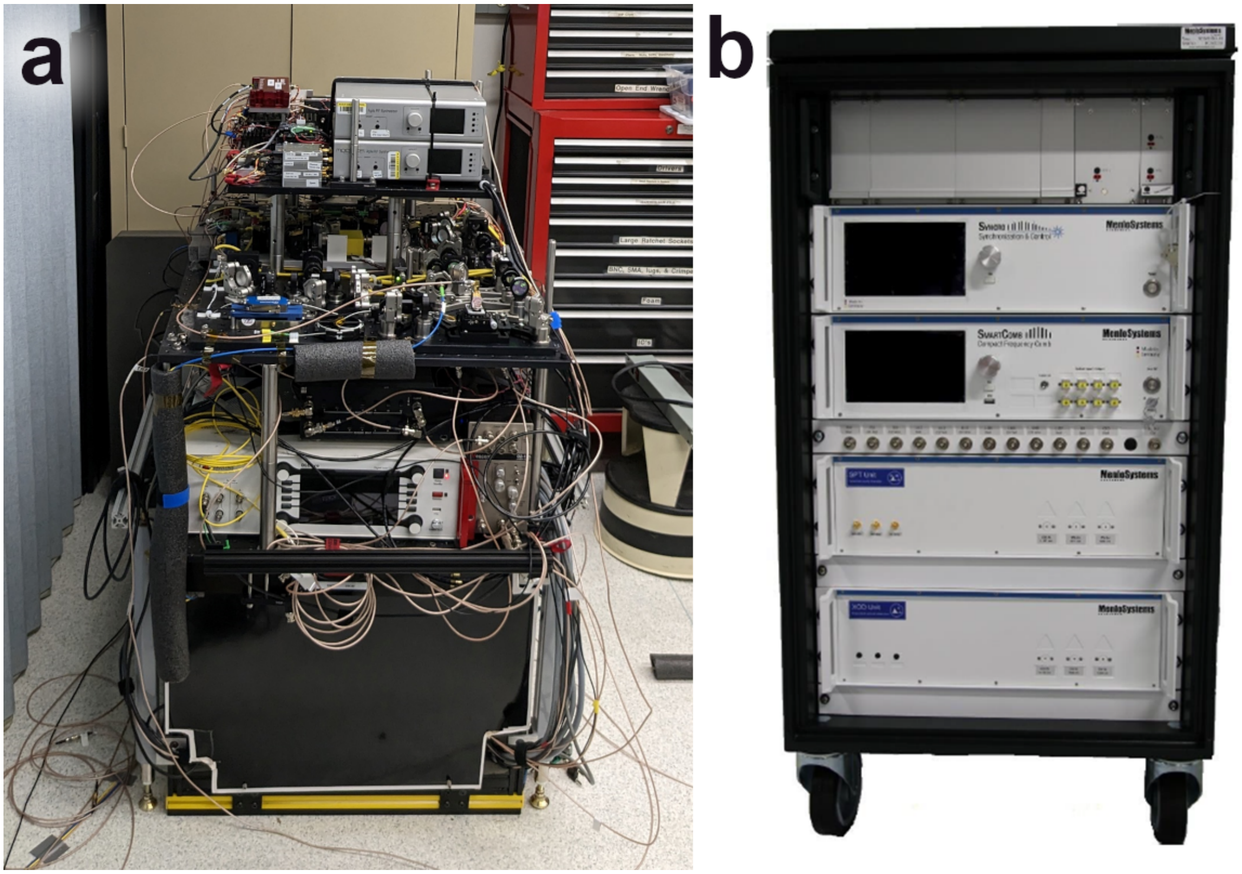

# Chapter 3

# Deployment to US Naval Observatory

## 3.1 Preparation for the deployment

In March of 2023 the system was shipped nearly 3,000 km from NIST in Boulder, Colorado to the United States Naval Observatory in Washington DC. At this time, the atomic apparatus was split across three racks including a multicolor cavity from Stable Laser Systems used for locking atom preparation lasers.

To prepare for this deployment, the atomic physics package was moved on a number of “training” missions. These training runs evolved from moving the system around NIST, to shipping the system on a 50 mile round trip straight back to NIST, and shipping the system to the nearby CU Boulder campus and setting it up in an available lab space. In this process, we learned 1) what components need to be made more robust for shipment, 2) best practices for shipping the system, and 3) how to quickly get the system operating after moving it.

A number of system components failed as a result of shipping in both practice runs and on the deployment to USNO. Some of the more dramatic failures are shown in Figure 3.1. Other components that failed include a second harmonic generation crystal that cracked, free space optical alignments that severely drifted, an EOM tank circuit whose resonant frequency drifted by several factors of its full width at half maximum, an integrated circuit on a servo board that melted on startup, and multiple fiber optic cables that stopped transmitting.

While we are sure interesting new problems will present themselves on future deploy-

Figure 3.1: Some of the issues we have encountered with transit **(a)** We shipped the cavity module for the first time on the deployment to USNO. Screws supporting the upper breadboard backed out and sheared under stress. **(b)** Another significant issue at USNO was that our commercial multicolor had an in-vacuum wire that came loose and blocked the TEM00 cavity mode. We locked the 556 nm and 759 nm lasers to the TEM11 modes instead which went 'around' the wire. The 1388 nm laser was locked with the wavemeter. **(c)** When moving the clock laser module at NIST the caster wheels failed. We switched to a method of raising the module on its hydraulic feet and moving it with a scissor jack instead.

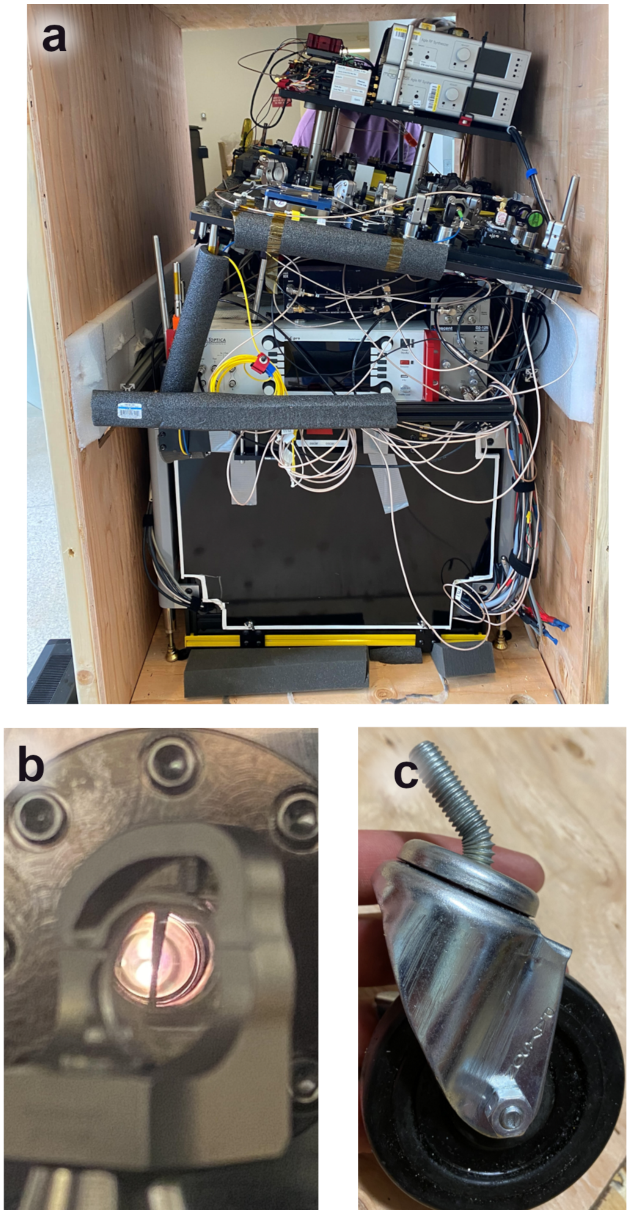

ments, we have made a number of upgrades to improve these issues. As discussed in section 2.1.1, thread locking adhesive is invaluable on rack mount screws to prevent them from backing out. Thread locker is also useful on other key infrastructure such as free space optical assemblies and assembled modules like the clock laser system. “Squishy” kinematic optical mounts should be replaced or tightened if possible. Irises, other alignment marks, and beam cameras make it much easier to align systems repeatably. We now only use metal-jacketed fiber optic cables for any cable that crosses between modules. Power conditioning and a turn on procedure protects electronics.

To move the system components, we used custom-made wooden shipping crates. Some details of the crates are shown in Figure 3.2. Good crates are easy to load and damp vibrations well. Another shipped lattice clock experienced up to $4g$ accelerations in a short distance of truck transportation [13]. Before packaging the system up we gradually turn down the temperature of hot components such as the atomic beam oven and gracefully shut down all electronics except the ion pumps which remain powered by the UPS battery. Then we wrap each of the atomic physics racks in anti-static cling film to prevent dust contamination from reaching the optics or electronics. The racks are wheeled into the crates and the UPS extension cord is routed through a hole for power later. The racks are wedged in tightly in all dimensions with stiff foam and the crates are securely closed with four 5/16” bolts. Crates are moved with a scissor jack. Ideally, the shipping point has its own elevating platform for getting the crates on to the shipping truck. After arriving, if time permits, then it is best practice to let the crates reach thermal equilibrium in their new environment before opening them. Racks are plugged in to the wall outlets to ground them before removing the cling film. Major electronic systems are turned on one-by-one and the electronics that control temperature servos are monitored as they are turned on to prevent servo railing.

Once the system is in a new location, it must be brought into full operation. Most details of operation and alignment are contained in appendix A. Many steps in resuming operation require practice and a strong conceptual understanding of the goals to be done

Figure 3.2: Shipping crates and components thereof. **(a)** The interior of one of the three shipping crates for the atomic clock system. On the far wall are foam pads that correspond spatially to the "bumpers" on the front of the rack systems, see Figure 2.1. The racks have soft foam pads attached to them on the crate door side. On the sides and top of the crate are adhered stiff foam rails. Additional foam "spears" are jammed in tightly to secure the rack in place and prevent motion within the crate. A layer of rubber "horse trailer matting," an inexpensive material for damping vibrations [105], is glued to the floor of the crate. **(b)** Ramps made with beams having long mitered cuts work very well. **(c)** Ramps with cross studs and hinges are harder to maneuver heavy equipment on. **(d)** The cavity rack had foam feet for the scissor jack which is another possible tool for vibration damping.

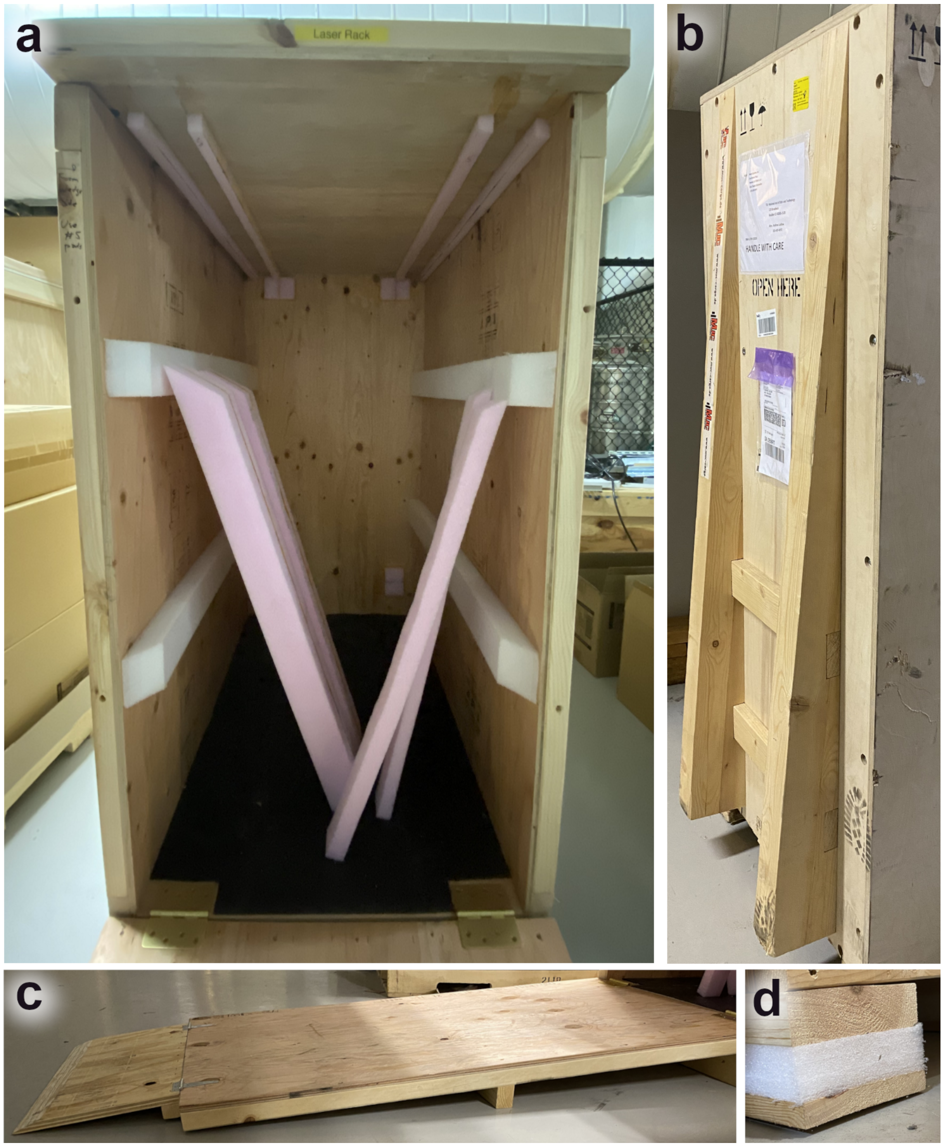

efficiently, but generally the only “hard” steps are loading atoms into the lattice and diagnosing anything that broke. Since the polarizations, frequencies, and intensities have already been optimized, MOT alignment is usually rapid. Fiber coupling of the 399 nm and 759 nm lasers may be tedious if the misalignment is severe, but is not usually difficult. The worst misalignments of these systems after transport were likely (my) user error that resulted in premature adjustment of mirrors far upstream in the system. Magnetic field zeroing and optical pumping alignment can take time, but are uncomplicated. A good method of making the field zeroing simpler is to use a compass several feet from the chamber (to avoid ion pump fields) and align the chamber to Earth’s field in a consistent way when unpacking the clock. The magnetic quantization axis of the chamber is presently facing northwest ±5°.

## 3.2 Comparison at the US Naval Observatory

Following the previous preparations for deployment and characterization of the transportable clock laser module, the entire clock system (3 atomic racks, frequency comb, and comb module) were shipped to USNO. The full truck is shown in Figure 3.3. During the nearly 3,000 km journey to USNO, power was lost during a rain storm owing to water causing an electrical short. This power loss resulted in the cavity vacuum chamber needing to be turbo-pumped upon arrival to restart the ion pump. Further, the full clock laser assembly suffered several structural failures arising from vibrations loosening screws during shipping, see Figure 3.1(a). Despite these complications, the ultrastable cavity and optics remained fully aligned. Within 1 day of arrival all repairs were made and the cavity was found to still be fully aligned to the TEM00 mode, requiring no realignment. The cavity stability against the USNO ultrastable laser was shown previously in Figure 2.20(b), demonstrating consistent performance before and after shipping.

The physics packages arrived mostly free of harm, with the exception of the multicolor cavity which had an in-vacuum wire come loose, blocking the cavity mode. We found with the 556 nm laser that what was most likely the TEM11 spatial mode transmitted around

Figure 3.3: The full portable Yb OLC system prepared for shipment within a commercial shipping truck. Each apparatus component is individually stored in a custom wooden crate, with additional boxes for general lab supplies. Battery power within crates enabled movement of the system with uninterrupted power to vacuum pumps and heaters. The truck was supposed to supply electrical power throughout the journey, but an intense rainstorm caused a breaker-flipping short that resulted in the loss of power for over an hour.

the wire tolerably well, and that the laser could be locked to this mode. Using the atoms as a frequency reference, we adjusted the frequency of the cavity offset PDH lock so that the laser could be used for cooling. We used the same offset frequency correction for the 759 nm laser so that its frequency was expected to be within 1 MHz of the magic wavelength. A wavemeter verified the frequency of the lattice laser to be within 50 MHz of the magic wavelength. The 759 nm laser's lock was tenuous throughout the deployment and much of the technical effort on the atom machine was spent on optimizing this lock. The 1388 nm laser was locked with feedback from the wavemeter instead of the cavity, which was adequate for its operation. Otherwise, most operations went smoothly and atoms were trapped in the lattice within several hours of arrival.

Within two days, the entire transportable Yb OLC was fully operational. Clock spectroscopy measured the optical cavity resonance to have shifted approximately 200 kHz over 8 days, largely explained by the cavity drift rate. This provided a critical verification of the transportable cavity architecture, demonstrating standard broadband clock spectroscopy was easily capable of finding the clock cavity mode, supporting the potential of comb free operation during deployments. The clock was locked using Rabi $\pi$-pulse times ranging from 8 to 35 ms, observing similar excitation performance and locking abilities as before shipping. We referenced the transportable comb to the spectroscopically stabilized light to carry out comparisons at 10 GHz between the transportable comb and a similar lab-based model at USNO. Frequency stability comparisons between the Yb system and the USNO Rb fountain [106, 107] were then performed in the microwave domain. Figure 3.4 shows a schematic of this comparison.

Prior to its arrival, the Rb fountain was set up to use the USNO ultrastable laser as a local oscillator (LO) to reduce short-term instability. A key objective of the deployment was to assess the enhanced performance of the Rb fountain using the portable Yb OLC. Several data runs were conducted to enhance both the clock uptime and the integrated Rb fountain/optical LO system. The deployment culminated with a nearly day long comparison,

Figure 3.4: The microwave frequency clock comparison at USNO. The USNO clock system had a central optical frequency comb that was locked to an optical cavity reference for stability at short times and received steering from a Rb fountain clock for long term stability. The 10 GHz photonic microwave outputs of both the USNO comb and transportable comb were mixed and sent to a phase noise analyzer (53100A, Microchip) for assessing the relative stability of the clocks. Edited version of a diagram supplied by USNO personnel.

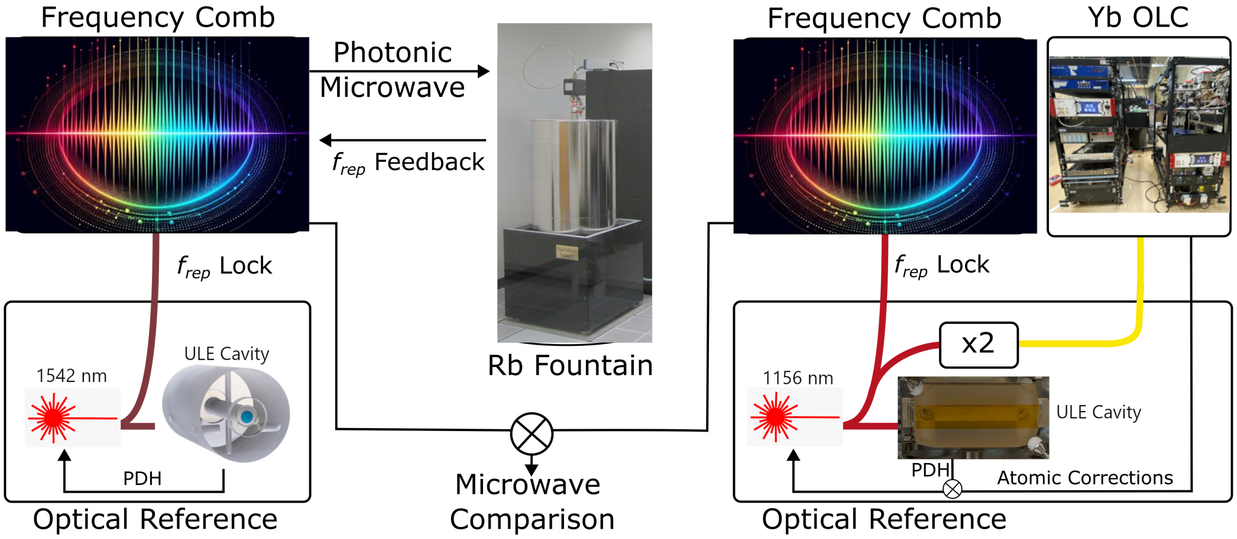

as depicted in Figure 3.5, achieving almost a full day of uninterrupted operation. This highlights the high uptime capability of the portable Yb OLC, which is essential for future frequency comparisons. The comparison between Yb OLC and Rb found an instability of $8.8 \times 10^{-14}/\sqrt{\tau}$, indicating the enhanced stability of the combined Rb fountain/optical LO system. This deployment validated the atomic physics package design, proving its ability to conduct frequency comparisons even after being transported over 3,000 km.

Figure 3.5: **a)** 80,000 s long frequency comparison between the transportable Yb OLC and the USNO Rb fountain. Data was collected from a continuous run. **b)** Modified Allan deviation in fractional frequency units for the comparison data. The transportable Yb OLC resolved the long term instability of the Rb fountain to be at $8.8 \times 10^{-14}/\sqrt{\tau}$, reaching the high $10^{-16}$ level after $10^4$ s of averaging.

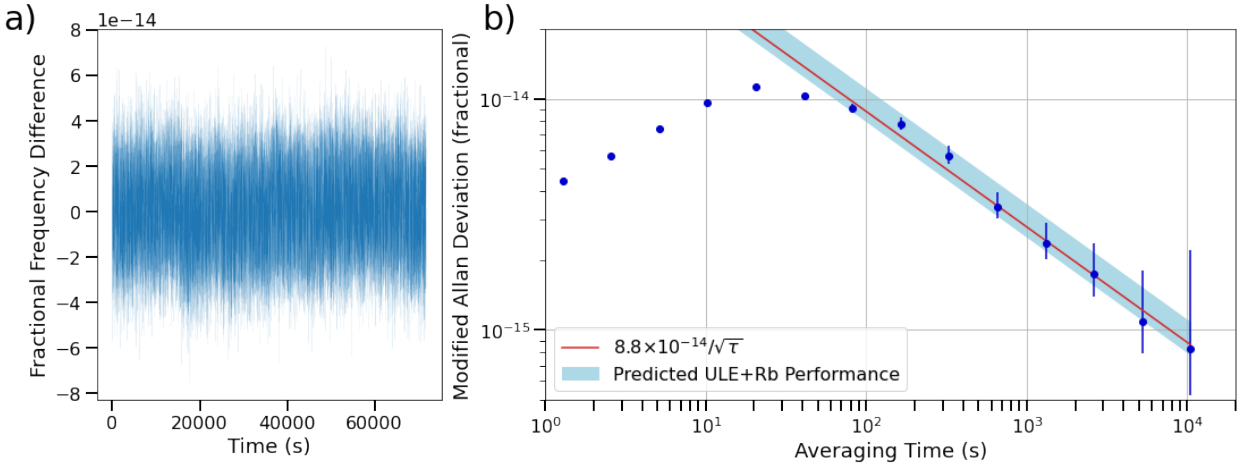

# Chapter 4

# The Uncertainty Budget

## 4.1 Overview

Systematic shifts are necessarily present in lattice clocks because the clock laser is locked to an atomic transition perturbed by the lattice trap and the clock laser itself. However, to make a universal frequency standard that is independent of the particular machine or observer, we want to extrapolate from the clock laser frequency to the unperturbed transition frequency. If we can measure the sum total of all systematic shifts, then we can successfully perform this extrapolation by making these corrections in either real-time or post-measurement analysis.

These systematic shifts are either measured with the clock system itself or by measuring the environment of the atomic sample. Measurements that can be orthogonalized from other clock systematics are performed by modulating one parameter that causes a systematic shift. Then a frequency shift is measured by interleaved comparison between two modulation setpoints of that parameter. The shift as a function of the modulated parameter can then be used compute the shift at operational conditions. For example, the cold collision shift is linear in atom number so a comparison can be made between high and low atom number samples to extrapolate a frequency shift per atom and, therefore, the resulting frequency shift at any operational atom number. Most of the major systematics in this thesis were measured in this manner. For some shifts that are not expected to be experiment dependent, we made use of existing measurements of atomic coefficients. We then only need to measure the corresponding environmental parameters. For example, the blackbody radiation (BBR) shift requires careful measurement of the thermal parameters of the spectroscopy chamber, while the atomic coefficients of response to BBR have been measured previously. Systematic uncertainty for these shifts is then a result of both the ability to control environmental conditions and the uncertainties in atomic coefficients from previous measurements.

Long measurements with high uptime and a stable clock laser enabled us to average frequency uncertainty to a low level. We were able to take advantage of the system's robustness, making many of the measurements overnight or for multiple days of lightly-monitored operation. The lab clock laser was used for these measurements to benefit from its additional stability resulting in reduced frequency uncertainty. Interleaved self-comparison measurements in this chapter typically had an instability of $6 \times 10^{-16}/\sqrt{\tau}$. Statistical uncertainty of the measurements was determined at at $\tau_{\mathrm{max}}/2$ by a fit of white-FM noise to the Allan deviation of the clock frequency for $\tau > 500$ s.

Our uncertainty budget is presented in Table 4.1. The table and the following subsections are grouped by the physics of the considered shifts. Frequency uncertainty from local geopotential is considered separately in the table since it does not represent an intrinsic systematic effect for the transportable clock, but rather an independent relativistic effect for measurements. This presentation of the uncertainty budget will also pay particular attention to some of the scaling laws that could adversely affect a portable clock, such as those related to a less stable local oscillator. Note that the measurements in support of this uncertainty budget were made with a clock laser locked to an ultrastable laboratory cavity.

## 4.2 Electromagnetic Field Systematics

A fundamental advantage of using atoms for clocks is that the internal electric field of an atom is very large compared to external fields. As a result, the energy levels of the bound states depend almost entirely on the internal structure of the atom. Nevertheless, when building a device that attempts to sense the difference in energy levels of an atom with

| | | **Transportable** | | **Stationary** | |
|---|---|---|---|---|---|
| **Shift** | **Section** | **corr.** | **unc.** | **corr.** | **unc.** |
| Electromagnetic fields | 4.2 | | | | |
| Lattice light | 4.2.3 | −3.0 | 3.2 | −1.5 | 0.8 |
| Traveling wave | 4.2.4 | 0 | 0.1 | 0 | <0.1 |
| Lattice spectral purity | 4.2.5 | 0 | 0.05 | 0 | <0.05 |
| BBR | 4.2.6 | −2462 | 1.7 | −2361.2 | 0.9 |
| DC Stark | 4.2.7 | 0 | <0.1 | 0 | <0.07 |
| Probe Stark | 4.2.8 | 0.02 | 0.01 | 0.02 | 0.01 |
| $2^{\text{nd}}$-order Zeeman | 4.2.9 | −199.1 | 0.2 | −118.1 | 0.2 |
| Two body shifts | 4.3 | | | | |
| Cold collisions | 4.3.1 | −3.3 | 0.6 | −0.21 | 0.07 |
| Spin polarization | 4.3.2 | 0 | 0.4 | 0 | <0.3 |
| Background gas collisions | 4.3.3 | −2.0 | 0.3 | −5.5 | 0.5 |
| Doppler | 4.4 | | | | |
| Doppler, clock delivery | 4.4.1 | 0 | 0.21 | 0 | <0.02 |
| Tunneling | 4.4.2 | 0 | 0.005 | 0 | <0.001 |
| Frequency control | 4.5 | | | | |
| Optical frequency synthesis | 4.5.1 | 0 | <0.1 | 0 | <0.1 |
| Servo Error | 4.5.3 | 0 | <0.05 | 0.03 | 0.05 |
| Line pulling | 4.5.4 | 0 | <0.01 | 0 | <0.1 |
| **Total** | | −2663.4 | 3.7 | −2486.5 | 1.4 |
| Geopotential | 4.6 | | | | |
| Absolute geopotential at NIST | | 180 736 | 6 | 180 819 | 6 |
| Relative geopotential at NIST | | −40.1 | 0.4 | | |

Table 4.1: Summary of clock frequency corrections applied to both the transportable and stationary lattice clocks used in this work. Units are in parts of $10^{-18}$ of fractional frequency.

eighteen digits of accuracy, even very small shifts to these energy levels are relevant. Indeed, some of the shifts from external fields like the BBR shift are tiny effects on an absolute scale at $2 \times 10^{-15}$, but large on the scale of the clock's uncertainty target.

### 4.2.1 Electric dipole couplings

First, we will consider the shift from electromagnetic fields due to the strong electric dipole ($E1$) coupling to external fields. When an atom is exposed to an electric field, $\boldsymbol{E}$, an electric dipole moment $\boldsymbol{p} \propto \boldsymbol{E}$ is induced. That is, the wave function of the outer, unshielded electrons, becomes stretched into alignment with the electric field. This polarization effect is both desirable in that it is responsible for the ultimate ability to trap and interrogate atoms and undesirable in that it is the source of the largest systematic shifts on the clock transition. In general, electric fields may be at some frequency $\omega$, hence $\boldsymbol{E}(\boldsymbol{r}, t) = E(\boldsymbol{r}, \omega)e^{-i\omega t}\hat{\mathbf{j}}$, where $\hat{\mathbf{j}}$ is an arbitrary unit vector and $E(\boldsymbol{r}, \omega)$ is the electric field strength at some position and electromagnetic frequency. Likewise, $\boldsymbol{p}(\omega) = \alpha(\omega)\boldsymbol{E}$ where $\alpha(\omega)$ is the atom's complex polarizability. The change to the electronic potential is then given by,

$$\Delta U(\omega) = \langle\psi|e\boldsymbol{E}\cdot\boldsymbol{r}|\psi\rangle = -\frac{1}{2}\langle\boldsymbol{pE}\rangle = -\frac{\mathrm{Re}(\alpha(\omega))|E(\boldsymbol{r}, \omega)|^2}{2}, \tag{4.1}$$

where the angle brackets indicate the time average over the oscillating electric fields and the factor of 1/2 comes from the fact that the dipole moment is an impermanent induced dipole [108]. For the rest of this discussion, we will only consider the real part of polarizability. In a clock, we are interested in the differential effect of this induced potential on the clock states, the ground, $6s^2\ ^1S_0$, and excited, $6s6p\ ^3P_0$, states. The induced potential difference is then,

$$\begin{aligned}\Delta U_{\text{clock transition}}(\omega) &= \Delta U_e(\omega) - \Delta U_g(\omega)\\ &= -\frac{E(\boldsymbol{r}, \omega)|^2}{2}(\alpha_e(\omega) - \alpha_e(\omega))\\ &= -\frac{E(\boldsymbol{r}, \omega)|^2}{2}\Delta\alpha(\omega),\end{aligned} \tag{4.2}$$

where we have defined the differential electric dipole polarizability, $\Delta\alpha(\omega)$, between the clock states. The electric dipole polarizability of an individual clock state $n$ from an electric field at some off resonant frequency $\omega/2\pi$ is

$$a_n(\omega) = \frac{2}{3\hbar}\sum_{n'\neq n} |\langle n'||\boldsymbol{D}||n\rangle|^2 \frac{\omega_{n'n}}{\omega_{n'n}^2 - \omega^2}, \tag{4.3}$$

where $\boldsymbol{D}$ is the electric dipole matrix operator for $^{171}$Yb and $\omega_{n'n}/2\pi$ is the frequency of an electric dipole transition between states $n$ and $n'$. As shown in Figure 4.1, the polarizability of the atoms, and therefore the induced shift, becomes dependent on the frequency beginning at low frequency in the near infrared spectrum. Fortunately, this means the problem of computing and correcting the shift from stray fields is largely decomposable into static (low frequency) and dynamic (high frequency) effects. Discussion will proceed describing the effects of: near-static electric fields, single optical frequency electric fields, and broad frequency spectrum electric fields.

Static (DC) fields and radiation at frequencies below $\approx$ 50 THz, like BBR, perturb the clock transition almost entirely through the differential static polarizability of the clock states,

$$\alpha_{\text{clock}}(0) = \alpha_e(0) - \alpha_e(0) = 36.2612(7)\text{kHz (kV/cm)}^{-2}. \tag{4.4}$$

This value was previously carefully characterized in another optical lattice clock by measuring the shift to the clock transition frequency by applying a large static electric field to the atoms from electrodes at a known potential and distance to the atoms [109]. The differential static polarizability then determines that the maximum static voltage that atoms may witness with a $< 1 \times 10^{-18}$ shift is 0.12 V. This constraint then determines the required accuracy in the modeling of the shielding factor needed in our grounded metallic vacuum chamber to suppress shifts from stray static fields. Likewise, the differential static polarizability will contribute the bulk of the BBR correction since BBR is predominately a low frequency effect that cannot be eliminated in a room temperature chamber.

Perturbations from laser electric fields detuned from resonances can be treated like

Figure 4.1: The physical origins of the magic wavelength and the BBR shift. The blue and orange lines are the polarizabilities of the ground and clock states of the atom, respectively, with their axes on the left. The poles of these polarizabilities occur at the frequencies of electric dipole transitions, where electric fields interact most strongly with the atoms. The wizards' staffs mark the "magic wavelengths" where the differential polarizability of the ground and clock state vanish. We operate at the lowest frequency magic wavelength. The gray line shows the spectral density of electromagnetic energy from a 300 K blackbody source as dictated by the Planck radiation law distribution with its axis on the right. The vast majority of the spectral content of the BBR is far red-detuned from the transitions available to the ground and clock states. Consequently, the BBR shift is mostly a result of the DC differential polarizability of the relevant states. However, accounting for the spectral content near the $^3P_0 \rightarrow\ ^3D_1$ transition where the differential polarizabilities are dramatically different is the source of the dynamic correction coefficients. Note that the magic wavelength near 540 THz requires a 3D lattice since the negative polarizability means that it has an anti-trapping force.

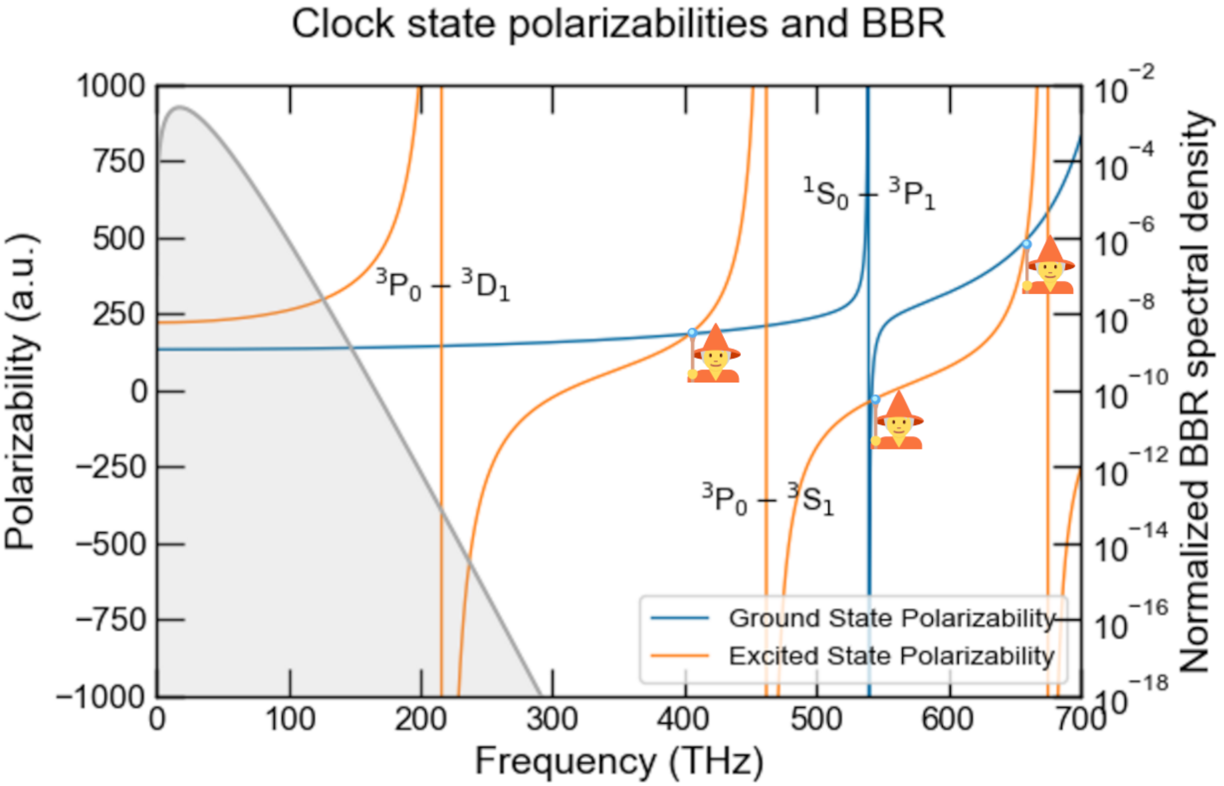

a static field shift in the simplest approximation since the laser frequency is effectively a delta function on the scale of the differential polarizability's response to frequency. Note that resonant lasers can impose enormous systematic shifts if not properly shuttered during operation. For example, prior to installation of a shutter in the 1388 nm module we witnessed time-varying shifts on the several Hz scale when comparing the portable clock to Yb1 due to inadequate extinction from the AOM alone. However, we are primarily concerned with the large off-resonant electric field from the lattice laser. Recalling equation 4.1, a trapping potential can be generated with a laser's electric field. Substituting the laser field intensity, $I = 2\varepsilon_0 c|E(\boldsymbol{r},\omega)|^2$, we derive the force from the laser field.

$$\boldsymbol{F}_{\text{lattice}}(r) = -\nabla U_{\text{lattice}}(\boldsymbol{r}) = \frac{1}{2\epsilon_0 c}\alpha(\omega)\nabla I(\boldsymbol{r},\omega). \tag{4.5}$$

The importance of the optical lattice is then illustrated, a standing wave field will have a non-zero gradient in three dimensions which is required for localizing atoms in the trap [108].

Naively, one might think that the light shift will necessarily be large since the potential needed to trap a thermal sample of atoms is also an energy level shift on the atomic ground state. However, owing to the different transitions available to ground and excited state atoms, their polarizabilities as expressed in equation 4.3 have unique responses to optical frequency electric fields. In particular, there exists a point, shown in Figure 4.1, at 759 nm where the electric dipole polarizabilities of the ground and excited states are identical, which is called the **magic wavelength**. As seen in Figure 4.1, there is more than one magic wavelength available for Yb. We use the magic wavelength at 759 nm because it is relatively convenient to generate the high optical powers needed for dipole trapping at this near-infrared color. Potential high power laser systems include diode lasers and tapered amplifiers as used in the portable system or with optically pump Ti:Sapphire lasers as used in the laboratory clocks. This magic wavelength additionally benefits from a comparatively low slope for the differential polarizability which requires less precise laser frequency control and less accurate magic wavelength characterization.

While operating the lattice at the magic wavelength cancels the majority of the induced light shift, higher order effects in optical intensity frustrate this cancellation. In the high intensity laser field, the quadratic hyperpolarizability effect along with electric quadrupole ($E2$) and magnetic dipole ($M1$) interactions can be a dominant source of systematic uncertainty unless carefully quantified [110]. Revisiting equation 2.1 for the spatial lattice potential $V_0(z, \rho)$, we can expand the lattice potential to include higher order effects

$$\begin{aligned} V(z,\rho) = V_0(z,\rho)\frac{\alpha_{E1}}{\alpha_{E1}} + V_0(z+\lambda_L/4,\rho)\frac{\alpha_{M1E2}}{\alpha_{E1}} + V_0^2(z,\rho)\frac{\beta}{\alpha_{E1}^2} \\ + \mathcal{O}(V_0^3(z,\rho)) + +\mathcal{O}(V_0^2(z+\lambda_L/4,\rho)) \end{aligned} \tag{4.6}$$

where $\alpha_{E1}$ is the electric dipole polarizability, $\alpha_{M1E2}$ is the combined $M1$ and $E2$ polarizabilities whose contribution to the potential are out of phase with the $E1$ polarizability by 1/4 of the lattice wavelength, $\lambda_L$, since they are strongest where the electric field gradient peaks, and $\beta$ is the quadratic hyperpolarizability coefficient. Since the potential acts differentially on the two clock states, we can define additional terms to quantify these effects on the transition frequency

$$\Delta\alpha'_{E1} \equiv \frac{\Delta\alpha_{E1}E_r}{\alpha_{E1}(\nu_{\text{magic}})h\nu_{\text{clock}}} \tag{4.7}$$

$$\Delta\alpha'_{M1E2} \equiv \frac{\Delta\alpha_{M1E2}E_r}{\alpha_{E1}(\nu_{\text{magic}})h\nu_{\text{clock}}} \tag{4.8}$$

$$\Delta\beta' \equiv \frac{\Delta\beta E_r^2}{\alpha_{E1}^2(\nu_{\text{magic}})h\nu_{\text{clock}}}, \tag{4.9}$$

where each term is the dimensionless differential effect of the $E1$ polarizability, $M1E2$ polarizability, and hyperpolarizability respectively.

Then the fractional frequency shift of the clock transition, $\nu_{\text{clock}}$, is given by,

$$\frac{\Delta\nu_{\text{clock}}}{\nu_{\text{clock}}} = -U\Delta\alpha'_{E1}X_{\mathbf{n}} - U\Delta\alpha'_{M1E2}Y_{\mathbf{n}} - U^2\Delta\beta' Z_{\mathbf{n}} \tag{4.10}$$

where $U$ is the trap depth in recoil units, and $\Delta\alpha_{E1}$, $\Delta\alpha_{M1E2}$, $\Delta\beta$ are the differential polarizability effects between clock states [110]. These differential polarizabilities are dependent on the lattice frequency. $X_{\mathbf{n}}$, $Y_{\mathbf{n}}$, and $Z_{\mathbf{n}}$ are expectation values of the spatial portion of the trapping potential for atoms in total motional state $\mathbf{n}$. These expectation values must be approximated. The strategy we follow from [110, 111] is to treat the frequency shift as a first order perturbation from the motional states in the simple harmonic oscillator motional basis. Note, however, that more sophisticated treatments are possible, such as a Born-Oppenheimer-like approximation [112]. Whereas the Born-Oppenheimer approximation separates electronic and nuclear degrees of freedom to describe the quantum states of molecules, this approximation separates the radial and longitudinal motional states since their energy scale also typically differs by orders of magnitude.

In this perturbative treatment, we may then apply the dimensionless lattice spatial potential operator, $\mathcal{U}(z,\rho) = V_0(z,\rho)/(-\alpha_{E1}E_0^2/4)$ equation 2.1, to the simple harmonic oscillator motional states $|\mathbf{n}\rangle$ to calculate the expectation values. Hence, in forms suggested by equation 4.6, $X_{\mathbf{n}} \equiv \langle\mathbf{n}|\mathcal{U}(\mathbf{z},\rho)|\mathbf{n}\rangle$, $Y_{\mathbf{n}} \equiv \langle\mathbf{n}|\mathcal{U}(\mathbf{z}+\lambda_{\mathbf{L}}/\mathbf{4},\rho)|\mathbf{n}\rangle$, and $Z_{\mathbf{n}} \equiv \langle\mathbf{n}|(\mathcal{U}(\mathbf{z},\rho))^{\mathbf{2}}|\mathbf{n}\rangle$ [110]. The lattice light shift then is determined in part by temperature since atoms at different temperatures sample the lattice light to different degrees. In section 4.2.3, we will apply a thermal model to compute these expectation values and reduce the lattice Stark shift to a form that can be fit with data from the portable experiment.

Broadband sources of radiation such as BBR cannot be precisely cancelled like the dipole lattice light shift and can require more care to minimize their effects. The energy shift on a particular clock state from dipole coupling to broadband radiation is the Cauchy principal value from evaluating

$$\Delta E_n = -2\pi \int_0^\infty u(\omega)\alpha_n(\omega)d\omega, \tag{4.11}$$

where $u(\omega)$ is the spectral energy density of the source and $\alpha_n$ comes from equation 4.3 [113]. For a BBR emitter, the spectral energy density function, $u(\omega)$, is given by Planck's law and the time-averaged electric field intensity at $T_0$ is $\langle E^2\rangle_T \approx (8.3193\text{V/cm})^2(T/T_0)^4$ [114]. Wien's Displacement Law states that the BBR frequency with the greatest intensity varies linearly with temperature, $T$, as $\omega_{\text{BBR, max}}(T)/2\pi = T/c \times 2.89$ mm/K. Since at room temperature, $T_0 = 300$ K, all of the transition frequencies in ytterbium are much higher than $\omega_{\text{BBR, max}}(T_0)$, the integral may be approximated as a Taylor expansion in $T/T_0$ [75]. Taking the difference between the expansions at the two clock states yields the equation

$$\Delta\nu_{BBR} = -\frac{1}{2}\frac{\Delta\alpha(0)}{h}\langle E^2\rangle_T \left[1 + \eta_{\text{dyn, }2}\left(\frac{T}{T_0}\right)^2 + \eta_{\text{dyn, }4}\left(\frac{T}{T_0}\right)^4\right], \tag{4.12}$$

where it may be seen that the BBR shift is predominately a static Stark shift from the thermal electric field with a small **dynamic correction** ($\approx 2\%$) for the frequency dependence of polarizability. Determination of the dynamic correction then depends on careful evaluation of the $^3P_0 \rightarrow\ ^3D_1$ dipole matrix element which dominates the strength of additional interaction for high frequency BBR [113, 32]. In $^{171}$Yb the dynamic corrections are $\eta_{\text{dyn, }2} = 0.0173(5)$ and $\eta_{\text{dyn, }4} = .00059(1)$ [113], where these values were assessed after careful measurement of the $^3D_1$ state lifetime. With this model for the clock shift and another model for the temperature experienced at the atoms, the BBR shift may be accurately characterized.

### 4.2.2 Magnetic dipole couplings

Shifts due to magnetic fields through the magnetic dipole ($M1$) coupling are also important systematic effects in clocks. The clock states in most alkaline earth lattice clocks are both $J = 0$ which makes them insensitive to magnetic fields. However, for the fermionic isotopes used in most lattice clocks, the clock states must be labeled by their total angular momentum $F = J + I$ where $I$ is the nuclear spin quantum number. The clock states then have $2I + 1$ substates. For $^{171}$Yb where $I = 1/2$, there are then only two substates, $m_{\text{F}} = \pm 1/2$. While the clock states do not have the zero magnetic sensitivity of a clock based on a bosonic isotope, the shifts from magnetic fields are scaled by the nuclear magneton, $\mu_N$, as opposed to the Bohr magneton, $\mu_B \approx 1836 \times \mu_N$ which would be the case for transitions between states with $J \neq 0$. The $^1S_0$ ground state is only sensitive to external magnetic fields through its nuclear magnetic moment and experiences a shift of

$$\Delta E_{g,B} = -g_I I_z \mu_N B_z, \tag{4.13}$$

where $B_z$ is the magnitude of the magnetic field in the $\hat{z}$ direction, $\mu_N$ is the nuclear magneton, and $g_I = 0.4919\mu_N/(I\mu_B) \approx 5.4 \times 10^{-4}$ is the nuclear $g$-factor for $^{171}$Yb [115, 116, 87]. In contrast, the $^3P_0$ state has an additional contribution to the magnetic energy shift arising from the hyperfine state mixing $g$-factor, resulting in a shift of

$$\Delta E_{e,B} = -(g_I + g_{\mathrm{HFS}}) I_z \mu_N B_z, \tag{4.14}$$

where, $g_{\mathrm{HFS}} = 2.73(10) \times 10^{-4}$ [87]. Since we use the $\pi$ transitions for spectroscopy, $|m_F = +1/2\rangle \rightarrow |m'_F = +1/2\rangle$ and $|m_F = -1/2\rangle \rightarrow |m'_F = -1/2\rangle$ and $J = 0$, the nuclear $g$-factors cancel and the measured frequency shift is

$$\Delta\nu_{\mathrm{Zeeman}} = m_F \frac{g_{\mathrm{HFS}}\ \mu_N B_z}{h}. \tag{4.15}$$

Since the shift is linearly dependent on $m_F$, we make use of a simple scheme to cancel the resulting shift by interleaving spectroscopy between the $\pm\pi$-transitions and taking the unperturbed frequency as the mean frequency of the two transitions.

This technique however, has the trade off that there is a resulting second-order Zeeman shift (sometimes called quadratic Zeeman) that is uncancelled by the interleaved interrogation due to its opposite symmetry. This trade off is a good one, however, because the second-order Zeeman shift is orders of magnitude smaller and made manageable by making use of the frequency difference between $\pi$ transitions from the first-order Zeeman shift to accurately measure the local magnetic field. Since the clock states are $J = 0$, they have no hyperfine structure. Hence, the physical origin of the second order Zeeman shift is from the 20.5 THz fine-structure splitting between the $^3P_0$ and $^3P_1$ states [116] (the $^1S_0$ ground state has neither fine nor hyperfine structure couplings). For alkaline-earth-like lattice clocks, this is yet another advantage over alkali microwave clocks which have second-order Zeeman effects from the coupling of clock states to other hyperfine levels. The stronger second-order Zeeman couplings in these clocks result in this shift requiring more care to manage [117].

Like shifts from the electric field, magnetic field shifts also depend on the frequency of magnetic fields as determined by the frequency dependent magnetic polarizability. In section 4.2.3, we treat the frequency dependent magnetic dipole shift from the lattice trapping optical frequency together with the $E2$ polarizability, since they have the same symmetry and dependence on trap depth. In general, ions must treat the AC Zeeman shift from the RF trapping potential more carefully [118]. For example, the heralded thorium-229$^{2/3+}$ nuclear clock transition may, in particular, be vulnerable to parasitic magnetic fields in the RF trap [119].

The broadband radiation from BBR might potentially interact with the atoms in a frequency dependent manner through magnetic couplings [120]. This effect should be largely suppressed by the relative strength of the magnetic field. The magnetic field, $B_0$, of a photon is related to its electric field, $E_0$, by $B_0 = E_0/c$. The potential that a photon's magnetic field exerts on a particle through induced polarization scales as $1/c^2$ compared to the electric field's effect. The only magnetic transition available to either clock state is the fine-structure transition between the $^3\mathrm{P}_0$ and $^3\mathrm{P}_1$ states as permitted by the even-parity magnetic dipole operator, $\mu$ [121]. By analogy to both the integration of BBR over the electric dipole polarizability in equation 4.11 and the frequency dependent dipole polarizability in equation 4.3, a similar integral for the magnetic BBR shift can be constructed. A previous calculation evaluates this is as a $10^{-5}$ correction to $\eta_{\mathrm{dyn},\,2}$ in equation 4.12 [121]. Since this correction is more than an order of magnitude below the uncertainty of the dynamic correction coefficient from knowledge of the electric dipole matrix element, this shift is a negligible component of the BBR uncertainty.

### 4.2.3 Lattice Light

In order to optically trap atoms, the atoms must be placed in a highly perturbing environment to create a deep potential well. When the lattice wavelength, $\lambda_L$, is at the magic wavelength, $\lambda_z$, the differential energy shift between the ground and excited clock states is zero and the unperturbed atomic frequency can be recovered [122, 123, 124]. However, couplings beyond the electric dipole approximation complicate this cancellation [110, 125, 111]. Continuing from the perturbative treatment in equation 4.10, we can calculate the expectation values of the positional states in the lattice to order $z^4$, $\rho^4$, and $z^2\rho^2$. Then, the fractional frequency shift of the clock transition is

$$\begin{aligned}\frac{\delta\nu_{\text{clock}}}{\nu_{\text{clock}}} =& n_5 \Delta\alpha'_{M1E2} \\ &+ [(n_1+n_2)\Delta\alpha'_{E1} - n_1\Delta\alpha'_{M1E2}]U^{\frac{1}{2}} \\ &- [\Delta\alpha'_{E1} + (n_3+n_4+4n_5)\Delta\beta']U \\ &+ [2\Delta\beta'(n_1+n_2)]U^{\frac{3}{2}} \\ &- 4\Delta\beta' U^2 \end{aligned} \tag{4.16}$$

and the values of $n_i$ are linear and quadratic functions of the axial and radial motional quantum numbers, $n_z$ and $n_\rho$ given by [110, 126]

$$\begin{aligned} n_1 &= \left(n_z + \frac{1}{2}\right), \\ n_2 &= \sqrt{\frac{2}{kw_0}}\left(n_\rho + 1\right), \\ n_3 &= \frac{3}{2}\left(n_z^2 + n_z + \frac{1}{2}\right), \\ n_4 &= \frac{8}{3k^2w_0^2}\left(n_\rho^2 + 2n_\rho + \frac{3}{2}\right), \\ n_5 &= -\frac{1}{\sqrt{2kw_0}}\left(n_z + \frac{1}{2}\right)\left(n_\rho + 1\right), \end{aligned}$$

where $k$ is the lattice wave number, and $w_0$ is the $1/e^2$ intensity radius (waist) of the lattice. The value of expressing the light shift in this way is that for a thermal atomic sample the expectation values of the positional states for all atoms $\langle n_i \rangle$ scale with the trap depth, $U$.

As we observed previously in Figure 2.13, the temperature of the atoms in our trap is indistinguishable from linear variation with trap depth. The mean occupation modes are determined by temperature, and in the approximation of a linear temperature fit, $\langle n_z \rangle, \langle n_\rho \rangle \propto U^{\frac{1}{2}}$. This approximation then has the effect that $\langle n_1 \rangle, \langle n_2 \rangle \propto U^{\frac{1}{2}}$ and $\langle n_3 \rangle, \langle n_4 \rangle, \langle n_5 \rangle \propto U$. Previous work in our group also found a linear relationship between temperature and trap depth, with a small quadratic correction that can be measured when accessing very high trap depths ($> 1000 E_r$) [110]. Since the portable clock cannot access those high trap depths, we will discard this aspect of the model (the $\gamma^* U^3$ term of [126]) while otherwise following the prior treatment. Uncertainty contributions from the linear temperature approximation will be discussed later as "model error." Given linear temperature dependence on trap depth, equation 4.16 may be reduced to the form

$$\frac{\delta \nu_{\text{clock}}}{\nu_{\text{clock}}} = -\frac{\partial \alpha^*}{\partial \nu_L}(\nu_L - \nu_{\text{zero}})U - \left(\frac{\partial \beta^*}{\partial \nu_L}(\nu_L - \nu_{\text{zero}}) + \beta^*\right) U^2, \tag{4.17}$$

where $\partial \alpha^* / \partial \nu_L$ is the thermally averaged linear sensitivity to lattice depth, which includes the contributions of $E1$, $M1$, and $E2$ polarizabilities and the $\beta^*$ terms are the thermally averaged sensitivity to hyperpolarizability. $\nu_L$ is the lattice optical frequency and $\nu_{\text{zero}}$ is the frequency where the effects linear in trap depth cancel. Since the magic wavelength frequency is defined as the frequency where the differential $E1$ polarizability is zero, $\nu_{\text{zero}}$ is different from the magic wavelength and depends on the lattice waist and atomic temperature unlike the magic wavelength which is a purely atomic parameter.

With this thermally averaged model, we can collect data to determine $\nu_{\text{zero}}$ and $\partial \alpha^* / \partial \nu_L$ in our lattice. While other measurements of these parameters for $^{171}$Yb have been made, these measurements are not wholly universal atomic parameters. These parameters depend on the temperature of the sample and the details of the lattice such as waist size, beam quality, and spectral purity. The value $\partial a^* / \partial \nu_L$ should be particularly sensitive to atomic temperature and could be used as an alternative thermometric probe since it is easy to measure this value alone by detuning the lattice far from the magic wavelength. Unfortunately, the portable lattice laser system has very little optical power overhead to measure the $\beta^*$ terms that are quadratic in $U$.

To ensure that trap-induced light shifts are controlled near the $10^{-18}$ level, we decided on a procedure to measure consistency with previous data on these coefficients. We first made lattice light shift measurements far- and near- detuned from the magic wavelength to constrain $\partial\alpha^*/\partial\nu_L$ for the portable system. This measurement is shown in Figure 4.2. Second, we made high accuracy measurements of the lattice Stark shift at different lattice depths and detunings near the magic wavelength to replicate the methodology of [110] over a more limited data range. Then, we fit the entire collection of data leaving the magic wavelength and $\partial\alpha^*/\partial\nu_L$ as free parameters. The parameters $\beta^*$ and $\partial\beta^*/\partial\nu_L$ would be fixed to model-adjusted values matching our temperatures from the measured values in [126] for sideband cooled atoms. This scheme would let us extract an independent measure of $\nu_{\text{zero}}$ for the portable system allowing comparison to previous determinations from laboratory clocks.

Lattice light shifts were measured by interleaved self-comparison between a reference trap depth of 70 $E_r$ and a test lattice depth, both with approximately 300 atoms. Taking advantage of the portable clock's high uptime and access to a stable clock laser, many of these self-comparisons had a statistical uncertainty of $2 \times 10^{-18}$. The samples were prepared by loading and sideband cooling in a consistent 150 $E_r$ trap and adiabatically ramping down to 70 $E_r$ before adiabatically ramping up to the target trap depth [127]. Sideband cooling suppresses $M1$ and $E2$ effects from atomic displacement from the lattice intensity maximum as seen in equation 4.6. Likewise, the temperature filtering process ensures both consistent temperature and a reduced radial atomic temperature. Sideband spectroscopy [84] was performed before each measurement to verify temperature and trap depth consistency. Cold collision shifts (section 4.3.1) and second order Zeeman shifts corrections from the vector Stark perturbation (section 4.2.9) were subtracted and their errors added to the measurement error [125]. The lattice frequency, being locked to our clock laser-stabilized

Figure 4.2: We directly measured the first-order differential polarizability coefficient, $\partial\alpha^*/\partial\nu_L$ in our trap. We detuned the lattice 125 MHz from the expected operationally magic wavelength and compared the shift between 70 $E_r$ and 150 $E_r$ lattices [110]. Fitting the slope between this case and the same depth comparisons at lattice frequencies close to the operational magic wavelength measured the parameter $\partial\alpha^*/\partial\nu_L$ at $3.80(6) \times 10^{-20}$ $\text{MHz}^{-1}E_r^{-1}$. The point errorbars are smaller than the markers and the reduced $\chi^2$ was 0.6. This measured value of $\partial\alpha^*/\partial\nu_L$ is 20% higher than a previous measurement for sideband cooled samples [126], which we attribute to the colder radial atomic temperatures reached in the lattice filtering step. This simple slope method results in over-fitting the four points closer to the magic wavelength since they are used in the main fit to determine the magic wavelength. In the global fitting method, we measured $\partial\alpha^*/\partial\nu_L = 3.90(6) \times 10^{-20}$ $\text{MHz}^{-1}E_r^{-1}$.

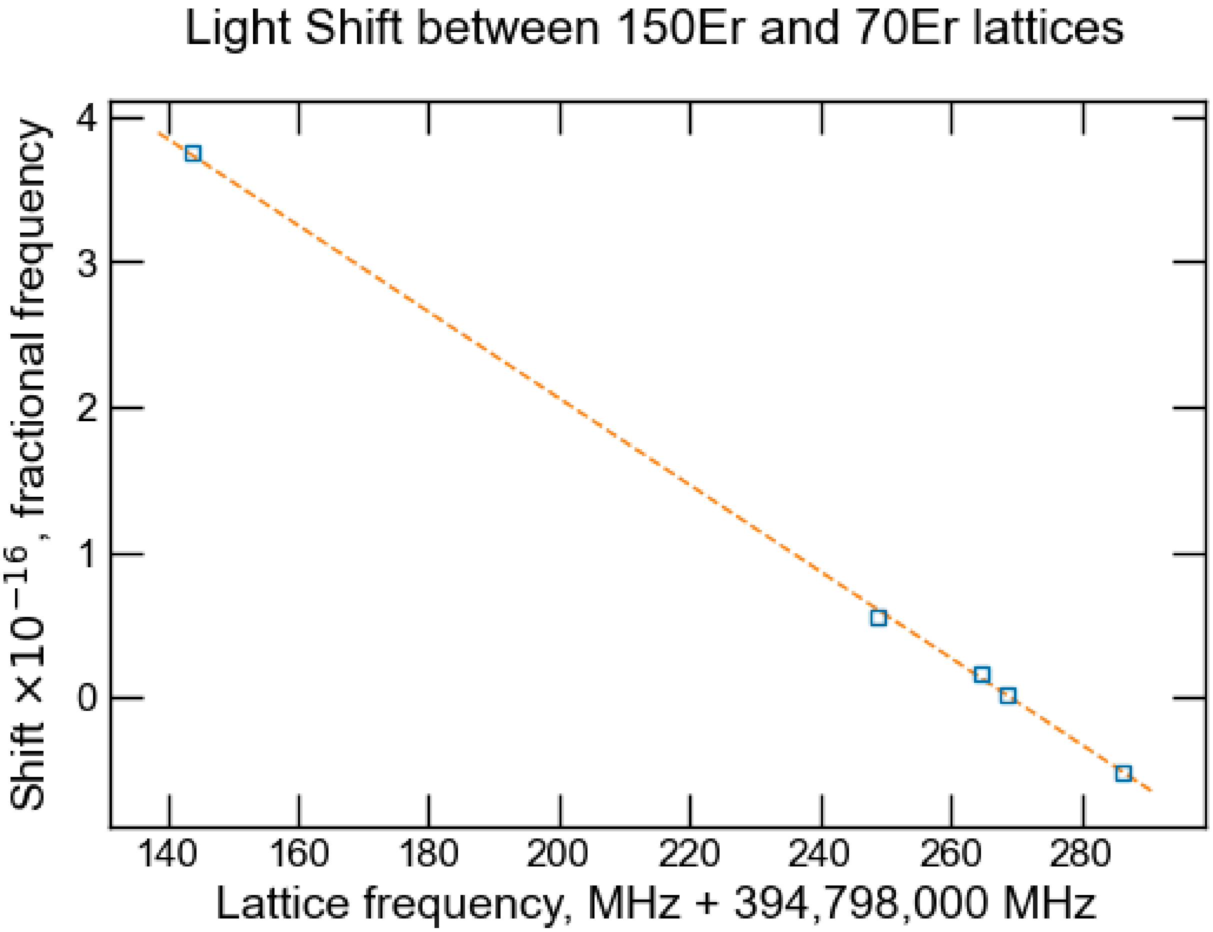

frequency comb, was always known with accuracy better than 100 Hz. These measurements were taken over a two month campaign.

We fit the measured frequency shifts at a range of depths and detunings to the model of equation 4.17. The fit was used to determine the laser detuning where the linear shift crossed zero, $\nu_{\text{zero}}$, with an uncertainty of 500 kHz. However, the resulting fit value differed from that found in [126] by 960 kHz, a difference of $0.9\sigma$, which we took as the dominant uncertainty on $\nu_{\text{zero}}$. This uncertainty was added in quadrature with the uncertainty from both the portable and lab clock measurements of $\nu_{\text{zero}}$. The complete set of parameters put into this model and extracted from it are shown in Table 4.2.

We also consider uncertainty from the model error of using a temperature fit linear in $U$ as opposed to a fit proportional to $\sqrt{U}$ which is better motivated by adiabatic ramping. In this case, $\langle n_z \rangle$ and $\langle n_\rho \rangle$ are constant with respect to trap depth. The full model for the thermally averaged shifts in equation 4.16 then reveals shifts scaling with $U^{\frac{1}{2}}$ and $U^{\frac{3}{2}}$. We sought to avoid the full model because $\Delta\alpha'_{M1E2}$ is not known with high accuracy, there are disagreements in the literature about the value of $\Delta\beta'$, and due to the simplicity of a polynomial model. Instead, to determine the model error, we compute the degree that $U^{\frac{1}{2}}$ and $U^{\frac{3}{2}}$ terms mix in to the polynomial fit given the near linear temperature fit over our range of accessible trap depths. In this way, our model will not strongly depend on precise values of $\Delta\alpha'_{M1E2}$ and $\Delta\beta'$. We take the absolute values of the normalized differences between $\sqrt{U}$ and $U$ in Figure 2.13 and compute the mean. The difference between the two models is then 12% for the axial temperatures and 1.6% for the radial temperatures. Following the model error calculations in [110, 33] that use a Boltzmann distribution to fill in $n_z$ and $n_\rho$ states that differ from the model temperatures, we assess a model error of $3 \times 10^{-19}$.

One potential hurdle for SI adoption of a lattice clock second is not only agreement about the unperturbed clock frequency as assessed through clock comparison, but agreement on the key values of atomic parameters used in uncertainty budgets. Determination of all relevant lattice light shifts for a clock by using only universal polarizability coefficients and experiment-dependent temperature and lattice waist parameters would be very desirable for the next generation of time-keeping lattice clocks. Lattice Stark evaluations are currently one of the most time-consuming systematic shifts to evaluate since they depend heavily on the details of the experiment. Unfortunately, measurements of the higher order polarizability coefficients have not yet converged for Yb clocks [110, 125]. Presently, the NIST Yb lab clocks are working on a high accuracy measurement of the $\Delta\alpha'_{M1E2}$ and $\Delta\beta'$ parameters. After this measurement is completed, we plan to reevaluate the lattice Stark shift by a direct fit to equation 4.16 given measured values of $\langle n_z \rangle$ and $\langle n_\rho \rangle$. This change of analysis would reduce our dissatisfaction with using a linear approximation of temperature with lattice depth since the $T \propto U^{\frac{1}{2}}$ model is better physically motivated. This change would also deemphasize difference from $\nu_{\text{zero}}$ as a source of error, since $\nu_{\text{zero}}$ should be different for clocks with atoms at different temperatures. Instead, the analysis would make use of a more sophisticated calculation of model error for a fit only to equation 4.16.

| Referenced parameter | |
|---|---|
| $\beta^*$ | -6.149(123)$\times 10^{-22}$ |
| $\frac{\partial\beta^*}{\partial\nu_L}$ | -7.28(46)$\times 10^{-24}$ MHz$^{-1}E_r^{-1}$ |
| Measured parameter | |
| $\nu_{\text{zero}}$ | 394,798,264.86(46) MHz |
| $\frac{\partial a^*}{\partial\nu_L}$ | 3.90(6)$\times 10^{-20}$ MHz$^{-1}E_r^{-1}$ |
| $\nu_{\text{operational magic}}$ | 394,798,267.10(124) MHz |
| Shift at $\nu_{\text{operational magic}}$ | -3.0(34)$\times 10^{-18}$ |

Table 4.2: Parameters used in the model for determining the portable magic wavelength. Note that $\nu_{\text{zero}}$ includes only model error from the portable fit, whereas $\nu_{\text{operationally magic}}$ also includes errors propagated from discrepancy with the lab clock measured value of the magic wavelength.

We do not operate the clock at $\nu_{\text{zero}}$ or the magic frequency. We operate at the operational magic frequency, a condition that makes the lattice light shift insensitive to intensity noise. This frequency is found by setting the derivative of the right-hand side of equation 4.17 with respect to trap depth, $U$, to zero and solving for the lattice frequency. At 70 $E_r$ for the parameters in our light shift model, the operational magic wavelength is

Figure 4.3: We fit the measured light shifts to the model in [110] using the high order parameters measured in [126] and leaving the magic wavelength frequency, $\nu_L$, and $\partial a^*/\partial \nu_L$ as free parameters in the fit. Individual points represent 14 to 62 hours of averaging and there errorbars come from the white-FM fits to the Allan deviation at $\tau/2$. Cold collision and vector Stark effects have been subtracted from the data.

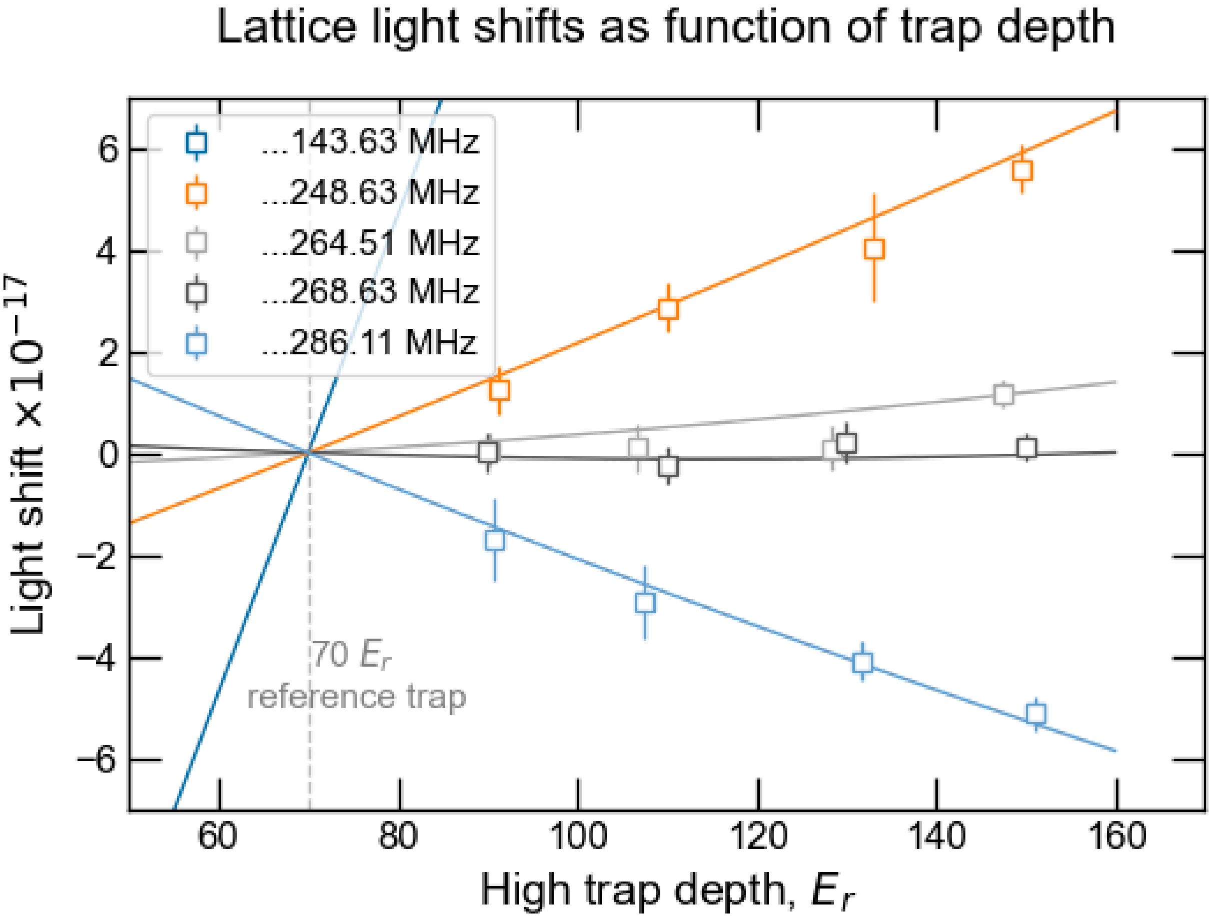

2.2 MHz blue-detuned form the magic wavelength. We note that at the test frequency blue-detuned by 1.4 MHz from the operationally magic wavelength, comparisons between 70 $E_r$ and all other test trap depths were consistent with a zero shift between the samples at the statistical error level (2-3 $\times 10^{-18}$). At an operational trap depth of 70 $E_r$, the light shift is assessed to be -3.0(34) $\times 10^{-18}$. The uncertainties that combine to give this value are shown in Table 4.3.

| **Uncertainty source** | **Uncertainty in $\nu_{\mathbf{zero}}$** | **Shift Unc.** $(\times 10^{-18}\nu_0)$ |
|---|---|---|
| Prior determination of $\nu_{\text{zero}}$ | 0.49 MHz | 1.3 |
| This determination of $\nu_{\text{zero}}$ | 0.46 MHz | 1.3 |
| Differences between $\nu_{\text{zero}}$ | 1.04 MHz | 2.8 |
| This $\frac{\partial a^*}{\partial \nu_L}$ | | 0.09 |
| Model error | | 0.3 |
| Total lattice Stark uncertainty | | 3.4 |

Table 4.3: Lattice light shift uncertainty table for transportable Yb clock. Shift uncertainties are given in fractional frequency units for the clock transition.

### 4.2.4 Lattice Travelling Wave

Due to non-unity transmissions of both the chamber windows and non-unity reflection of the lattice retro-reflection mirror, the lattice has some degree of intensity imbalance. This imbalance adds an additional shift from the forwards-propagating beam that is not treated in the standing-wave model of the lattice. We measured the lattice intensity transmission coefficient for the round trip from atoms to atoms with a germanium photodiode optical power meter (S132C, Thorlabs). The lattice optical power was reduced with the tapered amplifier current and servoed at a lower value for a stable reference during the measurement. Multiple experimenters measured the power to compute the mean and standard deviation of the powers at each point to account for spatial and angular variation of the power meter.

We directly measured the losses between optics compromising the retroreflection path to compute the relevant transmission coefficients as shown in Table 4.4. We measured the transmission coefficient $T$, for the round trip back to the atoms at 90% ± 2%. Since we align the retroreflector to maximize the lattice depth as discussed in section 2.2.3, we do not consider further effects to effective transmission from mismatched focusing. We follow the treatment in [126], where the transmission coefficient permits calculating the electric field mismatch parameter, $\xi = \sqrt{2-T} - 1 = 0.05(1)$, which is the fraction greater than unity of the forward propagating beam compared to the backward propagating beam. The small light shift on the atoms from this mismatched intensity at the operational magic wavelength is then given by

$$\frac{\Delta\nu_{\text{trav}}}{\nu_0} = -\xi^2 U(5.5\times10^{-19}) - \xi^2 U^2(2\times10^{-21}) - \xi^4 U^2(1\times10^{-21}), \tag{4.18}$$

where $U$ is the lattice depth in recoil units. The coefficients are upper bounds on the computed ratios of the differential multipolar polarizabilities and the magic wavelength polarizability [126, 110]. We assess a shift uncertainty at $1\times10^{-19}$ for our operational trap depth, where we consider the entire travelling wave shift to be an uncertainty.

### 4.2.5 Spectral purity of the lattice

Previous discussion of the lattice assumed that the frequency distribution of the lattice is a delta function at $\nu_L$. This assumption is not true for real lasers. Fortunately, the differential polarizability has a low enough frequency dependence that a laser detuned < 350 kHz from the magic wavelength will have less than a $1\times10^{-18}$ shift. This frequency

| Location | Measured optical power (mW) | Transmission coefficient |
|---|---|---|
| Before chamber power | 41.9(4) | - |
| After chamber power | 40.9(8) | - |
| Before retroreflector power | 39.3(1) | - |
| Retroreflector reflection (spec) | - | 0.998(2) |
| Single window transmission | - | 0.99(1) |
| Chamber to retro transmission | - | 0.96(2) |
| Atom to atom transmission | - | 0.90(2) |

Table 4.4: Measurement of transmission coefficients between optical surfaces.

dependence imposes only a weak linewidth constraint on the lattice laser. Since our lattice laser has a $< 10$ Hz in-loop beat note when locked to the frequency comb, this is a non-issue in our system.

However, early work on the portable project focused heavily on the ensuring adequate spectral purity of the lattice laser for magic wavelength trapping. For size reasons, we built the portable system with a diode-seeded tapered amplifier laser in contrast to the lab clocks which typically use a large Ti:Sapphire laser for the lattice. Continuous wave Ti:Sapphire lasers have high spectral purity, but tapered amplifiers are known to generate a large amplified spontaneous emission (ASE) background. This ASE background could be several THz away from the magic wavelength and create a large shift on the atoms even with trace spectral power density. To suppress this potential shift, we use a volume Bragg grating (VBG) with a 10 GHz passband to reject the vast majority of the ASE background. As described in detail elsewhere [93, 3], we measured the spectrum of our VBG filtered laser over 8 decades of frequency space from the magic wavelength to demonstrate suppression of the ASE. From this measurement, we estimated an uncertainty from residual ASE at $5 \times 10^{-20}$. Additionally, we interleaved between trapping with the filtered tapered amplifier laser and the Ti:Sapphire laser in one of the laboratory clocks and measured a shift consistent with zero at the $1 \times 10^{-18}$ level.

### 4.2.6 Blackbody Radiation

The frequency shift from the long wavelength electric field of the vacuum chamber BBR environment is the largest uncancelled systematic frequency correction and one of the largest sources of systematic uncertainty in both laboratory and transportable OLCs [34, 33, 12, 13, 32]. Our table detailing all of the considerations in our BBR uncertainty calculation is presented in Table 4.5. This section is organized in subsections following the table. This organization is roughly chronological in that environmental control motivated early chamber design before we could measure realized temperatures on the chamber and then consider minor environmental effects or values of atomic parameters measured elsewhere. An additional clarification is that although the thermal model for the spectroscopy chamber is developed in the first subsection, the thermistor-measured thermal gradient is treated in the second subsection.

#### 4.2.6.1 Temperature inhomogeneity

To limit uncertainty, we constrain BBR effects with a vacuum chamber that incorporates strategies from the in-vacuum BBR shield technique [75, 128], such as high-emissivity coatings, a mesh of temperature sensors, finite element thermal modeling, and chamber geometry with reduced sensitivity to thermal apertures. Inserting coefficients into equation 4.12, the BBR shift from a uniform thermal field at temperature, $T$, with $T_0 = 300$ K, is given by:

$$\Delta\nu_{\mathrm{BBR}} = \nu_4 \left(\frac{T}{T_0}\right)^4 + \nu_6 \left(\frac{T}{T_0}\right)^6 + \nu_8 \left(\frac{T}{T_0}\right)^8 + \mathcal{O}\left(\frac{T}{T_0}\right)^{10}. \tag{4.19}$$

$\nu_4 = -1.254871(24)$ Hz is the product of the differential static polarizability between the clock states and the mean-squared electric field of thermal radiation, and $\nu_6 = -21.98(48)$ mHz and $\nu_8 = -744(20)$ $\mu$Hz are the dynamic corrections for the frequency dependence of polarizability [75]. At 300 K, $\partial\Delta\nu_{\mathrm{BBR}}/\partial T = -171.1894(4)$ mHz/K, therefore a $1 \times 10^{-18}$ uncertainty requires knowledge of the thermal environment at the 30 mK level.

As in [75, 34, 128, 129], we characterized the BBR environment of our chamber with thermal modeling and thermometry. Assisted by finite element analysis (FEA) [96, 130], we determined the effective solid angles, $\Omega_i^{\mathrm{eff}}$, of each surface element, $i$, in the chamber [75]. Knowledge of each element's effective solid angle and its respective temperature, $T_i$, can be used to calculate the the effective BBR temperature

$$T_{\mathrm{eff}}^4 = \sum_i \frac{\Omega_i^{\mathrm{eff}}}{4\pi} T_i^4 \tag{4.20}$$

where $T_{\mathrm{eff}}$ is the effective BBR temperature sampled by the atoms [75]. In a spherical chamber, the effective solid angle of the surface would be reduced to the product of the

Table 4.5: BBR shift uncertainty table for transportable Yb clock at normal operating temperatures (T = 26.8 C = 299.9 K). Shift uncertainties are given in fractional frequencies units of ($\times 10^{-19}\nu_0$).

| **Section** | **Temperature Unc.** | **Shift Unc.** |
|---|---|---|
| I. Temperature Inhomogeneity | | |
| Spectroscopy Chamber | 35 mK | 12 |
| N-BK7 Windows | 100 mK | 4.5 |
| Entry Aperture / Oven Shutter | 10 K | 5.0 |
| Exit Aperture | 5 K | 2.3 |
| II. Thermistor Accuracy | | |
| Calibration | 6.0 mK | 2.0 |
| Post Calibration Fidelity | 0.5 mK | 0.2 |
| Digital Multimeter (2 wire) | 1.0 mK | 0.3 |
| Self-Heating | 0.6 mK | 0.2 |
| Parasitic Conduction | 0.0 mK | 0.0 |
| III. Minor Environmental Effects | | |
| Application of $T_{\text{eff}}$ in Dynamic Correction | | 0.01 |
| Residual Transmission via Windows | | 0.05 |
| Atomic Position / Dimensional Tolerance | | 0.7 |
| BBR Anisotropy (Non-scalar Stark) | | 0.01 |
| IV. Atomic Response to BBR | | |
| Differential Static Polarizability | | 0.46 |
| Dynamic Correction with $T^6$ | | 9.2 |
| Dynamic Correction with $T^8$ | | 0.38 |
| BBR Zeeman (M1) Factor | | 0.1 |
| Total BBR Environment | | 14.1 |
| Total Atomic Response | | 9.2 |
| Total | | 16.8 |

solid angle of the element to the atoms and the emissivity of the element normalized by the condition $\sum_i \Omega_i^{\text{eff}} = 4\pi$.

By design, the total geometric solid angle of the entry and exit apertures for the atomic beam was constrained below 2%, since the surfaces beyond these apertures have relatively uncontrolled and uncharacterized temperatures. Likewise, these apertures had no lines-of-sight to any potentially reflective window surfaces. FEA found that if the chamber walls had an emissivity $\geq 0.8$, then the effective solid angle of the apertures was maintained below 2% with vanishing sensitivity to the emissivity of the chamber windows. As shown in Table 4.6, this meant that we did not need to carefully measure the emissivities of the windows to constrain the effective solid angle of the apertures.

| Element | Temperature (K) | Geometric solid angle, $\Omega^{\text{geom}}/4\pi$ | Effective solid angle, $\Omega^{\text{eff}}/4\pi$ | Environmental uncertainty ($\times 10^{-19}$) |
|---|---|---|---|---|
| Entry aperture | 303(10) | 0.0017 | 0.00150(3) | 5.0 |
| Exit aperture | 293(5) | 0.015 | 0.0145(15) | 2.3 |
| Windows | 293.0(1) | 0.19 | 0.15(10) | 4.5 |

Table 4.6: Environmental uncertainty budget for blackbody radiation shifts is calculated using Monte Carlo analysis. The effective solid angle ranges are derived from sampling the emissivities over a uniform distribution by assuming that the chamber has an emissivity greater than 0.8 and the window has an emissivity greater than 0.2. The effective solid angle of the chamber is adjusted accordingly to meet the normalization constraint. Table reproduced from [3].

We used a Monte Carlo method to estimate the effect of emissivity and temperature variations on the uncertainty of the BBR shift. The model drew temperatures from a normal distribution, where the entry aperture, exit aperture, and windows had 10 K, 5 K, and 100 mK ranges respectively, which we considered to be worse than our expected ability to control temperatures on these surfaces. The model also drew emissivities from a box distribution where we conservatively assumed the chamber emissivity was $> 0.8$ and the N-BK7 window emissivity was merely $> 0.2$. This computation found a $7.2 \times 10^{-19}$ environmental uncertainty floor from the uncertainty of temperature and effective solid angles of the apertures and windows [3]. The environmental uncertainty contribution from individual components is shown in Table 4.6. In operation, however, the environmental uncertainty is limited by the ability to control gradients on the high emissivity chamber which dominates the effective solid angle.

We characterized possible thermal gradients in the windows with infrared imaging thermometry to ensure uncertainties consistent with the Monte Carlo model. We imaged accessible chamber windows with a thermal camera during an operational sequence with five times the normal coil duty cycle (40%) to amplify possible air-cooling gradients in the windows. We averaged 75 images to generate a composite image, an example averaged thermal image is shown in Figure 4.4(a). We then fit a quadratic polynomial to the horizontal and vertical cross sections of the windows, as shown in Figure 4.4(b). We observed an edges-to-center parabolic gradient of 22(5) mK. Even under the enhanced condition, this gradient is less than the window temperature uncertainty used in our Monte Carlo model.

#### 4.2.6.2 Thermistor accuracy

We measure the chamber temperature during the clock sequence with nine thermistors (30 kΩ at 25 C) distributed evenly around the chamber including on the edges of the windows thermistor placement is shown in Figure 4.5(a). The thermistors were secured with a hardening boron nitride thermal paste overlaid with kapton tape. The boron nitride paste is not recommended in the future; although it hardens and bonds to the chamber, the dry paste is friable and could degrade during transportation.

For the sake of rapidly building our chamber, we calibrated the thermistors in two stages. In the first, we immersed twelve thermistors in an isothermal bath, a hole in an aluminum block filled with mineral oil and wrapped with insulation and aluminum foil. Then we slowly varied the room temperature to calibrate the thermistors against each other. We reserved three 'reference' thermistors from this ensemble and attached the other thermistors to the chamber. Several months later, we rebuilt the isothermal bath, using instead a tem-

Figure 4.4: Characterization of the BBR uncertainty from the windows in a temperature enhanced condition. (a) Shows the composite image of one of the vertical viewports averaged from 75 images of the viewport. The brazing rings and titanium surfaces at the edge of the window can be seen due to their different surface emissivities. Likewise, shadowing and reflection effects can be seen on the window since it has less than unit emissivity (optical glasses like N-BK7 typically have emissivities between 0.6 and 0.8 in the mid-infrared) [131]. Data for this particular measurement was collected on the line between the two yellow points where we were careful to avoid reflection effects. (b) The data from that image, after subtracting the mean value, is displayed as orange points and the quadratic fit is displayed as a blue line. Even after averaging, the dispersion of the data points is large relative to the signal. However we were still able to extract a meaningful quadratic coefficient from the data indicating the presence of a center-cooling effect due to the windows' access to air currents. The linear coefficient was disregarded since this measurement was taken before we installed the counter heater to suppress the gradient on the oven-slowing axis.

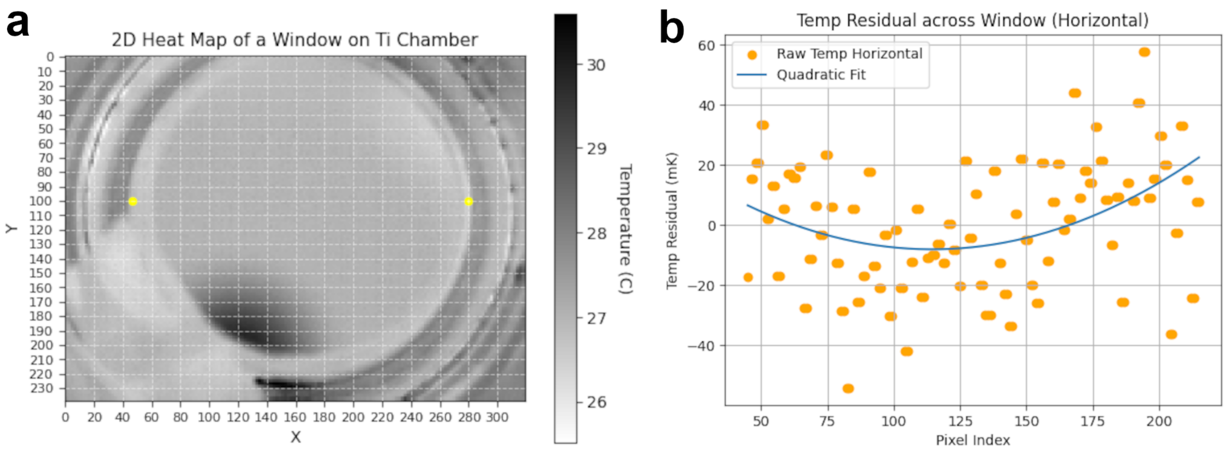

Figure 4.5: (a) shows the locations of the thermistors on the chamber, some are placed in pre-machined holes intended for temperature sensing and others are placed inside the window braze rings. (b) shows the the residuals of the thermistors during a 14 hour clock measurement while we setup the oven counter-heater. At about 1300 hours, we adjusted the servo setpoint which decreased the dispersion between slowing side thermistors (2, 3, and 9) and the oven side thermistors (6, 10, 11, 12). Thermistor 13 on the top viewport is suspected of having relatively worse thermal contact with the chamber since it sees more severe air current noise. (c) shows the mean (left) and the scale parameter (right) of the chamber temperature distribution. Prior to the servo adjustment the mean temperature was range-bound within 30 mK, indicating a stability of the uncorrected BBR shift at the $1 \times 10^{-18}$ level.

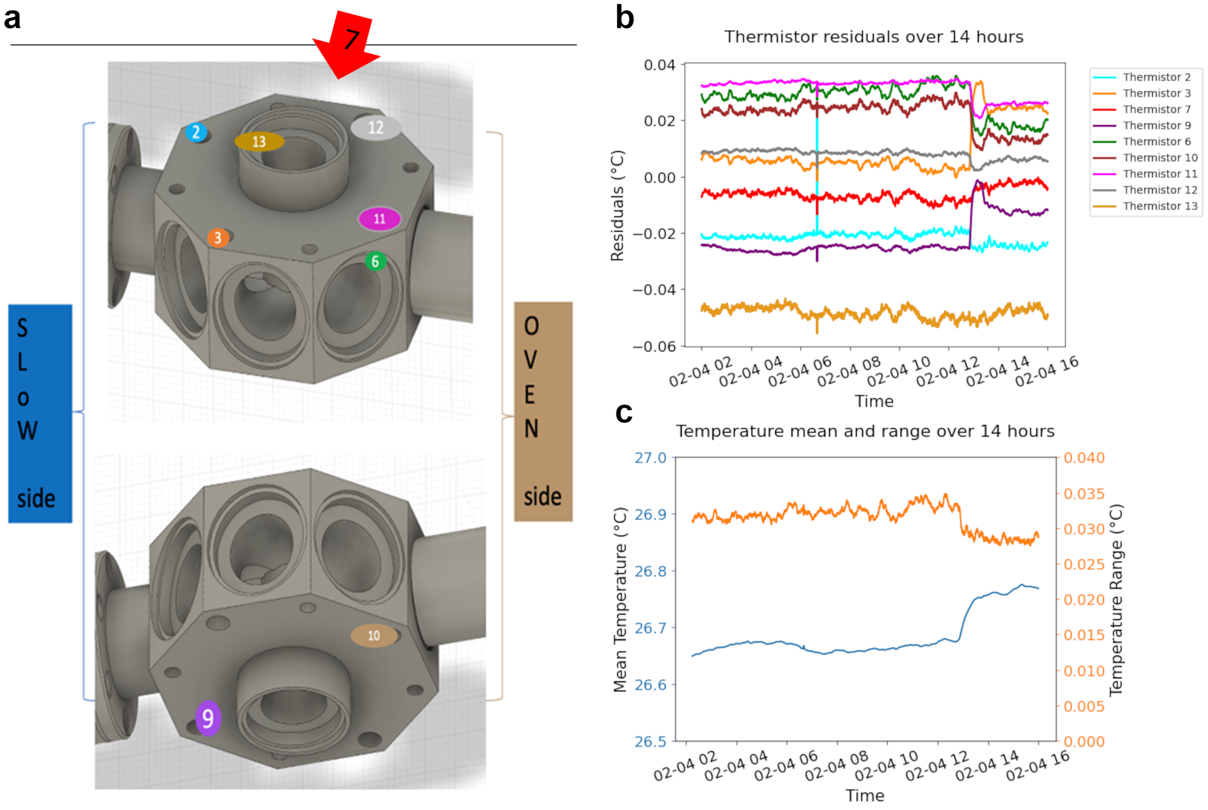

perature servoed heating and cooling plate, and calibrated the three reference thermistors with a set of three Pt100 resistance thermal detectors. The Pt100 manufacturer quoted a 4 mK accuracy for these devices. We then were capable of measuring exact Steinhart-Hart coefficients for the reference thermistors using the Pt100 temperature data. This calibration is shown in Figure 4.6(a) for an example reference thermistor. Over the fitting model range of interest for our chamber's expected temperature, the error is $< 200$ $\mu$K. Additionally, the residuals of the Pt100s against their mean was $< 300$ $\mu$K near the chamber's operating temperature. Using the reference thermistors as a source of temperature truth in the older data, we were able to also update the Steinhart-Hart coefficients of the installed thermistors [132]. Fits for three example thermistors are shown in Figure 4.6(b). Unfortunately, for that earlier data we had not realized that the chamber would reach nearly 27 C in operation and the calibration only covers 19-24 C. The model error is therefore larger in this measurement at 1.5 mK, since it involves extrapolation. Nevertheless, even taking the simple sum of these two model errors with Pt100 manufacturing tolerance and residuals, the thermistor accuracy contributes only a 6 mK error to the BBR environment.

We also considered other effects that may degrade the accuracy of our thermistors. The Pt100 measurements used a 4 wire configuration and the thermistor measurements generally used a two wire configuration, benefiting from their much greater resistance. We assessed the error from using two wire measurements on the chamber with one reference thermistor by interleaving between a four wire measurement and two wire measurement. We measured a temperature difference consistent with zero with 1 mK error. We additionally assessed a self-heating error at $0.65 \text{ mK} = (10\ \mu\text{A})^2 \times 26,000\Omega \times 1/4\text{K/mW}$ where the the electronic terms come from our sense current and thermistor resistance at the operational temperature and the dissipation is a reasonable estimate for a thermistor thermally bonded to a metal structure [133]. We performed an additional test several months later when calibrating new thermistors for an upgraded chamber. We included the same three reserved thermistors using their measured coefficients and compared against the Pt100s finding a maximum

Figure 4.6: (a) shows the fitting of one of the reference thermistors to the mean temperature of the PT100s. The temperature of the Pt100s is shown in blue on the left axis and model error of the fit is shown in orange on the right axis. The error bars of the data are much smaller than the points with standard deviation of the thermistor resistance below 25 Ω and the Pt100 temperature below 100 $\mu$K over the 30+ minutes each point was collected. (b) shows the fitting of three chamber thermistors to the reference thermistors. Because this data (overlapping blue squares) was taken prior to full construction of the chamber, it did not include the final operating temperature of the chamber. The fits (thin blue lines), therefore have a larger model uncertainty (orange lines) at the operating temperature of the chamber.

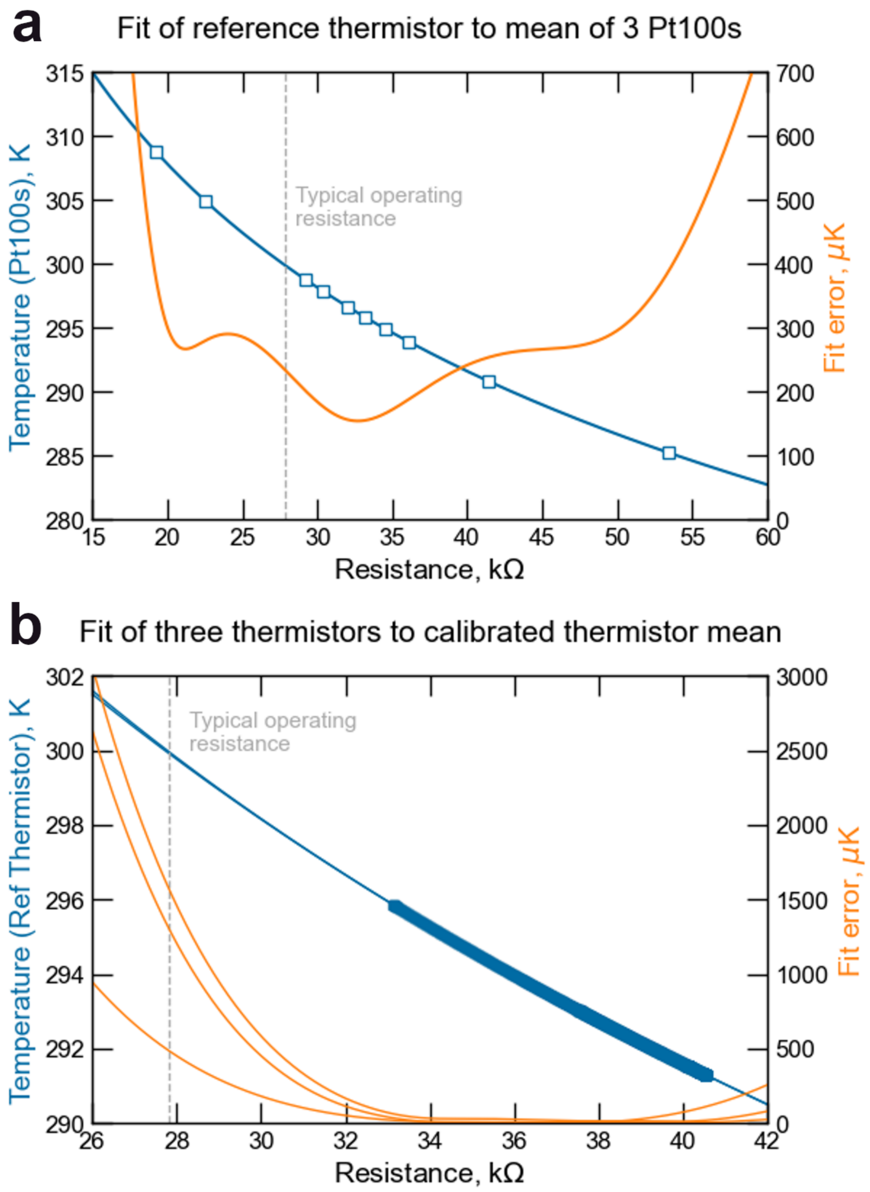

discrepancy of 0.5 mK in the expected operating temperature range, which we assessed as post-calibration fidelity error. In-vacuum temperature shields consider the parasitic conductance of the thermistor leads to the vacuum electrical feed through. Even in these systems, the conductance is considered a sub-100 $\mu$K effect [75]. Given that the thermistor leads are taped to the chamber and out of vacuum, we consider this negligible for our thermistor accuracy.

On the chamber, the thermistors sense thermal gradients that arise from heat propagation from the atomic oven and from the MOT quadrupole coils. The gradient originating from coil heat dissipation was mitigated by coil design and 399 nm MOT loading sufficiently efficient to permit a low duty cycle. Additionally, the atomic oven conducts a temperature gradient down the chamber; this effect can be seen in Figure 4.5(b). We counterbalance the temperature gradient using a temperature-servoed heater on the side of the chamber opposite the oven and suppress it below the level of other residual gradients. The remaining gradient appears to be cylindrically symmetric radially outwards from the atomic beam axis, likely as a result of the oven and counterbalance heat sources being effectively on the axis. Future efforts to mitigate this effect will include water cooling the oven and coils so that the chamber is at room temperature and building a box around the physics package to servo the air temperature.

We use Student's $t$-distribution [134] to analyze the uncertainty of the thermal ensemble with the degrees of freedom parameter set at $N-1$, where $N$ is the number of temperature sensors. Some other statistical analyses that experimenters have used in their analysis of an ensemble of temperature sensors have included: simply divide the full range by two, the box distribution (divide the range by $\sqrt{12}$), and the normal distribution. The $t$-distribution leads to a more conservative estimate than the box and normal distribution since it makes a less strong claim about the underlying potential temperature distribution that the atoms might experience as a result of the finite number of temperature probes. It also has the intuitively desirable property that increasing the number of probes decreases the uncertainty of the temperature which is not true of the other distributions. That said, the difference between the temperature uncertainties from the different distributions when applied to our thermistor collection is only about 10 mK.

Over several hours of experimental data, the $t$-distribution of the thermistor ensemble varies from 28-35 mK, as shown in Figure 4.5(c). This temperature uncertainty is consistent with a $0.9-1.2\times10^{-18}$ BBR uncertainty from the environmental contribution of the high emissivity chamber. Furthermore, the mean of the ensemble varies at a 25 mK level indicating a stability of the uncorrected BBR shift just below the $1\times10^{-18}$ level.

#### 4.2.6.3 Minor environmental effects

We additionally considered several minor effects on the calculation of the BBR shift. First, we consider the effects of the difference between the experimentally realizable measurement of the mean temperature which we consider to be the effective temperature and the exact temperature given from integrating all of the solid angle elements and their respective temperatures by their area. The effective temperature is applied to equation 4.19 under a nearly isothermal assumption. However, we may consider a calculation of the shift as [135]

$$\Delta\nu_{\text{BBR}} = \nu_4\langle T^4\rangle + \nu_6\langle T^6\rangle + \nu_8\langle T^8\rangle + \mathcal{O}\ \langle T^10\rangle, \tag{4.21}$$

where $\langle T^n\rangle$ is the $n$-th power of the surface temperature of the spectroscopy chamber averaged over the effective solid angles of the thermal surface

$$\langle T^n\rangle = \frac{1}{4\pi}\int T^n\left(\frac{d\Omega_{\text{eff}}}{dA}\right)dA. \tag{4.22}$$

The assumption of our thermal model [130] is that these values have an identity relationship where $\langle T^4\rangle = T_{\text{eff}}^4$, but that assumption does not generally hold for higher powers, $n$.

The unpublished reference [135] makes the argument that the individual contribution terms of 4.21 may be written as

$$\nu_n(1+\xi_n)T_{\text{eff}}^n \tag{4.23}$$

where the parameters $\xi_n$ are given by

$$\xi_n = \frac{\langle T^4 \rangle}{T_{\mathrm{eff}}^4} - 1 \leq \frac{n(n-2)}{2} \times \left( \frac{T_{\max} - T_{\min}}{T_{\max} + T_{\min}} \right)^2 . \tag{4.24}$$

We use twice the values of the residuals from the measurements from the maximum and minimum values of our thermistors in Figure 4.5 in case we are undersampling a peak gradient. We find the high order temperature corrections $\xi_6 = 8.5 \times 10^{-7}$ and $\xi_8 = 1.7 \times 10^{-6}$. These values are several orders of magnitude less than the fractional uncertainties of $\nu_6$ and $\nu_8$, and we assess a $< 1 \times 10^{-21}$ contribution to the BBR uncertainty from the effective temperature assessment.

Next, we consider residual BBR transmission through the vacuum chamber viewports. N-BK7 glass has strong optical-phonon interaction beginning at colors infrared of a 2.5 $\mu$m wavelength that shields the atoms from most BBR external to the chamber. However, there is still some residual transmission at higher frequencies which might interact with the atoms in the spectral vicinity of the $^3\mathrm{P}_0 \rightarrow {}^3\mathrm{D}_1$ transition as previously seen in Figure 4.1. The transmitting BBR is at a different characteristic temperature from the chamber BBR since the coil and oven-warmed chamber is at $\approx$ 27 C and the environment when the chamber is “boxed” up is at $\approx$ 20 C. Our group has previously been interested in this calculation since it may be a more significant effect in the BBR shift for clocks that have cryogenic vacuum envelopes with windows to room-temperature surfaces [136, 137, 138]. As shown in Figure 4.7, we compute the the effective spectral difference from the model by calculating the difference BBR spectrum between the two temperatures, applying a measured filter function for N-BK7 glass, and multiply by the geometric sold angle of the viewports. The integral of the product of this spectrum and the differential polarizability of the atoms then is a shift correction. The correction is computed to be $5 \times 10^{-21}$ which we take to be additional uncertainty on the BBR shift.

Additionally, we consider the effect of the lattice position on the effective temperatures witnessed by the atoms. Our thermal model assumed that the lattice standing wave is in

Figure 4.7: (a) shows in blue on the left axis the wavelength dependent transmission of N-BK7 as compiled from the maximum values of [139, 140, 141]. The major transmissive feature of N-BK7 is the vanishing transmission above 2.5 $\mu$m which is somewhat obscured by measurement technique changes in the combined transmission data. The right axis shows in orange the fractional change in total BBR spectrum after accounting for the temperature difference between the viewports and chamber exterior, the viewport transmission, and the geometric solid angle of the viewports. (b) shows the computed fractional frequency shift per Hz of BBR spectrum after multiplying the spectral difference by the differential polarizabilities of the clock states. The integrated value is $5 \times 10^{-21}$.

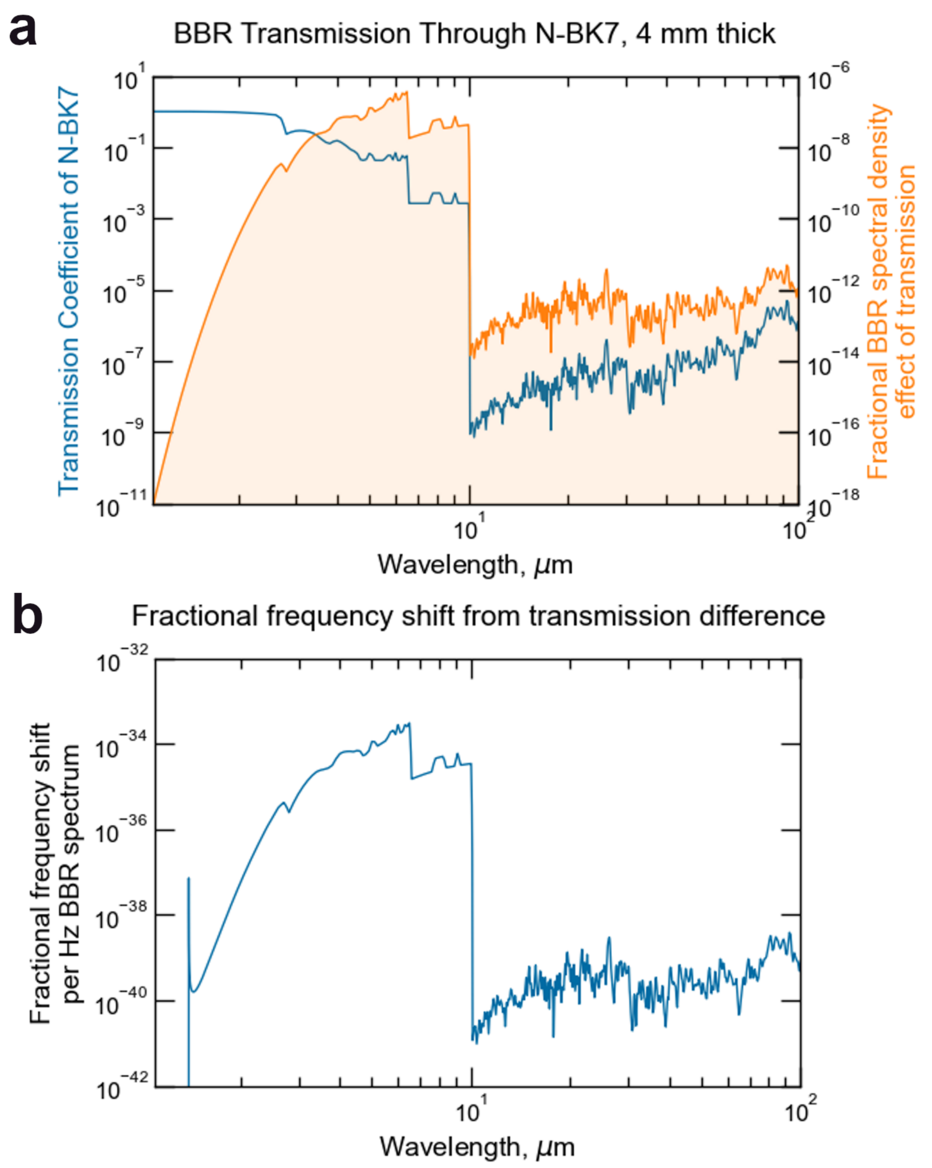

the geometric center of the chamber, but in practice, the lattice is aligned to the final stage of the 556 nm MOT whose location of formation is dictated by local magnetic fields. In several deployment locations, the MOT has always formed within 0.5 mm of the center along the atom beam axis, as assessed by diffuse reflection of the lattice beam off the top and bottom viewport after alignment. (There is a tiny scratch on the upper viewport which, for better or worse, is a useful alignment reference since the lattice always aligns closely to it.) The location along the atom beam axis dominates the uncertainty from this term since that determines changes to how the atoms sample temperature from the entry and exit apertures which have relatively uncontrolled temperatures. For the entry (exit) aperture, 0.5 mm greater proximity increases the geometric solid angle to $0.00177/4\pi$ $(0.0155/4\pi)$ and contributes a maximum 4% (30%) increase to the environmental uncertainty from this surface. The additional environmental uncertainty is then $7 \times 10^{-20}$.

Finally, we consider the effects of an anisotropic BBR environment which might interact with the atoms through non-scalar Stark terms. Since the clock states are both $J = 0$ any such effect would be highly suppressed since the electron cloud is nearly spherically symmetric up to the contribution of hyperfine mixing in the excited clock state of $^{171}$Yb. The most extreme possible anisotropy in our chamber is $(T^4_{\text{max}} - T^4_{\text{min}})/T^4_{\text{mean}} \leq .001$ where half of the chamber is at the max thermistor temperature and half is at the low temperature. The maximum sensitivity to anisotropy is given by previous analysis of the vector polarizability of $^{171}$Yb as $4 \times 10^{-4}$ the scalar polarizability [142, 143]. With a maximum correction at $4 \times 10^{-7}$ of the BBR shift, we assess the uncertainty from this source as $< 1 \times 10^{-21}$.

#### 4.2.6.4 Atomic response to BBR

The leading room-temperature laboratory optical lattice clocks [32, 33] are limited in their uncertainties by knowledge of the dynamic correction coefficients. Future progress in the lowest uncertainty clocks will involve spectroscopy chambers cooled to 200 K or below to suppress the wavelength dependent effects of BBR [138, 137, 13]. While the portable Yb clock does not yet perform at this level, it is not far from this target. This work made no effort to improve the measurements of the coefficients involved in these corrections and so will only report the uncertainty contributions from knowledge of the corrections. Operating at a slightly higher temperature than the lab clocks we report greater uncertainty for the atomic corrections. Following equation 4.19, the BBR correction from the differential static polarizability term associated with $\nu_4$, is $-2424.1(5) \times 10^{-18}$, the second order dynamic correction term associated with $\nu_6$, is $-42.3(9) \times 10^{-18}$, and the fourth order dynamic correction term associated with $\nu_8$, is $-1.4(4) \times 10^{-18}$. Additionally, as described in section 4.2.2, there is a correction for magnetic interaction with the BBR field assessed at $1(1) \times 10^{-20}$.

#### 4.2.6.5 BBR summary

The quadrature sum of all of the uncertainties discussed so far, results in a total error of $1.7 \times 10^{-18}$. Since the uncertainty is dominated by the measured temperature gradient on the spectroscopy chamber, this uncertainty is not static and will need to be tracked for the duration of each clock measurement.

If the portable clock were to operate with a less stable local oscillator in the future, these shifts are likely to scale unfavorably. One of the contributors to thermal gradients on the chamber is the the high power dissipated in the quadrupole MOT coils. If the spectroscopy time were decreased, but the rest of the clock cycle were unchanged, then the duty cycle of the MOT coils would necessarily increase. While no scaling law can be derived a priori, we have seen peak-to-peak thermistor values as high as 200 mK while setting up the system with spectroscopy times $< 100$ ms. If the gradient determined by the $t$-distribution is only 100 mK, the uncertainty from BBR could reach $4 \times 10^{-18}$.

### 4.2.7 DC Stark

Our atomic chamber is designed as a Faraday cage with a conductive ITO coating on the windows and a conductive high emissivity coating on metal surfaces [144, 145]. The surface closest to the atoms without a conductive connection to ground is the in-vacuum slowing mirror $> 20$ cm from the atoms. The mirror is a UV-enhanced aluminum type which has a thin dielectric layer over the aluminum reflector on a 5 mm glass substrate. The dielectric surface is electrically contacted to the mount with a screw holding the mirror in place. The mount is electrically isolated from the chamber with an electrical feed through and can be externally connected to an arbitrary potential up to 8 kV. However, we typically ground the mount to discharge any potential build up on it. The mirror surface is well shielded by the vacuum chamber and a finite element analysis shows that even a 1 MV potential applied would exert a $< 1 \times 10^{-18}$ shift on the atoms which makes it infeasible to probe the DC field from this surface. Moreover, with only the thin dielectric coating capable of accumulating charge, we expect that the breakdown voltage to the mount is $< 10$ kV. Even if the mirror were maximally charged, the shift from it would be below the $1 \times 10^{-21}$ level.

We considered the potential failure of the ITO coating, which is temperature sensitive, during the brazing process. Prior to brazing the viewports to the chamber, we used a padded resistance probe to verify electrical contact from the window surfaces to the brazing rings. If the ITO coating were damaged in a thin annulus adjacent to the brazing ring on one of the vertical windows, which are nearest to the atoms, the electric potential build-up on the annulus could create a shift on the atoms. We simulated this potential build up with finite element analysis [96] to calculate the shielding factor of the chamber to this annulus, as shown in Figure 4.8(b). We found that the shielding factor is large enough that a 100 V potential on the annulus would create a $1 \times 10^{-18}$ shift. External-to-the-chamber measurements of the uncoated sides of the viewports with a standoff voltmeter found an electric potential of $0 \pm 1$ V at a 2.4 cm distance. Replicating the model in Figure 4.8(b) but for an external field to the chamber found that a 30 V charge on the annulus would be required to generate a 1 V measurement by the standoff voltmeter.

We assessed the possibility that dust on the windows resulted in many small points

Figure 4.8: a. Shows a COMSOL model with the most conservative model of a charged window where the voltage source is uniformly distributed. In this model, a $1 \times 10^{-18}$ shift on the atoms requires an 11 V potential on the window which generates a 0.07 V potential at the atoms. We use this model in calculating the possible shift from dispersed dust masking the ITO coating. b. Shows a more probable mode of failure where the ITO coating near the edges of the windows fails in the brazing process and voltage is accumulated in a thin annulus. This annulus would need to be charged to 100 V potential to effect a $1 \times 10^{-18}$ shift on the atoms.

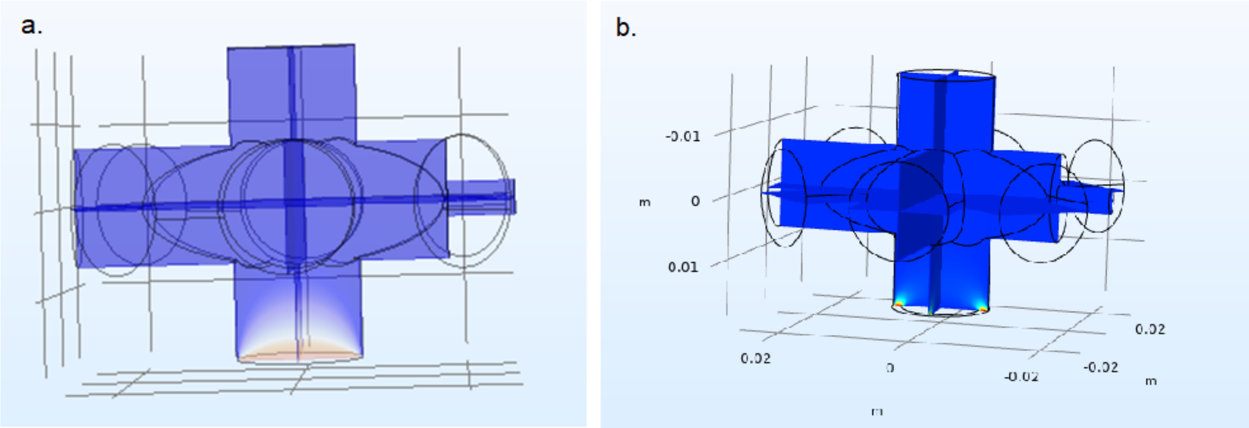

of ITO failure or that later additions of charged dust partially masked the ITO coating. This failure mode would result in a relatively uniform potential build up on the window as shown in 4.8(a). From reference [146], we use the value of $\sigma = 50\ e^{-}\ \mu\mathrm{m}^{-2}$ as a worst-case scenario for charge build-up on in-vacuum glass. Small patch charges on a grounded plane give dipole-like potentials, from which it is straightforward to compute the potential at the atoms as a function of compromised glass area,

$$V = \frac{1}{4\pi\varepsilon_0}\frac{\sigma A}{D^2} \tag{4.25}$$

where $D$ is the diameter of the dust-based patch charge, $A$ is the compromised area, and $\varepsilon_0$ is the permittivity of free space. Given the window diameter, 14 mm, and the shielding factor of the chamber, we calculated the percentage of area of the window that would need to be compromised to result in a $1 \times 10^{-18}$ DC Stark shift. Figure 4.9 shows the results of this calculation along with an empirically-derived curve for the aerosol density of different dust sizes in the western United States. Due to the strong shielding effect of the grounded plane, small aerosol dust contamination would have to be catastrophic ($> 10\%$) to create a DC Stark shift. However, macroscopic dusts at the near-millimeter scale with maximal charge could potentially pose a DC Stark problem. We observed the windows on the assembled chamber under illumination and did not observe any visible contamination of the surfaces, assuring that large dust contamination was not potentially compromising the electric field environment. We assess the DC Stark uncertainty at $< 1 \times 10^{-19}$.

### 4.2.8 Probe Stark

The clock laser itself causes a shift on the clock transition as a result of differential polarizability of the ground and excited states. In fermionic ytterbium, hyperfine mixing causes the ${}^1S_0 \rightarrow {}^3P_0$ transition to be less forbidden than in the bosonic nuclear spin zero case. Hence, the weakly allowed clock transition may be driven with sub-$\mu$W levels of optical power and the AC Stark shift from the clock light is much smaller than in bosonic

Figure 4.9: Computation of the fraction of the nearest window to the atoms that would need to be compromised with dust-masking that results in charged glass surfaces for a 1 × $10^{-18}$ shift. Above a few percent, the grounded plane assumption is certainly violated, but the plot is illustrative of the fact that small particle contamination is strongly shielded. The data for local dust aerosols came from [147].

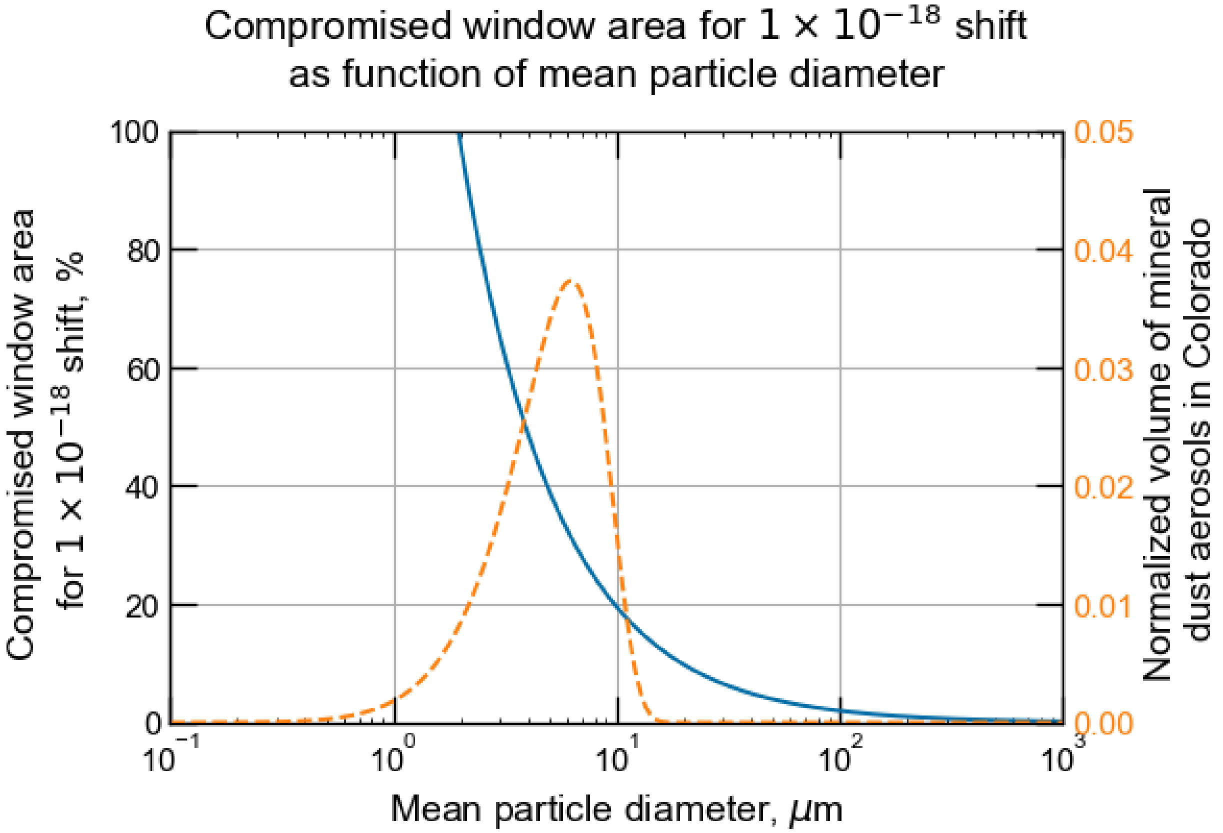

species [148]. Since for clock lasers of similar spectral purity and identical spectrosocpy times, the shift should not be experiment dependent, we use the shift and uncertainty values reported in [33]. Moreover, for the purposes of comparison with the lab clock, the shift will cancel in common mode since we are using the same laser.

In the future, as we develop an independent clock laser system, we will measure the probe Stark shift with that laser. We will use the technique in [149, 33] where the clock laser is detuned several MHz from resonance with the AOM and a low power tone at the detuning frequency is applied to an EOM to modulate the clock laser so that there are weak sidebands resonant with the atoms. The detuned carrier light will then cause a Stark shift on the atoms that can be measured by interleaving with normal operation. A linear fit to the intensity of the off resonant light can then be used to compute the shift from probe light at normal operational powers. Since the probe Stark shift scales with the intensity, $I$, of the clock laser while the $\pi$ pulse time scales with $1/\sqrt{I}$, this effect should only reach the $1 \times 10^{-18}$ level if the portable clock laser system is limited in stability to supporting $\leq 56$ ms interrogation times.

### 4.2.9 Second-order Zeeman

We set the bias field to 130 $\mu$T during spectroscopy to separate each of the two $\pi$ transitions by 260 Hz from center with the first-order Zeeman shift. We will call the separation from the center frequency the magnetic correction, $\delta_{\mathrm{mag}}$. As shown in Fig. 4.10, during a typical run $> 100,000$ s, the Allan deviation of the magnetic correction random walks to 20 mHz at 30,000 s, which we take as the statistical error of the magnetic correction, before beginning to average down as white-FM. Since this Allan deviation peak occurs at the same time interval as observed in Figure 4.21 which is expected to occur as result of room temperature fluctuation, a reasonable guess for the source of magnetic noise is temperature changes to the nearby ion pump magnets.

Residual polarization impurity in the lattice results in a vector Stark shift that varies

Figure 4.10: An overlapping Allan deviation from an individual cold collision shift comparison where the magnetic correction is plotted in Hz. The magnetic correction exhibits bounded random walk behavior where it wanders for 20,000 s before beginning to average down like white-FM noise. We do not currently use any passive or active techniques to stabilize the magnetic field. All long datasets where we plotted the Allan deviation of the magnetic correction showed a characteristic turn in the noise at 20,000 to 40,000 seconds indicating an approximately half day cycle in magnetic field. The last point is at $\tau$ and should be ignored.

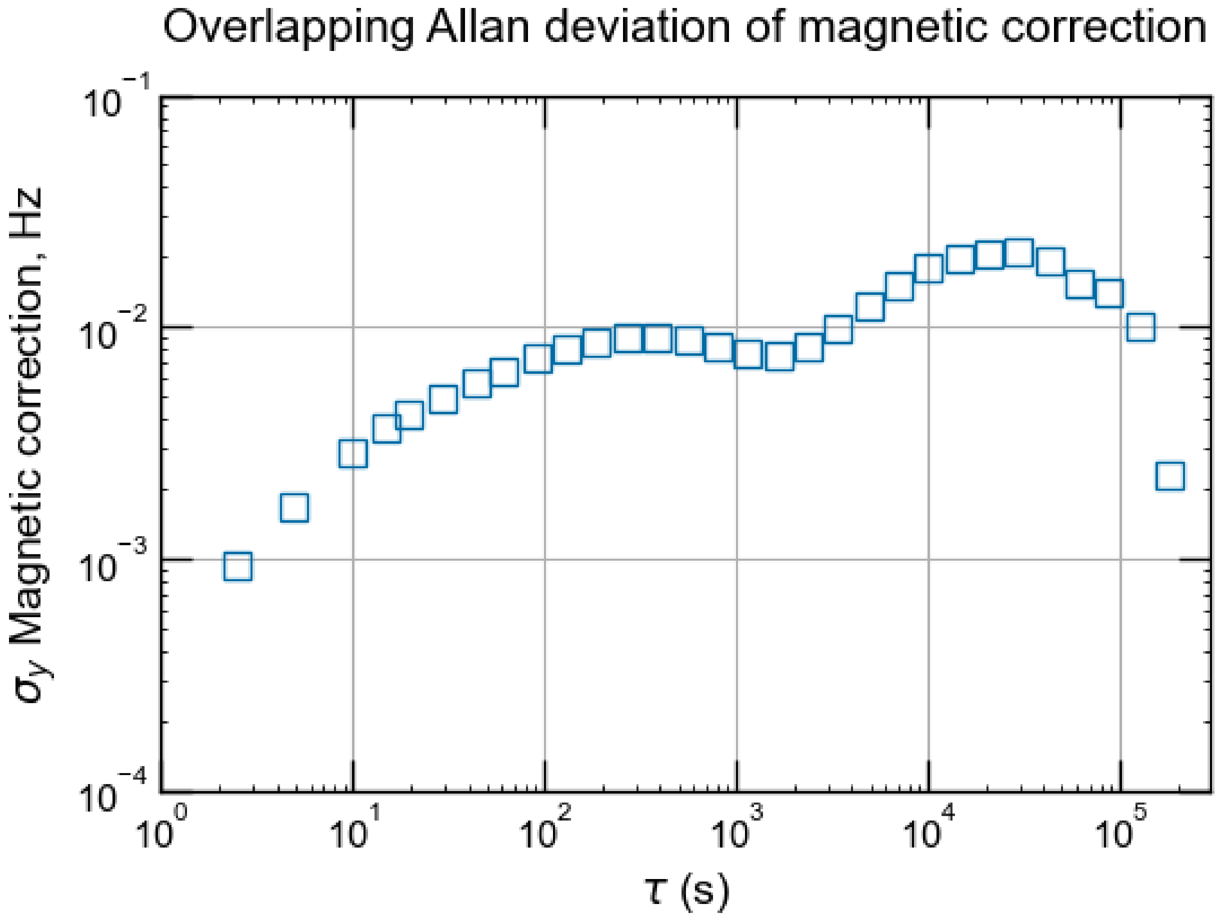

the magnetic correction linearly with trap depth. As shown in Figure 4.11, we measured the slope of the vector Stark magnetic correction as a function of trap depth to be $\Delta_{\text{VS}} = 5.1(4)$ mHz/$E_r$. Theoretically, the vector Stark shift is given by

$$\Delta\nu_{\text{VS}} = -\frac{m_F}{2hF} A\alpha_{\text{VS}} \left(\frac{1}{2}E_{\text{lattice}}\right)^2 \tag{4.26}$$

$$= -\frac{m_F}{2hF} A \frac{\alpha_{\text{VS}}}{\alpha_{\text{g,e}}(\omega_{\text{magic}})} V_0, \tag{4.27}$$

where $A$ is the circularity of the lattice polarization defined on an interval between -1 and +1, $\alpha_{\text{VS}}$ is the vector polarizability, $\alpha_{\text{g,e}}(\omega_{\text{magic}})$ is the scalar polarizability at the magic wavelength (by definition the same for the ground and excited states), $E_0$ is the lattice electric field, and $V_0$ is the lattice trap depth [87, 83]. Since the vector Stark shift depends on the magnetic quantum number, $m_F$, it can be thought of as a pseudomagnetic field in the direction of the lattice $k$-vector. For this reason, the vector Stark shift is cancelled by our alternating interrogation of transitions from $m_F \pm 1/2$ ground states. While the vector Stark shift is not a direct error on the transition frequency, it is an error on the magnetic correction that adds uncertainty to the computation of the second-order Zeeman shift. By design, we suppress the effect of the vector Stark shift on this uncertainty by setting the magnetic quantization axis in the same direction as the lattice polarization such that the effective fields add in quadrature while the real magnetic field is much larger. We can find the level of circular polarization of our lattice for $^{171}$Yb given the measurement of $\Delta_{\text{VS}}$. Two useful relations are the polarizability ratio $\alpha_{\text{VS}}/\alpha_{\text{g,e}}(\omega_{\text{magic}}) = 0.08\text{a.u.}/187\text{a.u.} = 1/2340$ [142, 143] and the conversion between magic wavelength trap depth in $^{171}$Yb and SI energy units is $1.34 \times 10^{-30}\text{J}/E_r$. Then, rearranging equation 4.27 and accounting for measurement of the magnetic correction as a splitting from center with a factor of two we find the level of circular polarization to be

$$A = 2310 E_r \text{ mHz}^{-1} \Delta_{\text{VS}} = 1.18\%. \tag{4.28}$$

The lattice light is presently polarized with a polarizing beam splitter cube that has a 1043:1 extinction ratio at 759 nm so it is likely that circular impurities are a result of birefringence in the vacuum viewports, focusing lenses, or a longpass dichroic mirror. It is possible that we could use a waveplate to cancel the vector Stark shift further by pre-correcting for birefringence, but there is not currently an available location to place this optic in the setup that does not affect other beams.

For calculating the Zeeman corrections, we used the first order Zeeman coefficient, $Z_1 = 199.516(2)$ Hz/G, and the second order Zeeman coefficient, $Z_2 = -0.06095(7)$ Hz/G$^2$ measured in [33]. Then the total correction from the zero-magnetic field state is given by,

$$\Delta\nu_{\text{Zeeman}} = \frac{Z_2}{(Z_1)^2}(\delta_{\text{mag}} - \Delta_{\text{VS}}U)^2 \tag{4.29}$$

where $U$ is the trap depth in recoil units. We calculate a second order Zeeman shift of $-1.9913(25) \times 10^{-16}$ from the zero magnetic field state, where we propagated the uncertainties from the second order Zeeman coefficient and from the statistical and vector Stark uncertainties of the magnetic correction.

A greater magnetic correction is needed to separate the two $\pi$ transitions if the linewidths are large due to short interrogation times, however a larger magnetic splitting will incur a greater uncertainty from applying the Zeeman coefficients. The magnetic correction we use was already chosen in anticipation of a potentially less stable local oscillator that only supports shorter $\pi$ pulse times. No adverse scaling of this uncertainty is expected outside the lab, however the stability of the local magnetic field may be worse. Most likely, all that would be required to counteract greater field instability is adjusting the gain of the Artiq software loop filter that tracks the magnetic correction.

## 4.3 Two Body Systematics

Interactions between atoms and other quantum particles causes shifts from the interactions of their potentials. These interactions can arise both from other cold atoms in the clock sample and background gas molecules in the vacuum chamber. This section details our calculations related to both types of collisional shifts, however this introduction primarily

Figure 4.11: The fit of the vector Stark correction to trap depth difference is shown as an orange line and the data is shown as blue squares with small error bars. We used the data from evaluating the lattice AC Stark shift to measure the relative effect of trap depth on the magnetic correction term. The error bars come from the Allan deviation of the two clock magnetic correction difference and were then scale up by a factor of five to reach a reduced chi squared value of one.

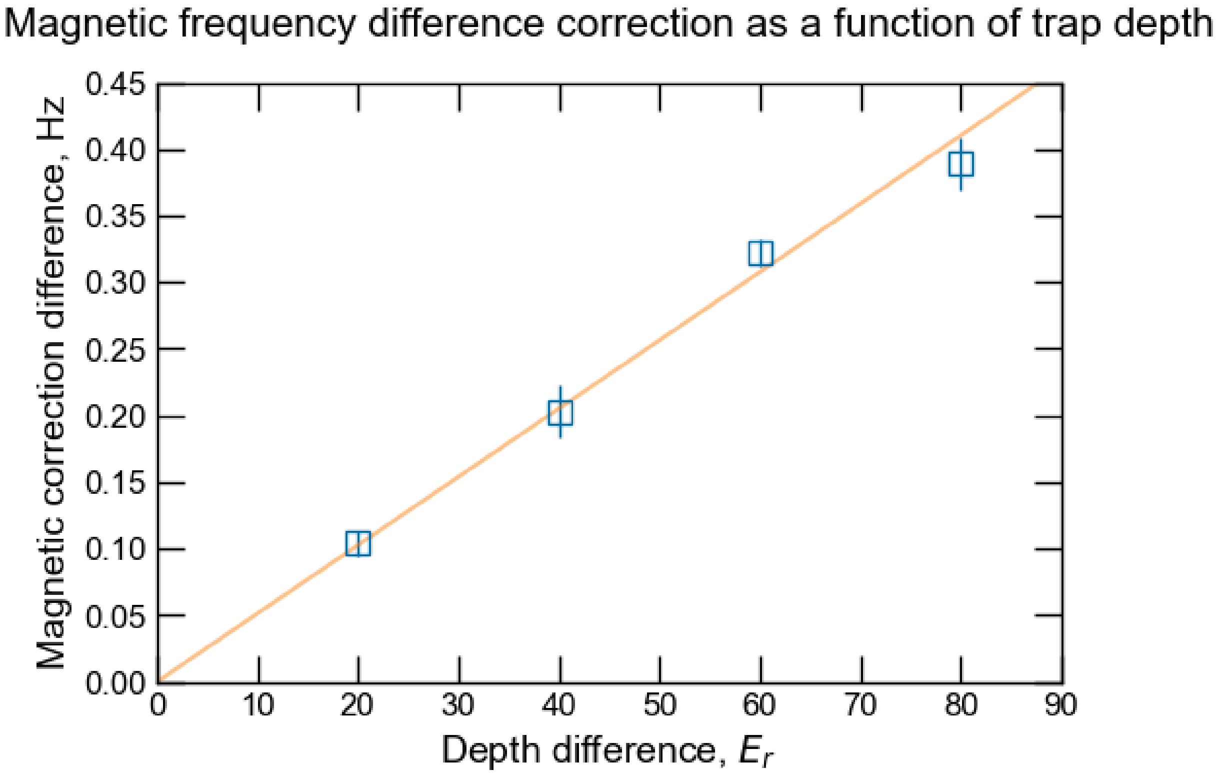

motivates the theory of cold-collisions between atoms in the spectroscopic sample.

A key advantage of optical lattice clocks is that their high atom number lets them operate with a greatly reduced quantum projection noise. Clocks with fewer quantum energy references recover less information about frequency per cycle and suffer an instability from this quantum projection noise $\sigma_{\mathrm{QPN}} \propto 1/\sqrt{N}$ [150]. A trade-off that optical lattice clocks make against optical ion clocks is that for greater experimental complexity in trapping a cold atom sample (more cooling lasers and more frequent loading), lattice clocks get a far higher atom number to suppress this noise source. However, they also pay a price in that the greater the number of atoms in the sample, the greater their interaction rate, and therefore their systematic shift from atom number will be increased. A simple strategy in handling this second trade-off is to operate with an atom number just high enough that Dick Effect-limited clock stability dominates the noise performance instead of quantum projection noise (QPN). This shift is not unique to lattice clocks, the most accurate cesium and rubidium fountain clocks also must carefully account for density effects [117, 151, 107].

Since $^{171}$Yb atoms have half-integer nuclear spin, they are fermions obeying Fermi-Dirac statistics. An atomic sample that is spin-polarized into a single $m_F = \pm 1/2$ state should then have no distinguishable particles and as a result, should have strongly suppressed interactions due to the Pauli exclusion principle. However, when targeting $10^{-18}$ levels of performance, even weak interactions can be troublesome. In general, elastic two-body collisions in a cold, dilute quantum gas can be described with a wave function in the center of mass frame

$$\psi(\mathbf{r}) \approx e^{i\mathbf{k}\cdot\mathbf{r}} + f(\mathbf{k},\theta)\frac{e^{ikr}}{r} \tag{4.30}$$

where the first term is an incident plane wave and the second term is the scattered spherical wave [152, 153]. The scattering amplitude, $f(\mathbf{k},\theta)$ depends on the particles and their states. The wave function and scattering amplitude can be expanded in spherical harmonic ‘partial waves’ in the standard way [154]. As a result, cold atom collisions can be classified by the angular momentum of the interaction channel with $s$-wave collisions ($l = 0$), $p$-wave collisions ($l = 1$), $d$-wave collisions ($l = 2$), etc. Higher angular momentum collisions ($l \geq 0$) are suppressed by centrifugal barriers between the atoms when sufficiently cold. In $^{171}$Yb this $p$-wave "freeze out" temperature was calculated to be 30 $\mu$K [155]. Thus in the early history of optical lattice clocks the most emphasis was made on measuring the contribution of $s$-wave collisions [156, 157, 158, 159, 160]. However, more recent measurements have shown that $s$-wave collisional shifts, while large if there are distinguishable particles in the spectroscopic sample, can be nearly eliminated with high purity of indistinguishable particles. In contrast, $p$-wave collisions can linger even for indistinguishable particles [161, 87, 162, 163].

We prepare our sample with $> 99.9\%$ spin-purity, where the measurement is detailed in 4.3.2. This technique lets us operate in a regime with negligible $s$-wave collisions from spin-impure atoms, since there is, on average, less than one spin-impure atom per sample of 300 atoms. We achieve this high purity with a long and low power spin-polarizing step as detailed in 2.2.3. While spin-impurity is the dominant source of distinguishable particles, there are several others. Atoms in the $^3P_2$ state, as could occur due to branching from $^3\mathrm{D}_1$ from repumping during the sideband cooling process could contaminate the sample. However, prior measurements show that due to negative polarizability at the magic wavelength, $^3P_2$ is anti-trapped by the lattice. Atoms in neighboring lattice sites are distinguishable by site during clock excitation due to differential sampling of the clock laser phase. If the tunnelling rate is high enough, these atoms could participate in off-site $s$-wave collisions. However, this effect is only a significant concern in very low-trap depth lattices [162]. Finally, due to excitation inhomogeneities of atoms at slightly different temperatures, they will evolve from ground to excited clock states at slightly different Rabi frequencies. In this way, atoms become distinguishable during the spectroscopy pulse.

Assuming a mean-field-like interaction of spin-identical particles at root-mean-square temperature $T_{\mathrm{RMS}}$ (to average over the three dimensions) and mass $m$, the collisional shifts for both $s$-wave and $p$-wave interactions may be written as

$$\Delta\nu_s = \frac{2\hbar}{m} G^{(2)} a_{eg}^3 (\rho_g - \rho_e) \tag{4.31}$$

$$\Delta\nu_p = \frac{2\pi k_B}{h} \langle n_D \rangle T_{\mathrm{RMS}} \left[ a_{ee}^3 \rho_e - a_{gg}^3 \rho_g + a_{eg}^3 (\rho_g - \rho_e) \right], \tag{4.32}$$

where $\rho_{g(e)}$ is the population fraction in the ground (excited) state [83, 88, 87, 157]. The $s$ and $p$ wave scattering lengths are $a$ and $b$ where the subscripts indicate the states of the interacting pair, with $s$-wave interactions only occurring between distinguishable particles. $G^{(2)}$ is the two-body correlation function which varies between 0 for identical particles and 1 for distinguishable particles. $\langle n_D \rangle$ is the mean number density per lattice site. The number density in a particular lattice site is

$$n_D = \frac{N_{\mathrm{site}}}{\pi^{3/2} L_x L_y L_z} \tag{4.33}$$

where $N_{\mathrm{site}}$ is the number of particles in that site. The effective trapping lengths, $L_i$ for particles in the lattice's simple harmonic oscillator potential are

$$L_i = \sqrt{\frac{\hbar (2\langle n_i \rangle + 1)}{m\omega_i}}. \tag{4.34}$$

$\omega_i$ is the trap frequency in the $i$ direction and the mean quantum harmonic oscillator level in that direction is given in equation 2.5. We can use these relations to analyze our measurements and determine useful scaling relationships. In our collection of data for AC Stark and cold-collision shift evaluations, we measured the temperature and trap depths before each clock measurement run with resolved sideband spectroscopy which let us determine the mean occupied lattice motional mode as shown in Figure 2.14. We can then use that information with equations 4.34 and 4.33 to calculate the inverse volume of the lattice sites as shown in Figure 4.12 (a).

Using equation, 4.32 we can estimate the density shift from $p$-wave collisions from the calculated lattice site volumes. We can make this estimate with the interaction length coefficients in [161], $b_{eg} \approx -74a_0$, $b_{ee} \approx -34a_0$, and $b_{gg} \approx 0$ where $a_0$ is the Bohr radius, but

Figure 4.12: (a) shows the scaling of the reciprocal effective lattice site volume as a function of trap depth based on our measurements of temperature. The temperature determines the spatial extent of the atomic motional wavefunctions. The reciprocal lattice site volume is proportional to the number density of the atoms, while the number density could in principle be observed directly with a good camera, we do not have that capability. (b) shows how the size of the cold collision shift should scale as a function of trap depth. We fit the data to a power law $aU^b$ and measured $b$ to be 1.23(34) consistent with the expected scaling for sideband cooled atoms in 4.36. This data is only an estimate and not the measured value of density shift discussed in the next section.

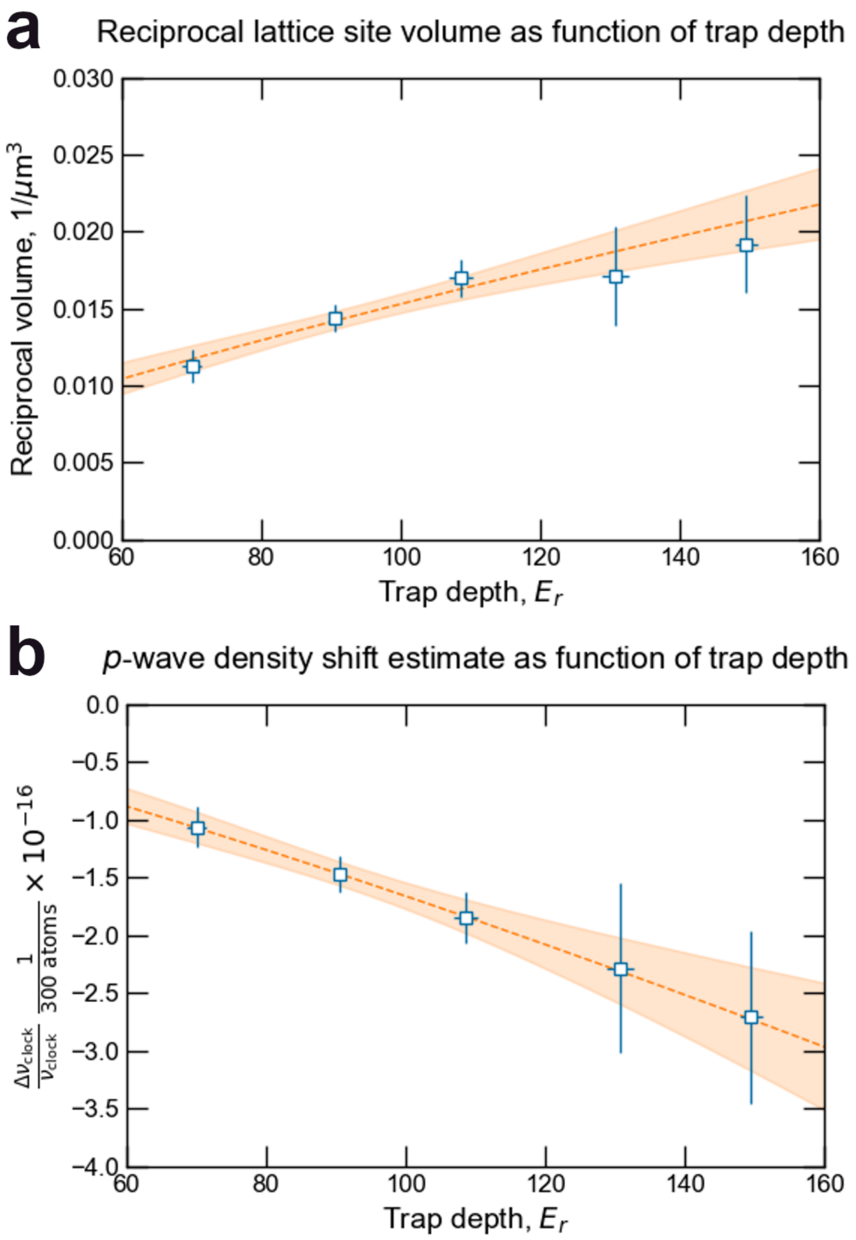

note that the coefficients are not known accurately. We compute the expected density shift for our atomic ensemble with trap depth as shown in Figure 4.12(b). The measured scaling at $U^{1.23}$ matches the theoretical scaling in [88], which gives the cold-collision shift scaling with trap depth for a sideband-cooled sample and a thermal sample as

$$\Delta\nu_{\text{sideband cooled}} \propto NU^{5/4} \tag{4.35}$$

$$\Delta\nu_{\text{thermal}} \propto \frac{NU^{3/2}}{\sqrt{T}}. \tag{4.36}$$

The density shift that we measure in the next section turns out to be significantly lower than the estimate in Figure 4.12(b). This difference is not concerning to us, however, because of the low accuracy of the interaction length coefficients and the dependence of the shift on details of the distribution of motional states that the atoms occupy. However, the measured density shift can be fit to a similar power law.

### 4.3.1 Cold Collisions

To reduce our quantum projection noise limited clock stability below the level of our clock laser noise, we operate our clock with a sample of at least 300 atoms. However, the two-body $p$-wave interactions that result from populating lattice sites with multiple atoms create density-dependent clock frequency shifts [163, 161, 164, 156, 165]. We measure this shift by interleaving between a high and low atom number sample, and measuring the clock transition frequency difference between the two samples. We vary the atom number by analog control of the servo setpoint of the slowing laser intensity. This control scheme permits modulating the final atomic number density in the lattice. Importantly, modulating only the slowing beam is unlikely to introduce other systematic shifts between measurements. Varying the 556 nm MOT parameters might change the temperature of the lattice trapped atoms and varying the 399 nm MOT loading times between the two measurements might result in differential effects from AOM or coil thermalization. However, for all cold collision shift measurements we operate with a 300 ms 399 nm MOT loading time to maximize our lever arm from atom

Figure 4.13: Detail of an individual cold collision shift measurement at 70 $E_r$. (a) shows the atom number over time in both the high and low atom cases. (b) shows the OADEV of the measurement on the left axis and the OADEV of the atom number ratio on the right axis. The white-FM fit at $\tau/2$ was used to determine the uncertainty on all individual cold collision shift measurements. This particular measurement found a $9.7(30) \times 10^{-18}$ shift between high and low, or a $3.5(11) \times 10^{-18}$ shift when scaled to 300 atoms.

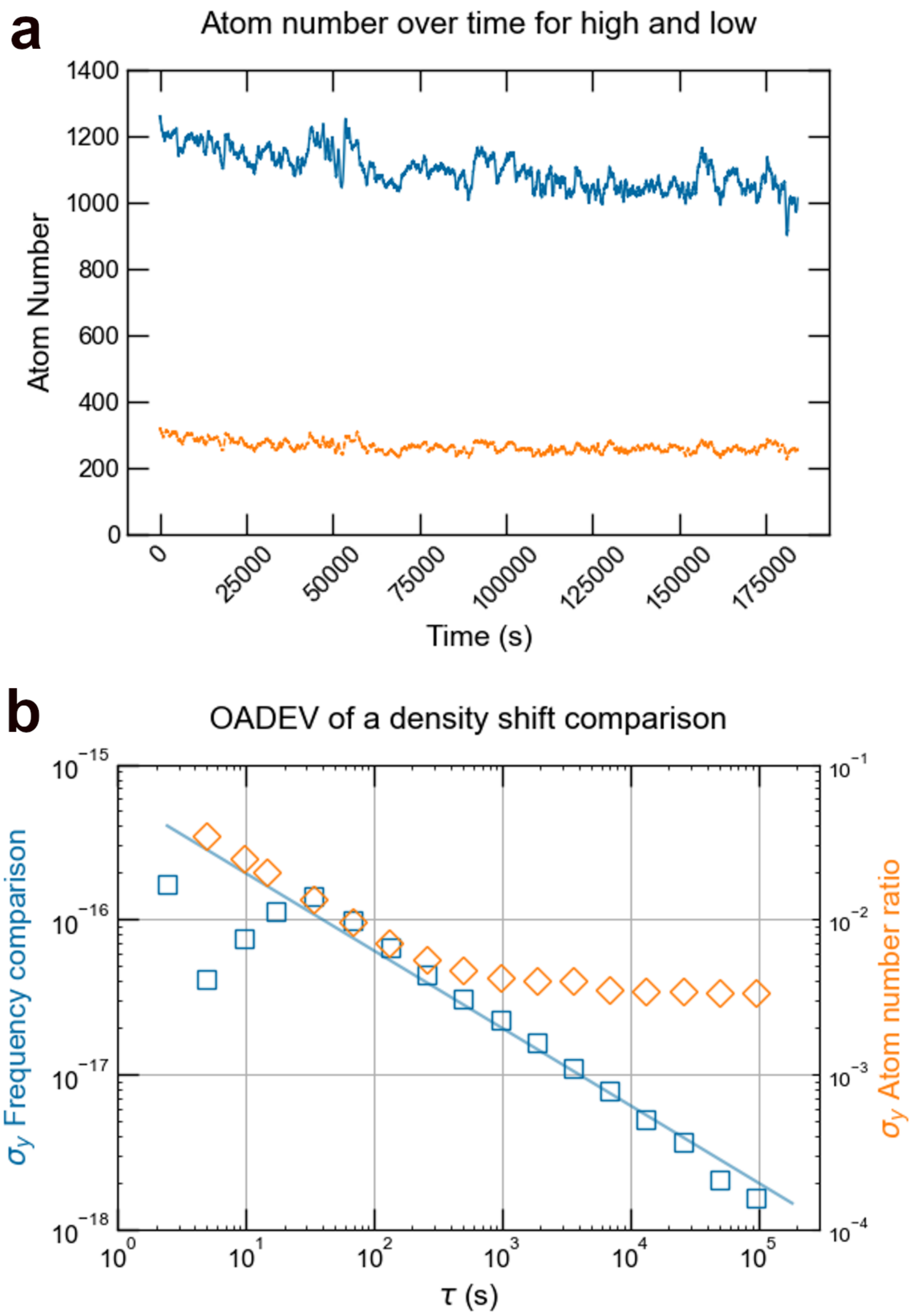

number comparison. While we don't operate the clock in "accuracy mode" with long loading times because the coil heating introduces BBR gradients, this effect is cancelled in common mode for the interleaved measurement. After comparing the frequency difference between high and low atom numbers, we then extrapolate the shift at 300 atoms with a linear model of density-dependent shift. An example of an individual cold collision measurement is shown in Figure 4.13.

Since the apparent atomic density in the lattice for a fixed atom number can be changed in principle by subtle variations in experimental parameters, we repeatedly measured the density shift over several months as shown in Figure 4.15. These variations could include temperature changes from alignment, intensity, or polarization of the laser cooling system; overlap and beam quality of the lattice beam in both directions; and alignment of the atomic fluorescence detection beam or PMT and collection lens. The repeated measurement demonstrated that the shift at 70 $E_r$ and 150 $E_r$ is stable at the $1 \times 10^{-18}$ level. Additionally, the atom number typically averages down to a 4% flicker floor during most measurement runs indicating high in-measurement stability of the density shift. From the uncertainty weighted average of our data at 70 $E_r$, we can conclude that the cold collision shift at that depth is $-3.3(0.6) \times 10^{-18}$.

We evaluated the cold collision shift at multiple trap depths for subsequent subtraction of the shift from measurements of the lattice AC Stark shift. These measurements are shown in Figure 4.16. We first fit our data to a model with the form $a + b \times U^{5/4}$, where $U$ represents the trap depth as suggested by the trap depth scaling laws presented in the previous section. However, this fit required a $4.5(1.3) \times 10^{-18}$ offset to fit well (forcing the offset to zero resulted in reduced chi-squared of 87). While a several $10^{-18}$ offset like this is not impossible to physically explain, it is unexpected based on previous measurements in ytterbium clocks [33]. In fact, the work in [162] makes use of a smaller offset from the positively signed off-site $s$ wave effect to find a zero-crossing in the total cold collision shift. Nonetheless, for analyzing AC Stark data we chose the conservative option of using no fit

Figure 4.14: We evaluated the linearity of the density shift by comparing between a 300 atom sample and a varied higher atom number sample. Then we normalized the shift to the number of atoms in the high atom number sample. We found the expected linear scaling with atom number, indicating that many body interactions do not play a significant role in the collision shift.

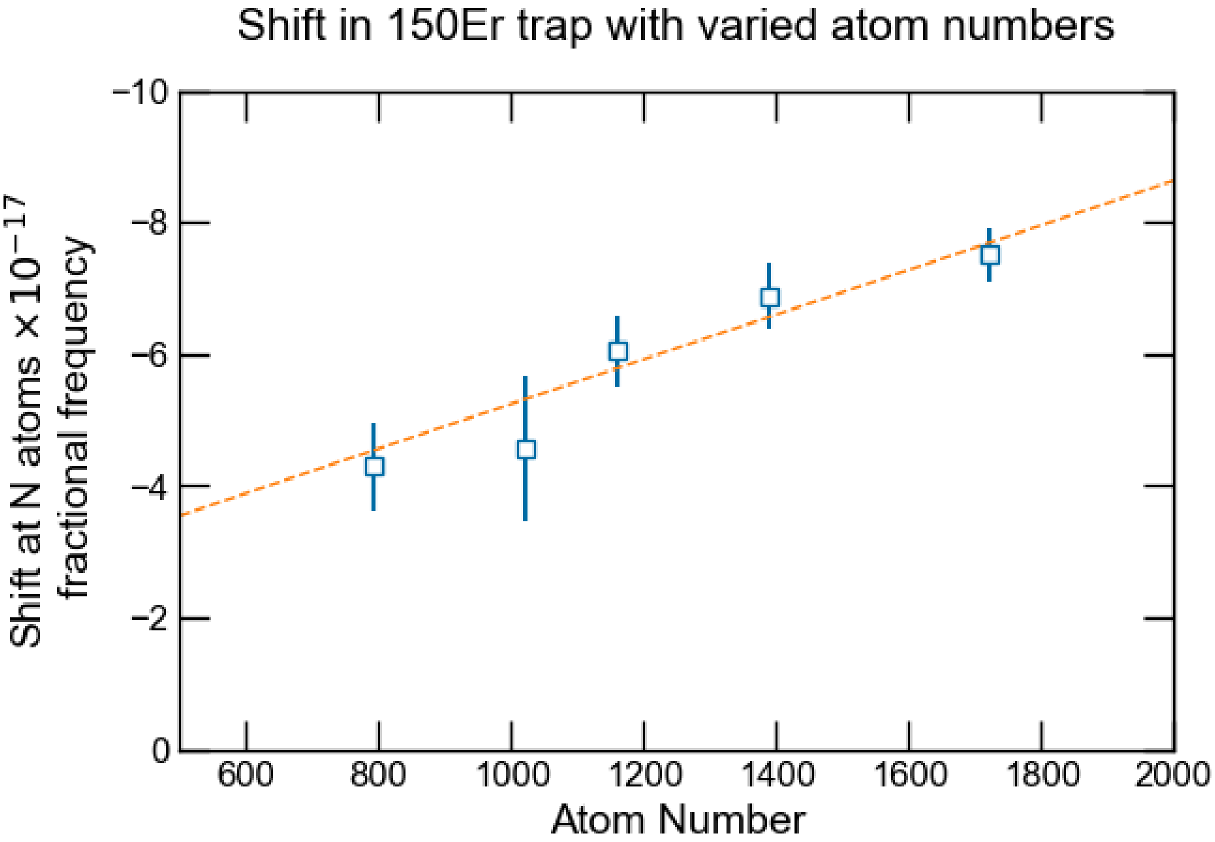

Figure 4.15: Cold collision shift measurements were performed over four months at the same target trap conditions. The shift at 70 $E_r$ is shown with blue squares, and the weighted mean with combined uncertainty is shown by the solid blue line which fits the data with a reduced chi-squared of 0.46. The shift at 150 $E_r$ is shown with orange diamonds, and the weighted mean with combined uncertainty is shown by the dashed orange line with a reduced chi-squared of 1.10. Since the measurements at 150 Er have more atoms, they have a larger available lever arm in scaling to 300 atoms which helps to reduce the errorbars without multi day measurements as in Figure 4.13.

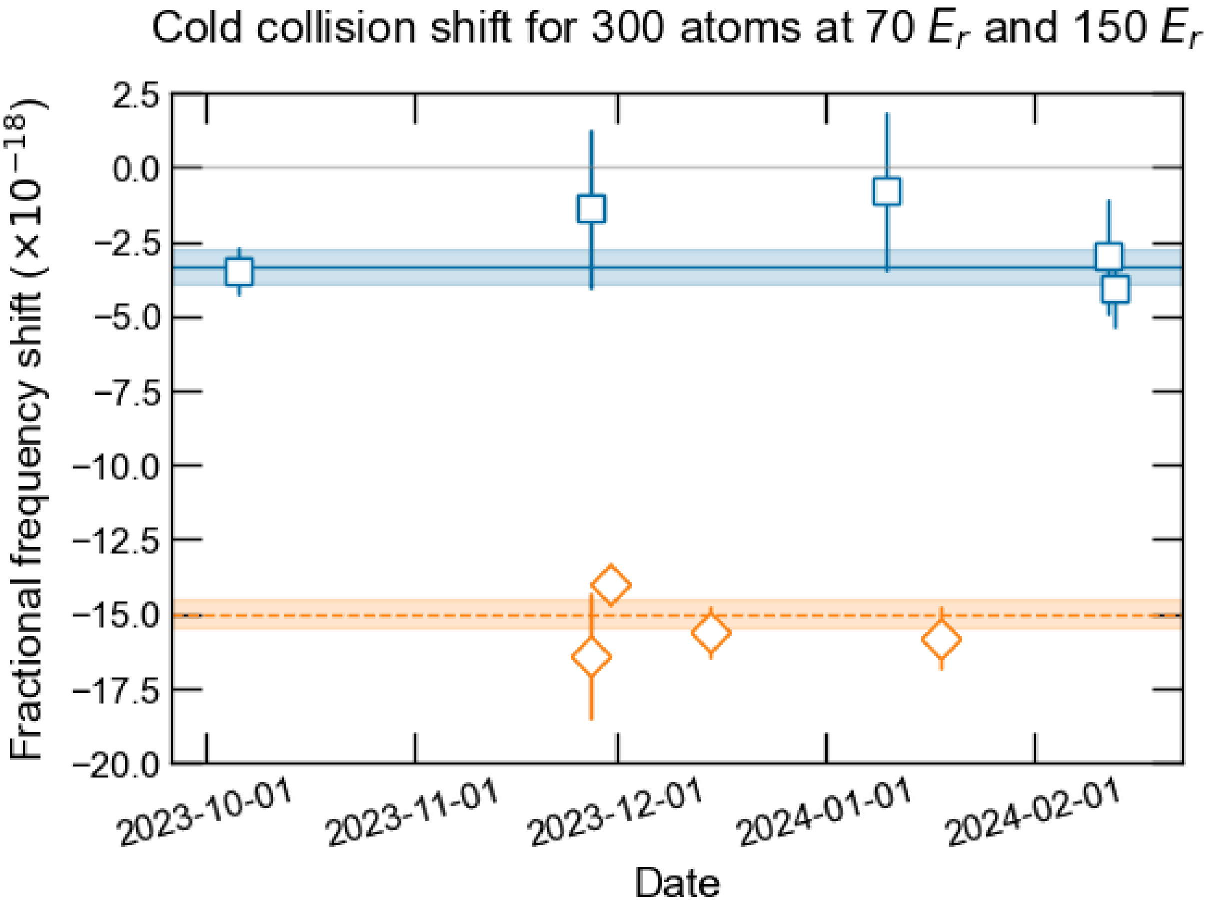

and only directly correcting the AC Stark data with measured trap depth dependent cold collision shifts. In the future, we hope to leverage improved laser cooling to reach lower trap depths and explore this shift's depth dependence further.

### 4.3.2 Spin Polarization

Spin-distinguishable atoms interact with the spectroscopic sample with strongly perturbing $s$-wave collisions. The fractional frequency shift at our operational 300 atom sample size scales with $\eta$, the proportion of atoms remaining in the unwanted spin state $m_F = \pm\frac{1}{2}$ after optically pumping to the target state $m_F = \mp\frac{1}{2}$. As shown in Figure 4.17(a), we measured a shift in our system of $[5.31(14) \times 10^{-16}]\eta$. This value of the shift scaling is greater on a per atom basis than previous measurements [33]. There are several reasons this shift is enhanced in our trap, all originating in greater atom density: our lattice waist is smaller at 50 $\mu$m compared to 70 $\mu$m, we use a compressive magnetic field to assist the MOT to lattice transfer, and both sideband spectra and measurements of the temperature-sensitive $d\alpha^*/d\nu_L$ coefficient indicate a colder atomic sample. Similarly, our $p$-wave dominated cold collision shift is several times higher per atom as well. Measurements at different trap depths, shown in Figure 4.17(b), determined that the $s$-wave collision shift was nearly insensitive to trap depth in our usable range. Trap depth insensitivity of the spin-impure shift is a surprising result that requires further investigation. Measurements without sideband-cooling and adiabatic filtering determined and that $\eta$ halved at higher atomic sample temperatures, 4.5(5)$\mu$K axial and radial, which is expected. Additional measurements are shown in Table 4.7. Unable to reduce the large coefficient of the $s$-wave dependent shift, spin purity requirements in our system were more stringent.

We developed a technique of continuously probing the spin purity to measure the purity with very high accuracy. The clock laser is kept locked to the atomic transition with a normal clock operation sequence of four steps probing both sides of the two $\pi$ transitions to generate an error signal. These steps are interleaved with four other steps to resonantly probe the

Figure 4.16: (a) shows the cold collision shift corrections and uncertainties as a function of trap depth that were applied to the lattice Stark data. These corrections are entirely the empirical results that we measured. (b) shows the raw collision shift data fit to a scaling law of the form $a + b \times U^{5/4}$. The orange dashed fit line has a shaded region around it representing the uncertainty as computed from correlated error propagation. We did not use this fit in correcting the lattice Stark data due to uncertainty in interpretation of the offset term. A scaling law of $a \times U^2$ fits the data well without an offset term, however, there is no physical basis for a squared law.

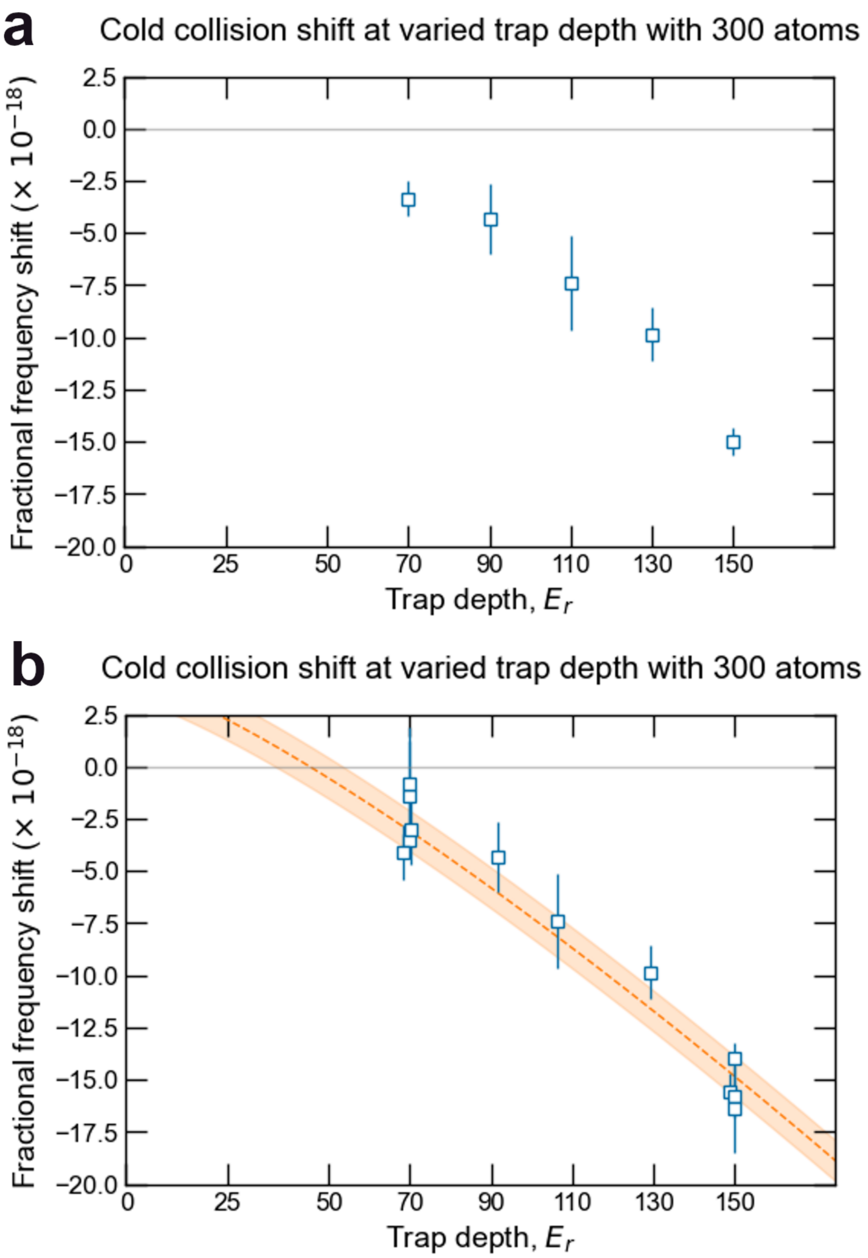

Figure 4.17: (a) shows a measurement of the linear spin-purity coefficient that determines the shift with some quantity of impure atoms $\eta$. These measurements were performed with the normal method for measuring a cold-collision shift (Figure 4.13) at different levels of spin purity. 50% purity was obtained by blocking the optical pumping beam and 25% impurity was obtained with an additional neutral density filter to further weaken the optical pumping beam. (b) shows that the shift with a 50% pure sample was nearly insensitive to trap depth, in contrast to the cold collision shift of polarized atoms (Figure 4.16).

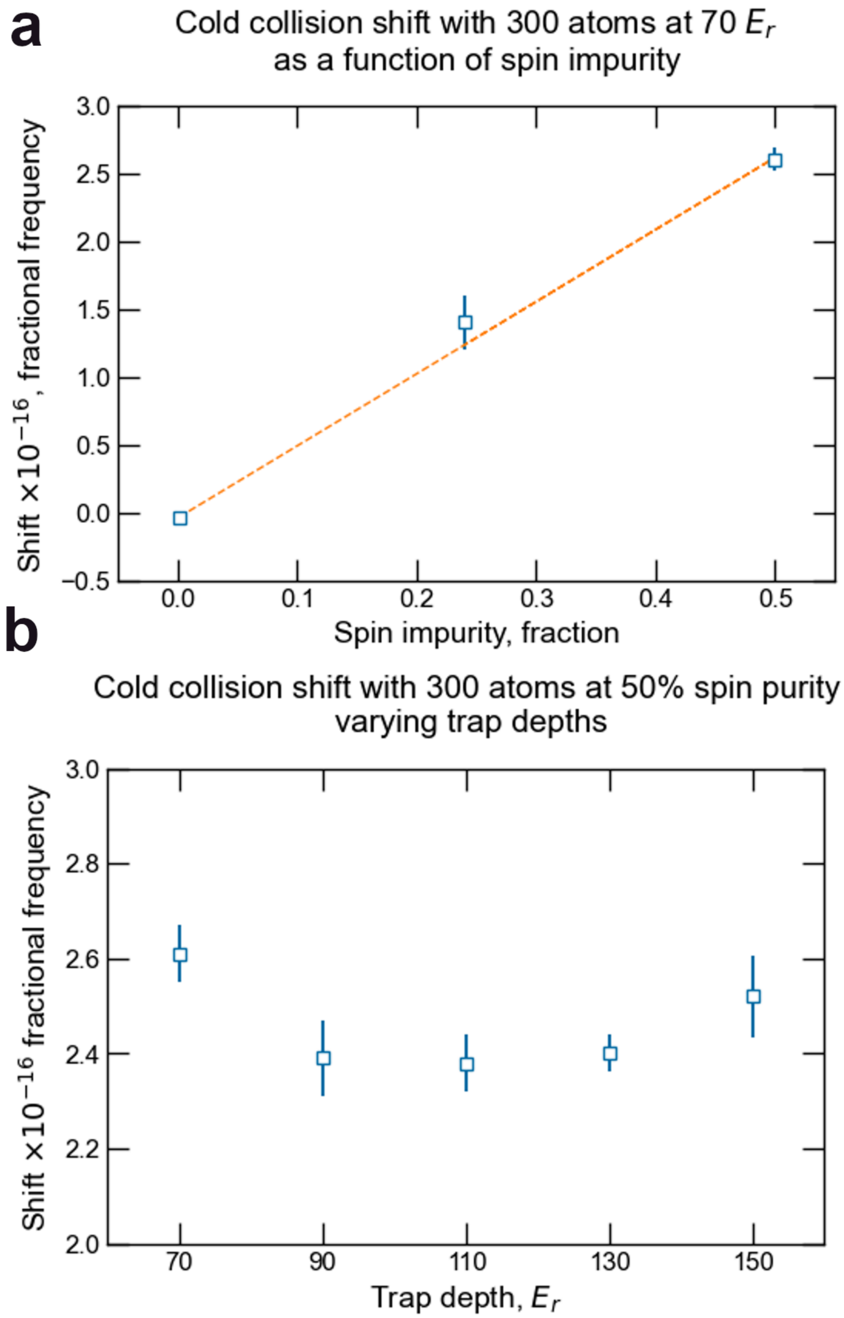

| Spin impurity | 70 Er Lattice, Cold | 150 Er Lattice, Cold | 150 Er Lattice, Hot |
|---|---|---|---|
| $< 0.5\%$ | -3.3(6)$\times10^{-18}$ | -1.5(1)$\times10^{-17}$ | -2.0(8)$\times10^{-17}$ |
| $25\% \pm 1\%$ | 1.4(2)$\times10^{-16}$ | 1.7(2)$\times10^{-16}$ | 5.4(1)$\times10^{-17}$ |
| 50% | 2.6(2)$\times10^{-16}$ | 2.5(1)$\times10^{-16}$ | 1.0(1)$\times10^{-16}$ |

Table 4.7: Shifts given in the table are in fractional frequency units. The “cold” samples were sideband cooled and filtered at 70 $E_r$, while the “hot” samples had no additional cooling after the 556 nm MOT. The $s$-wave shift has almost no apparent dependence on trap depth, but is halved without the sideband cooling and filtering. One interesting aspect of this data is that the sign of the $p$-wave dominated shifts in the high purity cases are opposite of $s$-wave dominated shifts. In principle, this sign-flip means there is a “magic spin purity” where the $s$ and $p$-wave collisions cancel which is $\approx 1\%$ impurity for 70 $E_r$ and $\approx 2\%$ impurity for the cold 150 $E_r$ samples. This purity could be prepared at high fidelity with a fractional $\pi$ pulse of the clock laser. However, this scheme may suffer from accuracy or stability issues with control of the lattice intensity or atomic temperature.

four combinations of $\pi^{\pm}$ transitions from $m_F = \pm\frac{1}{2}$ ground states. In principle, those four probe steps will measure a maximum excitation fraction when the $m_F$ state corresponds to the probed $\pi$ transition and zero excitation when the atoms are in the "wrong" $m_F$ state for the probed $\pi$ transition. An additional step measures a background level with the clock light far-detuned (-5 kHz) from resonance. A short measurement with this technique to $> 99.5\%$ purity is a common diagnostic that we run before making other measurements. However, for our error table we made a long measurement with this technique averaging down over 42,000 seconds of this operation. The results of this measurement are shown in Fig. 4.18 where the overlapping Allan deviation for the impurity in both spin states separately and together are plotted. We measured spin impurities, $\eta$, of $-0.00009(89)$ in $m_F = +\frac{1}{2}$ and $-0.00047(94)$ in $m_F = -\frac{1}{2}$ where the error bars come from the fit to the Allan deviation of the measured spin purity at $\tau_{\text{max}}/2$. With a worst-case impurity of 0.00094, we assess the uncertainty of the shift from the residual spin impurity at $5 \times 10^{-19}$.

### 4.3.3 Background Gas Collisions

Collisions with background gases can have two effects: they may either eject atoms from the lattice or differentially alter the energy levels of the ground and excited states, the latter leading to a measurable frequency shift [166]. This frequency shift is linearly proportional to the pressure of the background gases, which is predominantly hydrogen gas in ultra-high vacuum environments, as documented in previous measurements of this shift [33]. To quantify these collisions, we can measure the lifetime of the atoms in the lattice. Then, with previously measured coefficients [33] that lifetime can be used to compute the interaction rate and therefore the frequency shift caused by background gases. However, the background gas shift of this model depends on the vast majority of the gas being hydrogen, since other gases will have different interaction stengths and therefore different frequency shift scalings with pressure. As we will see, the close proximity of the oven to the atomic trapping chamber results in the vacuum lifetime depending on the oven temperature, due

Figure 4.18: The OADEV of the spin-state preparation purity over 42,000 seconds. The $m_F = +(-)\frac{1}{2}$ purity is shown with blue squares (orange diamonds) and the white-FM fit is shown with a blue solid line (orange dashed line). The combined data averages down with the expected $\sqrt{2}$ improvement to $\eta = -0.00028(67)$ as shown with the gray circles and gray dotted line for the white-FM fit.

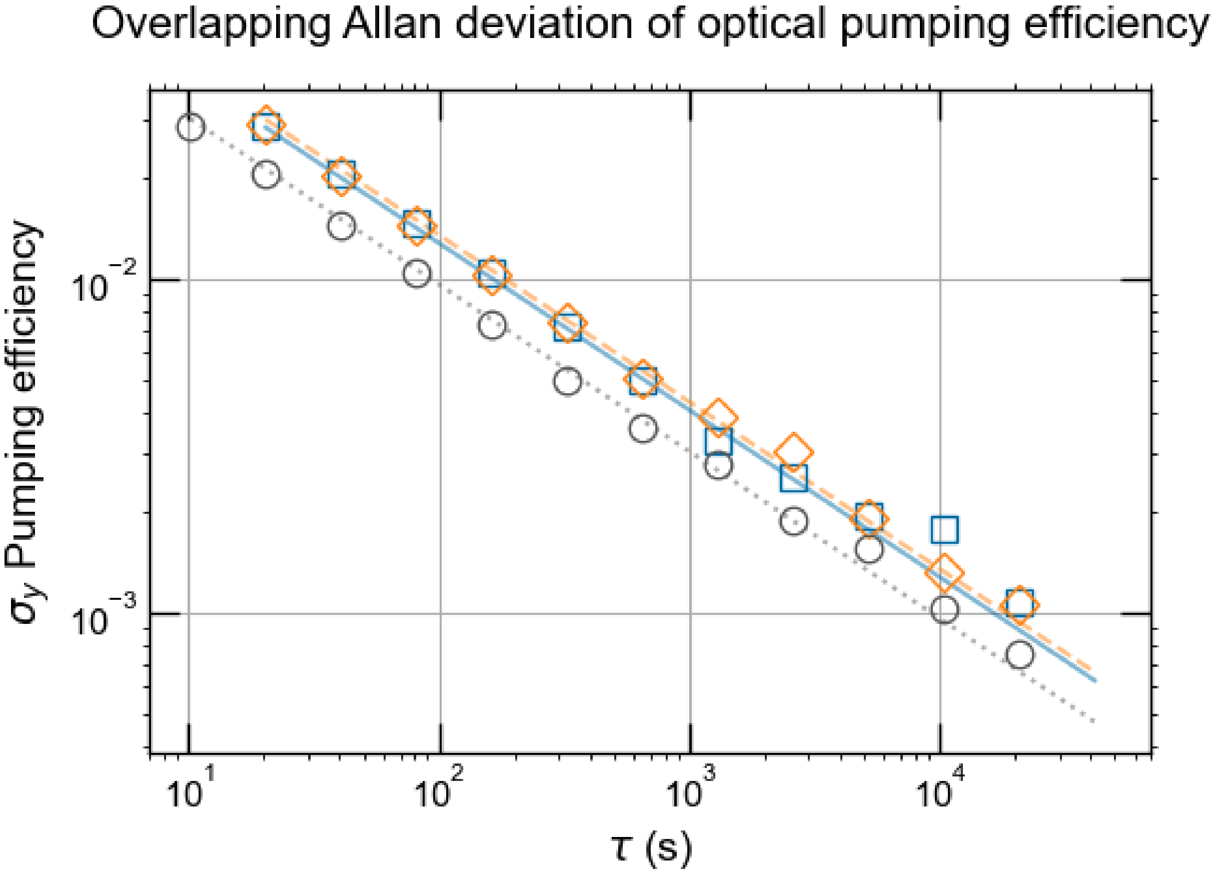

to hydrogen outgassing of the oven materials. Our in-vacuum shutter fully blocks the beam of thermal atoms from the spectroscopy chamber during spectroscopy, so thermal ytterbium collisions are not considered.

We measured the ground state lifetime in the lattice for different oven temperatures (450-480 C in 5 C increments) and trap depths (50, 70, and 150 $E_r$). As shown in Figure 4.20(a), we simply varied the holding time in the lattice before probing to measure the remaining atoms and then fit an exponential decay coefficient to the data. We found an exponential dependence of lifetime, $\lambda$ on oven temperature, $\tau(T) = \tau_0 \exp(-.004T)$, for the high depth lattice, indicating that at high depths the lifetime was vacuum-limited by outgassing from the oven.

Surprisingly, we also found that at low trap depths the lifetimes were diminished compared to the high depths and had a weaker dependence on oven temperature. One hypothesis for lower lifetimes at lower trap depths is lattice heating from frequency or intensity noise that is near the lattice sideband frequencies for low trap depths, but not for high trap depths. We assessed this hypothesis with sideband spectroscopy both immediately after sample preparation and after holding the atoms for three seconds. We measured no observable increase in either the axial or radial temperatures of the atoms, as shown in Figure 4.19. With a sideband-cooled sample, even a small change in the axial temperature should have been readily observable as the re-emergence of a red-detuned sideband feature. While we did not observe radial heating, the signal to noise was degraded for the radial temperature since there were fewer atoms remaining to resolve the wide and shallow band structure. We also made measurements of the trap lifetime separately without frequency stabilization and without intensity stabilization of the lattice laser. In neither case, did we observe increased lifetime indicating that feedback-driven oscillations are not a source of atom heating in the low depth trap.

Another hypothesis is that atoms are slowly tunneling out of the lattice since the lattice is tilted at 15 degrees relative to gravity. The main effect of adiabatically ramping the lattice

Figure 4.19: Sideband spectroscopy to assess the possibility of in-lattice heating. A sample at 70 $E_r$ was prepared in the usual way and the sidebands were measured either immediately or after a three second delay. Neither the axial nor radial temperature increased after the delay. In fact, the radial temperature decreased by 20% which is statistically significant. Note that the signal to noise is worse after the delay because of the atom loss. A similar measurement was performed at 150 $E_r$ and no statistically significant temperature change was observed in either dimension.

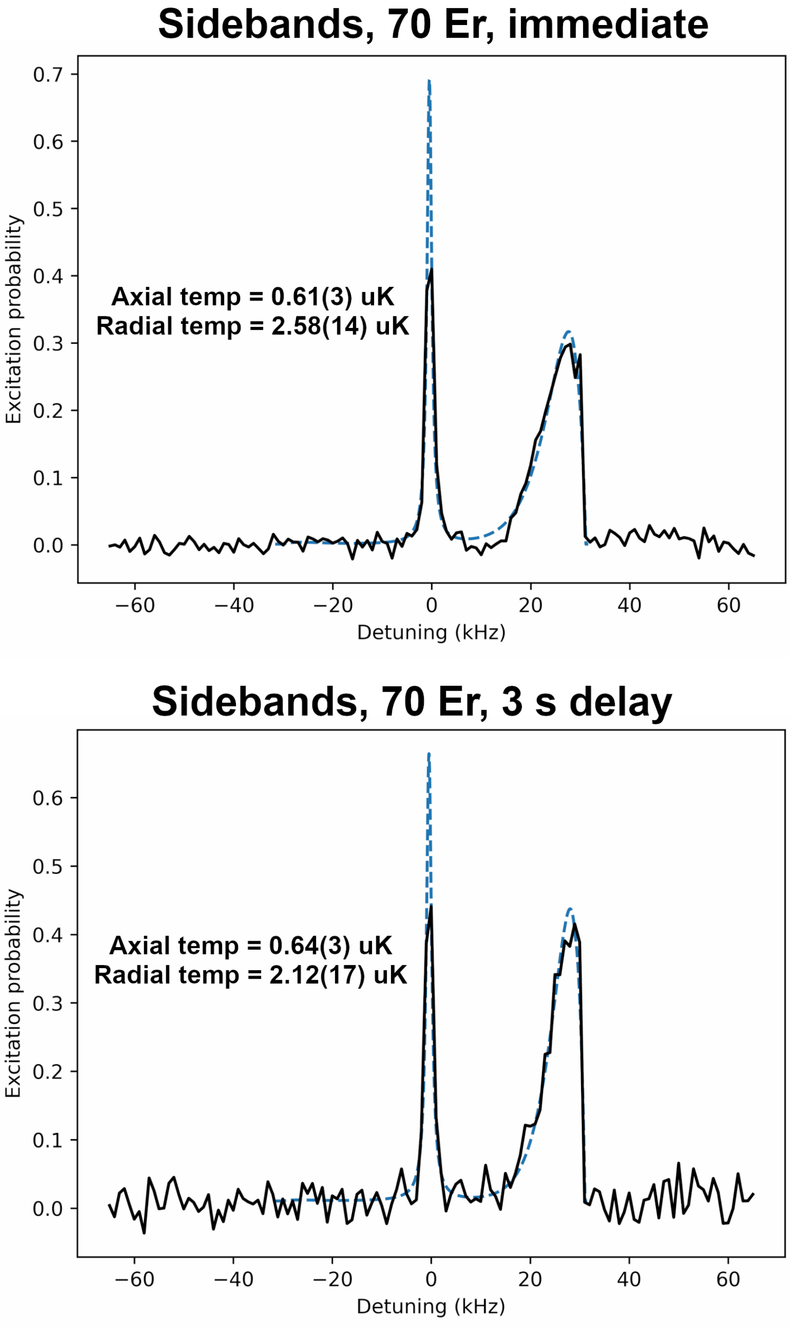

depth lower should be the immediate loss of atoms in untrapped $n_\rho$ states, but it is possible that atoms below that threshold are leaking out more slowly. However, the peak radial force in a lattice is $F_{L,\rho} = -2UE_r/\sqrt{e}w_0$ while gravity exerts a force on the radially trapped atoms of $F_{g,\rho} = mg\sin 15^\circ$. For our lattice with a waist radius $w = 45$ $\mu$m, a minimum trap depth of 20 $E_r$ to counterbalance the radial gravitational force. Previous work in a 15 degree tilted lattice with $w = 70$ $\mu$m [125] found atom numbers were only acceptable above 60 $E_r$, however no mention is made of this being a lifetime effect. At present, this hypothesis is still plausible and worth further exploration since vacuum and lattice heating effects have been largely ruled out.

Nevertheless, we needed to recover a background gas lifetime in order to properly account for the effect of this shift. We used the pressure as measured by the oven-side ion pump as a proxy for the pressure in the spectroscopy chamber. We did not use the ion gauge to measure pressure since the hot gauge's outgassing negatively effects the vacuum lifetime. Additionally, the pressures measured by spectroscopy-side ion pump were consistently low enough that they could not be considered reliable since the current that the pressure is calculated from would be dominated by leakage currents. Then, we fit the following equation,

$$\tau(p) = \left(\frac{1}{\tau_{\text{lattice}}} + \frac{p/p_0}{\tau_{\text{vacuum}}}\right)^{-1} \tag{4.37}$$

to fit the collection of data as shown in Figure 4.20(b). $\tau_{\text{lattice}}$ is the lattice lifetime for a particular trap depth, $\tau_{\text{vacuum}}$ is the vacuum lifetime for a particular pressure, $p$ is the measured oven-side pressure, and $p_0$ is the reference pressure at our oven's typical operating temperature of 465 C. From this dataset, we measured a trap depth independent vacuum lifetime of 8.2(8) s with a 465 C oven. Lattice lifetimes at the different trap depths are shown in Table 4.8. Higher temperatures result in more atoms in the initial lattice trapped sample and this temperature gives a good compromise of vacuum lifetime to trapped atoms. Using the previously measured coefficients from [33], we compute a $-2.0(3) \times 10^{-18}$ shift from background gases.

Figure 4.20: (a) shows an individual lifetime measurement with the conditions of a 150 $E_r$ trap depth and a 470 C atomic beam oven temperature. In these conditions, the measured lifetime was 5.9(2) s. (b) shows data taken across a range of oven temperatures with trap depths at 50, 70, and 150 $E_r$. We fit this data to a combined vacuum and lattice lifetime model to extract a trap depth independent vacuum lifetime of 8.2(8) s. The error bars on this data were scaled up by a factor of 4 to get a reduced $\chi^2$ of 1, however, it is more likely that there are x-axis errors from using the oven side pressure as measured by the ion pump current as a proxy for spectroscopy chamber background pressure.

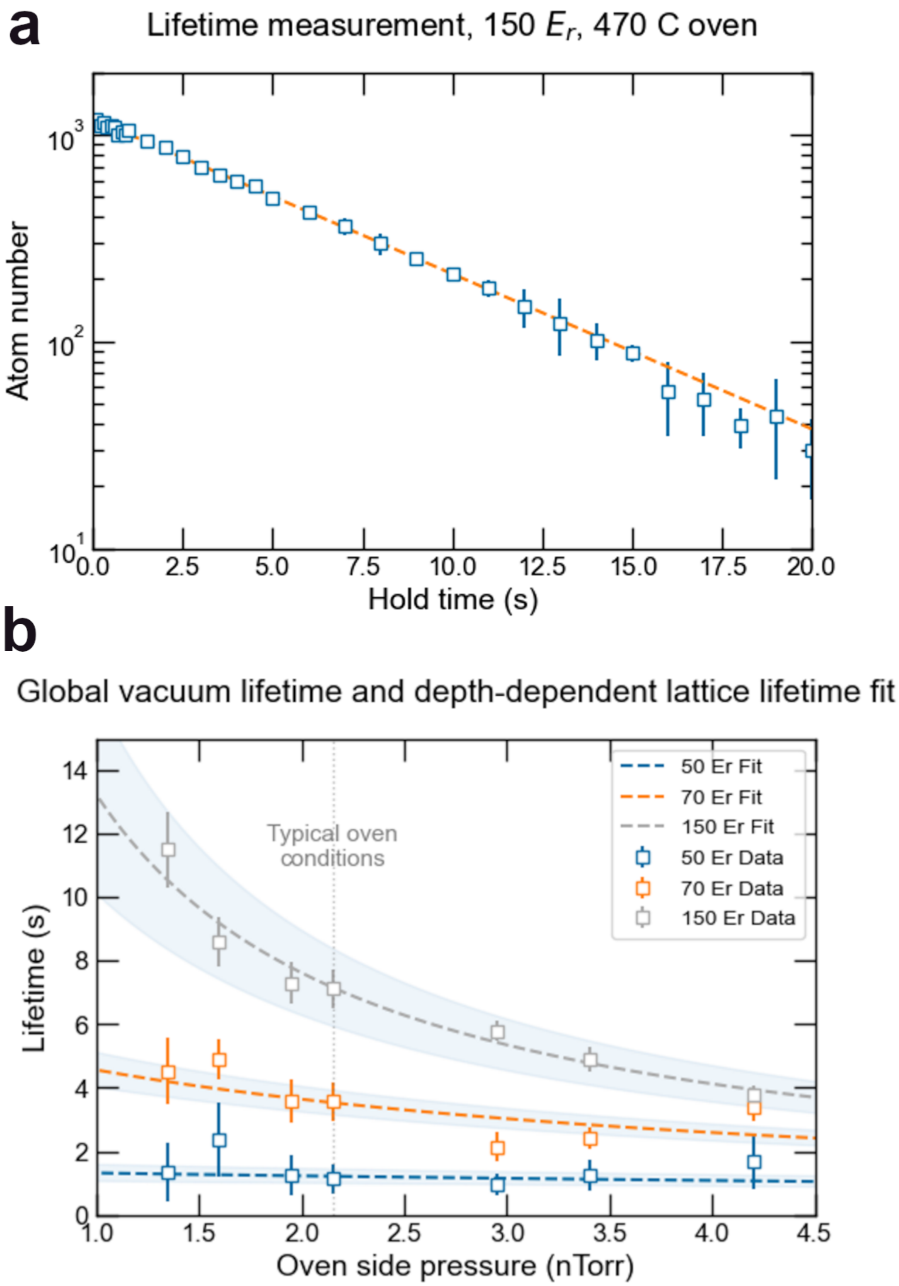

| **Trap depth, $E_r$** | **Lattice lifetime, s** |
|---|---|
| 150 | 50(30) |
| 70 | 6.1(9) |
| 50 | 1.4(3) |
| **Oven temperature, C** | **Vacuum lifetime, s** |
| 450 | 13(1) |
| 455 | 11(1) |
| 460 | 9.0(9) |
| 465 | 8.2(8) |
| 470 | 5.9(6) |
| 475 | 5.2(5) |
| 480 | 4.2(4) |

Table 4.8: Lattice lifetimes at varied trap depths as assessed from the fit in Figure 4.20. At high trap depths the lattice lifetime cannot be accurately determined due to the much greater influence of vacuum lifetime. We would like to operate at a trap depth of 50 $E_r$ or lower to suppress the lattice Stark shift, but the low lattice lifetime at this depth makes this unlikely in the near future.

### 4.3.4 Optimal strategies for measuring cold collision shift

Measurement of the cold collision shift can be difficult in a system with a relatively low number of atoms like ours. Our original epoxy-sealed chamber suffered from a short vacuum lifetime ($\approx 400$ ms) and our titanium chamber observed $> 5$ s vacuum lifetimes, but at $< 100E_r$ trap depths suffered from diminished lattice lifetimes ($\approx 1.5$ s at $50E_r$). For this reason, we calculated optimal experimental parameters to reduce the uncertainty of the density shift when the experiment is suffering from atom lifetime limitations. In the low lifetime regime, the quantum projection noise (QPN) from a small atom number sample will dominate the uncertainty of the cold collision shift. Therefore, both the spectroscopy time which causes more atom loss and the ratio between the high and low atom number samples must be optimized.

After a $\pi$ pulse, the vacuum (or lattice) lifetime-limited sample of atoms, $N$ remaining is

$$N = N_{\text{Max}} e^{-\tau_\pi/\tau_v}, \tag{4.38}$$

where $\tau_\pi$ is the $\pi$ pulse time and $\tau_v$ is the vacuum lifetime. Cold collision shift measurements are made as comparisons between a high atom number $N_{\text{Hi}}$ sample and a low atom number $N_{\text{Lo}} = \delta N_{\text{Hi}}$ sample, where $\delta$ is the ratio between high and low atom numbers, a value between zero and one. The linear coefficient of frequency shift per atom, $\boldsymbol{D}$ for density, is then measured from the frequency difference, $\Delta\nu_{\text{Hi - Lo}}$, between the interleaved high and low atom number samples,

$$\begin{aligned} \boldsymbol{D} &= \frac{\Delta\nu_{\text{Hi - Lo}}}{N_{\text{Hi}} - N_{\text{Lo}}} \\ &= \frac{\nu_{\text{Hi}} - \nu_{\text{Lo}}}{\Delta N}. \end{aligned} \tag{4.39}$$

$\nu_{\text{Hi}}$ and $\nu_{\text{Lo}}$ are the absolute frequencies that samples at the high and low atom condition would have although the absolute frequencies are not experimentally accessible. The atom number difference is given by $\Delta N = N_{\text{max}}(1-\delta)e^{-\tau_\pi/\tau_v}$.

Now we want to calculate the uncertainty on the determination of the shift per atom, $\boldsymbol{D}$, and then find measurement techniques to minimize the uncertainty. We suppose that the technical noise on measuring the relative atom number is small compared to frequency noise. The QPN-limited measurement uncertainty of $\nu_{\mathrm{Lo}}$ is

$$\sigma(\nu_{\mathrm{Lo}}) \propto \frac{1}{\sqrt{N_{\mathrm{Lo}}\tau_\pi}}, \tag{4.40}$$

and similar for $\nu_{\mathrm{Hi}}$ [150]. The uncertainty of $\boldsymbol{D}$ after a measurement for some arbitrary length of time is the quadrature sum of the QPN-limited uncertainties from the individual frequencies

$$\begin{aligned} \frac{\sigma(\boldsymbol{D})}{\nu_{\mathrm{clock}}} &= \sqrt{\left(\frac{\sigma(\nu_{\mathrm{Lo}})}{\Delta N}\right)^2 + \left(\frac{\sigma(\nu_{\mathrm{Hi}})}{\Delta N}\right)^2} \\ &= \frac{e^{(3/2)(\tau_\pi/\tau_v)}}{N_{\mathrm{Max}}^{3/2}\tau_\pi^{1/2}}\sqrt{\frac{1+(1-\delta)\delta}{(1-\delta)\delta}}, \end{aligned} \tag{4.41}$$

where the frequencies, $\nu_{\mathrm{clock}} \approx \nu_{\mathrm{Hi}} \approx \nu_{\mathrm{Lo}}$, were simplified since they will agree at the $1\times10^{-15}$ level or better. The uncertainty for $\boldsymbol{D}$ is now in two independent terms: the $\tau_\pi$ term and $\delta$ term which will simplify optimization.

The optimal $\pi$ pulse time in the low lifetime limit is then given by the minimization of the uncertainty in $\boldsymbol{D}$

$$\frac{\mathrm{d}\sigma(\boldsymbol{D})/\nu_{\mathrm{clock}}}{\mathrm{d}\tau_\pi} = 0 = \frac{(3\tau_\pi - \tau_v)e^{(3/2)(\tau_\pi/\tau_v)}}{2\tau_\pi^{3/2}\tau_v}, \tag{4.42}$$

which simplifies to the useful rule

$$\tau_\pi = \frac{\tau_v}{3}. \tag{4.43}$$

This rule corresponds to our experimental observation in the epoxy-sealed chamber that we obtained the best early cold collision shift measurements at about a 140 ms spectroscopy time. Likewise, the rule indicates that we should be just able to attain useful density shift data in the 50 $E_r$ trap with our normal 560 ms spectroscopy time, given the 1.5 s lattice lifetime at that depth.

Conventional clock wisdom says that best cold collision shift measurements have a large lever arm between high and low atom number since the uncertainty will be divided down by that much. While that is true for the case where QPN is not a factor in the measurement, or is only beginning to be a factor for the low atom number measurement, it is not true when QPN is adversely effecting both measurements. The optimal atom number fraction, $\delta$, in the low atom number sample is computed in the same way as

$$\delta = \frac{1}{2} \tag{4.44}$$

indicating the importance of maximizing clock stability when severely atom-starved. This result might also be useful for clocks with excellent reference cavities where even at higher atom numbers the quantum projection noise limits the stability of the clock.

## 4.4 Doppler Systematics

One of the greatest attractions of the lattice clock architecture is its potential to be virtually Doppler free. Atoms trapped in the lattice have quantized motion, and by phase locking the clock laser to the lattice reference surface, the atom motional frame and clock laser field can be made phase coherent. Other high-accuracy clocks can suppress Doppler shifts to a high degree, but it is difficult to make them fully Doppler free. Fountain clocks suppress Doppler shifts by interrogating atoms moving with equal and opposite vertical velocities as they travel through the microwave cavity. However, the freely expanding atom cloud can sample imperfections in the cavity resonator leading to what is called the distributed cavity phase shift [167, 168]. Optical ion clocks use an ion trapped in a quantum ground state of motion and phase-lock the clock laser to a nearby optical surface reference to eliminate fiber phase noise. Small static electric fields on the RF trap surfaces, however, can push the atoms out of the trap center which causes them to have low amplitude oscillations in the trap. This excess oscillation is called micromotion and leads to a second order Doppler shift that is the leading shift uncertainty in many ion clock uncertainty budgets [169, 170, 171].

Interestingly, both of these uncertainties are results of the clocks ultimately being man-made artifacts. While lattice clocks can be Doppler free by design, elimination of Doppler shifts is only possible to the extent that the clock laser can be phase locked to the lattice reference surface and that residual motional effects can be controlled.

### 4.4.1 Doppler shift from clock light delivery

We evaluate the residual Doppler frequency shift arising from imperfect delivery of the 578 nm clock light to the atomic reference frame during the clock cycle [89]. Clock light is delivered to the atoms via fiber and a small length of free space before the phase reference mirror. As is conventional, we detect and actively correct for accumulated phase noise from optical propagation via an AOM. We measured the uncancelled phase noise throughout the entire optical propagation length by interleaving a clock measurement between a cycle providing phase noise cancellation feedback to the clock AOM and a cycle without feedback. The Allan deviation of this measurement is shown in Figure 4.21. The resulting cycle-correlated Doppler noise yielded a $9.90(16) \times 10^{-17}$ shift.

We measured the phase noise suppression capability of the fiber phase noise cancellation (PNC) feedback loop. We inserted an electro-optic modulator (EOM) into the optical path before fiber coupling to apply intentional phase chirp to the clock light. The clock light polarization must be identical in both directions through the EOM crystal to avoid violating the assumption of reciprocal phase noise in the fiber phase noise cancellation scheme, since the EOM's applied phase is polarization dependent. This optical arrangement is shown with the chapter 2 discussion of the clock laser system with Fig. 2.17 where the additional EOM and polarization optics are inside a labelled box.

We compared three cases. Case one: serrodyne phase modulation on the EOM was applied over the entire spectroscopy time and the phase noise was left uncancelled. Case two: identical EOM phase modulation was applied as in case one, and AOM phase noise correction was applied to cancel the introduced phase chirp. Case three: no EOM phase modulation

Figure 4.21: The overlapping Allan deviation from the comparison between the use of fiber phase noise cancellation and without cancellation. At 235,121 seconds, this is the longest dataset we took while building our uncertainty budget, using the brute force method to meaningfully measure the shift. The long servo attack time and bumps on the ADEV are most likely signatures of room-temperature oscillation in 1G106 and 1G108. Also of note is that the mean excitation without PNC compared to with PNC dropped to about 35% from 48%. Presumably, this happened because frequency broadening and drift of the clock probe during spectroscopy lowered the effective Rabi frequency. If during setup of the clock, it is noticed that the Rabi rate has dropped unexpectedly, checking the PNC quality is prudent.

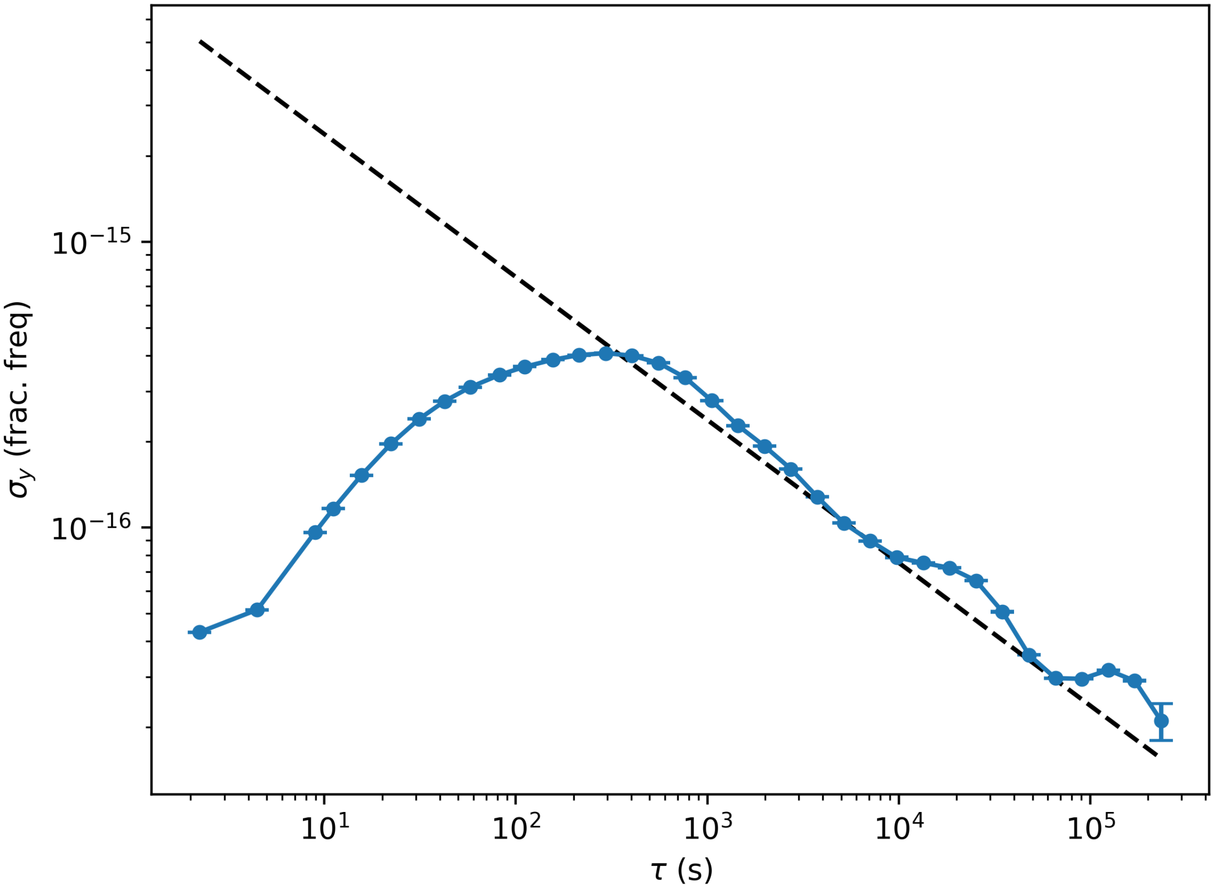

was applied and AOM phase noise correction was applied. Interleaving cases one and three, we measure the applied frequency offset as a result of the phase ramp. Interleaving cases two and three, we measure the residual frequency shift that the PNC fails to cancel from the phase ramp. Figure 4.22 shows these three cases as applied to a single swept $\pi$ transition. The serrodyne modulation was generated by a TTL controlled synthesizer feeding a high voltage amplifier. We found the optimal serrodyne tone for a high effective Doppler speed without unlocking the PNC started with a ramp from 0 V to +180 V and then ramped from -180 V to +180 V two more times over the 560 ms spectroscopy time. Using the half-wave voltage at 578 nm from the EOM's data sheet and the details of the serrodyne phase modulation, we can compute an effective Doppler velocity that this modulation imparts on the light as 8 $\mu$m/s. Then, we expect to measure an imposed Doppler shift of $v/c = 2.7 \times 10^{-14}$.

With cases one and three, we measured an applied frequency offset of $2.79(4) \times 10^{-14}$, consistent with the expected Doppler shift. With cases two and three, we measured the residual frequency shift at $-5.95(39) \times 10^{-17}$, demonstrating a factor of 470 suppression in applied frequency shift. The PNC loop's suppression factor on frequency shift is less than that of frequency noise which is approximately 2000 for averaging times greater than 500 seconds. We believe that the residual frequency shift was limited by our ability to obtain identical polarizations through the EOM in both directions, which also explains the change in sign. Nevertheless, applying this lower bound suppression of 470 to the cycle-correlated noise gives a $2.1 \times 10^{-19}$ phase noise shift uncertainty, where the unsuppressed shift and measurement error have been added in quadrature.

We performed additional tests to measure cycle-correlated acoustic noise that might create a Doppler shift. In one test, we interleaved between our normal clock sequence and the same clock sequence with a delay between state preparation and beginning clock spectroscopy. This delay permits us to probe if there is a cycle-correlated Doppler shift, perhaps as a consequence of vibration from the atomic beam shutter or the switching magnetic fields. Over two decades of delay, we measured no significant change in the measured frequency at

Figure 4.22: The three cases we compared for the Doppler shift measurement are shown here as scans over the spectroscopic feature. Here, the green “Stage 2.0” corresponds to case one where the phase ramp displaces the spectroscopic feature by 14 Hz and the lack of PNC additionally causes broadening and diminished contrast of the feature. The blue “Stage 0.0” corresponds to case three, where the PNC loop is enabled and no phase ramp is applied to the EOM. The orange “Stage 1.0” corresponds to case two, and shows how the PNC loop is capable of suppressing the effect of the phase ramp. Note that in both cases with noise suppression a high quality sinc$^2$ line shape is observed.

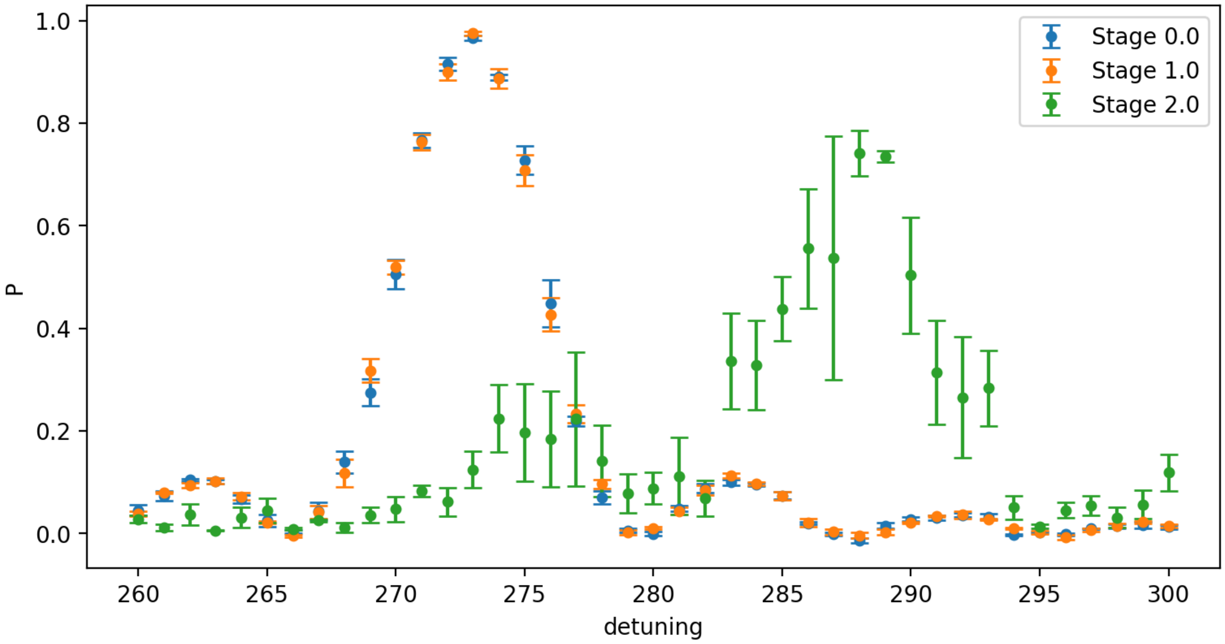

Figure 4.23: Lattice hold time versus frequency shift relative to zero additional hold time clock cycle. There is no significant shift over two decades of hold time showing the suppression of any cycle-correlated Fourier components. These measurements were intended to be quick verifications of insensitivity to cycle times rather than rigorous measurements for the error table like the previous measurement of the phase noise suppression.

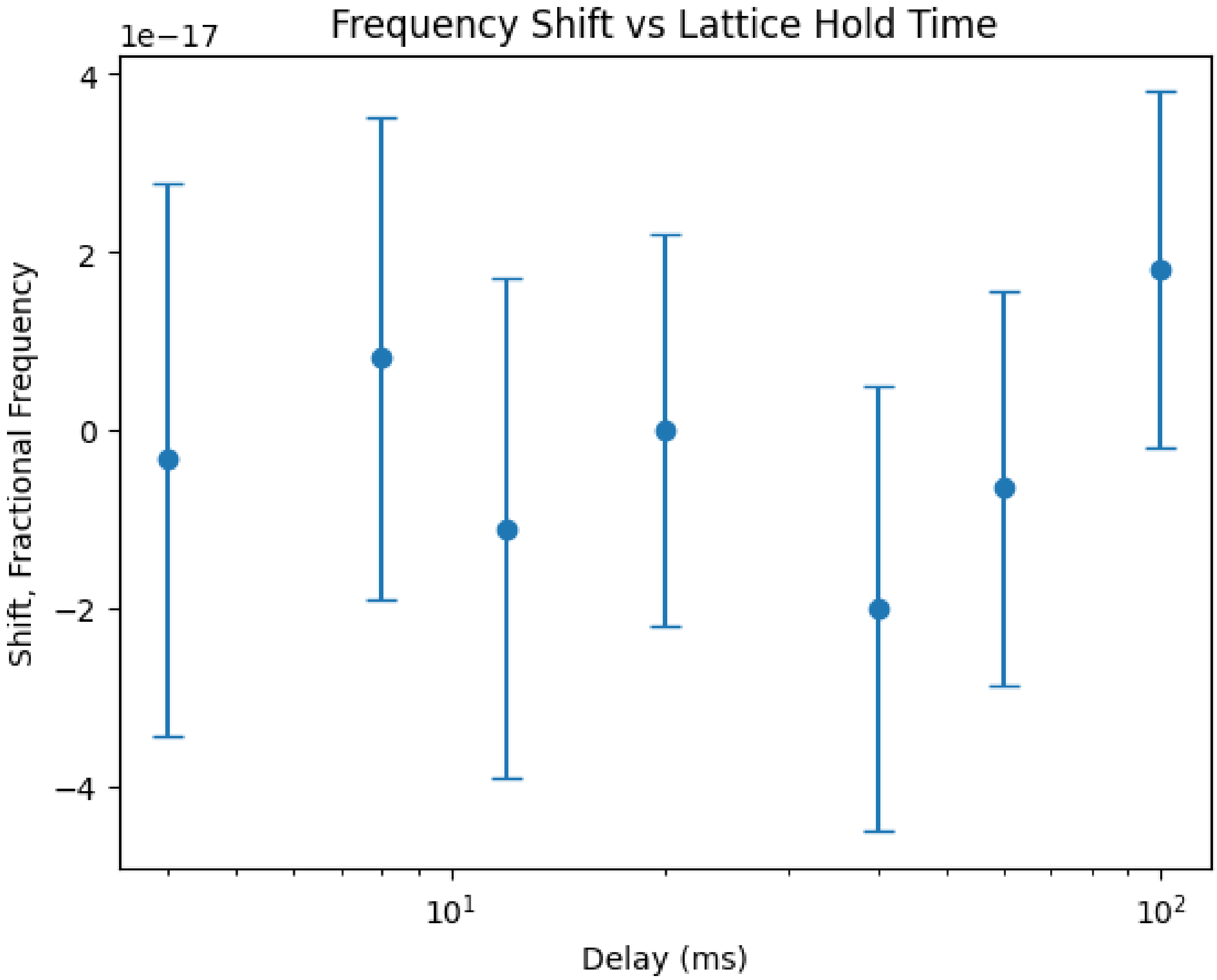

the low $10^{-17}$ level, as shown in Figure 4.23.

Another direct test of the cycle-correlated noise was to place accelerometers in different locations and orientations on the physics package. These measurements, shown in Figure 4.24 demonstrate that there is an acceleration frequency component at the clock cycle frequency. The acceleration at this frequency is strongest on the mezzanine breadboard which should be relatively unsampled by the clock light which is on the base plate as is the phase reference mirror. Considering the non-zero offset in the first measurement we made comparing with and without PNC, it is reasonable to suppose that the acceleration component at the cycle frequency is the source of the net Doppler shift. However, because of the strong suppression from PNC, that residual shift is safely at the low $10^{-19}$ level.

### 4.4.2 Atomic Tunnelling

Atomic tunnelling between adjacent lattice sites could result in residual Doppler effects [172]. We suppress atomic tunneling both by operating the lattice at a relatively large depth compared to the clock photon recoil energy and by orienting the lattice mostly along gravity to break the degeneracy between neighboring lattice sites.

Following the analysis of [172, 173], and using measurements [33, 174] and calculations from [32, 174], we calculate a 1540 Hz Bloch sideband frequency and a Rabi frequency of the first order Bloch sideband that is $10^{-4}$ suppressed from the Rabi frequency of the clock transition. We estimate a possible shift at the $< 1 \times 10^{-21}$ level for typical operating conditions.

## 4.5 Frequency Control Systematics

A lattice clock is a device that stabilizes the frequency of an optical oscillator whose frequency may be then used to measure time intervals. The set of systematics related to frequency control assesses how well the electrical and optical techniques used in the clock can faithfully steer the local oscillator to the atomic transition frequency. If a clock is well-built,

Figure 4.24: Frequency dependent acceleration measurements of the physics package with the accelerometer in different locations and orientations. The second upper mezzanine breadboard (top plate) where the lattice laser is focused shows generally greater accelerations, especially in the north/south direction which is orthogonal to the beam propagation direction. Notably, nearby human activity causes an order of magnitude increase in accelerations. Much of our ADEV data shows greater stability after business hours which may be an effect of either reduced vibrations or reduced temperature fluctuations.

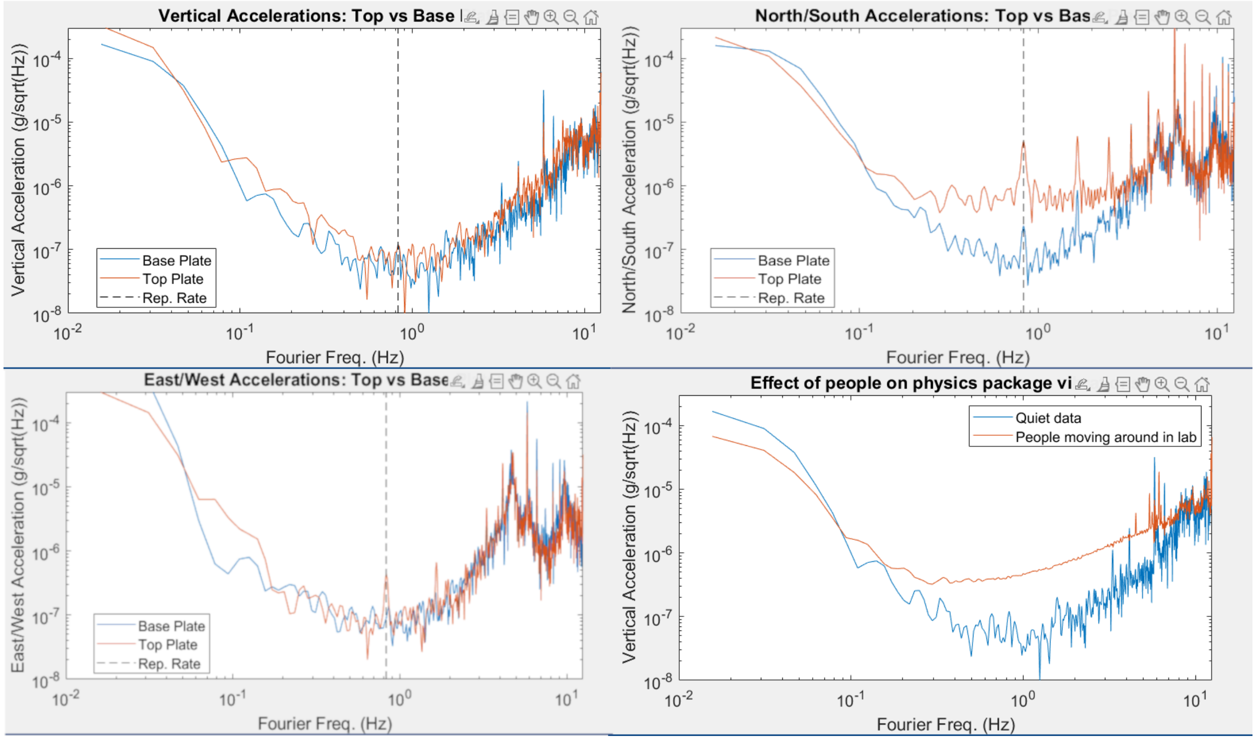

these systematics should generally be very small relative to the potential energy-level shifts affecting the atomic transition. Nevertheless, they are fundamental to the operation and understanding of the lattice clock architecture.

### 4.5.1 Optical Frequency Synthesis

The clock laser light is pulsed on the atoms with the same AOM that phase stabilizes the light to the lattice reference surface. AOMs are useful experimental devices because they can add or subtract radio frequencies from an optical frequency with little error. Pulsing the AOM on however, introduces a transient phase excursion which integrates to a frequency offset as the active phase stabilization servo engages. In our clock, when the in-loop error signal is averaged for many cycles, the mean phase chirp reaches a maximum phase error of 0.8 rad and is suppressed within 70 $\mu$s. The phase chirp is shown in Fig. 4.25 where the chirp was measured from error signal voltage and multiplied by $2\pi/560$ mV where 560 mV was the peak-to-peak voltage when the error signal was permitted to phase wrap by disabling the servo feedback. AOMs have another possible source of phase error from thermalization that we were unable to detect with this method. Presumably, this error was undetectable because thermalization happens on a timescale much longer than the servo bandwidth and can therefore be actively corrected.

Given both the total pulse length, $T = 560$ ms, and the detuning from the excitation peak that we use to generate an error signal, $\nu_{\mathrm{dev}} = 0.8$ Hz, we can compute the effect of the measured phase chirp on the atoms. We used the phase sensitivity function,

$$\frac{dg(t)}{dt} = \frac{-\pi}{1+(2\nu_{\mathrm{dev}}T)^2}\left[(1-\cos\Omega_2)\cos\Omega_1 - (1-\cos\Omega_1)\cos\Omega_2\right] \tag{4.45}$$

in [175], where

$$\Omega_1 = \pi\sqrt{1+(2\nu_{\mathrm{dev}}T)^2} \times \frac{t}{T} \tag{4.46}$$

and

$$\Omega_2 = \pi\sqrt{1+(2\nu_{\mathrm{dev}}T)^2} \times \frac{T-t}{T} \tag{4.47}$$

Figure 4.25: 128 error signals were averaged on an oscilloscope while the AOM switches on and achieves phase-lock to the heterodyne reference frequency for phase noise cancellation. The blue solid line is the product of that error signal and a phase-voltage calibration factor from the observed phase wrapping of the error signal. The axes for the phase error are on the left. The orange dashed line is the time-integrated change in excitation fraction of the atoms as a result of the phase chirp, such that the value at 85 $\mu$s is $\delta_p$. The axes for the excitation fraction change are on the right.

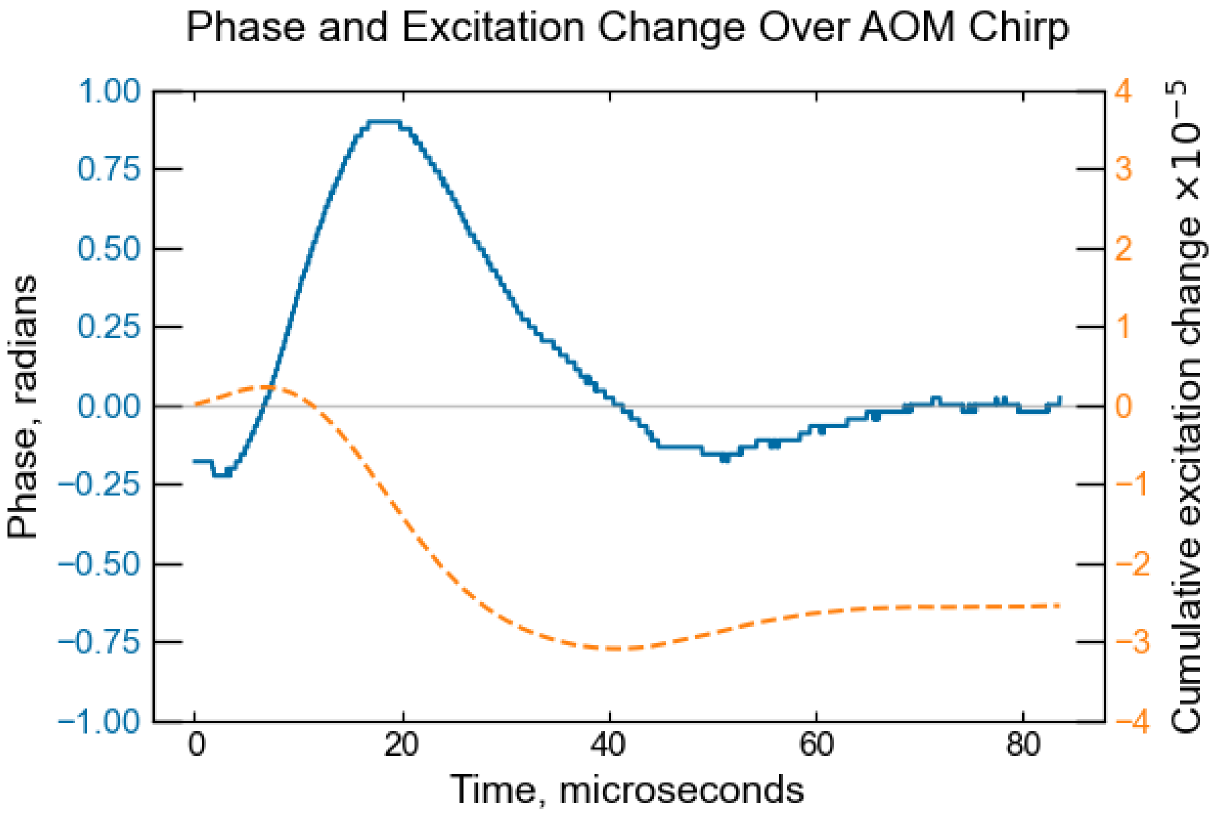

to compute the average change of the excitation fraction

$$\delta_p = \int_0^T \phi(t) \frac{dg(t)}{dt}\, dt, \tag{4.48}$$

for each measurement. The phase sensitivity function is illustrated in Figure 4.26. The net effect is a small change in excitation between the red and blue detuned probing of the spectroscopic feature, $\Delta P = 2\delta_p P_{\text{max}}$, where $P_{\text{max}}$ is the maximum contrast observed for the Rabi line shape, typically 92%. The small change in excitation between the red and blue detuned probing results in a small bias to the observed frequency of the clock transition $\Delta\nu_{\text{clock}} = \nu_{\text{dev}}\Delta P/P_{\text{max}}$. The error from the measured phase chirp is then $7.9 \times 10^{-20}$.

We additionally tested whether the pulsed direct digital synthesizer output from Artiq, that serves as the reference signal for the phase noise cancellation beat, could introduce a systematic error. We set a second DDS referenced to the same 10 MHz maser and generated a 198 MHz tone identical to the one expected from the pulsed DDS. We mixed the two signals together and measured the phase excursion on an oscilloscope in a manner much like the AOM chirp measurement. The phase mismatch averaged to zero within 10 $\mu$s of the Artiq DDS output turning on. However, in our sequence, the DDS reference signal for phase noise cancellation turns on 30 ms before the optical pulse begins. The optical pulse is controlled by a TTL-driven RF switch to the AOM. We consider DDS phase chirp to be a negligible source of error.

### 4.5.2 Clock stability and the AOM phase chirp

Since for the portable system, we may need to use a less stable cavity in the future and therefore will need to use a shorter spectroscopy time, we wish to determine a scaling law for a constant phase chirp with diminished spectroscopy time. Consider some arbitrary servo lock on the phase as a damped oscillator such that

$$\phi(t) = Ae^{-\lambda t}\cos(\omega t + \phi), \tag{4.49}$$

Figure 4.26: The sensitivity, $dg(t)/dt$, of the atoms to errors in phase per unit time for the 560 ms Rabi pulse used in our typical clock sequence. The atoms are most sensitive to phase errors near at the beginning of the pulse where phase errors occur as the fiber noise cancellation scheme achieves phase lock.

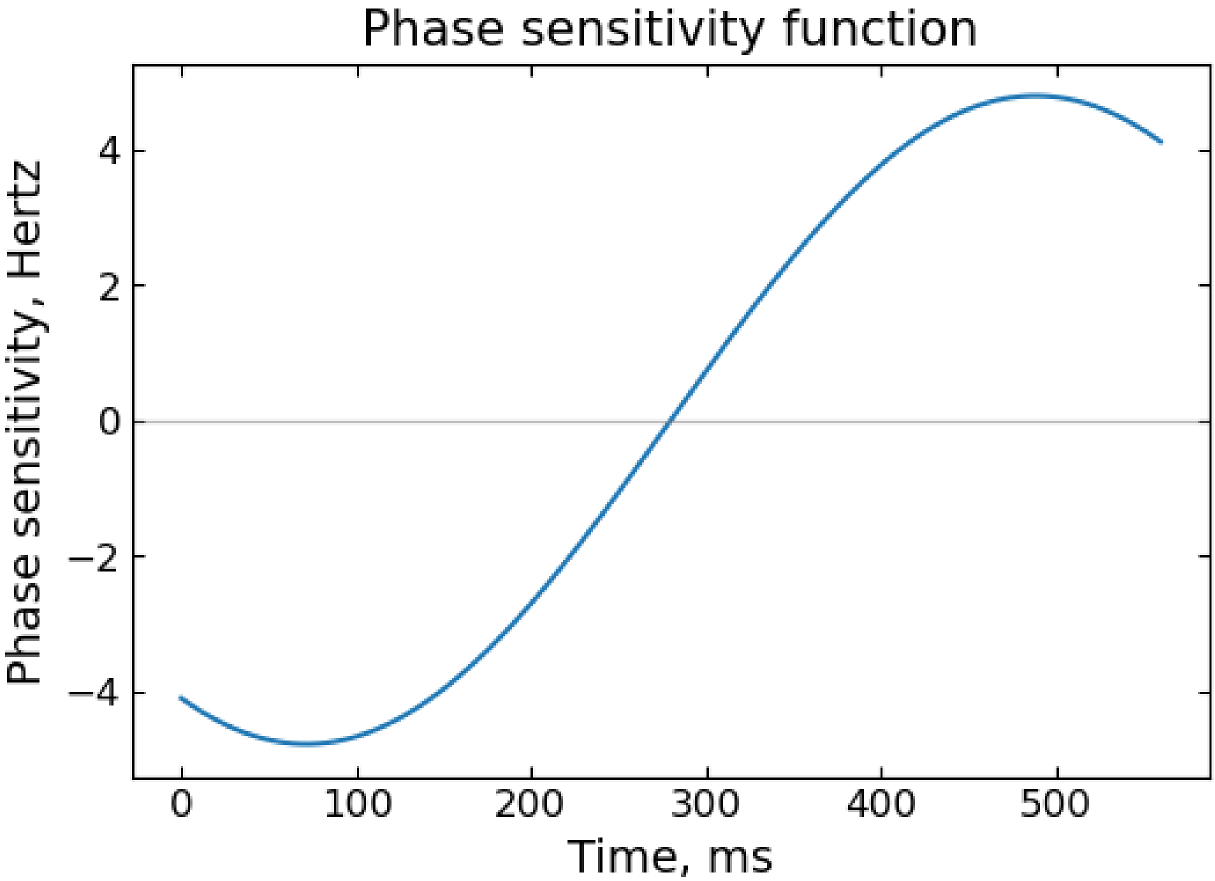

where $A$ is the amplitude of the phase oscillation, $\lambda$ is the damping rate of the servo, $\omega$ is the phase oscillation that the servo damps out, and $\phi$ is a phase offset. This model is a reasonable one given both our own slightly underdamped servo data in Figure 4.25 and the underdamped servo oscillation that was carefully fitted to a function with the form of equation 4.49 in [175]. The optimal detuning for error signal sensitivity is $\nu_{\text{dev}} = 0.3999343/T \equiv \delta^*/T$ as calculated in [176]. Given this value, we will also redefine the constants $\psi \equiv (2\nu_{\text{dev}}T)^2 \approx 0.6398$ and $\Psi \equiv \pi\sqrt{1+\psi^2} \approx 4.022$. Making the appropriate substitutions into equation 4.48, we then have

$$\delta_p = \frac{2\pi\delta^* A}{T(1+\psi)} \int_0^T e^{-\lambda t}\cos(\omega t + \phi)\left[\cos\left(\frac{\Psi t}{T}\right) - \cos\left(\frac{\Psi(T-t)}{T}\right)\right] dt. \tag{4.50}$$

Assuming that the servo attack time is acceptable and that oscillations are short relative to spectroscopy time, $e^{-\lambda T} \to 0$ and $T\omega, T\lambda \gg \Psi$, we can then evaluate and simplify the definite integral as follows

$$\begin{aligned}\delta_p &= -\frac{4\pi\delta^*}{1+\psi}\sin^2\left(\frac{\Psi}{2}\right)\frac{A}{T(\lambda^2+\omega^2)}\left(\lambda\cos\phi - \omega\sin\phi\right)\\ &\approx -2.507\frac{A}{T(\lambda^2+\omega^2)}\left(\lambda\cos\phi - \omega\sin\phi\right).\end{aligned} \tag{4.51}$$

Following the previous arguments, we can apply the change in excitation fraction to determine a change in measured frequency and also combine trigonometric terms

$$\Delta\nu_{\text{clock}} \approx -2.005\frac{A}{T^2\sqrt{\lambda^2+\omega^2}}\cos\left(\phi + \tan^{-1}\left(-\frac{\omega}{\lambda}\right)\right). \tag{4.52}$$

Fitting the prior experimental data in Figure 4.25, we recover $A = 0.51\times\pi$, $\lambda = 2\pi\times 6.0$ kHz, $\omega = 2\pi \times 14$ kHz, and $\phi = -0.64 \times \pi$. Computed with equation 4.52, the error from phase chirp is $8.0 \times 10^{-20}$ demonstrating negligible error compared to the measured result.

We can gain further understanding of this equation, by remembering that the damping of the oscillation is the result of control by a two-pole PI loop and applying the techniques of control theory. The simplest controlled system to behave as a damped oscillator is a second order system with complex poles. Therefore, the poles are $s_0^{\pm} = \lambda \pm \omega = \zeta\omega_n \pm \omega_n\sqrt{\zeta^2-1}$

where the natural frequency of the oscillator, $\omega_n$, and the dimensionless damping ratio, $\zeta$, are defined by $\omega \equiv \omega_n\sqrt{1-\zeta^2}$ and $\lambda \equiv \zeta\omega_n$ [177]. The gain of the transfer function at complex frequency $s$ is then

$$G(s) = \frac{A\omega_n^2}{s^2 + 2s\zeta\omega_n + \omega_n^2}. \tag{4.53}$$

Applying these definitions to equation 4.52, we find the frequency shift is

$$\Delta\nu_{\text{clock}} \approx -2\frac{G(s')}{\omega_n T^2} \;\; \rightarrow \;\; -2\frac{G(0)}{\omega_n T^2}\cos\phi \text{ as } \zeta \rightarrow 1, \tag{4.54}$$

where $s'$ are the solutions of $(s'-s_0^+)(s'-s_0^-) = \omega_n^2/\cos\left(\phi + \cos^{-1}(\zeta)\right)$. The limit assumes that the servo is close to critically damping the oscillation. Equation 4.54 shows that there is a limit to the ability to servo out the phase oscillation based on the natural frequency of the resonance and the DC loop gain required to perform adequate phase noise cancellation. For the experimental data, $G(0) = 1.6$, $\omega_n = 2\pi \times 15$ kHz, and $\zeta = 0.39$. Despite the poor fit of $\zeta$ to the critical damping limit, equation 4.54 still accurately recovers a phase error of $8.4 \times 10^{-20}$.

Since the phase error is not static, it will add instability to the clock servo in the form of white-FM. We can compute the maximum contributed fractional instability, $\sigma_{\text{clock}}$, as the standard error with the assumption that the initial phase error is drawn randomly from between $-\pi$ and $\pi$, finding that

$$\begin{aligned}
\sigma_{\text{clock}} \text{ at } 1\text{ s} &= \frac{1}{\nu_{\text{clock}}\sqrt{R \times 1\text{ s}}}\sqrt{\langle(\Delta\nu_{\text{clock}})^2\rangle - \langle\Delta\nu_{\text{clock}}\rangle^2} \\
&= 2\frac{G(0)}{\omega_n T^2}\frac{1}{\nu_{\text{clock}}\sqrt{R \times 1\text{ s}}} \times \sqrt{\int_{-\pi}^{\pi}\cos^2\phi\, d\phi - \left(\int_{-\pi}^{\pi}\cos\phi d\phi\right)^2} \\
&= 2\sqrt{\pi}\frac{G(0)}{\omega_n T^2}\frac{1}{\nu_{\text{clock}}\sqrt{R \times 1\text{ s}}},
\end{aligned} \tag{4.55}$$

where $R$ is the clock cycle rate (about 1 Hz for the portable clock). Therefore, the additional instability introduced is only a potential issue for clocks where the uncertainty from the AOM phase chirp is of the same order as the local oscillator (LO) instability. For a poorly performing LO, this is a possibility since short spectroscopy times will greatly exacerbate the phase chirp uncertainty leading to an instability compounding effect.

For completeness, we give the same treatment as above to Ramsey spectroscopy with an interaction time $t_i$ and dark time $T_d$. The phase sensitivity for Ramsey spectroscopy may be written as [175, 176]

$$\frac{dg(t)}{dt} = \begin{cases} \frac{\pi}{2t_i}\cos\left(\frac{\pi t}{2}\frac{t}{t_i}\right) & \text{for } 0 \le t < t_i, \\ 0 & \text{for } t_i \le t < t_i + T_d, \\ \frac{\pi}{2t_i}\sin\left(\frac{\pi}{2}\frac{(t-T_d)}{t_i}\right) & \text{for } t_i + T_d \le t < T_d + 2t_i. \end{cases} \tag{4.56}$$

Only the first element of the piece-wise function is sensitive to transient phase chirps at the beginning of the pulse. Assuming a damped oscillation as in 4.49 and performing the same sort of integration as in 4.50, we recover a fractional frequency change of

$$\begin{aligned} \Delta\nu_{\text{clock}} &\approx -0.3136\frac{A}{t_i T_d\sqrt{\lambda^2+\omega^2}}\cos\left(\phi + \tan^{-1}\left(-\frac{\omega}{\lambda}\right)\right) \\ &\to \; -0.3136\frac{G(0)}{\omega_n t_i T_d}\cos\phi \text{ as } \zeta \to 1 \end{aligned} \tag{4.57}$$

where in the second step, we followed an identical control theory analysis as for Rabi spectroscopy. Ramsey spectroscopy then has a lower coefficient of sensitivity than Rabi spectroscopy exhibits in 4.54, but since $T_d \gg t_i$ this shift can be expected to scale more adversely than in Rabi spectroscopy. Likewise, we can calculate the instability from AOM phase chirp in Ramsey spectroscopy to be

$$\sigma_{\text{clock}} = 0.3136\sqrt{\pi}\frac{G(0)}{\omega_n t_i T_d}\frac{1}{\nu_{\text{clock}}\sqrt{R \times 1\text{ s}}}. \tag{4.58}$$

A reasonable Ramsey spectroscopy sequence for the portable clock with a 5 ms interaction time and 560 ms dark time would have eighteen times higher instability and inaccuracy from phase chirp, putting this uncertainty term above the $1 \times 10^{-18}$ level. This contribution to uncertainty and instability from short pulses is a factor that makes Ramsey spectroscopy in optical lattice clocks relatively more difficult than Rabi spectroscopy; as a result the majority of operational lattice clocks use Rabi spectroscopy.

Equation 4.54 demonstrates a scaling law that heavily penalizes short spectroscopy times with high uncertainties from the phase chirp. The 8 ms pulse we used at the US

Naval Observatory for our long dataset would have contributed a $4 \times 10^{-16}$ uncertainty and $1.2 \times 10^{-15}$ instability at 1 s (half of the LO noise!) if the phase chirp profile were the same as observed here. The uncertainty scaling might also impose a significant technical challenge for reaching $< 1 \times 10^{-18}$ uncertainties in optical clocks with comparatively short excited state lifetimes such as neutral thulium ($\tau = 112$ ms) [178] and indium ions ($\tau = 195$ ms) [179].

If we need to operate with a shorter spectroscopy time in the future, equation 4.54 shows that the most straightforward way to improve the systematic is servo optimization. However, if this capability has been taken to its limit, several methods are available that could suppress both the uncertainty and instability from this effect. The method used by the lab clocks is to prestabilize the light before tuning it to resonance. They turn on the clock light several hundred kHz from resonance to let the servo engage before a rapid linear frequency ramp to the target frequency. This technique trades phase chirp for a very small amount of frequency chirp as the laser-atom interaction turns on while being brought into resonance. If the spectroscopy time available to us with a future portable cavity is low, then we may need to use this approach. An important caveat though, is that the Artiq control system does not permit smooth frequency ramps since the DDS outputs at a quantized frequency and has some finite update rate. The trick, then, will be to find a sweep rate and number of steps such that the phase servo does not unlock from an excessive step size. Another possible technique to suppress the effect of the phase chirp is to turn the clock light on low power and wait for it to phase-stabilize before turning it up to full power. This technique is inferior to frequency ramping because the signal for the servo scales linearly with optical power while Rabi frequency scales with the square root of optical power. The result is that one will run out of signal to operate the phase lock long before the phase chirp is significantly suppressed. Additionally, the servo gain, scaling with input signal will be time-varying absent some additional correction. For clocks that only permit sub-millisecond pulse times such as the proposed cesium lattice clock [180, 181], more sophisticated techniques may be required such as continuously supplying far-detuned clock light with high bandwidth phase noise suppression that is then turned on resonance with a fast out-of-loop EOM for lock-in detection. Alternative "hyper Ramsey" interrogation sequences that lead to phase chirp cancellation are also a possibility for full cancellation of the phase chirp effect and are discussed in [175]. Yet another technique to cancel the phase chirp is to record the error signal from the first half of the Rabi pulse and play that error, time-reversed, into the loop bias during the second half of the pulse where the atomic response has the opposite sign.

### 4.5.3 Servo Error

The local oscillator drifts in a way that is largely linear on the timescale of a typical measurement run. This drift could potentially cause a frequency offset since sequential probing of the different detunings required to generate an error signal gives the local oscillator frequency time to evolve relative to the atomic transition. We use several methods to suppress the potential frequency offset. First, we use an AOM and a direct digital synthesizer with $\mu$Hz resolution to provide feed-forward cancellation of the drift below 500 $\mu$Hz $s^{-1}$. When using the laboratory local oscillator, this is done by updating the "Drifty" program in 1G104. Second, we probe the points used to generate the error signal alternately in ascending and descending frequency order. If there is an offset from linear drift we are alternately adding and subtracting the offset as we probe the points in the opposite directions. Third, we use a digital $I^2$ lock to the atomic transition in the Artiq FPGA which suppresses linear drifts. It is known that the cavity has quadratic and long period drifts in it's frequency, but these effects are on long time scales relative to typical measurements and are much smaller than the linear drift. While an $I^2$ loop is not an optimal Kalman filter to eliminate offsets from higher order and cyclical effects, these effects are nearly negligible [182].

The in-loop error signal from the atomic excitation can also be used to measure the ability of the loop to subtract frequency offsets. First, the error signal must be converted into a detuning error, $\delta_{\text{error}}$, which will be treated in frequency units. At the $\pi$ pulse time, when the laser frequency detuning from resonance, $\delta$, is swept, then the excitation fraction,

$P$, traces out the Rabi line shape

$$\mathrm{P}(\delta) = P_{\mathrm{max}}\Omega^2 \left(\frac{1}{\Omega^2 + 4\pi^2\delta^2}\right) \left(\sin\left(\frac{\sqrt{\Omega^2 + 4\pi^2\delta^2}\pi}{2\Omega}\right)\right)^2 \tag{4.59}$$

where $\Omega$ is the Rabi frequency in angular frequency units and $P_{\mathrm{max}}$ is the maximum contrast [183]. For a $\pi$ pulse, $\Omega = \pi/T$, and we typically operate with a $T = 560$ ms spectroscopy time. From here I will develop two different approaches to recovering a frequency correction from excitation difference and then show that they are numerically equivalent with the example of our experimental parameters.

At this point, we need to separate the detuning from frequency error due to local oscillator noise or drift, $\delta_{\mathrm{error}}$, and the intentional detuning from probing on opposite sides of the Rabi line shape for error signal generation that we call, $\delta_{\mathrm{dev}}$ or "dev" in our control program. We will consider derivatives with respect to $\delta = \delta_{\mathrm{error}}$ to find the response to frequency error, but evaluate these derivatives at $\delta = \delta_{\mathrm{dev}}$ where we have the set clock laser for probing. The derivative of the response of the excitation fraction to detuning noise is

$$\frac{d\mathrm{P}(\delta_{\mathrm{dev}})}{d\delta_{\mathrm{error}}} = 2P_{\mathrm{max}}\pi^2 y\Omega \left(\frac{2\Omega(-1 + \cos\left(\frac{\pi\sqrt{4\pi^2\delta_{\mathrm{dev}}^2+\Omega^2}}{\Omega}\right))}{(4\pi^2\delta_{\mathrm{dev}}^2 + \Omega^2)^2} + \frac{\pi\sin\left(\frac{\pi\sqrt{4\pi^2\delta_{\mathrm{dev}}^2+\Omega^2}}{\Omega}\right)}{(4\pi^2\delta_{\mathrm{dev}}^2 + \Omega^2)^{3/2}}\right) \tag{4.60}$$

when measured at $\delta_{\mathrm{dev}}$. The first order frequency correction, $\delta^{(1)}_{\mathrm{error}}$, from probing both sides of the line shape is then

$$\delta^{(1)}_{\mathrm{error}}(\Delta\mathrm{P}) = \frac{\Delta\mathrm{P}}{2 \times \frac{d\mathrm{P}(\delta_{\mathrm{dev}})}{d\delta_{\mathrm{error}}}} \tag{4.61}$$

where $\Delta\mathrm{P}$ is the measured difference in excitation fraction between both sides of the line shape, which is the natural linear gain from spectroscopy. While the gain is dominated by the linear term as should be the case for a simple feedback servo, the Rabi line shape has curvature and higher order terms should be considered. Since the line shape is a symmetric function, the error signal from it will only include antisymmetric terms. Moreover, since the value of $\Delta\mathrm{P}$ is constrained to the domain between $-P_{\mathrm{max}}$ and $P_{\mathrm{max}}$, the effects of terms at

$\mathcal{O}(\Delta\text{P})^5$ and beyond is relatively small. The next term is the cubic correction, which takes the form

$$\delta^{(3)}_{\text{error}}(\Delta\text{P}) = \frac{(\Delta\text{P})^3}{2 \times \frac{d^3\text{P}(\delta_{\text{dev}})}{d\delta^3_{\text{error}}}} \tag{4.62}$$

where computing the third derivative of $P(\delta_{dev})$ is left to computational tools. Then, the frequency error is

$$\delta_{\text{error}} = \delta^{(1)}_{\text{error}} \times \Delta\text{P} + \delta^{(3)}_{\text{error}} \times (\Delta\text{P})^3 + \mathcal{O}(\Delta\text{P})^5 \tag{4.63}$$

where I have redefined $\delta^{(N)}_{\text{error}}$ as coefficients. Additional terms can be calculated in the same pattern as the third order term but add frequency correction contributions of $< 0.2\%$ in the excitation difference region $|\Delta\text{P}| < 30\%$ that our stability normally keeps the system.

Another method, which may be more computationally feasible in certain software applications, involves determining the coefficients for the frequency error by approximating the function using a power series expansion based on the measured excitation difference. The Taylor expansion of the Rabi line shape is given by

$$\text{P}(\delta) \approx P_{\max} \times \left[1 - \frac{4\pi^2}{\Omega^2}\delta^2 + \frac{\pi^4}{\Omega^4}(16 - \pi^2)\delta^4 + \mathcal{O}\delta^6\right] \tag{4.64}$$

where taking more terms would increase the accuracy of later computations. The difference between the excitation fractions, $\Delta\text{P} = \text{P}(\delta_{\text{error}} + \delta_{\text{dev}}) - \text{P}(\delta_{\text{error}} - \delta_{\text{dev}})$, is again the quantity we use to compute the frequency correction. The similarity of this expression to the limit definition of the derivative underlies why this approximate method will give the same result as the previous derivative method. $\Delta\text{P}$ will be an expression in odd powers of $\delta_{\text{error}}$ since only the cross terms from $(\delta_{\text{error}} \pm \delta_{\text{dev}})^{2N}$ will not be subtracted out. Since $\Delta\text{P}$ is also power series, it can be inverted to a power series representation of $\delta_{\text{error}} = \Sigma_i a_i(\Delta\text{P})^i$ with coefficients $a_i$ using the Lagrange inversion theorem [184]. Using only the first two terms in the prior expansion of $\text{P}(\delta)$, the series representation of the frequency error is

$$\begin{aligned}\delta_{\text{error}} = &\frac{-\Omega^4}{(8\ P_{\max}\ \delta_{dev}\pi^2)[\pi^2\delta^2_{dev}(\pi^2 - 16) + 2\Omega^2]} \times \Delta\text{P} \\ &- \frac{(\pi^2 - 16)\Omega^{12}}{(512\ P^3_{\max}\ \delta^3_{dev})\left[\pi^3(\pi^2 - 16)\delta^2_{dev} + 2\pi\Omega^2\right]^4} \times (\Delta\text{P})^3 + \mathcal{O}(\Delta\text{P})^5\end{aligned} \tag{4.65}$$

Figure 4.27: The solid blue line shows the linear term of frequency correction as a function of excitation difference for a single peak when probed with Rabi spectroscopy for our spectroscopy conditions. The linear term is dominant throughout the range for which the correction is defined. The frequency correction including the third order term is shown as a dashed orange line and its inclusion slightly improves the ability of the servo error Allan deviation to average down at long times. Without inclusion of this term the Allan deviation in Fig. 4.28, would more clearly shift to averaging as white-FM at the $3 \times 10^{-19}$ level. Inclusion of the fifth order term, $-0.019 \times (\Delta \mathrm{P})^5$, shown as the gray dotted line, makes nearly no change to the frequency correction.

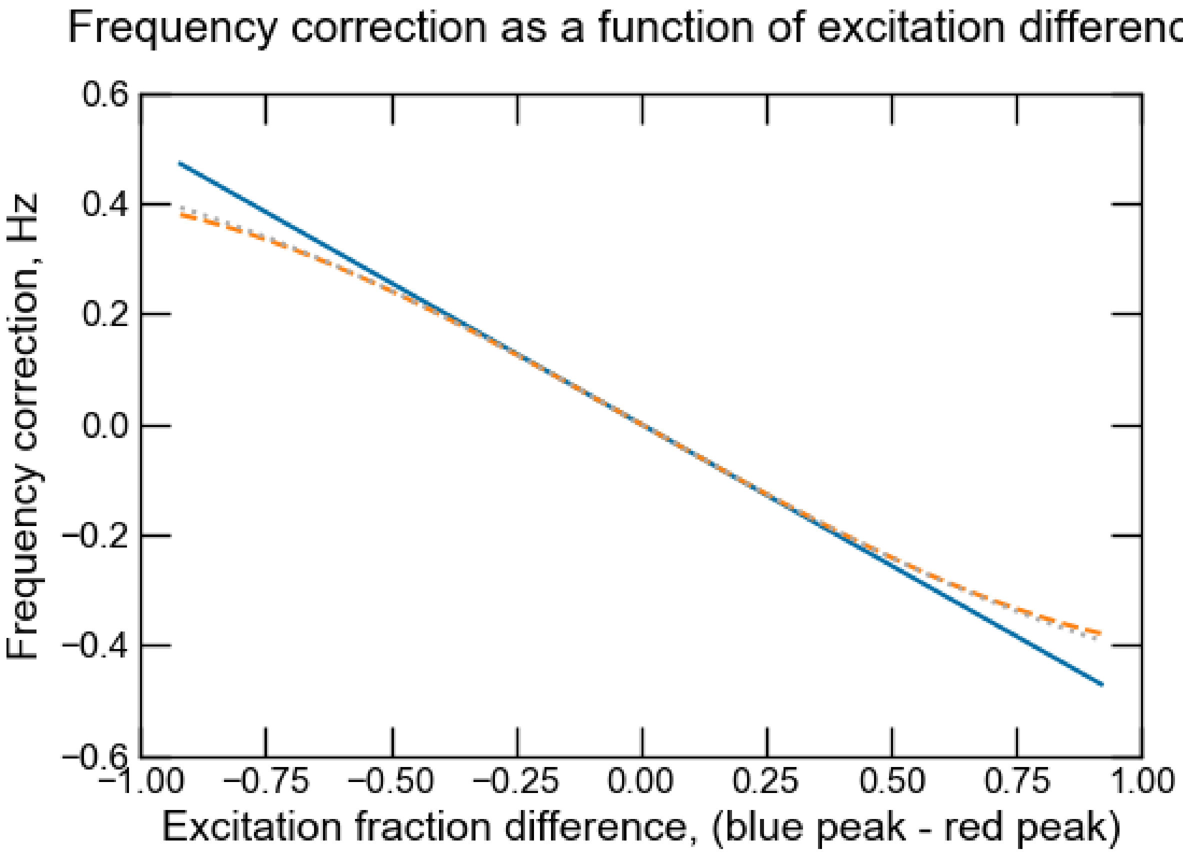

however, more terms (usually to $\delta^8$) from the first expansion, as could be supplied in computational software, are required for convergence with the derivative result.

When our operational values are used in both representations of the frequency correction, we obtain the numerical formula

$$\delta_{\text{error}} = \left(-0.528\Delta\text{P} + 0.118(\Delta\text{P})^3\right)\ \text{Hz} \tag{4.66}$$

which can then be applied to the measured excitations in a dataset to convert them to frequencies. Note that since we use a four point lock with the two Zeeman sublevels, this gain will need to be divided by a further factor of two when applied to the composite error signal. We demonstrate this by analyzing the in-loop atomic excitation error signal during a 220,000 s measurement. This example measurement was from a lattice stark shift comparison. This overlapping Allan deviation measurement is shown in Fig. 4.28 where the noise averages like white phase noise for the first 10,000 s. The error signal was consistent with zero at the $< 5 \times 10^{-20}$ level which we take as the uncertainty from servo error.

### 4.5.4 Line Pulling

Off resonant excitation of the radial sidebands, $\sigma_\pm$ transitions, and $\pi$ transitions (from the spin-impure population) produces a systematic shift from line-pulling. First, we consider the fraction of the excited state population driven by off-resonant excitation. This fraction has a distorting effecting on the error signal from the near-resonant Rabi line shape. Using equations 4.59 and its derivative 4.60, we compute the fractional frequency error $\delta_{\text{OR}}$ from off-resonant excitation

$$\delta_{\text{OR}}(\nu_{\text{clock}}) = \frac{\text{P}_{\text{OR}}(\nu_{\text{OR}} - \nu_{\text{clock}},\ P_{\text{OR, max}},\ \Omega_{\text{OR}})}{\frac{d\text{P}_R(\nu_{\text{R}} - \nu_{\text{clock}}, \Omega_{\text{R}})}{d\nu_{\text{clock}}}}, \tag{4.67}$$

where $\nu_{\text{clock}}$ is the clock laser frequency, $\nu_{\text{OR}}$ is the frequency where the Rabi maximum of the off resonant excitation occurs, $P_{\text{OR, max}}$ is the maximum excitation probability of the off-resonant excitation, and $\Omega_{\text{OR}}$ is the Rabi frequency of the off-resonant peak, $\nu_{\text{R}}$ is the

Figure 4.28: An Allan deviation from an individual lattice light shift comparison where the two clock measurement is shown as blue squares which has a white-FM fit shown as a blue line and the in-loop error signal is shown as orange diamonds which has a white-PM fit shown as a dashed orange line. This measurement exemplifies the ability of the clock to run for long periods (221,000 s) without operator intervention.

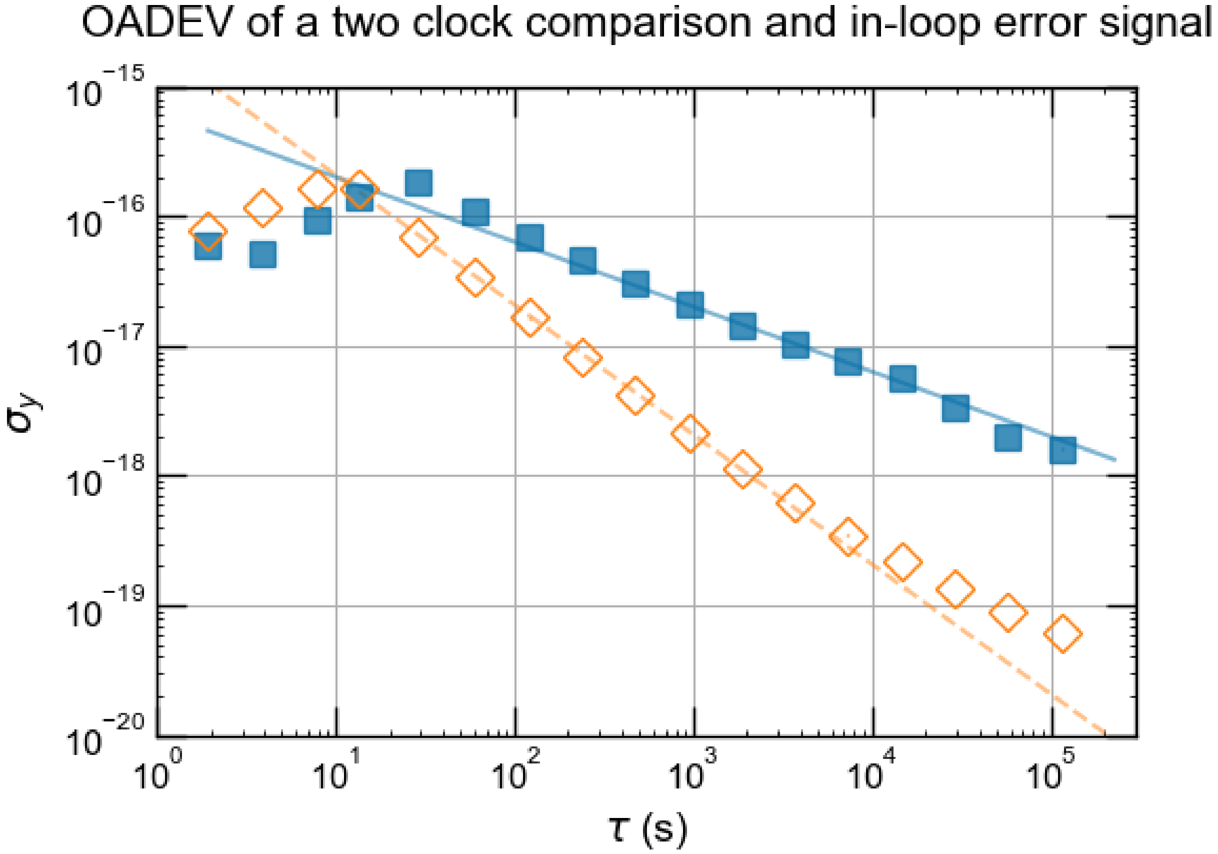

frequency where the Rabi maximum of the intended resonant excitation occurs, and $\Omega_{\mathrm{R}}$ is the Rabi frequency of the resonant excitation. Off-resonant excitations are suppressed not only by their detuning but also by the low amplitudes and Rabi frequencies of the off-resonant transitions. Spin-pure state preparation suppresses the amplitudes of the nearest $\pi$ and $\sigma$ transitions. Alignment of the clock laser to the lattice couples the clock laser only weakly to radial motion and lowers the Rabi frequency of this nearby transition.

The radial and axial sidebands, which have inhomogeneously broadened linewidths, $\Gamma_{\mathrm{OR}}$, have their shift enhanced by a factor of $(\nu_{\mathrm{OR}} - \nu_{\mathrm{clock}})^2/\Gamma_{\mathrm{OR}}^2$. Symmetry will nearly eliminate the shift from radial sidebands, however we conservatively assume there is only one radial sideband to maximize this shift. For the antisymmetric cases of off-resonant $\pi$ and $\sigma$ transitions, the shift will be reduced mostly to a magnetic correction at the 50 nHz level which does not significantly affect the second order Zeeman correction. However, these transitions could create a frequency shift if the contrast of the two peaks were imbalanced. Therefore, we multiply the single line shift of the $\pi$ transition by a worst case estimate of the line contrast at 5% (usually it is $< 1\%$) between the two $\pi$ transitions. We also consider the effect of the Fourier component of the clock light since it is driven for a finite amount of time. This calculation will not be treated in detail here, because it results in a shift $\approx 10^{-3}$ of the primary line pulling shift at our spectroscopy time.

We measured the detunings, amplitudes, and Rabi frequencies of the off-resonant excitations and calculated their contributions to line-pulling. The results of the calculations with the above considerations are shown in Table 4.9. The more closely detuned radial sidebands dominate the line-pulling shift. However, parallel alignment of the clock laser to the lattice was measured to suppress the Rabi frequency of the radial sideband to be $< 3 \times 10^{-3}$ of the Rabi frequency of the clock transition. An alignment technique that interleaves between resonant clock excitation to keep the clock Rabi frequency high and resonant radial sideband excitation to suppress this excitation might be expected to suppress this effect even further. The residual shift from line-pulling is conservatively assessed to have a maximum value of

$1 \times 10^{-20}$. This effect will scale adversely with shorter $\pi$ pulse times, likely with $1/T^2$ scaling since the linewidths of both the targeted and off resonant transitions will scale with spectroscopy time, but we have not worked out the details of that calculation since this shift is very small.

| Spectral feature | Detuning, Hz | $\frac{\Omega_{OR}}{\Omega_R}$ | $\frac{P_{\text{OR, max}}}{P_{\text{R, max}}}$ | Line pulling | Fourier pulling |
|---|---|---|---|---|---|
| Radial sidebands | 120 | $< 3 \times 10^{-3}$ | .5 | $4 \times 10^{-23}$ | $6 \times 10^{-25}$ |
| Axial sideband | 30,000 | $< 0.1$ | .5 | $5 \times 10^{-24}$ | $5 \times 10^{-26}$ |
| Opposite $m_F$ $\pi$ | 560 | 1 | $< .01$ | $3 \times 10^{-24}$ | $7 \times 10^{-27}$ |
| Same $m_F$ $\sigma$ | 1800 | 1 | 1 | $4 \times 10^{-23}$ | $3 \times 10^{-26}$ |
| Opposite $m_F$ $\sigma$ | 1250 | 1 | $< .01$ | $1 \times 10^{-24}$ | $1 \times 10^{-27}$ |

Table 4.9: Calculated effects of line pulling and the line pulling from an off-resonant Fourier component of the pulsed clock laser electric field. Both line pulling shifts are in fractional frequency units of the clock frequency. The off resonant Rabi frequencies are in proportion to the resonant $\pi$ transition Rabi frequency that we are intentionally exciting. Similarly, the amplitudes og the off resonant excitation given by the probability maxima are in proportion to the contrast of the resonant $\pi$ transition.

## 4.6 Relative Geopotential

For comparisons of distant clocks, the gravitational redshift can be the largest measurement shift, whereas in relative comparisons of nearby clocks the redshift is largely subtracted in common-mode. For the lab clock, Yb1, previous spirit-leveling measurements found a height difference of 743.3(2) cm from the NIST Yb1 in-lab geodetic marker (811G104) relative to USGS marker Q407. The height of Yb1 from the lab marker was 142.0(2) cm [33]. The geodetic marker of the nearby transportable clock lab (811G108) was recently surveyed to be at a height of 742.4(2) cm relative to Q407 [185]. We verified independently with a laser leveling device that the nearby labs have a $\approx 1$ cm drop between them. The same laser level was used to measure the height of the center line of the portable clock's spectroscopy chamber relative to the marker at 106.15(20) cm, and a camera verified that the lattice fluoresced in the vertical center of the chamber. The total gravitational redshift of the transportable clock system at NIST relative to the International Terrestrial Reference Frame was $180,736(6) \times 10^{-18}$. However, the relative geopotential redshift of the transportable system relative to Yb1 was constrained to $-40.1(4) \times 10^{-18}$ since the proximity of Yb1 enabled measuring that its atomic sample is higher than the portable clock's sample by 36.8(4) cm. To our great regret, we do not account for the either the effects of super-galactic gravitational structure which accounts for a roughly $3 \times 10^{-6}$ fractional frequency redshift [186] (about 5000 times greater than the total redshift from Earth on its surface) or the special relativistic effect of the sun's rotation about the galaxy core at $10^{-4}c$ resulting in a $10^{-7}$ shift. Development of a Universal timescale with $10^{-18}$ accuracy will have to wait.

## 4.7 Uncertainty Conclusion

Combining all of the previous uncertainties in quadrature, we claim a final uncertainty evaluation of $3.7 \times 10^{-18}$, a new record for portable clock performance. At this level of accuracy, the NIST portable Yb OLC is capable of making comparative measurements necessary towards redefinition of the SI second. This level of accuracy is not quite at the level needed to outperform the best classical geodetic techniques, but it is close and we hope that with the improvements discussed in the next chapter, the clock will reach that level of performance. Given generous assumptions about possible up times for the clock, we present a time deviation plot (TDEV) detailing the performance of the NIST transportable Yb OLC compared to other timekeeping systems in Figure 4.29.

The total shift from the prior uncertainty budget is $-2663.4 \times 10^{-18}$ indicating our ability to measure and control the systematic shifts on the clock transition at the part per thousand level. This is not the exact shift that will subtracted from the clock in operation. The BBR, second order Zeeman, and cold collision shifts are based on parameters that are comparatively unstable (temperature, local magnetic field, and atom number) which necessitates their correction. Generally, this correction is done in post-processing for a comparison. However, with the capabilities of our Artiq control unit, we could potentially compute these corrections in real time for a continuously high-accuracy time base. Geodetic effects will have to be corrected every time the clock is moved.

Figure 4.29: The TDEV of the NIST portable Yb optical lattice clock and many other clocks. The legend is in descending order of TDEV at one second.

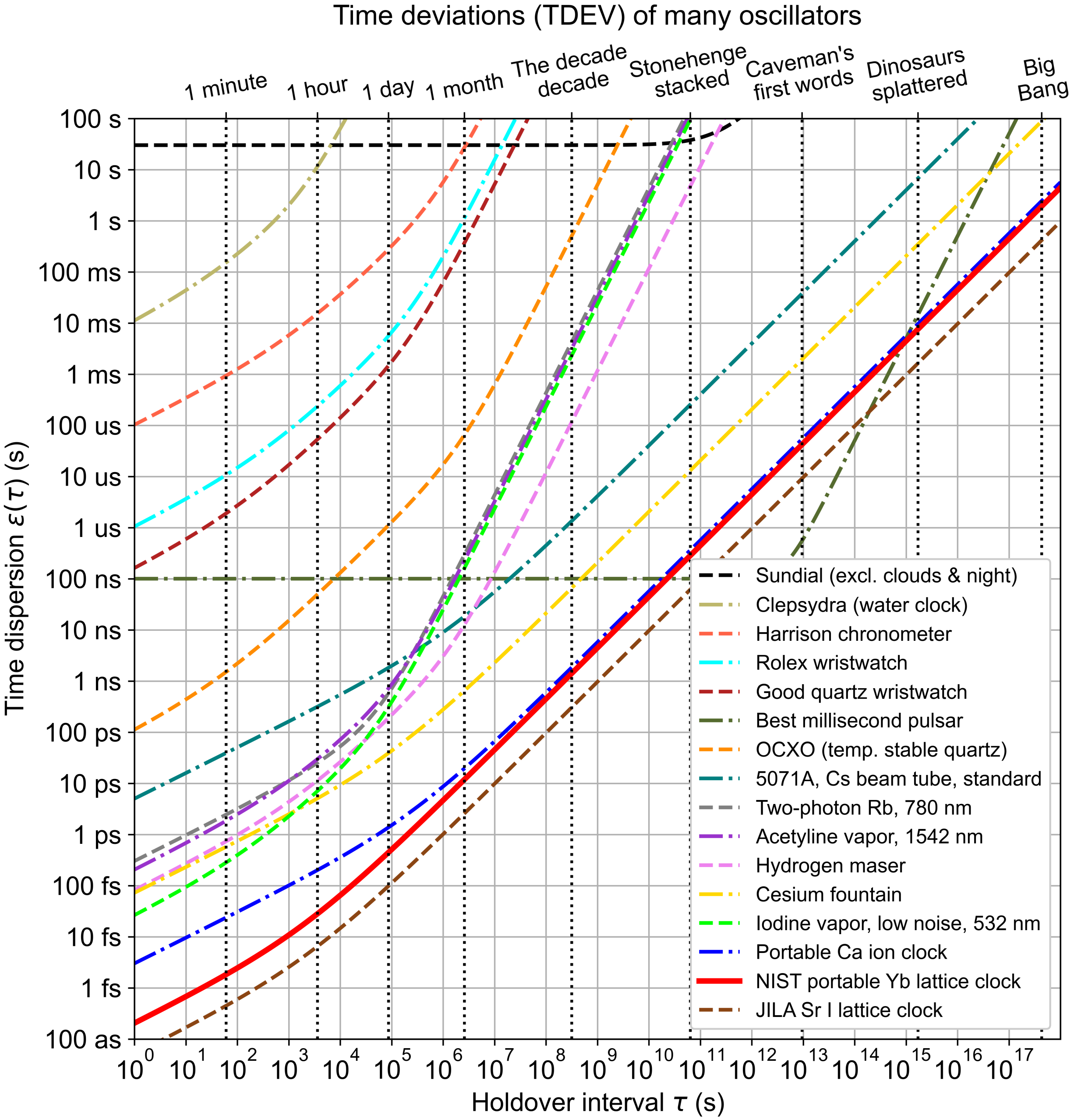

# Chapter 5

# Outlook

The outlook for the NIST transportable Yb lattice clock will be divided in two sections: upgrades to the clock system to further improve accuracy and stability and future experimental goals using the mobility and accuracy of the clock.

## 5.1 Upgrades

The primary focus of our next round of improvements to the transportable clock system will be focused on the clock laser module. These upgrades will be focused on both the clock laser itself and the ultrastable reference cavity. One design goal is to develop an all-fiber clock laser system to avoid having another bulky free space tapered amplifier laser. We are in the process of testing an 1156 nm Yb:Fiber DFB laser with 10 mW output for suitability as a clock laser. If it is found to have acceptable phase noise performance, then a full clock laser system will be built around it. The DFB seed laser will be configured to have the option to either be PDH locked to a local cavity reference or offset phase-locked to a remote stable laser. The DFB laser will seed a semiconductor optical amplifier and will be frequency doubled to 578 nm. The 578 nm clock light will be controlled by Artiq and capable of being switched between off, to a high power sideband cooling/spectroscopy arm, and to a phase-stabilized path to the lattice retroreflector with a fiber-coupled AOM and switch. The entire clock light generation system will be inside a temperature-stabilized box with acoustic isolation to suppress phase noise.

The cavity will receive upgrades both in the vacuum chamber and mounting. Figure 5.1(b) shows a test set up of precision machined plastic spacers that are hoped will improve the reproducibility of the cavity acceleration sensitivity. Tests will be done with a depth micrometer to confirm repeatable mounting of the cavity within the positional tolerances of the model used to design the cavity [3]. Additional tests on an improved flip table structure will measure the acceleration sensitivity of the cavity. We have also received a new aluminum vacuum chamber, Figure 5.1(c), with three layers of in-vacuum thermal shields to suppress the effects of temperature fluctuations on the cavity. Active random amplitude modulation (RAM) suppression will also be added to the PDH configuration. We hope that between these upgrades, the cavity can perform closer to its design thermal noise floor at $2 \times 10^{-16}$ at 1 s.

Upgrades for the atomic system will seek to suppress the dominant systematic shift uncertainties even further. We plan to implement features such as Sisyphus cooling with the clock transition to cool the atomic sample to below the ${}^1S_0 \rightarrow {}^3P_1$ Doppler limit [174, 187, 188]. Atomic temperatures at $< 500$ nK in both axial and radial directions will allow clock operation at even lower trap depths, which is the most straightforward way to suppress the lattice Stark shift. Switching to a completely vertically oriented lattice might also further increase the range of usable trap depths. Additionally, operating the portable clock in an identical atomic temperature regime as the NIST Yb1 and Yb2 lab clocks, which use enhanced cooling methods, will enable us to better use their precise characterizations of the lattice Stark shift. To reduce the BBR shift, we are building a second vacuum chamber apparatus with water cooling to actively stabilize the oven and quadrupole coils. Suppression of temperature gradients on the chamber to below the 15 mK level will further constrain the uncertainty of the BBR environment to the dynamic correction uncertainty limit which is just below the $10^{-18}$ level. Various atomic means of improving other systematics are under consideration [189, 190].

Figure 5.1: Upgrades in progress for the portable clock. **(a)** A set of water-cooled quadrupole coils on a test rig with a second titanium chamber. Water cools a copper plate that sits between the coils and the chamber setting a thermal boundary condition to suppress coil driven gradients on the chamber. The coils themselves are adhered to a second water cooled plate with a conductive epoxy for extracting most of the heat that the coils generate. **(b)** A metal dummy cavity is used to test precision mounting pieces so that the cavity can be secured in a repeatable manner. **(c)** The full cavity vacuum chamber includes three layers of thermal shields to suppress the effect of room temperature fluctuations on the cavity.

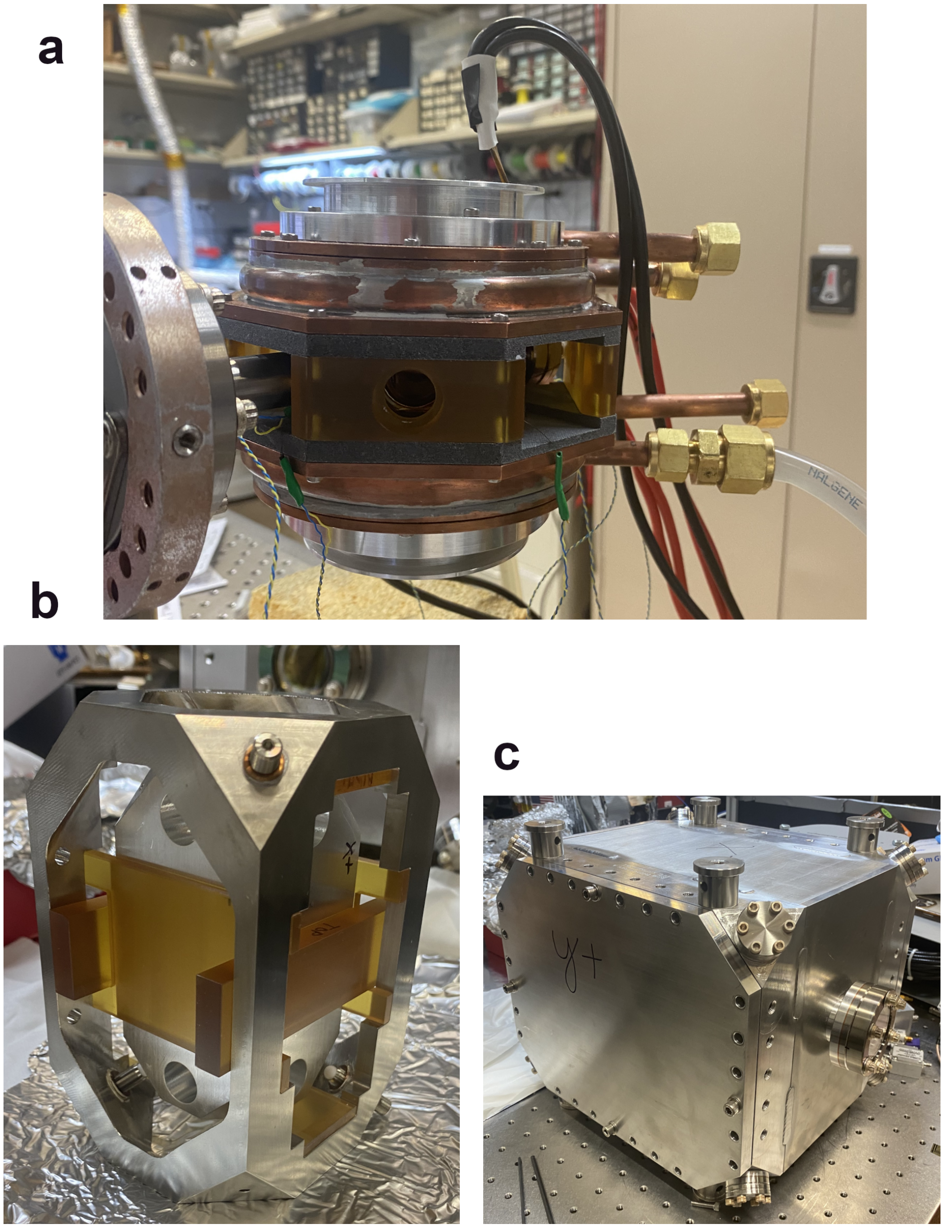

## 5.2 Future Experiments

In the next few months, we intend to validate the uncertainty budget presented here with a measurement campaign comparing the portable clock to one or both of the laboratory clocks. We will use the shared light from the laboratory ultrastable cavity for a direct comparison. Electrical connections have already been made for synchronous comparison which reduces averaging time by making the clock laser noise common mode to the atomic systems. Multiple comparisons will be made to demonstrate the reproducibility of the clock.

Next, we will validate the performance of the clock when operated remotely. We will ship the atomic system to CU Boulder in the same way as described in chapter 3. 200 $\mu$W of cavity-stabilized light will be delivered from the NIST clock laser system by phase-noise cancelled optical fiber to a lab at CU Boulder. This light will be used to phase-lock the new transportable all-fiber clock light generation system. We will check for consistency of the cold-collision shift at CU in traps at both 70 $E_r$ and 150 $E_r$, since this shift can be sensitive to the details of the temperature and alignment to the lattice. We will then make another direct comparison between the clock frequencies with the aim of demonstrating a shift consistent with the difference in geopotential between the locations.

Contributions to international timekeeping would also further the portable clock's goals of contributing to the redefinition of the SI second. The portable clock's high uptime makes it suitable for comparison to international atomic time (TAI) through NIST's exiting TWSTFT infrastructure. Other comparisons to frequency standards, either regionally or internationally, are also likely in the future as part of our SI redefinition efforts.

The experiment that we most eagerly anticipate is a geodetic measurement with the portable clock at the top of Mt Blue Sky, one of the 14,000 foot peaks of Colorado. In this collaboration with the groups of Diddams, Sinclair, and Van Westrum, we will use optical free space time and frequency transfer techniques [50, 56, 52] to compare the frequencies of the lab and portable clocks. As shown in 5.2, the clock will be based in an astronomical observatory and use a two-way composite frequency link that switches between free space and fiber frequency transfer. This measurement will be a difficult one to make, requiring robustness of all systems at high altitude and high uptime of every component to permit averaging down to the low $10^{-18}$ level during the windows of cooperative weather conditions.

Figure 5.2: A major experimental goal is to compare the portable clock to the lab-based clocks from the top of Mt Blue Sky in Colorado. Comparing clocks with a nearly 3000 m height difference will result in a $3 \times 10^{-13}$ shift from geopotential. A clock with $< 2 \times 10^{-18}$ uncertainty would be capable of resolving the height difference more accurately than classical geodetic techniques. Image from the Blue Sky collaboration.

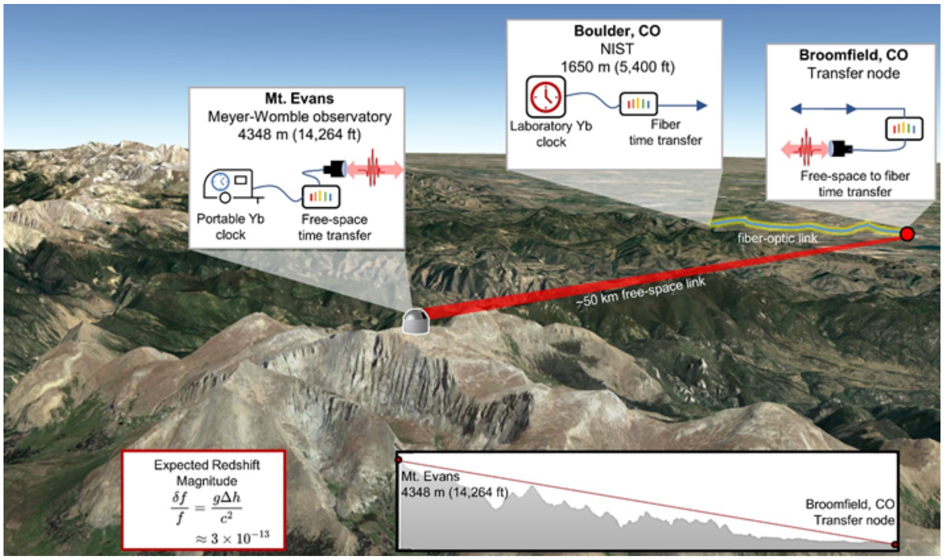

This thesis demonstrates both the high accuracy of the NIST transportable optical lattice clock system and the robustness of our system in transport. These two key qualities enable the clock to move $10^{-18}$ timekeeping outside of the lab.

# Bibliography

[1] Online Alarm Clock. The world's most accurate clocks, 2015. Accessed: 2024-04-22.

[2] Andrew D. Ludlow, Martin M. Boyd, Jun Ye, E. Peik, and P. O. Schmidt. Optical atomic clocks. Rev. Mod. Phys., 87:637–701, Jun 2015.

[3] R. J. Fasano. A Transportable Ytterbium Optical Lattice Clock. PhD thesis, University of Colorado, 2022.

[4] M. Takamoto, Y. Tanaka, and H. Katori. A perspective on the future of transportable optical lattice clocks. Applied Physics Letters, 120(140502), 2022.

[5] Markus Gellesch, Jonathan Jones, Richard Barron, Alok Singh, Qiushuo Sun, Kai Bongs, and Yeshpal Singh. Transportable optical atomic clocks for use in out-of-the-lab environments. Advances in Optical Technologies, 9(5):313–325, 2020.

[6] Martin Vermeer. Chronometric levelling. Suomen Geodeettinen laitos, 1983.

[7] Guillaume Lion, Isabelle Panet, Peter Wolf, Christine Guerlin, Sébastien Bize, and Pacôme Delva. Determination of a high spatial resolution geopotential model using atomic clock comparisons. Journal of Geodesy, 91(6):597–611, 2017.

[8] Ruxandra Bondarescu, Andreas Schärer, Andrew Lundgren, György Hetényi, Nicolas Houlié, Philippe Jetzer, and Mihai Bondarescu. Ground-based optical atomic clocks as a tool to monitor vertical surface motion. Geophysical Journal International, 202(3):1770–1774, 2015.

[9] Heiner Denker, Ludger Timmen, Christian Voigt, Stefan Weyers, Ekkehard Peik, Helen S Margolis, Pacôme Delva, Peter Wolf, and Gérard Petit. Geodetic methods to determine the relativistic redshift at the level of $10^{-18}$ in the context of international timescales: a review and practical results. Journal of Geodesy, 92:487–516, 2018.

[10] J Grotti, I Nosske, SB Koller, S Herbers, H Denker, L Timmen, G Vishnyakova, G Grosche, T Waterholter, A Kuhl, et al. Long-distance chronometric leveling with a transportable optical clock. arXiv preprint arXiv:2309.14953, 2023.

[11] Yoshiyuki Tanaka and Hidetoshi Katori. Exploring potential applications of optical lattice clocks in a plate subduction zone. Journal of Geodesy, 95:93, 2021.

[12] S. B. Koller, J. Grotti, St. Vogt, A. Al-Masoudi, S. Dörscher, S. Häfner, U. Sterr, and Ch. Lisdat. Transportable optical lattice clock with $7 \times 10^{-17}$ uncertainty. Phys. Rev. Lett., 118:073601, Feb 2017.

[13] Noriaki Ohmae, Masao Takamoto, Yosuke Takahashi, Motohide Kokubun, Kuniya Araki, Andrew Hinton, Ichiro Ushijima, Takashi Muramatsu, Tetsuo Furumiya, Yuya Sakai, Naoji Moriya, Naohiro Kamiya, Kazuaki Fujii, Ryuya Muramatsu, Toshihiro Shiimado, and Hidetoshi Katori. Transportable strontium optical lattice clocks operated outside laboratory at the level of $10^{-18}$ uncertainty. Advanced Quantum Technologies, 4(8):2100015, 2021.

[14] S. Origlia, M. S. Pramod, S. Schiller, Y. Singh, K. Bongs, R. Schwarz, A. Al-Masoudi, S. Dörscher, S. Herbers, S. Häfner, U. Sterr, and Ch. Lisdat. Towards an optical clock for space: Compact, high-performance optical lattice clock based on bosonic atoms. Physical Review A, 98(053443), 2018.

[15] Jian Cao, Ping Zhang, Junjuan Shang, Kaifeng Cui, Jinbo Yuan, Sijia Chao, Shaomao Wang, Hualin Shu, and Xueren Huang. A compact, transportable single-ion optical clock with $7.8 \times 10^{-17}$ systematic uncertainty. Applied Physics B, 123:1–9, 2017.

[16] Mengyan Zeng, Yao Huang, Baolin Zhang, Yanmei Hao, Zixiao Ma, Ruming Hu, Huaqing Zhang, Zheng Chen, Miao Wang, Hua Guan, and Kelin Gao. Toward a transportable $Ca^+$ optical clock with a systematic uncertainty of $4.8 \times 10^{-18}$. Phys. Rev. Appl., 19:064004, Jun 2023.

[17] J. Stuhler, M. S. Pramod, S. Schiller, Y. Singh, K. Bongs, R. Schwarz, A. Al-Masoudi, S. Dörscher, S. Herbers, S. Häfner, U. Sterr, Ch. Lisdat, et al. Opticlock: Transportable and easy-to-operate optical single-ion clock. Measurement: Sensors, 18:100264, 2021.

[18] Noel Dimarcq, Marina Gertsvolf, Gaetano Mileti, Sebastien Bize, Christopher Oates, Ekkehard Peik, Davide Calonico, Tetsuya Ido, Patrizia Tavella, Frédéric Meynadier, et al. Roadmap towards the redefinition of the second. Metrologia, 2023.

[19] Andrei Derevianko and Maxim Pospelov. Hunting for topological dark matter with atomic clocks. Nature Physics, 10(12):933–936, 2014.

[20] YV Stadnik and VV Flambaum. Searching for dark matter and variation of fundamental constants with laser and maser interferometry. Physical review letters, 114(16):161301, 2015.

[21] Asimina Arvanitaki, Junwu Huang, and Ken Van Tilburg. Searching for dilaton dark matter with atomic clocks. Physical Review D, 91(1):015015, 2015.

[22] P Wcisło, P Ablewski, K Beloy, S Bilicki, M Bober, R Brown, R Fasano, R Ciuryło, H Hachisu, T Ido, et al. New bounds on dark matter coupling from a global network of optical atomic clocks. Science Advances, 4(12):eaau4869, 2018.

[23] S. Kolkowitz, I. Pikovski, N. Langellier, M. D. Lukin, R. L. Walsworth, and J. Ye. Gravitational wave detection with optical lattice atomic clocks. Physical Review D, 94:124043, Dec 2016.

[24] M. S. Safronova, D. Budker, D. DeMille, Derek F. Jackson Kimball, A. Derevianko, and Charles W. Clark. Search for new physics with atoms and molecules. Rev. Mod. Phys., 90:025008, Jun 2018.

[25] Feifan He and Baocheng Zhang. A protocol of potential advantage in the low frequency range to gravitational wave detection with space based optical atomic clocks. Eur. Phys. J. D, 74:94, 2020.

[26] Jianfeng Su, Qiang Wang, Qinghua Wang, and Philippe Jetzer. Low-frequency gravitational wave detection via double optical clocks in space. Class. Quantum Grav., 35:085010, 2018.

[27] A. P. Vyalykh, A. V. Semenko, D. V. Sutyrin, G. S. Belotelov, and S. N. Slyusarev. Microgravity test complex for mobile and portable optical frequency standards. Measurement Techniques, 65(3):197–207, 2022.

[28] H. Schuh and D. Behrend. VLBI: A fascinating technique for geodesy and astrometry. Journal of Geodynamics, 61:68–80, 2012.

[29] Tetsushi Takano, Masao Takamoto, Ichiro Ushijima, Noriaki Ohmae, Tomoya Akatsuka, Atsushi Yamaguchi, Yuki Kuroishi, Hiroshi Munekane, Basara Miyahara, and Hidetoshi Katori. Geopotential measurements with synchronously linked optical lattice clocks. Nature Photonics, 10(10):662–666, 2016.

[30] Jacopo Grotti, Silvio Koller, Stefan Vogt, Sebastian Häfner, Uwe Sterr, Christian Lisdat, Heiner Denker, Christian Voigt, Ludger Timmen, Antoine Rolland, et al. Geodesy and metrology with a transportable optical clock. Nature Physics, 14(5):437–441, 2018.

[31] Masao Takamoto, Ichiro Ushijima, Noriaki Ohmae, Toshihiro Yahagi, Kensuke Kokado, Hisaaki Shinkai, and Hidetoshi Katori. Test of general relativity by a pair of transportable optical lattice clocks. Nature Photonics, 14(7):411–415, 2020.

[32] Alexander Aeppli, Kyungtae Kim, William Warfield, Marianna S. Safronova, and Jun Ye. A clock with $8 \times 10^{-19}$ systematic uncertainty, 2024.

[33] W. F. McGrew, X. Zhang, R. J. Fasano, S. A. Schäffer, K. Beloy, D. Nicolodi, R. C. Brown, N. Hinkley, G. Milani, M. Schioppo, T. H. Yoon, and A. D. Ludlow. Atomic clock performance enabling geodesy below the centimetre level. Nature, 564(7734):87–90, Dec 2018.

[34] Tobias Bothwell, Dhruv Kedar, Eric Oelker, John M. Robinson, Ross B. Sherman, Holly Leopardi, Tara M. Fortier, Michael V. Romalis, and Andrew D. Ludlow. JILA SrI optical lattice clock with uncertainty of $2.0 \times 10^{-18}$. Metrologia, 56:065004, 2019.

[35] T. L. Nicholson, S. L. Campbell, R. B. Hutson, G. E. Marti, B. J. Bloom, R. L. McNally, W. Zhang, M. D. Barrett, M. S. Safronova, G. F. Strouse, W. L. Tew, and J. Ye. Systematic evaluation of an atomic clock at $2 \times 10^{-18}$ total uncertainty. Nature Communications, 6:6896, 2015.

[36] Jie Li, Xing-Yang Cui, Zhi-Peng Jia, De-Quan Kong, Hai-Wei Yu, Xian-Qing Zhu, Xiao-Yong Liu, De-Zhong Wang, Xiang Zhang, Xin-Yun Huang, Ming-Yi Zhu, Yu-Meng Yang, Yi Hu, Xiang-Pei Liu, Xiao-Min Zhai, Peng Liu, Xiao Jiang, Ping Xu, Han-Ning Dai, Yu-Ao Chen, and Jian-Wei Pan. A strontium lattice clock with both stability and uncertainty below $5 \times 10^{-18}$. Metrologia, 61:015006, 2024.

[37] B. J. Bloom, T. L. Nicholson, J. R. Williams, S. L. Campbell, M. Bishof, X. Zhang, W. Zhang, S. L. Bromley, and J. Ye. An optical lattice clock with accuracy and stability at the $10^{-18}$ level. Nature, 506:71–75, 2014.

[38] S. M. Brewer, J.-S. Chen, A. M. Hankin, E. R. Clements, C. W. Chou, D. J. Wineland, D. B. Hume, and D. R. Leibrandt. $^{27}\mathrm{Al}^{+}$ quantum-logic clock with a systematic uncertainty below $10^{-18}$. Physical Review Letters, 123:033201, 2019.

[39] Zhang Zhiqiang, Kyle J. Arnold, Rattakorn Kaewuam, and Murray D. Barrett. $^{176}\mathrm{Lu}^{+}$ clock comparison at the $10^{-18}$ level via correlation spectroscopy. Science Advances, 9(18):eadg1971, 2023.

[40] F. Riehle. Towards a redefinition of the second based on optical atomic clocks. C. R. Physique, 16:506–515, 2015.

[41] W. F. McGrew, X. Zhang, H. Leopardi, R. J. Fasano, D. Nicolodi, K. Beloy, J. Yao, J. A. Sherman, S. A. Schäffer, J. Savory, R. C. Brown, S. Römisch, C. W. Oates, T. E. Parker, T. M. Fortier, and A. D. Ludlow. Towards the optical second: Verifying optical clocks at the SI limit. Optica, 6(4):448–454, 2019.

[42] Atsushi Yamaguchi, Miho Fujieda, Motohiro Kumagai, Hidekazu Hachisu, Shigeo Nagano, Ying Li, Tetsuya Ido, Tetsushi Takano, Masao Takamoto, and Hidetoshi Katori. Direct comparison of distant optical lattice clocks at the $10^{-16}$ uncertainty. Applied Physics Express, 4:082203, 2011.

[43] K. Predehl, G. Grosche, S. M. F. Raupach, S. Droste, O. Terra, J. Alnis, T. Legero, T. W. Hänsch, Th. Udem, R. Holzwarth, and H. Schnatz. A 920-kilometer optical fiber link for frequency metrology at the 19th decimal place. Science, 336:441, 2012.

[44] D. Calonico, E. K. Bertacco, C. E. Calosso, C. Clivati, G. A. Costanzo, M. Frittelli, A. Godone, A. Mura, N. Poli, D. V. Sutyrin, G. Tino, M. E. Zucco, and F. Levi. High-accuracy coherent optical frequency transfer over a doubled 642-km fiber link. Applied Physics B, 117:979–986, 2014.

[45] Piotr Morzyński, Marcin Bober, Dobrosława Bartoszek-Bober, Jerzy Nawrocki, Przemysław Krehlik, Łukasz Śliwczyński, Marcin Lipiński, Piotr Masłowski, Agata Cygan, Piotr Dunst, Michał Garus, Daniel Lisak, Jerzy Zachorowski, Wojciech Gawlik,

Czesław Radzewicz, Roman Ciuryło, and Michał Zawada. Absolute measurement of the $^1S_0 - ^3P_0$ clock transition in neutral $^{88}$Sr over the 330 km-long stabilized fibre optic link. Scientific Reports, 5:17495, 2015.

[46] C. Lisdat, G. Grosche, N. Quintin, C. Shi, S. M. F. Raupach, C. Grebing, D. Nicolodi, F. Stefani, A. Al-Masoudi, S. Dörscher, S. Häfner, J.-L. Robyr, N. Chiodo, S. Bilicki, E. Bookjans, A. Koczwara, S. Koke, A. Kuhl, F. Wiotte, F. Meynadier, E. Camisard, M. Abgrall, M. Lours, T. Legero, H. Schnatz, U. Sterr, H. Denker, C. Chardonnet, Y. Le Coq, G. Santarelli, A. Amy-Klein, R. Le Targat, J. Lodewyck, O. Lopez, and P.-E. Pottie. A clock network for geodesy and fundamental science. Nature Communications, 7:12443, 2016.

[47] BACON Collaboration. Frequency ratio measurements at 18-digit accuracy using an optical clock network. Nature, 591(7851):564–569, 2021.

[48] M. Schioppo, J. Kronjäger, A. Silva, R. Ilieva, J. W. Paterson, C. F. A. Baynham, W. Bowden, I. R. Hill, R. Hobson, A. Vianello, M. Dovale-Álvarez, R. A. Williams, G. Marra, H. S. Margolis, A. Amy-Klein, O. Lopez, E. Cantin, H. Álvarez Martínez, R. Le Targat, P. E. Pottie, N. Quintin, T. Legero, S. Häfner, U. Sterr, R. Schwarz, S. Dörscher, C. Lisdat, S. Koke, A. Kuhl, T. Waterholter, E. Benkler, and G. Grosche. Comparing ultrastable lasers at $7 \times 10^{-17}$ fractional frequency instability through a 2220 km optical fibre network. Nature Communications, 13:212, 2022.

[49] Hugo Bergeron, Laura C. Sinclair, William C. Swann, Craig W. Nelson, Jean-Daniel Deschênes, Esther Baumann, Fabrizio R. Giorgetta, Ian Coddington, and Nathan R. Newbury. Tight real-time synchronization of a microwave clock to an optical clock across a turbulent air path. Optica, 3(4):441–447, April 2016.

[50] Laura C. Sinclair, Hugo Bergeron, William C. Swann, Esther Baumann, Jean-Daniel Deschênes, and Nathan R. Newbury. Comparing optical oscillators across the air to milliradians in phase and $10^{-17}$ in frequency. Physical Review Letters, 120(5):050801, January 2018.

[51] Hugo Bergeron, Jean-Daniel Deschênes, Ian Khader, Laura C. Sinclair, William C. Swann, Kevin C. Cossel, Michael Cermak, and Nathan R. Newbury. Optical two-way time and frequency transfer over free space. Nature Communications, 10:1819, 2019.

[52] Martha I. Bodine, Jennifer L. Ellis, William C. Swann, Sarah A. Stevenson, Jean-Daniel Deschênes, Emily D. Hannah, Paritosh Manurkar, Nathan R. Newbury, and Laura C. Sinclair. Optical time-frequency transfer across a free-space, three-node network. APL Photonics, 5:076113, July 2020.

[53] Jennifer L. Ellis, Martha I. Bodine, William C. Swann, Sarah A. Stevenson, Emily D. Caldwell, Laura C. Sinclair, Nathan R. Newbury, and Jean-Daniel Deschênes. Scaling up frequency-comb-based optical time transfer to long terrestrial distances. Physical Review Applied, 15:034002, March 2021.

[54] Qi Shen, Jian-Yu Guan, Ting Zeng, Qi-Ming Lu, Liang Huang, Yuan Cao, Jiu-Peng Chen, Tian-Qi Tao, Jin-Cai Wu, Lei Hou, Sheng-Kai Liao, Ji-Gang Ren, Juan Yin, Jian-Jun Jia, Hai-Feng Jiang, Cheng-Zhi Peng, Qiang Zhang, and Jian-Wei Pan. Experimental simulation of time and frequency transfer via an optical satellite–ground link at $10^{-18}$ instability. Optica, 8(4):471–476, April 2021.

[55] Qi Shen, Jian-Yu Guan, Ji-Gang Ren, Ting Zeng, Lei Hou, Min Li, Yuan Cao, Jin-Jian Han, Meng-Zhe Lian, Yan-Wei Chen, Xin-Xin Peng, Shao-Mao Wang, Dan-Yang Zhu, Xi-Ping Shi, Zheng-Guo Wang, Ye Li, Wei-Yue Liu, Ge-Sheng Pan, Yong Wang, Zhao-Hui Li, Jin-Cai Wu, Yan-Yan Zhang, Fa-Xi Chen, Chao-Yang Lu, Sheng-Kai Liao, Juan Yin, Jian-Jun Jia, Cheng-Zhi Peng, Hai-Feng Jiang, Qiang Zhang, and Jian-Wei Pan. Free-space dissemination of time and frequency with $10^{-19}$ instability over 113 km. Nature, 610:661–666, October 2022.

[56] Emily D. Caldwell, Jean-Daniel Deschenes, Jennifer Ellis, William C. Swann, Benjamin K. Stuhl, Hugo Bergeron, Nathan R. Newbury, and Laura C. Sinclair. Quantum-limited optical time transfer for future geosynchronous links. Nature, 618:721–726, June 2023.

[57] H. Hachisu, M. Fujieda, S. Nagano, T. Gotoh, A. Nogami, T. Ido, St. Falke, N. Huntemann, C. Grebing, B. Lipphardt, Ch. Lisdat, and D. Piester. Direct comparison of optical lattice clocks with an intercontinental baseline of 9000 km. OPTICS LETTERS, 39(14):4072–4075, July 2014.

[58] Miho Fujieda, Tadahiro Gotoh, Fumimaru Nakagawa, Ryo Tabuchi, Masanori Aida, and Jun Amagai. Carrier-phase-based two-way satellite time and frequency transfer. IEEE transactions on ultrasonics, ferroelectrics, and frequency control, 59(12):2625–2630, 2012.

[59] Miho Fujieda, Ryo Tabuchi, and Tadahiro Gotoh. A new twstft modem with code and carrier phases. In 2019 Joint Conference of the IEEE International Frequency Control Symposium and European Frequency and Time Forum (EFTF/IFC), pages 1–2. IEEE, 2019.

[60] T E Parker, V Zhang, G Petit, J Yao, R C Brown, and J L Hanssen. A three-cornered hat analysis of instabilities in two-way and GPS carrier phase time transfer systems. Metrologia, 59:035007, May 2022.

[61] Marco Pizzocaro, Mamoru Sekido, Kazuhiro Takefuji, Hideki Ujihara, Hidekazu Hachisu, Nils Nemitz, Masanori Tsutsumi, Tetsuro Kondo, Eiji Kawai, Ryuichi Ichikawa, Kunitaka Namba, Yoshihiro Okamoto, Rumi Takahashi, Junichi Komuro, Cecilia Clivati, Filippo Bregolin, Piero Barbieri, Alberto Mura, Elena Cantoni, Giancarlo Cerretto, Filippo Levi, Giuseppe Maccaferri, Mauro Roma, Claudio Bortolotti, Monia Negusini, Roberto Ricci, Giampaolo Zacchiroli, Juri Roda, Julia Leute, Gérard Petit, Federico Perini, Davide Calonico, and Tetsuya Ido. Intercontinental comparison of optical atomic clocks through very long baseline interferometry. Nature Physics, 17:223–227, February 2020.

[62] Dariusz Świerad, Sebastian Häfner, Stefan Vogt, Bertrand Venon, David Holleville, Sébastien Bize, Andrė Kulosa, Sebastian Bode, Yeshpal Singh, Kai Bongs, Ernst Maria Rasel, Jérôme Lodewyck, Rodolphe Le Targat, Christian Lisdat, and Uwe Sterr. Ultra-stable clock laser system development towards space applications. Scientific Reports, 6:33973, 2016.

[63] Liang Liu, De-Sheng Lü, Wei-Biao Chen, Tang Li, Qiu-Zhi Qu, Bin Wang, Lin Li, Wei Ren, Zuo-Ren Dong, Jian-Bo Zhao, et al. In-orbit operation of an atomic clock based on laser-cooled 87rb atoms. Nature Communications, 9:2760, 2018.

[64] C. W. Chou, D. B. Hume, T. Rosenband, and D. J. Wineland. Optical clocks and relativity. Science, 329:1630–1633, 2010.

[65] Tobias Bothwell, Colin J. Kennedy, Alexander Aeppli, Dhruv Kedar, John M. Robinson, Eric Oelker, Alexander Staron, and Jun Ye. Resolving the gravitational redshift across a millimetre-scale atomic sample. Nature, 602:423, 2022.

[66] S. Herrmann, F. Finke, M. Lülf, O. Kichakova, D. Puetzfeld, D. Knickmann, M. List, B. Rievers, G. Giorgi, C. Günther, H. Dittus, R. Prieto-Cerdeira, F. Dilssner, F. Gonzalez, E. Schönemann, J. Ventura-Traveset, and C. Lämmerzahl. Test of the gravitational redshift with galileo satellites in an eccentric orbit. Physical Review Letters, 121, 2018.

[67] Tobias Bothwell and et al. Transportable Yb optical lattice clock and cavity. Manuscript in preparation, 2024.

[68] Feng Guo, Wei Tan, Chi-hua Zhou, Jian Xia, Ying-xin Chen, Ting Liang, Qiang Liu, Yun Liu, De-jing He, Yong-zhuang Zhou, Wen-hai Wang, Yong Shen, Hong-xin Zou, and Hong Chang. A proof-of-concept model of compact and high-performance $^{87}$Sr optical lattice clock for space. AIP Advances, 11:125116, 2021.

[69] Liu Yun, Wang Wen-Hai, He De-Jing, Zhou Yong-Zhuang, Shen Yong, and Zou Hong-Xin. Laser system of cold atom optical clock in China Space Station. Acta Physica Sinica, 72(18):184202, 2023.

[70] Kai Bongs, Yeshpal Singh, Lyndsie Smith, Wei He, Ole Kock, Dariusz Świerad, Joshua Hughes, Stephan Schiller, Soroosh Alighanbari, Stefano Origlia, Stefan Vogt, Uwe Sterr, Christian Lisdat, Rodolphe Le Targat, Jérôme Lodewyck, David Holleville, Bertrand Venon, Sébastien Bize, Geoffrey P. Barwood, Patrick Gill, Ian R. Hill, Yuri B. Ovchinnikov, Nicola Poli, Guglielmo M. Tino, Jürgen Stuhler, and Wilhelm Kaenders. Development of a strontium optical lattice clock for the SOC mission on the ISS. Comptes Rendus Physique, 16:553–564, 2015.

[71] G.S. Belotelov, D.V. Sutyrin, and S.N. Slyusarev. Towards a transportable optical frequency standard on neutral ytterbium atoms. Rocket and Space Instrumentation and Information Systems, 6:24–31, 2019.

[72] Zhao Fang-Jing, Gao Feng, Han Jian-Xin, Zhou Chi-Hua, Meng Jun-Wei, Wang Ye-Bing, Guo Yang, Zhang Shou-Gang, and Chang Hong. Miniaturization of physics system in Sr optical clock. Acta Physica Sinica, 67:050601, 2018.

[73] Yogeshwar B. Kale, Alok Singh, Markus Gellesch, Jonathan M. Jones, David Morris, Matthew Aldous, Kai Bongs, and Yeshpal Singh. Field deployable atomics package for an optical lattice clock. Quantum Science and Technology, 7:045004, 2022.

[74] A. Golovizin, D. Tregubov, D. Mishin, D. Provorchenko, and N. Kolachevsky. Compact magneto-optical trap of thulium atoms for a transportable optical clock. Optics Express, 29(22):36734–36744, 2021.

[75] K. Beloy, N. Hinkley, N. B. Phillips, J. A. Sherman, M. Schioppo, J. Lehman, A. Feldman, L. M. Hanssen, C. W. Oates, and A. D. Ludlow. Atomic clock with $1 \times 10^{-18}$ room-temperature blackbody Stark uncertainty. Phys. Rev. Lett., 113:260801, Dec 2014.

[76] Oliver S. Burrow, Robert J. Fasano, Wesley Brand, Michael W. Wright, Wenbo Li, Andrew D. Ludlow, Erling Riis, Paul F. Griffin, and Aidan S. Arnold. Optimal binary gratings for multi-wavelength magneto-optical traps. Optica Publishing Group, 2023.

[77] J. P. McGilligan, K. R. Moore, A. Dellis, G. D. Martinez, E. de Clercq, P. F. Griffin, A. S. Arnold, E. Riis, R. Boudot, and J. Kitching. Laser cooling in a chip-scale platform. arXiv preprint arXiv:2005.05818, May 2020.

[78] G. Zürn. Towards a Few-Fermion System. PhD thesis, Ruprecht-Karls-Universität Heidelberg, 2009.

[79] J. Huckans, W. Dubosclard, E. Maréchal, O. Gorceix, B. Laburthe-Tolra, and M. Robert-de Saint-Vincent. Note on the reflectance of mirrors exposed to a strontium beam. arXiv:1802.08499v2 [physics.atom-ph], May 2018.

[80] Harold J. Metcalf and Peter van der Straten. Laser Cooling and Trapping. Graduate Texts in Contemporary Physics. Springer New York, NY, 1 edition, 1999.

[81] Raymon S. Watson and John J. McFerran. Simulation of optical lattice trap loading from a cold atomic ensemble. Journal of the Optical Society of America B, 38:36–43, January 2021.

[82] R. H. Dicke. The effect of collisions upon the doppler width of spectral lines. Physical Review, 89:472–473, 1953.

[83] Andrew D. Ludlow. The Strontium Optical Lattice Clock: Optical Spectroscopy with Sub-Hertz Accuracy. Ph.d. dissertation, University of Colorado, Colorado, June 2008.

[84] S. Blatt, J. W. Thomsen, G. K. Campbell, A. D. Ludlow, M. D. Swallows, M. J. Martin, M. M. Boyd, and J. Ye. Rabi spectroscopy and excitation inhomogeneity in a one-dimensional optical lattice clock. Phys. Rev. A, 80:052703, Nov 2009.

[85] Di Ai, Taoyun Jin, Tao Zhang, Limeng Luo, Luhua Liu, Min Zhou, and Xinye Xu. Erratum: Absolute frequency measurement of the $6s6p^3p_0 \rightarrow 5d6s^3d_1$ transition based on ultracold ytterbium atoms [phys. rev. a 107, 063107 (2023)]. Physical Review A, 109:039902, March 2024.

[86] Nils Nemitz, Takuya Ohkubo, Masao Takamoto, Ichiro Ushijima, Manoj Das, Noriaki Ohmae, and Hidetoshi Katori. Frequency ratio of Yb and Sr clocks with $5 \times 10^{-17}$ uncertainty at 150 seconds averaging time. Nature Photonics, 10, Apr 2016.

[87] Nathan D. Lemke. Optical Lattice Clock with Spin-1/2 Ytterbium Atoms. Ph.d. dissertation, University of Colorado, Colorado, 2012.

[88] Travis L. Nicholson. A New Record in Atomic Clock Performance. Ph.d. dissertation, University of Colorado, Colorado, May 2015.

[89] Long-Sheng Ma, Peter Jungner, Jun Ye, and John L. Hall. Delivering the same optical frequency at two places: accurate cancellation of phase noise introduced by an optical fiber or other time-varying path. Optics Letters, 19(21):1777–1779, 1994.

[90] Hamamatsu Photonics K. K. Photomultiplier Tubes: Basics and Applications. Hamamatsu Photonics, Japan, 3rd edition, 2006.

[91] Takehiko Tanabe, Daisuke Akamatsu, Hajime Inaba, Sho Okubo, Takumi Kobayashi, Masami Yasuda, Kazumoto Hosaka, and Feng-Lei Hong. A frequency-stabilized light source at 399 nm using an yb hollow-cathode lamp. Japanese Journal of Applied Physics, 57(6):062501, apr 2018.

[92] Marco Pomponio, Archita Hati, and Craig Nelson. FPGA-based low-latency digital servo for optical physics experiments. In 2020 Joint Conference of the IEEE International Frequency Control Symposium and International Symposium on Applications of Ferroelectrics (IFCS-ISAF). IEEE, Oct 2020.

[93] R.J. Fasano, Y.J. Chen, W.F. McGrew, W.J. Brand, R.W. Fox, and A.D. Ludlow. Characterization and suppression of background light shifts in an optical lattice clock. Phys. Rev. Appl., 15:044016, Apr 2021.

[94] M. Schioppo et al. Ultrastable optical clock with two cold-atom ensembles. Nature Photonics, 11:48–52, 2017.

[95] Stephen Webster and Patrick Gill. Force-insensitive optical cavity. Optics Letters, 36(18):3572–3574, September 2011.

[96] COMSOL, Inc. COMSOL Multiphysics Reference Manual, version 5.3, 2017.

[97] Garrett D. Cole, Wei Zhang, Michael J. Martin, Jun Ye, and Markus Aspelmeyer. Tenfold reduction of brownian noise in high-reflectivity optical coatings. Nature Photonics, 7:644–650, August 2013.

[98] J. L. Valencia. Extending Coherence for Atomic Clocks. Ph.d. dissertation, University of Colorado, Colorado, 2023.

[99] John M. Robinson, Eric Oelker, William R. Milner, Wei Zhang, Thomas Legero, Dan G. Matei, Fritz Riehle, Uwe Sterr, and Jun Ye. Crystalline optical cavity at 4 k with thermal-noise-limited instability and ultralow drift. Optica, 6(2):240–243, February 2019.

[100] J. Davila-Rodriguez, F. N. Baynes, A. D. Ludlow, T. M. Fortier, H. Leopardi, S. A. Diddams, and F. Quinlan. Compact, thermal-noise-limited reference cavity for ultra-low-noise microwave generation. Optics Letters, 42:1277–1280, March 2017.

[101] Richard W. Fox. Temperature analysis of low-expansion fabry-perot cavities. Optics Express, 17(17):15023–15031, August 2009.

[102] Wolfgang Hänsel, Heinar Hoogland, Michele Giunta, Sebastian Schmid, Tilo Steinmetz, Ralf Doubek, Peter Mayer, Sven Dobner, Carsten Cleff, Marc Fischer, and Ronald Holzwarth. All polarization-maintaining fiber laser architecture for robust femtosecond pulse generation. Applied Physics B, 123:41, 2017.

[103] Michele Giunta, Wolfgang Hänsel, Marc Fischer, Matthias Lezius, Thomas Udem, and Ronald Holzwarth. Optical frequency measurements to the 20th decimal using real-time phase tracking and dichroic heterodyne detection. Nature Photonics, 14:44–49, January 2020.

[104] Michele Giunta, Jialiang Yu, Maurice Lessing, Marc Fischer, Matthias Lezius, Xiaopeng Xie, Giorgio Santarelli, Yann Le Coq, and Ronald Holzwarth. Compact and ultrastable photonic microwave oscillator. Optics Letters, 45(5):1140–1144, March 2020.

[105] Mark Rippetoe. Starting Strength: Basic Barbell Training. The Aasgaard Company, 3 edition, 2017.

[106] Steven Peil, James L. Hanssen, Thomas B. Swanson, Jennifer Taylor, and Christopher R. Ekstrom. Evaluation of long term performance of continuously running atomic fountains. arXiv, 2014.

[107] Steven Peil, James Hanssen, Thomas B. Swanson, Jennifer Taylor, and Christopher R. Ekstrom. The usno rubidium fountains. arXiv, 2016.

[108] Rudolf Grimm, Matthias Weidemüller, and Yuri B. Ovchinnikov. Optical Dipole Traps for Neutral Atoms, volume 42, pages 95–170. Academic Press, 2000.

[109] J. A. Sherman, N. D. Lemke, N. Hinkley, M. Pizzocaro, R. W. Fox, A. D. Ludlow, and C. W. Oates. High-accuracy measurement of atomic polarizability in an optical lattice clock. Physical Review Letters, 108:153002, 2012.

[110] R. C. Brown, N. B. Phillips, K. Beloy, W. F. McGrew, M. Schioppo, R. J. Fasano, G. Milani, X. Zhang, N. Hinkley, H. Leopardi, T. H. Yoon, D. Nicolodi, T. M. Fortier, and A. D. Ludlow. Hyperpolarizability and operational magic wavelength in an optical lattice clock. Phys. Rev. Lett., 119:253001, Dec 2017.

[111] Hidetoshi Katori, V. D. Ovsiannikov, S. I. Marmo, and V. G. Palchikov. Strategies for reducing the light shift in atomic clocks. Phys. Rev. A, 91:052503, May 2015.

[112] K. Beloy, W. F. McGrew, X. Zhang, D. Nicolodi, R. J. Fasano, Y. S. Hassan, R. C. Brown, and A. D. Ludlow. Modeling motional energy spectra and lattice light shifts in optical lattice clocks. Phys. Rev. A, 101:053416, May 2020.

[113] K. Beloy, J. A. Sherman, N. D. Lemke, N. Hinkley, C. W. Oates, and A. D. Ludlow. Determination of the $5d6s$ $^3D_1$ state lifetime and blackbody-radiation clock shift in Yb. Phys. Rev. A, 86:051404, Nov 2012.

[114] Michael Engstmann and Harold L. Partner. The role of blackbody radiation in the hyperfine splitting of cesium-133 and its implications for atomic clocks. J. Quantum Spectrosc. Radiat. Transfer, 101:487–501, 2006.

[115] J.E. Sansonetti and W.C. Martin. Handbook of basic atomic spectroscopic data. Quantum Measurement Division, PML, NIST Standard Reference Database 108, 2013. Accessed: 2024-04-20.

[116] Martin M. Boyd, Tanya Zelevinsky, Andrew D. Ludlow, Sebastian Blatt, Thomas Zanon-Willette, Seth M. Foreman, and Jun Ye. Nuclear spin effects in optical lattice clocks. Physical Review A, 76:022510, 2007.

[117] Thomas P. Heavner, Elizabeth A. Donley, Filippo Levi, Giovanni A. Costanzo, Thomas E. Parker, John H. Shirley, Neil Ashby, Stephen Barlow, and Steven R. Jefferts. First accuracy evaluation of nist-f2. Metrologia, 51:174–182, 2014.

[118] S. M. Brewer, J.-S. Chen, K. Beloy, A. M. Hankin, E. R. Clements, C. W. Chou, W. F. McGrew, X. Zhang, R. J. Fasano, D. Nicolodi, H. Leopardi, T. M. Fortier, S. A. Diddams, A. D. Ludlow, D. J. Wineland, D. R. Leibrandt, and D. B. Hume. Measurements of $^{27}$al$^+$ and $^{25}$mg$^+$ magnetic constants for improved ion-clock accuracy. Physical Review A, 100:013409, July 2019.

[119] K. Beloy. Trap-induced ac zeeman shift of the thorium-229 nuclear clock frequency. Physical Review Letters, 130:103201, March 2023.

[120] Sergey G. Porsev and Andrei Derevianko. Multipolar theory of blackbody radiation shift of atomic energy levels and its implications for optical lattice clocks. Physical Review A, 74:020502, 2006.

[121] K. Beloy, J. A. Sherman, N. D. Lemke, N. Hinkley, C. W. Oates, and A. D. Ludlow. Determination of the 5d6s 3d1 state lifetime and blackbody radiation clock shift in yb. arXiv:1208.0552v1 [physics.atom-ph], November 2012. arXiv preprint with additional information not peer-reviewed.

[122] Masao Takamoto, Feng-Lei Hong, Ryoichi Higashi, and Hidetoshi Katori. An optical lattice clock. Nature, 435(7040):321–324, 2005.

[123] Hidetoshi Katori, Masao Takamoto, V. G. Pal'chikov, and V. D. Ovsiannikov. Ultrastable optical clock with neutral atoms in an engineered light shift trap. Phys. Rev. Lett., 91:173005, Oct 2003.

[124] Kyungtae Kim, Alexander Aeppli, Tobias Bothwell, and Jun Ye. Evaluation of lattice light shift at low $10^{-19}$ uncertainty for a shallow lattice Sr optical clock. Phys. Rev. Lett., 130:113203, Mar 2023.

[125] Nils Nemitz, Asbjørn Arvad Jørgensen, Ryotatsu Yanagimoto, Filippo Bregolin, and Hidetoshi Katori. Modeling light shifts in optical lattice clocks. Physical Review A, 99(033424), 2019.

[126] W. F. McGrew. An Ytterbium Optical Lattice Clock with Eighteen Digits of Uncertainty, Instability, and Reproducibility. PhD thesis, University of Colorado, 2020.

[127] Stephan Falke, Nathan Lemke, Christian Grebing, Burghard Lipphardt, Stefan Weyers, Vladislav Gerginov, Nils Huntemann, Christian Hagemann, Ali Al-Masoudi, Sebastian Häfner, Stefan Vogt, Uwe Sterr, and Christian Lisdat. A strontium lattice clock with $3 \times 10^{-17}$ inaccuracy and its frequency. New Journal of Physics, 16:073023, July 2014.

[128] Myoung-Sun Heo, Huidong Kim, Dai-Hyuk Yu, Won-Kyu Lee, and Chang Yong Park. Evaluation of the blackbody radiation shift of an yb optical lattice clock at kriss. Metrologia, 59:055002, 2022.

[129] Dezhi Xiong, Qiang Zhu, Jinqi Wang, Ang Zhang, Congcong Tian, Bing Wang, Lingxiang He, Zhuanxian Xiong, and Baolong Lyu. Finite element analysis of blackbody radiation environment for an ytterbium lattice clock operated at room temperature. Metrologia, 58:035005, April 2021.

[130] M. F. Modest and S. Mazumder. Radiative Heat Transfer. Academic Press, 4 edition, 2021.

[131] Piotr Ablewski, Marcin Bober, and Michał Zawada. Emissivities of vacuum compatible materials: towards minimising blackbody radiation shift uncertainty in optical atomic clocks at room temperatures. Metrologia, 57:035004, 2020.

[132] John S. Steinhart and Stanley R. Hart. Calibration curves for thermistors. Deep-Sea Research, 15:497–503, April 1968. Pergamon Press, Printed in Great Britain.

[133] Hadi Ebrahimi-Darkhaneh. Measurement error caused by self-heating in ntc and ptc thermistors. Texas Instruments Analog Design Journal, Third Quarter 2019.

[134] P. R. Bevington and D. K. Robinson. Data reduction and error analysis for the physical sciences. McGraw-Hill, 3 edition, 2003.

[135] K. Beloy, A.D. Ludlow, M. Schioppo, N. Hinkley, J. A. Sherman, N. B. Phillips, and C.W. Oates. Departures from ideal blackbody radiation environments in atomic clocks. Unpublished manuscript, September 2015, 2015.

[136] Youssef S. Hassan, Kyle Beloy, Chun-Chia Chen, Jacob Seigel, Tanner Grogan, Xiaogang Zhang, and Andrew D. Ludlow. Dynamic cryogenic radiation shield for sub-$10^{-19}$ blackbody radiation shift uncertainty in optical lattice clocks. In The 27th International Conference on Atomic Physics, 7 2022. Poster presentation.

[137] Youssef S. Hassan, Kyle Beloy, Chun-Chia Chen, Kurt Gibble, Jacob L. Siegel, Tanner Grogan, Benjamin D. Hunt, and Andrew D. Ludlow. Dynamic cryogenic radiation shield for controlling blackbody radiation shift in optical lattice clocks. In 9th Symposium on Frequency Standards and Metrology, Kingscliff, NSW, Australia, 10 2023. Invited Poster in the session: Molecular, Atomic, Ion and Nuclear Clocks.

[138] Roman Schwarz. A Cryogenic Strontium Lattice Clock. PhD thesis, Gottfried Wilhelm Leibniz Universität Hannover, Hannover, Germany, 3 2022. PhD thesis.

[139] LaserOptik. Characteristics and transmission curves of standard substrates. `https://www.laseroptik.com/en/substrates/standard-substrates/characteristics-and-transmission-curves`, 2024. Accessed: 27-April-2024.

[140] SCHOTT AG. N-bk7 optical glass. Datasheet, Available online, 2024.

[141] Ali Khalas Anfoos Al-Masoudi. A Strontium lattice clock with reduced blackbody radiation shift. PhD thesis, Gottfried Wilhelm Leibniz Universität Hannover, Hannover, Germany, 9 2016. Dissertation.

[142] Sergey G. Porsev, Andrei Derevianko, and E. N. Fortson. Possibility of an optical clock using the $6\,^1s_0 \rightarrow 6\,^3p_0$ transition in $^{171,173}$yb atoms held in an optical lattice. Physical Review A, 69:021403, 2004.

[143] N. D. Lemke, A. D. Ludlow, Z. W. Barber, T. M. Fortier, S. A. Diddams, Y. Jiang, S. R. Jefferts, T. P. Heavner, T. E. Parker, and C. W. Oates. Spin-1/2 optical lattice clock. Physical Review Letters, 103:063001, August 2009.

[144] K. Beloy, X. Zhang, W. F. McGrew, N. Hinkley, T. H. Yoon, D. Nicolodi, R. J. Fasano, S. A. Schäffer, R. C. Brown, and A. D. Ludlow. Faraday-shielded dc Stark-shift-free optical lattice clock. Phys. Rev. Lett., 120:183201, May 2018.

[145] Jérôme Lodewyck, Michal Zawada, Luca Lorini, Mikhail Gurov, and Pierre Lemonde. Observation and cancellation of a perturbing dc Stark shift in strontium optical lattice clocks. IEEE Transactions on Ultrasonics, Ferroelectrics, and Frequency Control, 59(3), 2012.

[146] Florian R Ong, Klemens Schüppert, Pierre Jobez, Markus Teller, Ben Ames, Dario A Fioretto, Konstantin Friebe, Moonjoo Lee, Yves Colombe, Rainer Blatt, and Tracy E Northup. Probing surface charge densities on optical fibers with a trapped ion. New Journal of Physics, 22:063018, 2020.

[147] Li Zhang, Jasper F. Kok, Daven K. Henze, Qinbin Li, and Chun Zhao. Improving simulations of fine dust surface concentrations over the western united states by optimizing the particle size distribution. Geophys. Res. Lett., 40:3270–3275, 2013.

[148] N. Poli, Z. W. Barber, N. D. Lemke, C. W. Oates, L. S. Ma, J. E. Stalnaker, T. M. Fortier, S. A. Diddams, L. Hollberg, J. C. Bergquist, A. Brusch, S. Jefferts, T. Heavner, and T. Parker. Frequency evaluation of the doubly forbidden $^1S_0 \to ^3 P_0$ transition in bosonic $^{174}$Yb. Phys. Rev. A, 77:050501, May 2008.

[149] Qinfang Xu, Xiaotong Lu, Jingjing Xia, Yebing Wang, and Hong Chang. Measuring the probe Stark shift by frequency modulation spectroscopy in an $^{87}$Sr optical lattice clock. Applied Physics Letters, 119(10), 2021.

[150] W. M. Itano, J. C. Bergquist, J. J. Bollinger, J. M. Gilligan, D. J. Heinzen, F. L. Moore, M. G. Raizen, and D. J. Wineland. Quantum projection noise: Population fluctuations in two-level systems. Physical Review A, 47(5):3554–3570, May 1993.

[151] S. Weyers, V. Gerginov, M. Kazda, J. Rahm, B. Lipphardt, G. Dobrev, and K. Gibble. Advances in the accuracy, stability, and reliability of the ptb primary fountain clocks. arXiv:1809.03362v1 [physics.atom-ph], 2018.

[152] Immanuel Bloch, Jean Dalibard, and Wilhelm Zwerger. Many-body physics with ultracold gases. Rev. Mod. Phys., 80:885, 2008.

[153] Nelson Darkwah Oppong. Probing many-body physics with multiorbital quantum gases. PhD thesis, Ludwig-Maximilians-Universität München, München, 3 2021. Tag der mündlichen Prüfung: 2021-04-15.

[154] Ramamurti Shankar. Principles of Quantum Mechanics. Springer, New York, 2 edition, 2014.

[155] Paul S. Julienne and Frederick H. Mies. Collisions of ultracold trapped atoms. J. Opt. Soc. Am. B, 6(11):2257, 1989. Received April 4, 1989; accepted July 27, 1989.

[156] Matthew D Swallows, Michael J Martin, Michael Bishof, Craig Benko, Yige Lin, Sebastian Blatt, Ana Maria Rey, and Jun Ye. Operating a $^{87}$Sr optical lattice clock with high precision and at high density. IEEE transactions on ultrasonics, ferroelectrics, and frequency control, 59(3):416–425, 2012.

[157] G. K. Campbell, M. M. Boyd, J. W. Thomsen, M. J. Martin, S. Blatt, M. D. Swallows, T. L. Nicholson, T. Fortier, C. W. Oates, S. A. Diddams, N. D. Lemke, P. Naidon, P. Julienne, Jun Ye, and A. D. Ludlow. Probing interactions between ultracold fermions. Science, 324(5925):360, 2009.

[158] Zhenhua Yu and C. J. Pethick. Clock shifts of optical transitions in ultracold atomic gases. Physical Review Letters, 103(26):260401, 2009.

[159] Kurt Gibble. Decoherence and collisional frequency shifts of trapped bosons and fermions. Physical Review Letters, 103(11):113202, 2009.

[160] A. M. Rey, A. V. Gorshkov, and C. Rubbo. Many-body treatment of the collisional frequency shift in fermionic atoms. Physical Review Letters, 103(26):260402, 2009.

[161] N. D. Lemke, J. von Stecher, J. A. Sherman, A. M. Rey, C. W. Oates, and A. D. Ludlow. *p*-wave cold collisions in an optical lattice clock. Phys. Rev. Lett., 107:103902, Aug 2011.

[162] Alexander Aeppli, Anjun Chu, Tobias Bothwell, Colin J. Kennedy, Dhruv Kedar, Peiru He, Ana Maria Rey, and Jun Ye. Hamiltonian engineering of spin-orbit–coupled fermions in a wannier-stark optical lattice clock. Sci. Adv., 8:eadc9242, 2022.

[163] Tomoya Akatsuka, Masao Takamoto, and Hidetoshi Katori. Optical lattice clocks with non-interacting bosons and fermions. Nature Physics, 4(12):954–959, 2008.

[164] A. D. Ludlow, N. D. Lemke, J. A. Sherman, C. W. Oates, G. Quéméner, J. von Stecher, and A. M. Rey. Cold-collision-shift cancellation and inelastic scattering in a Yb optical lattice clock. Phys. Rev. A, 84:052724, Nov 2011.

[165] Sangkyung Lee, ChangYong Park, Won-Kyu Lee, and Dai-Hyuk Yu. Cancellation of collisional frequency shifts in optical lattice clocks with rabi spectroscopy. New J. Phys., 18:033030, 2016.

[166] Kurt Gibble. Scattering of cold-atom coherences by hot atoms: Frequency shifts from background-gas collisions. Phys. Rev. Lett., 110:180802, May 2013.

[167] Kurt Gibble. The difference between a photon's momentum and an atom's recoil. Optical Society of America, 2007. OCIS codes: (120.3180) Interferometry, (300.6320) Spectroscopy, high-resolution, (300.6370) Spectroscopy, microwave.

[168] Jocelyne Guéna, Ruoxin Li, Kurt Gibble, Sébastien Bize, and André Clairon. Evaluation of doppler shifts to improve the accuracy of primary atomic fountain clocks. Physical Review Letters, 106:130801, April 2011.

[169] Steven A. King, Lukas J. Spieß, Peter Micke, Alexander Wilzewski, Tobias Leopold, Erik Benkler, Richard Lange, Nils Huntemann, Andrey Surzhykov, Vladimir A. Yerokhin, José R. Crespo López-Urrutia, and Piet O. Schmidt. An optical atomic clock based on a highly charged ion. Nature, 611:43–47, November 2022.

[170] Y. Huang, H. Guan, M. Zeng, L. Tang, and K. Gao. $^{40}$ca$^{+}$ ion optical clock with micromotion-induced shifts below $1\times10^{-18}$. Physical Review A, 99:011401(R), January 2019.

[171] S. N. Miao, J. W. Zhang, Y. Zheng, H. R. Qin, N. C. Xin, Y. T. Chen, J. Z. Han, and L. J. Wang. Second-order doppler frequency shifts of trapped ions in a linear paul trap. Physical Review A, 106:033121, 2022.

[172] Pierre Lemonde and Peter Wolf. Optical lattice clock with atoms confined in a shallow trap. Phys. Rev. A, 72:033409, Sep 2005.

[173] S Kolkowitz, SL Bromley, T Bothwell, ML Wall, GE Marti, AP Koller, X Zhang, AM Rey, and J Ye. Spin–orbit-coupled fermions in an optical lattice clock. Nature, 542(7639):66–70, 2017.

[174] X. Zhang, K. Beloy, Y. S. Hassan, W. F. McGrew, C.-C. Chen, J. L. Siegel, T. Grogan, and A. D. Ludlow. Subrecoil clock-transition laser cooling enabling shallow optical lattice clocks. Phys. Rev. Lett., 129:113202, Sep 2022.

[175] S. Falke, M. Misera, U. Sterr, and C. Lisdat. Delivering pulsed and phase stable light to atoms of an optical clock. Applied Physics B, 107:301–311, 2011.

[176] G. John Dick. Local oscillator induced instabilities in trapped ion frequency standards. Nineteenth Annual Precise Time and Time Interval (PTTI) Applications and Planning Meeting, 1987. Presented at the Nineteenth Annual Precise Time and Time Interval (PTTI) Applications and Planning Meeting, Redondo Beach, CA, 1-3 Dec 1987.

[177] Ming Rao and Haiming Qiu. Process Control Engineering: A Textbook for Chemical, Mechanical and Electrical Engineers. CRC Press, 1993.

[178] A. Golovizin, E. Fedorova, D. Tregubov, D. Sukachev, K. Khabarova, V. Sorokin, and N. Kolachevsky. Inner-shell clock transition in atomic thulium with a small blackbody radiation shift. Nature Communications, 10:1724, 2019.

[179] H. N. Hausser, J. Keller, T. Nordmann, N. M. Bhatt, J. Kiethe, H. Liu, M. von Boehn, J. Rahm, S. Weyers, E. Benkler, B. Lipphardt, S. Doerscher, K. Stahl, J. Klose, C. Lisdat, M. Filzinger, N. Huntemann, E. Peik, and T. E. Mehlstäubler. An $^{115}$in$^{+}$-$^{172}$yb$^{+}$ coulomb crystal clock with $2.5 \times 10^{-18}$ systematic uncertainty. Physical Review Letters, 132:195301, 2024.

[180] A. Sharma, S. Kolkowitz, and M. Saffman. Analysis of a cesium lattice optical clock. arXiv preprint arXiv:2203.08708, March 2022.

[181] Jacob Scott, Shimon Kolkowitz, and Mark Saffman. A cesium lattice optical clock (cloc). In 54th Annual Meeting of the APS Division of Atomic, Molecular and Optical Physics. American Physical Society, June 2023.

[182] Takumi Kobayashi, Daisuke Akamatsu, Kazumoto Hosaka, Yusuke Hisai, Akiko Nishiyama, Akio Kawasaki, Masato Wada, Hajime Inaba, Takehiko Tanabe, Feng-Lei Hong, and Masami Yasuda. Generation of a precise time scale assisted by a near-continuously operating optical lattice clock. arXiv:2404.11062v1 [physics.atom-ph], April 2024.

[183] Richard P. Feynman, Robert B. Leighton, and Matthew Sands. The Feynman Lectures on Physics, Vol. III: The New Millennium Edition: Quantum Mechanics. Basic Books, 2015.

[184] M. Abramowitz and I. A. Stegun. Handbook of Mathematical Functions with Formulas, Graphs, and Mathematical Tables. Dover, New York, 9th printing edition, 1972.

[185] Derek van Westrum. Geodetic survey of nist and jila clock laboratories. NOAA Technical Memorandum NOS NGS 77, NOAA – National Geodetic Survey, February 2019.

[186] Radosław Wojtak, Steen H. Hansen, and Jens Hjorth. Gravitational redshift of galaxies in clusters as predicted by general relativity. Nature, 477:567–569, 2011.

[187] Chun-Chia Chen and et al. Clock-line-mediated Sisyphus cooling. Manuscript under review, 2024.

[188] Chun-Chia Chen, Shayne Bennetts, Rodrigo González Escudero, Florian Schreck, and Benjamin Pasquiou. Sisyphus optical lattice decelerator. Phys. Rev. A, 100:023401, Aug 2019.

[189] J.L. Siegel, W.F. McGrew, Y.S. Hassan, C.-C. Chen, K. Beloy, T. Grogan, X. Zhang, and A.D. Ludlow. Excited-band coherent delocalization for improved optical lattice clock performance. arXiv, Feb 2024. arXiv:2402.04968v1 [physics.atom-ph].

[190] Eric B. Norrgard, Stephen P. Eckel, Christopher L. Holloway, and Eric L. Shirley. Quantum blackbody thermometry. New Journal of Physics, 23:033037, March 2021.

# Appendix A

## Partial Manual of Operations

This manual will describe some of the operational concepts and techniques used to operate the clock that are not otherwise covered in the folder portable/Operators Manual. It will be organized in the manner of general startup and transportation procedures, individual laser modules, and the physics package. Some notable omissions from this manual are: software, operation of the multicolor cavity which was updated recently by other users, operation of the Menlo frequency comb which is either proprietary information or contained in our notes on the control laptop, and details of the portable clock laser setup sent to USNO which is now defunct. It is hoped that current users of the system retain good documentation on this hardware.

### A.1 Startup and shutdown

First, we will describe day-to-day startup and shutdown operations for the clock, as opposed to before and after shipment preparations.

### A.1.1 Startup

1. The atomic beam oven takes the longest to warmup so begin by setting the oven to its current operational parameters. At the time of writing the main section is set to 465 C and the tip is set to 515 C.

2. Turn on the 399 nm laser, its hollow cathode lamp, the 759 nm laser, and the atomic beam shutter driver with their front panel buttons.

3. Open the following software in Desktop/Software Time director:, in this order: InfluxDB (must be started before Argent), Argent, NuView, NKT Control, Cybel Cyworks, and Jupyter. Connect to the wavemeter with TCP/IP in NuView and run the calibrate command.

4. Turn on the 1112 nm NKT laser.. Turn on the Cybel amplifier in Cyworks. The seed must always be turned on before the amplifier.

5. Lock the comb's repetition rate to the laboratory stable laser.

6. Lock the 1112 nm laser to the frequency comb, the wavemeter should read 269,695.215(15) GHz and the 3 dB linewidth on a spectrum analyzer should be $< 10$ Hz if observed closely. Adjust the frequency offset in the NKT control program to center the slow output from the comb at 2-5 V.

7. Lock the 759 nm laser to the frequency comb, the wavemeter should read 394,798.267(15) GHz, assuming no changes have been made to the operational magic condition from either recomputation or changed trap depth. The 3 dB linewidth on a spectrum analyzer should also be $< 10$ Hz if observed closely and there should be minimal noise spurs above the noise floor out to 60 kHz.Adjust the piezo knob on the laser to center the slow output from the comb at 0 V.

8. We usually do not turn the 1388 nm laser on and off. Lock the 1388 nm laser to the frequency comb with the wavemeter reading 431,738.12(2) GHz (the F=3/2 transition after frequency doubling into the wavemeter's measurement band). The linewidth is between 100 kHZ and 1 MHz. The slow output controls the diode temperature and usually is near 300-450 mV. The slow control can be centered with the temperature trimpot on the diode controller board, but this is rearely necessary.

9. Lock the 399 nm laser to the hollow cathode lamp for the $^{171}$Yb transition. In your web browser navigate to the 399 nm Alpha 250 control panel (the IP address is 192.168.0.2).

Disable the integrator (by clicking the uppermost “1/s” button, it should turn yellow). Use the piezo knob to tune to 751,527.32(3) GHz on the wavemeter. Re-enable the integrator.

10. Now the system should be ready to run sequences with the Argent GUI and take commands in Jupyter notebook. The daily Jupyter notebook has more checks to run such as for adequate optical powers.

### A.1.2 Shutdown

1. End the current Argent sequence.

2. Turn down the atomic beam oven. Historically, we used 375 C main and 400 C tip, but given recent experiences with ytterbium buildup, we should use a lower setpoint.

3. It is best practice to turn off all frequency servos to prevent integrator wind-up while the laser is off, but not strictly necessary.

4. Turn off the 399 nm laser, hollow cathode lamp, the 759 nm laser, and the atomic beam shutter driver with their front panel buttons. It’s ideal for the beam shutter to fully block the aperture so if the sequence ended with it in the closed state, you might leave it on. Future software updates might have Argent automatically set the beam shutter to closed when turned off much like the coil driver is automatically set to low.

5. Turn off the Cybel 1112 nm amplifier and the NKT seed laser.

## A.2 Transportation

### A.2.1 Preparation for transport

Following the daily shutdown sequence, more systems are turned off in a controlled manner.

1. Turn down the atomic beam oven. First set both filaments to 150 C. After they reach this temperature switch to “MANual” mode and drop the power in three roughly equal increments of current squared. When the temperatures are below 40 C, the oven controller

can be fully shutdown with the button in the back.

2. On a high level, you want to turn off everything that plugs into a DC regulator board that is easily switched before unpowering the entire regulator supply box. This procedure is due to paranoia that some items that broke during prior moves may have been from a voltage spike. Unplug the power connection to the PMT integrator module and save the cord in a labelled box. Turn off Alpha 250's. Turn off SHG temperature controllers. Turn off photodiodes in 759 nm and 1156 nm modules. Disconnect the 556 nm and 1388 nm laser from their supplies. Now, you can turn off the big regulator box.

3.Power down everything remaining in the laser rack. Turn off the Toptica control boxes with the rear buttons. Turn off the Acopian DC supply for the coil control box and the wavemeter. Unplug the Artiq supply. Gracefully shut down the computer. When everything else is off, turn off the AC supply panels.

4. Shutdown everything in the physics rack other than the ion pumps. Toggle off all of the photodiodes on the physics package. Turn off the ion gauge controller, atomic beam shutter controller, and the Keithley multimeter. The UPS should now read on its panel that you have at least two hours of battery at the current consumption rate.

5. Decabling the fiber optic cables that go between racks. Have lots of protective caps on hand; in particular, I use both the plastic sliding and metal external thread tips to double protect cables, while I use plastic internal thread tips to protect female mating surfaces. Usually, I leave the 399 nm cables plugged in on the input side, coil them up, and tape them down securely onto the top of the Artiq box. Might not be the best for cable longevity, but it saves a lot of alignment time on arrival. The 1388 nm and 556 nm cables should be completely unplugged the physics-side alignment will not benefit from leaving them in). The 759 nm cables to the wavemeter and comb should also be completely unplugged. Coil the cables nicely and store in a labelled box. Disconnect the clock laser fiber from the switch box.

6. Unplug the large cables that supply the DC regulator boxes on both ends (possible

exception for the 556 nm input end which is a pain since it requires carefully loosening the regulator board). Check to make sure they still have their labels since they have different lengths and some cables work better with different modules. Store in a big labelled box. Bring extras since some are starting to degrade at the connector insertion.

7. Unplug all of the SMA cables that run between racks. Have a label maker ready to refresh any failing labels. It helps to use a velcro strap to strain relieve the cables against the rack so you are not also fighting tension.

8. Unplug all of the remaining connections between racks such as USB and ethernet. Store in labelled boxes. At this point, the only cable connection external to the racks should be to an AC outlet from the physics rack and the AC connection from the laser rack to the physics rack.

9. Tighten up all of the bumper connections. The metal half inch post pieces on the fron of the racks and the soft foam pieces on the rear of the racks.

10. Raise up any lowered feet on the racks as high as you can so that they do not catch on the crates.

11. Attach the metal side panels to the racks. The internal threadings are not great and tend to chew through screws, so be selective and toss out bad 10-32 screws.

12. Wrap the racks in anti-static cling wrap to protect the optics from dust. Form a crossed “roof” on the top of the rack and then wrap all around it.

13. Unplug the two AC cables and coil them up. We did this disconnection last so that the racks would be grounded while cling wrapping them in case of residual static.

14. The shipping crates are currently stored behind the big black mysterious Area 51 bag in the NIST attic. Each rack goes with a particular crate (the control rack crate is defunct). Wheel the racks into their respective crates with the hard bumper side towards the back. Push them all the way in. Pull the AC power cord for the physics rack out of the hole and keep it powered. Then jam the foam “spears” into the left side between the rack and crate with one above and the other below the foam bumper. Then jam the other

spears into the top between the guiding foam grooves. The rack should now feel firmly held in place. Shut the crate and cinch the bolts tightly. The atom apparatus is now ready to ship.

15. The frequency comb can be wheeled into its box where it fits fairly tightly on the sides. There is some additional foam around to wedge in the sides. The big bag of packing peanuts is thrown on top.

16. Previously we were required to put down a trail of fiber boards to transport the crates to the shipping elevator. Since the floor is now of much worse quality, I would ignore this time consuming step.

17. Have a plan for putting the crates into the shipping truck and getting access to AC power. It is not difficult to draw out what you need on graph paper.

### A.2.2 Setting up after transport

1. If possible, let the crates equilibrate at the new room temperature before opening.

2. Open the crates, remove packing foam, and roll the racks to the desired position. Use a magnetic compass to point the quantization axis of the physics rack in a similar direction as the previous setup if possible.

3. Get the physics rack on AC power and daisy chain the laser rack to the physics rack UPS. If adequate current available, then plug both the portable laser and comb into the same AC source so as to reduce ground loops. This is done early for static discharge protection.

4. Lower the feet on the physics rack.

5. Remove the cling wrap.

6. Reconnect all cables.

7. Turn everything on in the opposite order of the shutdown.

8. Turn up the oven starting in manual mode with a few current bumps and then switch to automatic mode once the temperatures are above 150 C.

9. Be ready for new and interesting problems.

## A.3 Common electronics in the laser modules

### A.3.1 Intensity servo boards

These homemade boards are common throughout the project as a means to servo the laser intensity with AOMs. They support about 50 kHZ of bandwidth making them useful for power control for everything but probe pulses. The circuit diagram can be found in portable/DipTrace PCB projects/Intensity Servo V2/intensity servo v2.pdf.

The board is powered with a ±15 V cable. The boards have the following SMA connections: photodiode signal in, photodiode monitor, setpoint select (all of our boards have a grounding cap here), setpoint in (called DAQ), setpoint monitor, auxiliary input, and control signal out. The most common mode of operation is to have Artiq send in a setpoint through the DAQ and use the servo to have the intensity follow the control signal. The board also has the option to use one of two fixed setpoint modes where the setpoints are set either by analog trimpots or digital trimpots. In the fixed setpoint mode an external trigger to the setpoint select terminal switches the servo between two setpoints of the same type. The fixed setpoint modes are selected with the use of jumpers.

The board also supports inverting the gain signal (with a jumper) which is useful when using the AOM zero-order mode for intensity control instead of the first-order mode as is more common. When inverting the gain, diode D1 should be de-soldered. If digital trimmer U10 is clamping negative voltages too much, it can also be desoldered and replaced with an appropriate analog trimpot.

Here's the standard procedure for tuning the board with the front switches. First disable the integrator with switch S3 (red knob, far right). Put the photodiode monitor on an oscilloscope. Then use switch S5 (black knob, third from right) to tune the offset. Hold the switch down to clear the digital trimmer it is connected to. Then tap the switch up until the photodiode signal reaches a maximum value and tune it back down one click. If the intensity will be moved around by Artiq, then turn on the desired sequence. Now use the gain switch S4 (black knob, second from right) to tune the servo gain. Tightly following the input without oscillating is usually good enough operation. For some servos that we want higher performance from (such as the clock and lattice lasers) it can be useful to separately tune the proportional and integral gain of the servo. This operation is performed by re-soldering resistor R7 and capacitor C44.

Here are some other useful possible changes. Altering the value of capacitor C1 permits more or less aggressive filtering of the setpoint input. The lattice servo had this done to improve the smoothness of the adiabatic ramp and reject kHz frequency noise. The 556 nm intensity servo makes use of the auxiliary input which overrides the servo signal output so that you can directly control the intensity. That board does this to have option to rail the board to high power. The auxiliary input is connected to the board +15 V and a TTL input from Artiq to Out Select turns on the rail high function during the 399 nm MOT.

### A.3.2 Koheron Alpha 250

The Alpha 250 with the daughter board made by NIST's Marco Pomponio is a very powerful tool for laser control. It features a suite of tools for generating and demodulating RF tones and for reading and writing slower analog voltages. This board is a Swiss army knife of capability for solving laser control problems. Much more detail is possible here, but most will be left to individual sections that use this FPGA board. We will note that whenever using the demodulation it is very important to exactly match the modulation frequency. One of the more interesting problems that we debugged was error signal inversion with a one day period that occurred because of a floating point level of frequency difference between modulation and demodulation frequencies.

Figure A.1: Shown is a generic Alpha 250 configuration for offset PDH locking to a cavity reference. The EOM RF generates a fundamental frequency for the offset lock that is itself modulated with another RF frequency for generating PDH sidebands. The reflection photodiode signal is then taken into IN0 and demodulated with same frequency as the PDH modulation. A first PID loop then provides fast feedback (for even higher bandwidth feedback this could have been done on the other channel and made use of the RF output). The output of the first PID loop is then piggybacked to a second PID loop which provides slower feedback.

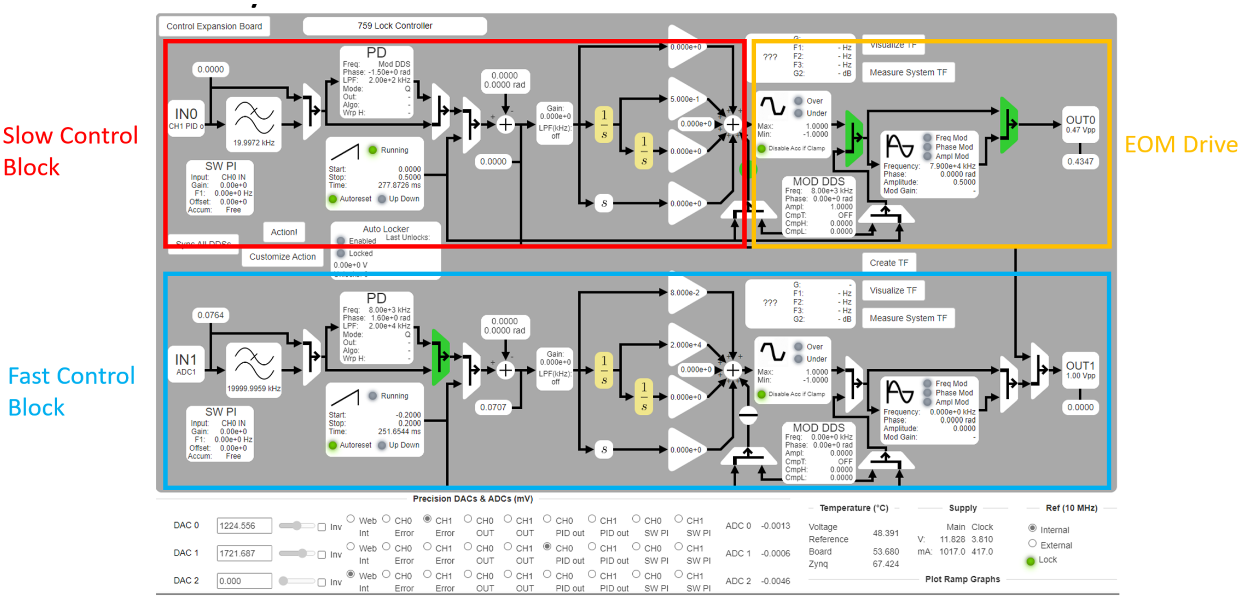

## A.4 399nm module

### A.4.0.1 Turn on procedure

1. Set the Toptica DL Pro to emit.

2. Turn on the spectroscopy lamp with the SRS high voltage supply. It should supply 1.5mA at about 156 V.

3. On the computer, open NuView to view the wavemeter and FOSC to set the

wavemeter to channel 1. Calibrate the wavemeter.

4. Open the Alpha250 control interface at 192.168.0.2. Disable the integrator (the 1/s button) on channel 0 by clicking so that it appears yellow.

5. Assuming the current is unchanged from last operation, use the DL Pro to tune the piezo until the wavemeter reads 751527.30(3) GHz.

6. Re-enable the integrator; the integrator button will appear white. If the lock is functioning correctly, then the wavemeter will still read 751527.30(3) GHz.

#### A.4.0.2 Typical frequency lock operating conditions

The laser is locked to the atomic transition using modulation transfer spectroscopy. The RF modulation necessary for this frequency servo is performed on an Alpha 250 FPGA board. Typical operating conditions are shown in Figure A.2.

Figure A.2: A high speed photodiode input goes into IN1 on the FPGA board. The fast EOM sideband modulation is demodulated in the first step and then routed to IN0 with internal logic. The square wave AM modulation is then demodulated to create an error signal. Finally, PID gain is applied for feedback to the laser piezo. This diagram shows a proposed change to the current setup in which the Alpha 250 generates and chops the 70 MHz AOM drive. The current system uses an external DDS and RF switch with the Alpha 250 only generating a 50 kHz square wave. This small upgrade would save some SWAP and eliminate the need for -5 V from the RF board regulator.

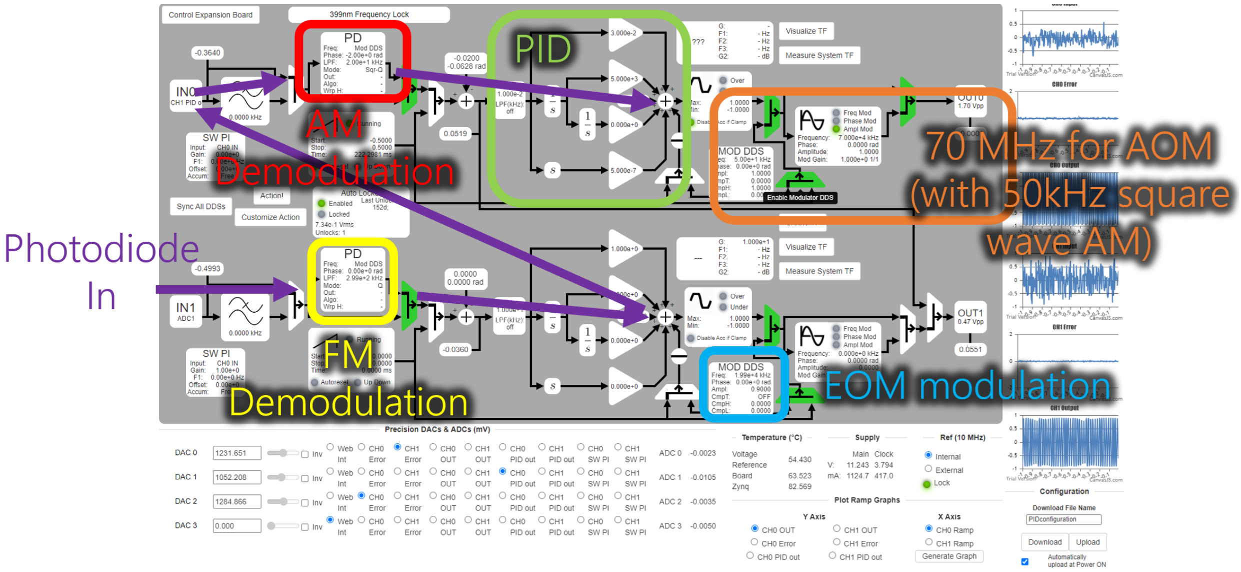

### A.4.0.3 Checking the error signal

Open the Alpha250 control interface at 192.168.0.2. Disable the channel 0 integrator and enable the channel 0 ramp. Usually, it is sufficient to click the rotation knob directly beneath the PID sum. If the system has been configured otherwise, then open the ramp box in channel 0 and set it to “Enable”, sawtooth, with ramp time 200ms, start at -0.5V, and stop at +0.5V.

Connect a scope to the SMB knob that is teed off from the front of the Toptica, on

Fast In 3. This signal is the ramp. Set the scope to trigger off this channel at 0V, falling edge and set the time spacing to view one sweep.

Connect a scope to the SMB knob labeled “Error Signal” coming from the front panel of the 399 RF breadboard.

You should be able to visualize an error signal like the one from Wen-Li Wang et al 2011 Chinese Phys. B 20 013201. Note that the lock point is the zero crossing on the right side of the 171 peak. With the +/- 0.5 V sweep centered on the lock point, you should only see the large 173/172 peak and the three smaller peaks to the right. Current signal gain settings result in the 173/172 peak saturating the demodulation out, but this is not a problem for the lower signal 171 error signal.

#### A.4.0.4 Optimizing intensity

For somewhat degraded intensity, just use a normal clock type sequence. For very poor intensity, setup a sequence that runs only the first step with the cooling and slowing beams on constantly (or a sequence with the probe on continuously). Make sure to protect the quad coil driver from excess heating by disabling the control input in its GUI console.

Disable the slowing and cooling intensity servos. Usually, I just reach in from the side and toggle the on/off switches, the cooling servo is the second from the front and the slowing is the third from the front. The probe servo is the most forwards, but it responds too slowly and is never on. The on/off switch is the red toggle furthest to the left on all of the boards.

Optimize the half-wave plate angle at the fiber output for each beam. In practice, there is almost never a benefit to using the waveplate before the fiber to align to the PM axis—it is well optimized and does not change.

Try re-engaging the intensity servos. If at any point in this optimization process, the intensity waveform has a 1ms peak before dropping down to the servo value, then you are done. You can also check the PDs section of the optical powers table below to verify that you are getting enough power a the photodiodes.

Attempt a 1D walk of the beams onto the fiber with the mirror nearest the fiber.

Attempt a 2D walk of the beams with two mirrors nearest to the fiber.

If at this point, the intensity servo is still unable to grab on, try tapping on the fibers near point where they join the bundle on the 399 module. They may need a little Kapton tape to hold them in the right way to optimize their bend radii.

- As a last resort, you can use a wand photodetector and the scope to optimize the efficiency of the AOM.

- If you started with a constant power sequence, make sure to go back to the clock sequence to reoptimize, since the AOM pointing is temperature sensitive.

#### A.4.0.5 Optical powers table

| | |
|---|---|
| **Probe PD Typical** | 930 mV |
| **Probe PD gain** | 20 dB |
| **Probe Servo Setpoint** | n/a |
| **MOT PD Max** | 508 mV |
| **MOT PD gain** | 20 dB |
| **MOT Servo Setpoint** | 410 mV |
| **MOT Servo Power** | 984 mV |
| **Slowing PD Max** | 308 mV |
| **Slowing PD gain** | 20 dB |
| **Slowing Servo Setpoint** | 240 mV |
| **Slowing Servo Power** | 576 mV |

#### A.4.0.6 RF powers table

| | |
|---|---|
| **Probe Artiq Atten** | 4 dB |
| **Probe RF Power at AOM** | 24.1 dBm |
| **Cooling Artiq Atten** | 1 dB |
| **Cooling RF Power at AOM** | 26.1 dBm |
| **Slowing Artiq Atten** | 4 dB |
| **Slowing RF Power at AOM** | 26.5 dBm |
| **Spectroscopy AOM Pickoff** | -11.1 dBm @ 223.5 MHZ, Switching disabled = 32 dB nominal |
| **Spectroscopy EOM Pickoff** | -32 dBm @19.97MHz = 23 dB nominal |

### A.4.1 Optical layout diagram

Figure A.3: Shown here is an ambitious early optical schematic. The schematic is entirely accurate even for current operation with the exception that the MEMS mirrors and second clock path have been removed. The MEMS proved themselves to be delicate and costly to optical power.

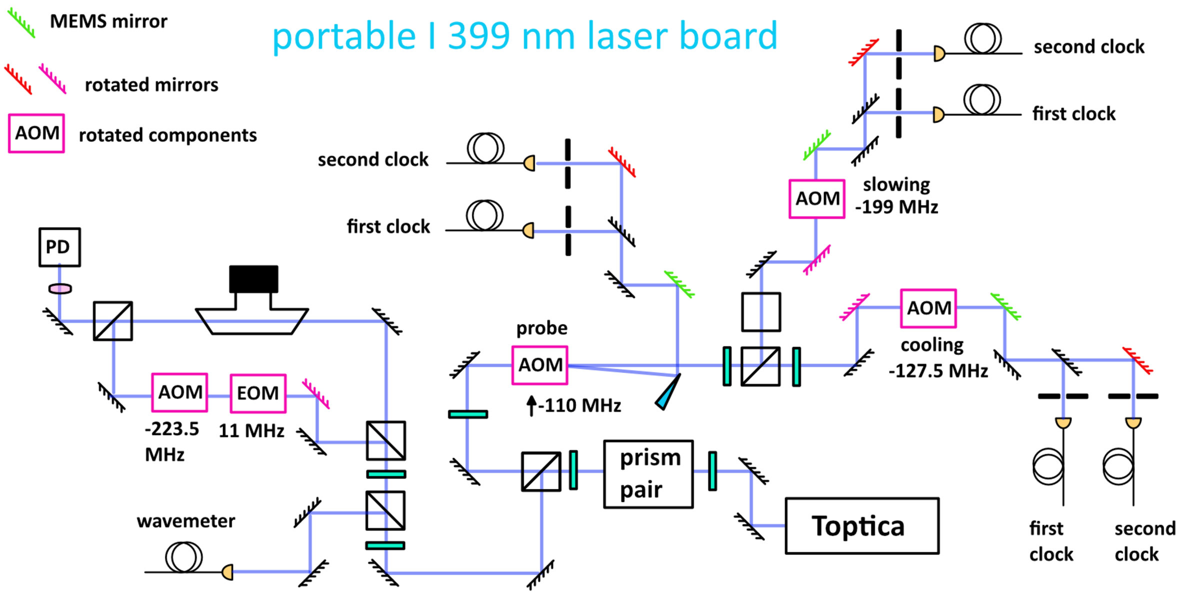

### A.4.2 RF board layout diagram

Figure A.4: Shown here is the layout of the RF control board for the four AOMs, one EOM, and frequency lock of the laser.

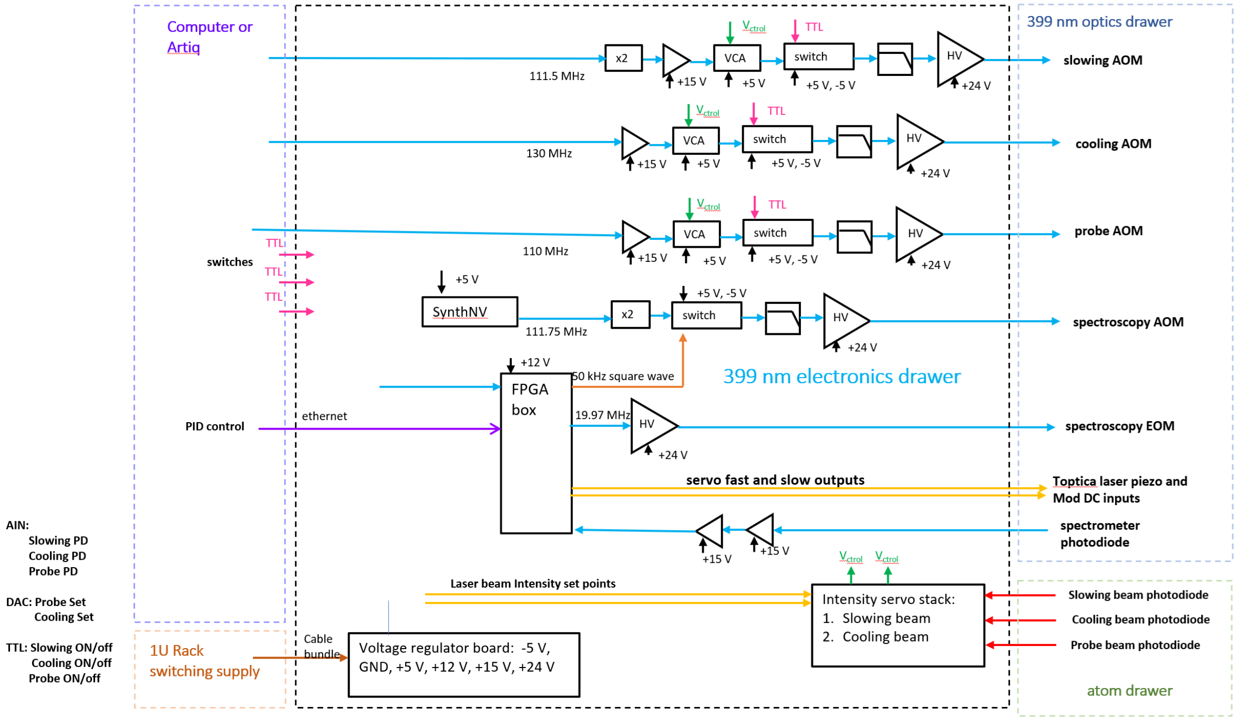

### A.4.3 Some common issues

#### A.4.3.1 Lock suddenly not working

The laser is slowly drifting/degrading. Visualize the error signal on an oscilloscope. There is most likely a mode hop near the transition of interest. Tune the current lower until the mode hop disappears. Since tuning the current lower decreases the power, you will need to adjust the current upwards and temperature downwards after a couple of these fixes to restore optimal power levels.

#### A.4.3.2 After transportation

Be patient here and avoid jumping to high upstream optics. Start by reloading the saved settings on the Toptica control box. Then begin the alignment by getting the wavemeter back online. Since the alignment has some frequency sensitivity, the laser should be manually tuned near resonance. Next, get the spectrometer realigned, usually this is just topping off the error signal by improving the pump beam's overlap to the probe. If there is no error signal at the correct optical frequency, then check that both the AOM and EOM are receiving RF tones. If they are, then one interesting problem we've seen is that the EOM tank circuit resonance has shifted after transportation. Use a vector network analyzer to evaluate this possibility.

Assuming the spectrometer is now locked, the optical power delivery must now be optimized. Check the diffraction efficiency of the probe AOM. If it needs to be realigned, optimize it, but know that everything downstream will need to be realigned. If the probe AOM is fine, you're in luck, proceed to check the slowing and MOT AOM diffraction efficiencies. Finally, top off each fiber coupling in the usual way. Don't forget polarization optimization. If the fibers are severely misaligned and there is no starting photodiode signal, then there are two options: check directly down the fiber output to increase the photon flux (keeping enough distance between the fiber and your eyes that you don't injure your eyesight with the 30 mW max), or completely extract the fiber and use the dummy SM fiber and red laser backcoupler to get an initial coupling.

#### A.4.3.3 Aligning the spectrometer from scratch

Start by optimizing the pump beam intensity. The EOM and AOM have already been placed well enough that you only need to optimize the power in the -1 order. Disable the square wave modulation temporarily to improve contrast. Put a power meter in place to sample that order and 2D walk the mirror pair to max the power.

Next, align the probe beam through the lamp with the lamp off and maximize the transmission through the aperture. Then use a note card pair to optimize the pump/probe overlap starting by aligning the pump beam to the probe beam to the probe beam spot on the PBS that originally split them. Then align the probe beam to the pump/probe combining PBS. Iterate until they overlap in both places. Check to make sure the probe beam's transmission through the spectrometer has not degraded. Then align the probe beam visually to the photodiode.

Turn on the lamp. Continue to align the probe beam to the photodiode using the error signal strength as a guide. The alignment is not sensitive near the maximum signal. Then tweak the pump beam's alignment through the spectrometer to top off the error signal.

#### A.4.3.4 Photodegradation

A few optics have seen noticeable degradation over time, likely due to UV solarization. The fiber optic cables are the most notable. They exhibit reduced polarization extinction ratio over time. When the power starts to drift too much over the course of a clock measurement due to polarization effects, it is time to replace these cables. They usually last 1 to 2 years. Some of the PBS cubes have also degraded over time. Generally, this can be avoided with the use of optically contact PBS cubes instead of epoxy-bonded (we've used the "molecular fusion" cubes from Spectral Products).

## A.5 556nm module

Figure A.5: Shown here is the optical and electronic layout of the 556 nm laser board.

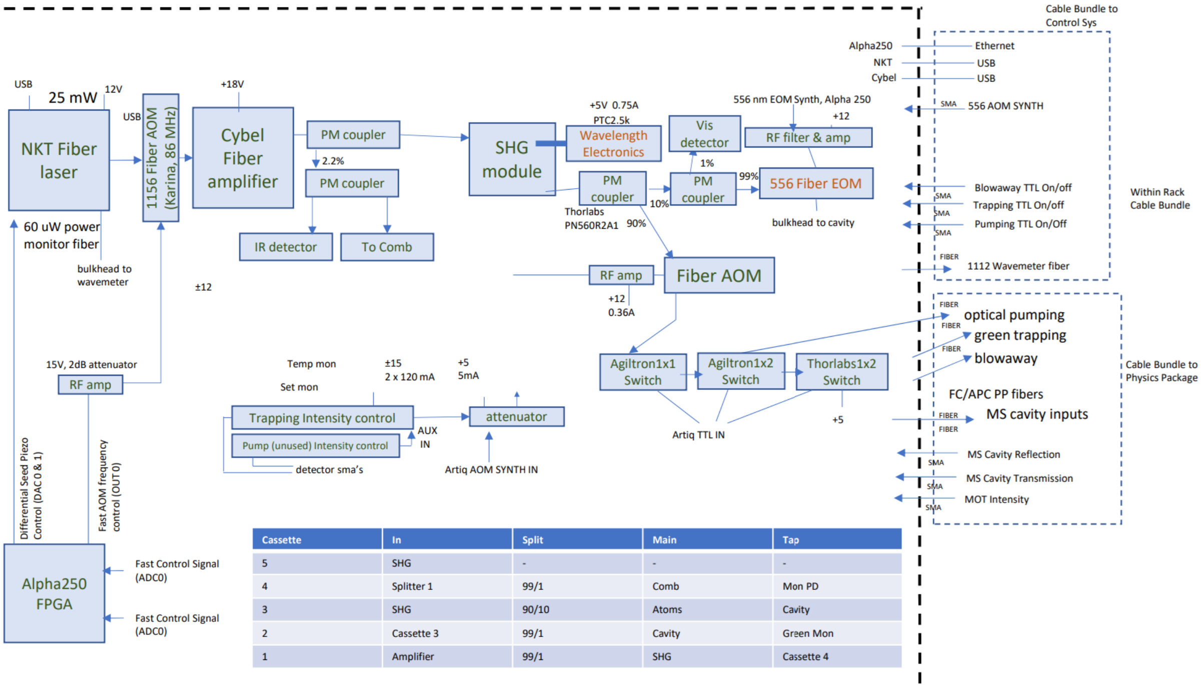

| Cassette | In | Split | Main | Tap |
|---|---|---|---|---|
| 5 | SHG | - | - | - |
| 4 | Splitter 1 | 99/1 | Comb | Mon PD |
| 3 | SHG | 90/10 | Atoms | Cavity |
| 2 | Cassette 3 | 99/1 | Cavity | Green Mon |
| 1 | Amplifier | 99/1 | SHG | Cassette 4 |

## A.6 1388nm module

Figure A.6: Shown here is the optical and electronic layout of the 1388 nm laser board.

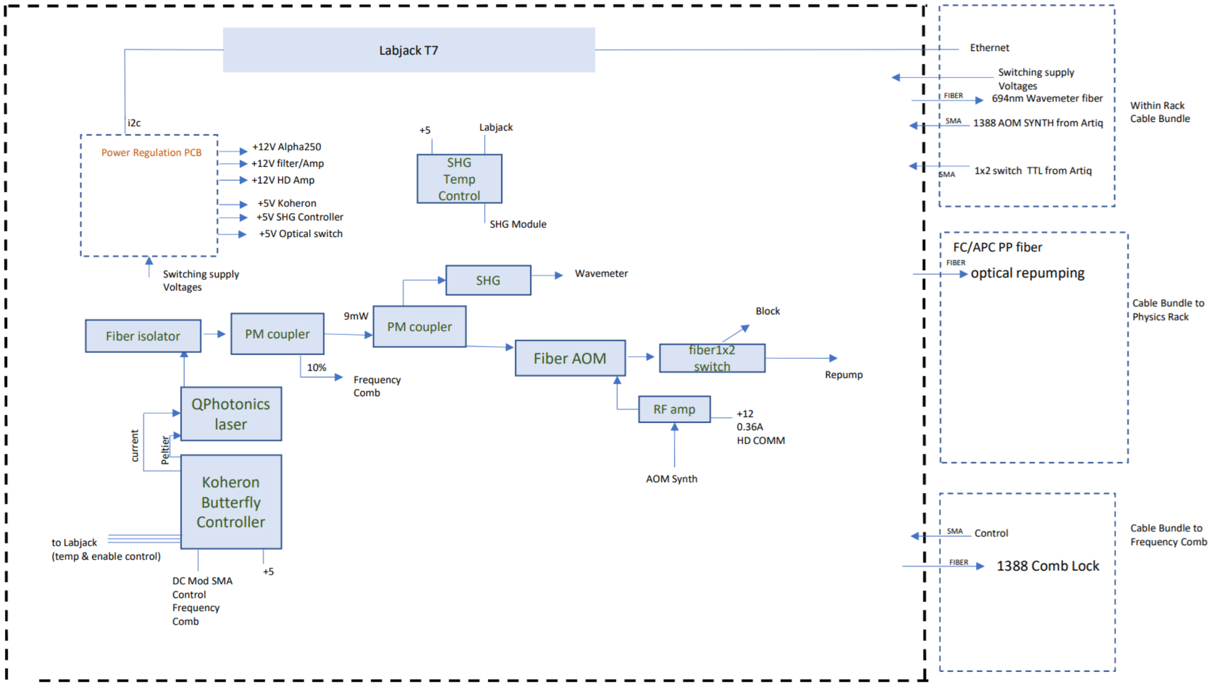

## A.7 759nm module

Figure A.7: Shown here is the optical and electronic layout of the 759 nm laser board.

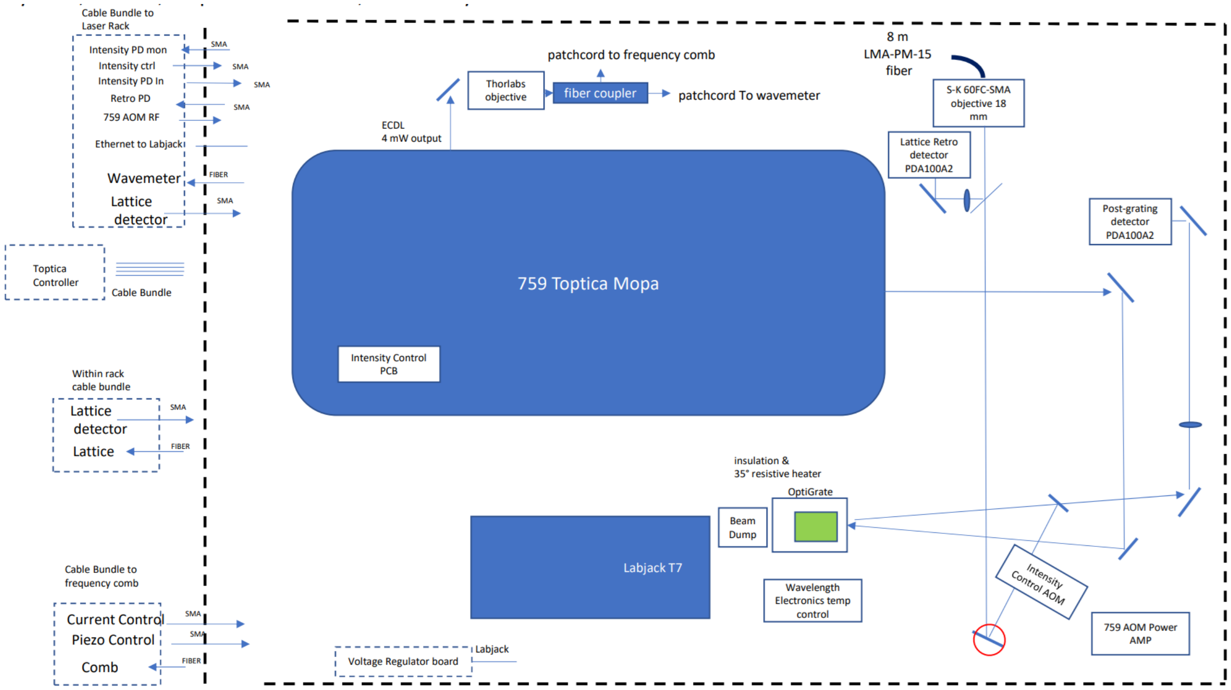

## A.8 Optical alignment of the physics package

This section will describe the complete details for optical alignment of the physics package in the order most commonly done for setting up the system from scratch.

### A.8.1 399 nm MOT alignment

#### A.8.1.1 Slowing-probe overlap

Polarizing plate beam splitters are deceptive optics. One might think that polarizing plate beam splitters can be used as kinematic mirrors for s-polarized light and as windows for p-polarized light, but this is not true. Changing the angle of a polarizing plate, even slightly, can significantly change the optic's interaction with polarized light. The kinematic plate splitter that transmits the slowing beam and reflects the probe beam can either be set up to maximize slowing transmission or to maximize the overlap of slowing and probe, **but not both at the same time**. The probe beam has been upgraded with a kinematic collimator that diminishes, but does not eliminate, this issue. The polarizing plate combiner has been kinematically aligned at an angle that gives the best compromise of transmission and overlap. The present compromise is that the slowing beam is penalized by 2 to 5% in power and the probe beam is maybe 2 or 3mm away from the slowing beam when measured just before going into the periscope. Changing the compromise without might gain 1-2% more slowing power or improve the slowing-probe beam overlap by a few arcminutes, but if the overlap is functional, then there are unlikely to be significant gains from adjusting this optic. Future designs should eliminate this unfortunate optic.

#### A.8.1.2 Setting up the optical alignment

Deliver the 399 nm slowing, 399 nm MOT, and 556 nm MOT light to the chamber with steady-state intensity. Green light will initially only be used as an alignment tool. Do not have the lattice on since you'll be sticking cards and things in beam paths. Insert a cube-shaped reflective optic after the first periscope and point the reflection at some far wall. Use the the "global green" mirror (and maybe the dichroic) kinematic mount to overlap the 556 nm MOT beam with the 399 nm MOT beam. Ensure the MOT beams are well collimated and coaxial for many meters. The beams should also have adequate intensity to servo at their traditional setpoints.

#### A.8.1.3 Setting up the camera

The camera is installed every time the MOT is set up from scratch. It just works much better. Remove the mirror that delivers the optical pumping beam to the chamber. Use the cage mount structure on the lattice delivery board to mount the Thorlabs Kiralux camera and position the lens close to the chamber. The camera should have a 395-405 nm color filter taped on to the lens. Connect the camera's USB 3.0 cable directly to the control computer's front panel (the USB breakout panel only supports USB 2.0). Then use the I/O cable and breakout board to connect the "trigger in" to the "Camera Trigger" channel on the red SMA bundler box. Note that the Thorlabs breakout board connection is very touchy and if you later cannot get the camera to trigger this is the first thing to suspect.

Start Thorlabs camera software, "ThorCam," and connect to the camera. Then, setup the camera in an untriggerered mode. Adjust the lens so that 1) it is on the lowest f-stop number, 2) the lens is focused roughly in between the two viewports. [F-stop is the ratio $f/D$ where $f$ is the lens focal length and $D$ is the diameter of the aperture. Setting the lens to the minimum f-stop, 1.8 for this lens, means the iris is maximally open which increases the number of photons the lens collects but decreases the thickness of the focal plane.] Adjust the camera gain, exposure time, and black level in software.

#### A.8.1.4 Geometric alignment of the slowing beam

Align the slowing beam to go down the axis of the differential pumping tube, straight to the oven nozzle. This alignment can be done by through the backside of the last mirror in the slowing beam path before the chamber which is backside-polished for this purpose. Turn off the room lights, then sight down the atomic beam axis where you should be able to faintly see the slowing beam illuminating the chamber's high emissivity coating. It may helpful to illuminate the inside of the chamber with a flashlight through the top viewport to first see the differential pumping tube. Figure A.8 shows the interior of the epoxy-sealed chamber as seen from the in-vacuum mirror reflection viewed through the slowing viewport.

Figure A.8: The view through the slowing viewport showing the differential pumping tube as reflected off of the in-vacuum slowing mirror. The chamber has been illuminated with a flashlight. This is one of the older epoxy-sealed chambers which has a ring of uncoated aluminum around the differential pumping tube. The newer titanium chambers do not have any masking of the high-emissivity coating, so the pumping tube is somewhat more difficult to see.

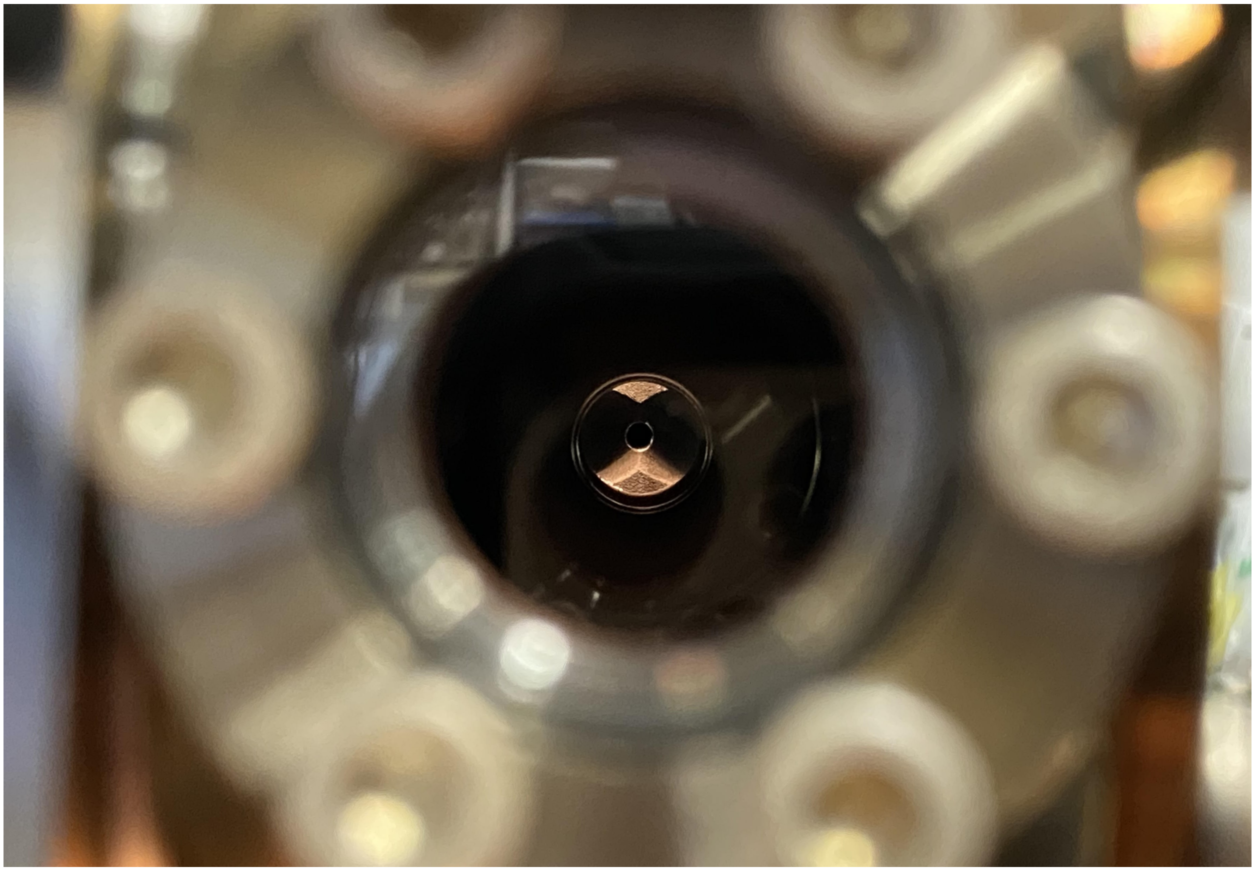

Then use the signal from the camera to maximize fluorescence of the slowing beam on the atoms. The camera gain will need to be very high with the room lights off to see this fluorescence. Use the beam fluorescence to improve the lens' focus and zoom with respect to the atoms. Another technique to align the slowing beam to the atoms is to ramp the 399 nm laser's detuning over the several isotopic transitions. Then, while observing the

PMT fluorescence signal, maximize the peak-to-peak change in fluorescence from the Yb$^{174}$ transition (the big one) with alignment. Yet another technique is to set up a sequence that pulses the quadrupole coils on and off at $\tilde{5}0$ Hz and optimize the atom-magnetic field-laser interaction with the PMT. The 399 nm laser should be locked to the Yb$^{174}$ transition. Note that because the PMT is magnetically sensitive this can produce misleading signals from background scatter.

#### A.8.1.5 Geometric alignment of the MOT beams

Align the horizontal trapping beams to pass through the center of the near chamber viewports using the mirror mounts below the periscopes. The vertical beam does not have this degree of freedom.

Align the trapping beams to be centered on the retroreflectors using the upper periscope mounts for the horizontal beams and the only input mount for the vertical beam. Some green light should be visible through the backside of the retro mirrors and can be used to give a very centered alignment onto the mirror when looking at the mirror from behind.

Use the retro mirrors to retroreflect the three MOT beams on themselves. You can visualize the alignment with a Tiffin lens tissue and notecard beam blocks. Align one path at a time, using notecards to block out all light going to the other paths. Then, occlude the beam path with the lens tissue so that you can see both the forward and backward propagating light. It is easier to start just outside the return viewport aperture and work backwards down the beam. Use the retro mirrors to completely overlap the beam on the lens tissue. Other lens tissues can have too much optical density for this to work. The vertical path can be initially aligned by overlapping the green beams on the lower D-shaped mirror and worked back further with the lens tissue.

#### A.8.1.6 Getting a MOT

Lock the 399 nm laser to the $\mathrm{Yb}^{174}$ transition and run a three-part sequence with the anti-Helmholtz coils on for 200 ms, the coils still on and the camera triggered for 0.01-5 ms, and the coils off for 200 ms. Camera exposure will need to be decreased as the MOT fluorescence improves.

Observe the fluorescence on a camera using high gain and exposure time. You should see broad fluorescence from the atomic beam, as well as a weak MOT somewhere within the atomic beam. An example of this is state is shown in Figure A.9. If no MOT is visible, the first thing to check is always the laser frequency. Unlock the laser and manually tune around the resonance. If this tuning produces a MOT, but the locked laser does not, then it may be necessary to adjust the setpoint of the lock in the Alpha250 GUI. If you still have no MOT, try playing with slowing alignment first, and then MOT alignment. Day to day, the number one cause of no MOT is incorrect frequency. Other potential problems are the oven is cold, the shutter is not open, the magnetic fields are off or wrong, the vacuum is degraded, the sequence and signal are not temporally aligned, the PMT or camera are not powered, have closed irises, are improperly focused, or have gain or other electronic setup errors. Form testable hypotheses and work to methodically eliminate possible issues.

You should NEVER adjust the MOT waveplates while optimizing the blue MOT if you are returning from a configuration that previously could load a lattice. Save that adjustment until you have atoms back in the lattice. The one exception to this rule is the final slowing waveplate, since it does not influence 556 nm MOT temperature; the slowing waveplate, however, has very little power to improve atom number. **AGAIN, DO NOT TOUCH POLARIZATION UNTIL ATOMS ARE BACK IN THE LATTICE.** On the other hand, when aligning a virgin MOT system and a MOT cannot be found for the first time, the issue, as Chris Oates told me, "is always polarization." The two beams perpendicular to coil axis should have the same handedness of their circular polarization and the beam along the coil axis should have the opposite. We operate the coils with the field pointing outwards. While it is possible to choose the correct handedness a priori, it is usually easier just to test the two valid options given the prior constraint. When we were using the epoxy sealed chamber finding the initial MOT was much harder because the window birefringence resulted in sensitivity to retro waveplate angle which a good MOT system is insensitive to.

Figure A.9: A weak MOT forming within the cloud of atoms fluorescing under the influence of the near resonant beams. Once a MOT is visualized, the camera focus can be adjusted again to improve image clarity.

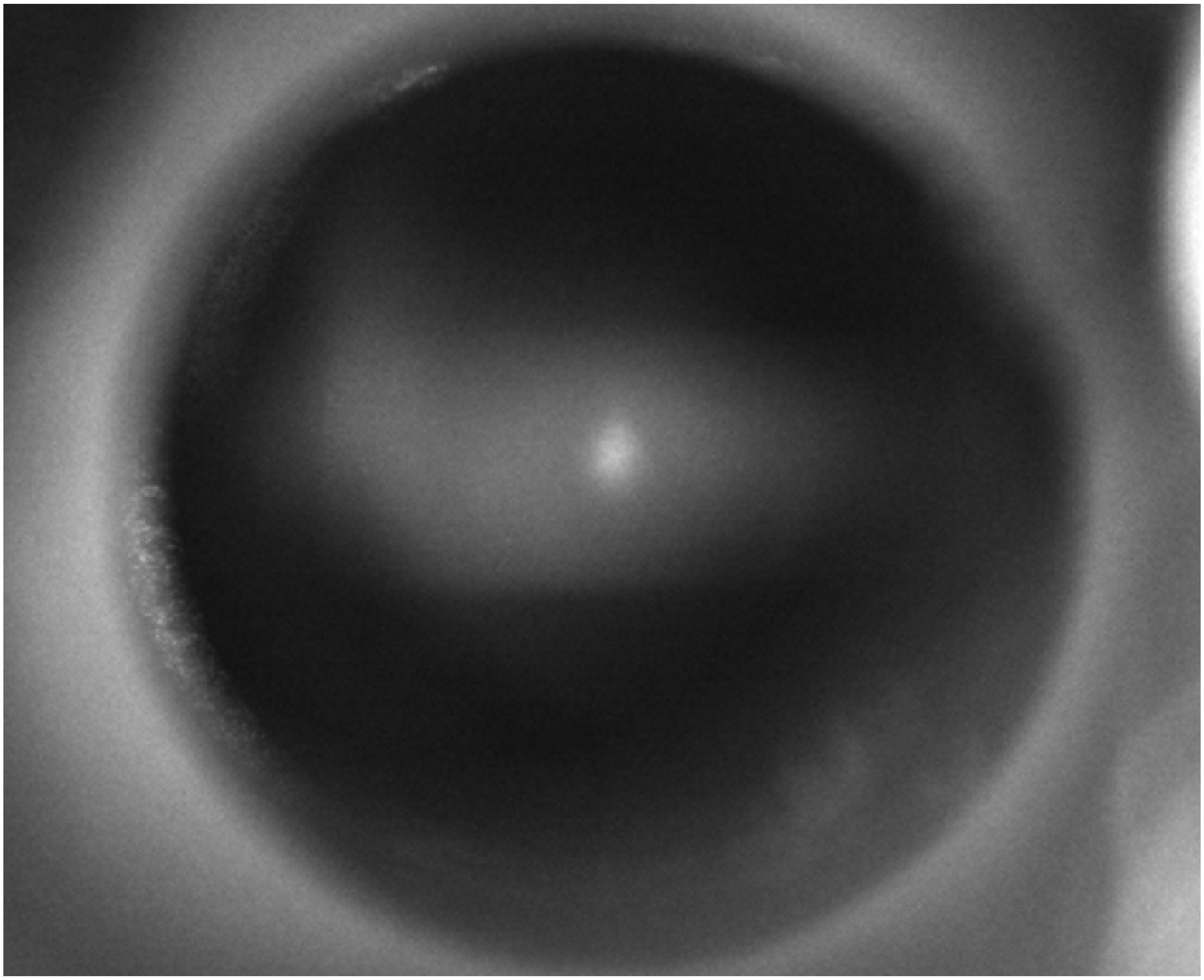

#### A.8.1.7 Optimizing the 399 nm MOT

First, tweak the slowing beam alignment to enhance MOT loading. The geometric optimum of the slowing beam always seems to be slightly off from the loading optimum, and rapid improvements in loading can be made by aligning the slowing beam. Figure A.10 shows the improved MOT after this first improvement.

Figure A.10: An improved MOT after only adjusting the slowing beam. This MOT is saturating the camera and the gain and/or the exposure time should be reduced. At this point, it is helpful to use the cross-section tool in "ThorCam" to put a cross-hair on the MOT which shows vertical and horizontal plots of the fluorescent intensity across the MOT. Set the gain/exposure so that the peak intensity is around 75% and then use alignment to get the fluorescence level off of the graph scale and repeat. A very strong MOT will be many times brighter than the residual fluorescence from the atomic beam. When the MOT is well optimized, and the gain and exposure have, as a result, been turned much lower, the camera will no longer be image the thermal atomic beam.

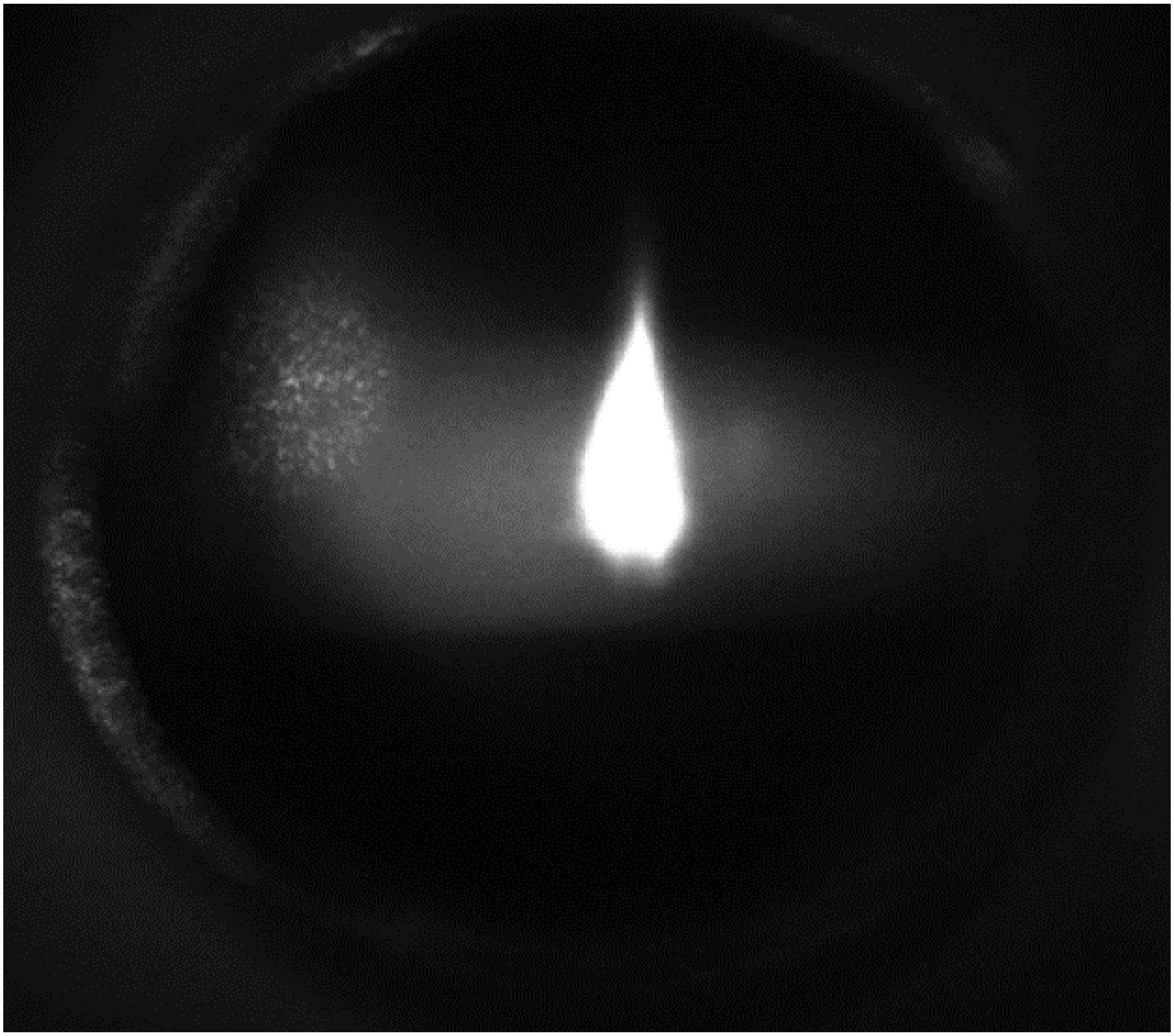

Now that there is a robust signal lock the 399 nm laser to the $\mathrm{Yb}^{171}$ transition. Iterate through alignment knobs in this order: each of the three input mirrors, each of the three retro mirrors, slowing alignment. Repeat this several times until the fluorescence signal converges, turning down the camera gain as necessary to avoid saturation. Now, as a final tune-up, do a two-dimensional walk on the input/retro pair for each arm and on the pair of mirrors that control the slowing beam. Perfection is the enemy of efficiency here. The optimal 399 nm MOT alignment is not the same as the optimal 556 nm MOT alignment and pouring time into pursuing the brightest possible 399 nm MOT will not be rewarded.

#### A.8.1.8 Aligning the probe beam

To align the probe beam, turn it on for a duration of 1 ms immediately after MOT loading (and remember the shutter takes 4 ms to actuate). Roughly overlap it with the slowing beam, then tweak the tip/tilt of the probe beam's independent kinematic mirror until a probe fluorescence signal is observed and maximized. If you are observing the MOT on a camera, a "Zapruder trail" of atoms leaving the MOT should form in the density-center of the MOT. If, for some reason, the probe/slowing beam-combiner were adjusted it might not be possible to get a good probe signal and then you'll need to go back to the first step to find a compromise alignment. Also note, that the probe beam has a tight collimation relative to the 399 nm MOT size and the probe fluorescence is often about half the MOT's fluorescence.

### A.8.2 556 nm MOT alignment

#### A.8.2.1 Setting up the sequence

Set up the camera to trigger simultaneously with the probe so that for the next steps you can easily switch between the camera and PMT signals.

Follow the exact Artiq cooling sequence that is already established. Figuring out the sequence of detunings, gradients, and intensities was the hard part with lattice loading, but now you already have it.

Set up a sequence that ends after the first stage green MOT and is capable of discriminating 556 nm trapping from 399 nm trapping. The sequence must hold the atoms in the first stage of only 556 nm MOT for 30 ms which is sufficient for untrapped atoms to leave the probe region. Have the sequence use the probe laser to read out the fluorescence, but also use the camera to align for density.

#### A.8.2.2 Aligning with the "global green."

First, align the probe to the baby green MOT since the MOT will move in the different B-field. Then use the knob called "global green" to maximize the number of atoms. Global green is the first reflective optic in the green beam path. The dichroic mirror that combines 399 nm and 556 nm is a much worse optic, avoid ever using it unless required for overlapping. Do a small round of tweaking all the retros for atom number. Then adjust the global green alignment one final time. NEVER TOUCH GLOBAL GREEN AGAIN UNLESS YOU WANT TO REALIGN FROM SCRATCH.

#### A.8.2.3 Aligning for a MOT that optimizes lattice loading

Move directly to the full green MOT loading sequence. Run the sequence through the lattice loading stage and immediately probe with normal 4 ms delay. Optimize the fluorescence using all of the knobs for probe and MOT input/retro in a sequence like that advised for the 399 MOT. If using the comb for 556 nm laser lock, there is no reason to adjust the green frequency but it should be checked anyways to ensure you are in a physically normal parameter regime. If locking with the multicolor cavity, 556 nm frequency adjustment is essential to getting lattice trapped atoms. Sweep the 'global_green_freq' in Artiq.

The signal should be near the maximum for the present preset value of 'global_green_freq', and the slope down to zero detuning from resonance should be steep. If using the cavity, adjust the offset sideband frequency in the Alpha250 rather than 'global_green_freq' to optimize atom number. Recall that the offset sideband frequency is multiplied by 8 in the RF chain. Since we are using a known good sequence and the polarization optics are unchanged, this should be enough to get a cold dense sample for loading the lattice. If, after great effort in subsequent steps, the lattice cannot be loaded, you may need to back up to here and use time of flight analysis to make sure the atomic cloud is at $< 20\ \mu$K.

### A.8.3 Lattice alignment

To get the first atoms loaded into the lattice, we align first with a resonant 556 beam to get the lattice on target with the atomic cloud.

#### A.8.3.1 Blowaway

Replace the the sideband spectroscopy fiber with the 556 blowaway fiber. Since the original was 578 nm, all the optics should work just fine.

Align 556 nm beam to overlap with the lattice beam. Use a cage-type optic inserted into the free space between the two mezzanine breadboards and pointed at the ceiling. LASER SAFETY: Keep your head far away from optic, and look obliquely from a distance at the back side of an index card for near field alignment. Align the 556 nm beam using both the collimator input and the dichroic turning mirror to get near perfect alignment with the lattice beam. Now you can turn off the lattice beam to avoid burning the chamber.

Optimize the blowaway sequence given the constraints of the switch. Probably best to find an old sequence and copy the blowaway parameters. The shutter takes several ms to begin closing once the TTL is delivered and has a ms or two of dark time in the middle. More signal can be attained by: 1) leaving the AOM on in MOT mode up until the switch begins, 2) killing the AOM drive in the intermediate state, and 3) blasting the AOM drive with a frequency that puts the blowaway on atomic resonance. Look at the signal on the

556 nm MOT photodiode to figure out the optimal timings.

Now with atoms in the final green MOT align the blowaway to the atoms with the gold-plated mirror on the upper mezzanine. Simply observe the probe's atomic fluorescence on the scope and try to minimize it. Block the lattice retro mirror with an index card so that you do not inadvertently align to a back reflection. Once at an optimum use either RF power in Artiq or an ND filter between the breadboard to further attenuate the blowaway beam. Tweaking the collimation/focus can help significantly since the collimated beam (being smaller than the lattice) will be much larger than the lattice at the atoms (diffraction limit). Defocusing the beam can help achieve higher powers at the atoms. Since the field is already picked to match the MOT size to the lattice, maximizing blowaway effect is the only goal. This process is complete when roughly 75% blowaway is achieved with maximum artiq RF attenuation and an ND=1.0 in place, but really, just find the local minimum. The SM fiber used for the blowaway switch is a curse and you will need to frequently optimize the paddles to keep the green MOT intensity topped off (observe the PD directly). Check that the blowaway signal you're seeing is real, by blocking the blowaway beam and seeing if the fluorescence rebounds.

#### A.8.3.2 Retro

Physically block the blowaway so it can't interfere any more, leave it connected for now though in case it is needed again. Now turn the lattice on low power. Use the lattice retro mirror to align the light back through the chamber. You can observe the forwards light faintly on the bottom viewport of the chamber when looking down and the retro light more strongly. Align the retro spot exactly on top of the forwards spot. At this point, the chamber should be safe as long you don't turn the retro knobs wildly and the lattice can be turned up to full power to enhance available signal. Now, dither the lattice retro knobs slightly while observing the lattice retro PD. If needed, occasionally check the chamber viewports. Once you get some light, it is usually very easy to maximize.

#### A.8.3.3 First lattice trapped atoms

Run a sequence to lattice trapping and permit at least 20 ms for green MOT atoms to dissipate. Use instead the 399 MOT beams to illuminate the chamber and observe the signal on the camera with  20 ms of exposure. If using only the probe beam and PMT (worse) permit at least 60 ms for green MOT atoms to dissipate. Other combinations of light and signal collector do not work well. With any luck, there should be a faint linear wisp of the lattice trapped atoms in the camera view. Verify by blocking the lattice light. Begin the optimization with 'global_green_freq' hopefully with a good cavity-comb setup this will find no difference, but with the multicolor cavity setup, this is crucial. Then, do a quick round of tweak up with the retro alignment. With an adequately strong looking signal on the camera, it will be time to switch to probe-PMT detection.

Top off the alignment of the probe beam to the lattice trapped sample. Now use the lattice input lens and retro mirror as translators to 2D walk the lattice to the optimal location in the atom cloud. This is done by using the top actuator to maximize atom number and the bottom actuator to optimize retro PD power. The top actuator is adjusted in $< 5°$ increments using the width of the Sharpie mark on the knobs as a reference. Later, when the retro mirror has been setup to reflect clock light for phase noise cancellation, you should use the retro lens as an actuator instead so as not to disturb the PNC alignment—you can also use the new technique of aligning for lattice depth with sideband spectroscopy once the sideband beam is back online

After aligning the lattice to the atoms, top off the probe alignment again. Then adjust the combos of input and retro mirrors as described previously. Improving the optical balance can help get colder atoms. Finally. Finally. You can adjust the waveplates for the MOT. Write down their values in the notebook before you begin tweaking them.

### A.8.4 578 Sideband alignment

Same alignment technique as aligning the 556 nm blowaway to lattice alignment, remember laser safety. Also fix collimation. At this point, the population in the edge of blue sideband can be used as an error signal to align the lattice for maximum depth. Align to bring this population up, then increase the sideband frequency and repeat. It might be wise to walk the retro lens and mirror so that maximum depth and maximum retro signal are coincident.

### A.8.5 1388 alignment

Use an IR card, turn off the lattice, turn on the sideband beam. Unfortunately this one cannot be overlapped exactly due to a tolerance error about transmitting through thick optics. However, very little power is needed in this beam so it works out. Use the IR card to align the beam so that just before the upper vertical D-mirror into the chamber the 1388 is 2 mm to the right of the sideband beam and just after the bottom turning D-mirror it is 2mm to the left of the sideband beam. Usually, this is all the alignment that is needed. Future breadboard versions should fix this inability to overlap.

### A.8.6 578 Clock alignment

The clock light enters on a 5 axis kinematic mount. Optimize the beat note with angle kinematics only. Optimize the alignment to the lattice beam with translation. To do so, turn off the room lights and turn down lattice power with both amplifier and polarization, center clock in lattice just after retro mirror and then check again between mezzanine breadboards. It might be a possible new problem that the lattice is severely off the clock axis, in which case the clock won't be able to both get through the Faraday rotator and center on the lattice beam. Walking the lattice with the top-actuated mirror and the retro mirror or lens would rectify this.

# Appendix B

## Construction Details of the Clock

Here's instructions for some of the more involved constructions.

### B.1 Machining the slowing mirror thermal feed through

Part: Power Feedthrough, 8000 Volts, 300 Amps, 1 Pin, 0.38”” Copper Conductor, 1.33” Conflat Flange, PN: A0221-2-CF

Cut vacuum side of copper feedthrough to 0.844” beyond the edge of the stainless flange. This operation should be performed on the lathe with the flange (not the copper) chucked with tight control for axial symmetry. Choose an excellent sharp cutting tool. Select an appropriate RPM to maintain 100-200 SFM of cutting and adjust that RPM every 1/16” of depth to maintain the correct SFM. Feed the cutting tool very slowly. Negligence in this process will result in a bent copper feedthrough. Kroil works best for cutting copper, but it's kind of gross to get it flung on you by the lathe, so coconut oil is acceptable.

Still in the lathe, on the axis of the vacuum-side copper: use a centering drill to begin the cut and cut deep enough to make a small chamfer. Then bore a #29 (.1360) hole to a 1/2” depth beyond the chamfer.

Tap the hole with the special blind hole tap for copper. It's a bottoming 8-32 spiral flute with WC coating (in the machine shop Yb drawer) and use Kroil to lubricate the cutting.

Flip the piece on the lathe to operate on the out of vacuum side. Again use a centering drill to make a small chamfer on axis. Then bore a #30 (.1285) hole to 1” (total) depth. The current 1/8” cartridge heater we are using expands and requires low precision on this hole ID. A previous design had an exact 1/8” cartridge heater and required boring a slightly undersize hole followed by reaming to 1/8”.

Do any deburring required. Then clean the piece very thoroughly in the normal methods of ultrasonic cleaning for vacuum preparation. Do not expose the piece to degreaser for overlong as this will cause the copper to oxidize.

## B.2 Mounting the atomic beam shutter

Part: Wobble stick for 1.33” CF, MDC Precision, PN: 693001 Cut the wobble stick to length on the vacuum side as measured from CAD file to reach center of atom beam + some. The cut length does not need to be very exact, as long as the stick will not catch on bottom of two-way port it will work but remember that the bellows will compress under vacuum. To get the blocking bead in the center, I estimate where it should be from the CAD file and then assemble the wobble stick into a Kimball two-way port with a 2.75” window on one side and a center-marked 2.75” blank on the other. Then I pull 10 Torr vacuum from the remaining 1.33” CF. Repeat the positioning until satisfied it is centered. Mark the spot that the bead needs to go and reassemble it with a little TorrSeal as both a thread locker and bead-stick glue.

## B.3 Pinch off tubes

You’ll need the CHA Industries guillotine pinch off tool and the attached Enerpack hydraulic actuator. They are currently on the shelf in the galley behind 1G108. The $\frac{3}{4}$” pinch off tubes with 1.33” CF to 2.75” CF flanges are on a higher shelf in the same area.

- Practice pinching off on sacrificial tubes several times. It’s better to over crush, but not by much. Tubes should separate on their own or with near zero additional force, if you must wiggle it, it’s not crushed enough. Excessive force can cause the jaws of the device to shatter.

- Our Enerpack leaks a little hydraulic fluid, so be careful not to make a mess. It may need new fluid at some point. If it's not crushing, it's probably because you don't have the pressure lock engaged.

- It is critical that no dirt, oil, or oxidation of any kind get inside the pinch-off tube. Treat it with even more care than standard vacuum components. The other most common way for the cold-weld to fail is that the metal prematurely work-hardens and no longer flows together under pressure. Most of the remaining tips aim to reduce work-hardening effects.

- Setup the vacuum system so that there is a valve between the turbopump and the pinch off tubes. Use rigid mountings with vacuum components to the turbopump to prevent bending and strain on the pinch tubes.

- Wrap the tube in UHV aluminum foil tightly and seal the edges with Kapton tape before the bakeout to reduce oxidation of the copper. The tubes can be baked to 300C. There is some possibility of a failure due to thermal hardening if they are baked at 250C+ for over 7 days. If your vacuum fails for some other reason during bakeout, you should assume that tubes are compromised due to internal oxidation and require replacement.

- Polish off any oxidation with a Scotchbrite/Brillo pad after the bakeout until you have a shiny finish.

- Lightly oil the tube and guillotine jaws with 3-in-1 oil or another light machine oil.

- Valve off the turbo pump before attempting the pinch-off so you don't kill the turbo if the pinch-off fails.

- Setup a pinch off device around the tube exactly in the middle of the tube and make sure it has a very rigid mount before beginning the pinch. It is much better to over engineer the mount to hold the bottom jaw exactly in place than to let it move around on you.

- Crush the tube completely and separate. Check the ion pump value for success. If there's a leak it will almost certainly put the pressure above 1e-6 Torr. Usually, leaks are symmetrical so you could check a gauge on the pumping station end as well.

- Clean off the tube with an acetone wipe and then protect the pinched edge with a coat of TorrSeal allowed to air cure overnight. Provide additional protection by shrouding the end with a 1” hot shrink-tube, heat-gunning the tube, and finger pinching it while still hot so that it bonds together over the pinch-off.

- We’ve been using copper successfully, but more expensive nickel tubes are supposedly less prone to failure although they also require higher peak pressures to cold-weld.

## B.4 Forming vacuum seals with epoxy

As discussed in the main text, epoxy seals supported operation at the $1 \times 10^{-10}$ Torr level briefly before evolving to sustained operation at the $2 \times 10^{-8}$ Torr level.

Here are some procedures for applying Epotek H77 for sealing optical windows. I have used both the regular H77 and the H77T high viscosity formulation.

### B.4.1 General procedure for applying epoxy

1. Design and machine the seat that the window will sit in.

Here is the design we used when hand milling test chambers, we now use CNC milled chambers with 14 mm windows. We created a “stepped” bore design to hold the window and the epoxy. The 1” window sits on a lip with a 7/” ID and 1” OD. The 1” bore has a depth 0.1” - 0.15” greater than height of the window’s chamfer. This tight tolerance region is important for both holding the window while applying epoxy, reducing the surface area of epoxy exposed to vacuum in case of gas flux from atmosphere, and because epoxies perform best in the minimum bond thickness regime. This region however probably increases risk of window breakage due to the CTE mismatch between the NBK7 windows and aluminum chamber we use. Then there’s a 1 & 1/16” bore with 0.1” to 0.2” depth that is the epoxy trench.

2. Prepare the surface of the seat for the epoxy.

After milling out the above design in aluminum, we hand sand the epoxy sealing surface with fine papers, finishing with a 30 micron grit optical sanding paper. One of the first epoxies we tested specified a surface roughness of 1 microinch for optimal bonding, although the H77 did not include such a spec. Then we clean the workpiece in an alconox sonic bath. To form a clean and dense aluminum oxide finish on the vacuum and sealing surfaces we treat them with 1 molar citric acid for 10 minutes followed by another alconox sonic bath to remove residual smut. Then we rinse the piece successively with distilled water, acetone, distilled water, methanol, and distilled water. We bake the piece dry at 120 C and now it is ready for applying epoxy.

3. Mix the epoxy at manufacturer's recommended ratio with a scale that supports 10mg measurements or better. We mix it in a glass beaker with a glass stir stick; some plastics seem to react with the epoxy.

4. Pull the epoxy into a syringe. We use the ones available from Thorlabs. Pull in some air, then squish out all the big bubbles.

5. Apply the epoxy into the trench surrounding the window. Fill it up and make a small "volcano" around the window.

6. There's some small pinprick bubbles in the epoxy leftover from the mixing and syringing. Put the part into a beaker to keep it dry and float the beaker in a sonic bath for 5 minutes to pop some of these bubbles and work the epoxy in to the bond region.

7. Permit the epoxy to room temperature cure for long enough that a sample of reserved epoxy from the application step no longer flows due to gravity.

8. Cure the epoxy. We put the workpiece into a sheetmetal box (if it can fit) before putting it in the oven to reduce thermal gradients and transients. Ramp the temperature up to 150 C at no more than 2 C/minute. Hold at 150 C for an hour. Then cool at the same rate. There's some goal competition here between thermal stress and final properties. Hotter faster cures result in denser epoxies which should improve vacuum properties and increase thermal conductivity, but they also risk breaking the windows.

8. The piece is ready for vacuum. The highest we've ever baked out the H77 is 180 C

although the data sheet says it can tolerate up to 250 C continuously. We usually are very careful with this part of the chamber and try to keep the ramp up/down to no greater than 0.5 C/minute. If you helium leak check your chamber while the epoxy is hot, you may notice some delayed inflow through the epoxy at the $10^{-11}$ Torr L/s level from the helium you put into the room.

9. After the bakeout, the dominant gases you should see will be from the rest of your chamber (e.g. H2 for stainless) followed by CO and CH4 at or below the $10^{-10}$ Torr level which seem to be released from the epoxy.

### B.4.2 Fixing a leak

We haven't had to do this with the H77 yet, but with the other epoxy this procedure worked to repair failed seals. During bakeout the seal sometimes failed at the $10^{-6}$ Torr level. Open up the foil and find the leak with the RGA and helium or the 66 AMU computer duster. Switch the RGA to N2. Smear on more epoxy with a microbrush. When you get the right spot N2 will plummet by a factor of 100 in 5 seconds. Resume bakeout.

### B.4.3 Removing epoxy

It is likely easier just to get a new part. But if you have to, the best method we've found is to start by smashing out the window. Then use a very hot soldering iron to soften the epoxy and gently scrape it away. Dissolve/soften the rest in a 24 hour dichloromethane bath. Scrape away the remainder with a razor. The bath might need to be repeated.